UNIVERSITI TEKNOLOGI MARA

DEVELOPMENT OF CIRCULAR POLARIZED WEARABLE TEXTILE ANTENNA WITH BANDWIDTH ENHANCEMENT FOR GLOBAL POSITIONING SYSTEM (GPS) APPLICATION

ANIS FARIZA MD. PAZIL

PhD

August 2026

UNIVERSITI TEKNOLOGI MARA

DEVELOPMENT OF CIRCULAR POLARIZED WEARABLE TEXTILE ANTENNA WITH BANDWIDTH ENHANCEMENT FOR GLOBAL POSITIONING SYSTEM (GPS) APPLICATION

ANIS FARIZA MD. PAZIL

Thesis submitted in fulfilment
of the requirements for the degree of
Doctor of Philosophy
(Electrical Engineering)

Faculty of Electrical Engineering

August 2026

CONFIRMATION BY PANEL OF EXAMINERS

I certify that a Panel of Examiners has met on 3rd June 2026 to conduct the final examination of Anis Fariza binti Md. Pazil on her Doctor of Philosophy thesis entitled "Development of Circular Polarized Wearable Textile Antenna with Bandwidth Enhancement for Global Positioning System (GPS) Application" in accordance with Universiti Teknologi MARA Act 1976 (Akta 173). The Panel of Examiners recommends that the student be awarded the relevant degree. The Panel of Examiners was as follows:

Mohamad Fahmi Hussin, PhD
Associate Professor
Faculty of Electrical Engineering
Universiti Teknologi MARA
(Chairman)

Suhaila Subahir, PhD
Senior Lecturer
Faculty of Electrical Engineering
Universiti Teknologi MARA
(Internal Examiner)

Saidatul Norlyana Azemi, PhD
Associate Professor
Faculty of Intelligent Computing
Universiti Malaysia Perlis
(External Examiner)

PROF DR HJH ZURAEDA IBRAHIM
Dean
Institute of Postgraduate Studies
Universiti Teknologi MARA

Date: 27 August 2026

AUTHOR'S DECLARATION

I declare that the work in this thesis was carried out in accordance with the regulations of Universiti Teknologi MARA. It is original and is the results of my own work, unless otherwise indicated or acknowledged as referenced work. This thesis has not been submitted to any other academic institution or non-academic institution for any degree or qualification.

I, hereby, acknowledge that I have been supplied with the Academic Rules and Regulations for Postgraduate, Universiti Teknologi MARA, regulating the conduct of my study and research.

Name of Student	:	Anis Fariza Md. Pazil
Student ID. No.	:	2017375011
Programme	:	Doctor of Philosophy (Electrical Engineering) – EE950
Faculty	:	Electrical Engineering
Thesis Title	:	Development of Circular Polarized Wearable Textile Antenna with Bandwidth Enhancement for Global Positioning System (GPS) Application
Signature of Student	:	
Date	:	August 2026

ABSTRACT

Wearable GPS-L1 antennas require stable circular polarization, wide angular coverage, and reliable performance under body movement, orientation variation, and bending deformation. However, many reported textile antennas are designed using manufactured substrate properties with limited fully textile implementation and are mainly evaluated under planar conditions. This creates uncertainty in predicting antenna performance because textile materials are porous, compressible, and thickness-sensitive. Moreover, the circular polarization can degrade significantly when the antenna is subjected to practical wearable deformation. Therefore, limited axial-ratio (AR) beamwidth, narrow circular polarization bandwidth, and reduced polarization purity remain critical challenges for fully textile GPS antennas. This research presents a systematic characterization design of a fully textile circularly polarized antenna for GPS-L1 operation at 1.575 GHz, focusing on improved bandwidth, wider axial-ratio coverage, and stable performance under bending. The electromagnetic behaviour of textile materials is systematically investigated by considering frequency, substrate thickness, conductivity, and transmission loss behaviour. Using the Transmission Line Method (TLM), 3 mm felt is identified as the most suitable substrate because it exhibited the lowest transmission loss compared with Tencel and denim. Based on the characterized substrate, a single-layer fully textile antenna is developed using dual L-shaped slots with corner truncation to generate circular polarization and enhance AR beamwidth. The proposed antenna achieved 3-dB AR beamwidths of 150° and 135° in the principal planes, and 120° and 165° in the diagonal planes. Right-hand circular polarization is obtained with a measured gain of 3.96 dBi and a front-to-back ratio of 16.86 dB. To improve bandwidth and bending robustness, a Defected Ground Structure (DGS) is integrated into the ground plane outside the patch footprint, thereby preserving the patch surface current distribution without requiring patch re-tuning or geometrical modification. The impedance bandwidth increased from 105 MHz to 140 MHz, while the AR bandwidth improved by 286%. The minimum AR is reduced to 0.99 dB and the cross-polarization discrimination reached 24.88 dB, indicating enhanced polarization purity. Under E-plane and H-plane bending, AR ≤ 3 dB is maintained within the GPS-L1 band, with AR beamwidth ranging from 75° to 150°. Overall, this research contributes a systematic textile electromagnetic characterization approach and a compact fully textile circularly polarized antenna with improved AR beamwidth, bandwidth, polarization purity, and bending stability for GPS-L1 wearable applications.

ACKNOWLEDGEMENT

In the name of Allah, the Most Gracious, the Most Merciful, I begin by offering my deepest gratitude to Allah s.w.t, the Creator, for His infinite guidance, blessings, and strength that have carried me through this incredibly long journey. Without His grace, none of this would have been possible. Praise be upon Him.

I am profoundly thankful to my dear supervisor, Associate Professor Ir. Dr. Nurul Huda binti Abd Rahman and co-supervisors Ts. Dr. Nurulazlina binti Ramli, and Dr. Robi'atun Adayiah binti Awang. Your wisdom, encouragement, and unwavering support have not only guided my research but also nurtured my growth as a scholar. May Allah grant you blessings and reward you Jannah for your invaluable contributions to my journey.

To my beloved husband, Nor Azrishahril bin Aris who has been by my side throughout this very long ride and to my pillars of strength Nurin Sofea, Nazrin Shahmi and Nazrin Shafy, this achievement is not mine alone; it belongs to you too. For every step I took, I took it with you by my side. May this journey in pursuit of knowledge inspire you to dream boldly and soar even higher in life.

There are prayers unheard by people, but never unheard by Allah. In every step that felt heavy, there were hands that never grew tired of being raised in supplication. In every moment of despair, there were lips that never ceased to mention my name in endless prayers. Thank you to my loving parents, Haji Md. Pazil bin Abdul Rahman and

my blessed parents-in-law, Haji Aris bin Jamali and

May every letter written on this doctoral degree become a continuous source of reward for you. To my siblings, Aizi Fariz, Dr. Afiza Hani, Afifah Hanim and Atiqah Hanis, thank you for being my comfort, and my greatest motivation.

To the members of the Antenna Research Centre (ARC), UiTM Shah Alam and SEGi University, thank you for your camaraderie, collaboration, and the invaluable knowledge we've shared. Your support has made this journey less solitary and more fulfilling.

Finally, I wish to honour the memory of my late supervisor, Allahyarham Prof. Tarmizi bin Ali, whose early guidance laid the foundation for this research. His legacy lives on in the work I have accomplished. To the late Senior Laboratory Officer, Allahyarham Encik Fadly bin Riduan, a deep gratitude for his dedication and assistance in this journey.

May Allah shower His mercy upon us and grant us His blessings and guidance in all our endeavours. Aamin ya Rabbal A'alamin.

TABLE OF CONTENTS

		Page
CONFIRMATION BY PANEL OF EXAMINERS		**ii**
AUTHOR'S DECLARATION		**iii**
ABSTRACT		**iv**
ACKNOWLEDGEMENT		**v**
TABLE OF CONTENTS		**vi**
LIST OF TABLES		**x**
LIST OF FIGURES		**xii**
LIST OF SYMBOLS		**xix**
LIST OF ABBREVIATIONS		**xx**
CHAPTER 1 INTRODUCTION		**1**
1.1	Research Background	1
1.2	Problem Statement	5
1.3	Research Objectives	8
1.4	Scope of Thesis	8
1.5	Thesis Organization	9
CHAPTER 2 LITERATURE REVIEW		**11**
2.1	Introduction	11
2.2	Wearable Technology and Applications	11
2.3	Textile Antenna Materials and Characterization	13
2.4	Electromagnetic Properties in Textile Materials	15
	2.4.1 Dielectric Properties of Textile Substrate	15
	2.4.2 Electrical Properties of Conductive Textile	22
2.5	Textile Antenna Performance for On-Body Application	24
	2.5.1 Effects of Bending on Textile Antenna Performance	24
	2.5.2 Bandwidth Enhancement Technique	28

2.6 Design of Wearable Textile Antenna for GPS Application 31
2.6.1 Circular Polarization Generation Techniques in Antenna Design 37
2.6.2 Circular Polarization Enhancement Techniques 41
2.6.3 Feeding Techniques 45
2.7 Summary of Research Context and Gap from the Existing Wearable Textile Circularly Polarized Antenna Studies for GPS Applications 48
2.8 Summary 50

CHAPTER 3 RESEARCH METHODOLOGY 52
3.1 Introduction 52
3.2 Flow of Research Work 52
3.3 Textile Antenna Design Requirements and Performance Specifications 57
3.4 Determination of Textile Components 58
3.5 Measurement of Thickness and Dielectric Properties of Substrate (Non-Conductive Layer) 59
3.5.1 Open-ended Coaxial Probe Measurement Method 61
3.5.2 Free Space Measurement Method 63
3.6 Transmission Loss Evaluation using Transmission Line Method 68
3.7 Design of Textile Antenna 71
3.7.1 Calculation of Antenna Dimension 71
3.7.2 Probe-feed Technique 73
3.8 Simulation of Textile Antenna 74
3.8.1 Development of Textile Antenna Model 75
3.8.2 Simulation of Antenna in Bending Conditions 76
3.9 Fabrication and Measurement of Textile Antenna 79
3.9.1 Antenna Fabrication and Assembly 79
3.9.2 Return Loss Measurement 81
3.9.3 Radiation Pattern Measurement 82
3.10 Legal, Ethical and Sustainability Considerations 84
3.11 Summary 85

CHAPTER 4 DEVELOPMENT OF CIRCULAR POLARIZED WEARABLE TEXTILE ANTENNA FOR GPS APPLICATION 87

4.1 Introduction 87

4.2 Transmission Line Method (TLM) Analysis for Dielectric Substrate Selection 87

4.2.1 Simulated Fabric Thickness and Conductivity Performance Analysis of Dielectric Substrates Selection 88

4.2.2 Measured Conductivity Performance Analysis of the Selected Dielectric Substrate 95

4.3 Parametric Study of Antenna Design 97

4.3.1 Effects of Corner Truncation Dimensions 98

4.3.2 Effects of Horizontal and Vertical Slot Variation 99

4.4 Simulation of Dual L-shaped Slotted Antenna with Circular Polarization 101

4.4.1 Evolution from Linearly Polarized to Circular Polarized Antenna 101

4.4.2 Surface Current Distribution Analysis for Circular Polarization Verification 104

4.5 Antenna Fabrication and Measurement 105

4.6 Performance Analysis of Simulated and Measured Key Parameters of Circular Polarization Antenna 107

4.7 Summary 115

CHAPTER 5 DEVELOPMENT OF WEARABLE TEXTILE ANTENNA WITH DEFECTED GROUND STRUCTURE 116

5.1 Introduction 116

5.2 Antenna Design with Defected Ground Structure (DGS) 116

5.2.1 DGS Design Parameters and Evolution 118

5.2.2 Surface Current Distribution Analysis 122

5.3 Effects of Bending on Antenna Performance 124

5.3.1 Simulation and Measurement Setup of Bending Analysis 125

5.3.2 Return Loss (S_{11}) Analysis 127

5.3.3 Gain and Radiation Pattern Analysis 133

5.3.4 RHCP and LHCP Performance Analysis 137

5.3.5 Axial Ratio (AR) Bandwidth Analysis 141
5.3.6 Axial Ratio 3-dB Beamwidth (ARBW) Analysis 145
5.3.7 Overall Effect of DGS under Bending and Simulation-Measurement Discrepancies 150
5.4 Specific Absorption Rate (SAR) in Wearable Antenna 152
5.5 Checklist for GPS Application and Comparison with Existing Works 154
5.6 Summary 157

CHAPTER 6 CONCLUSION 159
6.1 Conclusion 159
6.2 Research Contributions 164
6.2.1 Systematic Electromagnetic Characterization of Textile Materials 164
6.2.2 Integrated Single Layer Fully Textile Circularly Polarized Antenna with Wide Angular Coverage 165
6.2.3 Out-of-Patch-Footprint DGS for Bandwidth Enhancement, Beamwidth Preservation, and Bending Mitigation 166
6.3 Recommendations for Future Works 167

REFERENCES 168

APPENDICES 175

AUTHOR'S PROFILE 183

LIST OF TABLES

Tables	Title	Page
Table 2.1	Dielectric Properties of Non-Conductive Textile	17
Table 2.2	Electrical Properties of Conductive Textiles	24
Table 2.3	Summary of Research Context and Gap from the Existing Wearable Textile Circularly Polarized Antenna Studies for GPS Applications	49
Table 3.1	Specification of Textile Antenna Materials	57
Table 3.2	Simulation Parameters for Conductivity Measurement using Transmission Line Method (TLM)	57
Table 3.3	Target Specification for the Proposed Antenna Wearable Textile Antenna System	58
Table 3.4	Classification of Textile Variants	59
Table 3.5	Selected Textile Variants and Conductor	60
Table 3.6	The Parameter Measured Values of Selected Substrates for Open-ended Coaxial Probe Measurement Method	63
Table 3.7	The Parameter Measured Values of Selected Substrates for Free Space Measurement Method	68
Table 4.1	Fabric Thickness Performance on Return Loss (S_{11}) and Transmission Loss (S_{21}) Parameter	90
Table 4.2	Simulated and Measured Data of S1, S2 and S3	95
Table 4.3	Dimensions of the Proposed Antenna	102
Table 4.4	Comparative Analysis of the Reported CP Antennas for Wide Beamwidth and Textile GPS Application	114
Table 5.1	Parameters and Dimensions of the Proposed DGS-integrated Antenna	121
Table 5.2	Comparison of Simulated and Measured Antenna With and Without DGS	122
Table 5.3	Comparison of Simulated and Measured S_{11}, Detuning, Impedance and GPS Bandwidth Coverage under Planar, E-	130

	plane Bending and H-plane Bending With and Without DGS	
Table 5.4	Gain and Front-to-Back Ratio (FBR) Performance of the Antenna With and Without DGS at φ =0° and φ =90° under Planar and Bending Conditions	136
Table 5.5	RHCP/LHCP Gain Performance Comparison for the Antenna With and Without DGS at φ = 0° and φ = 90° under Planar and Bending Conditions	140
Table 5.6	Previous Studies of DGS-based Antenna on Cross-Polarization Discrimination (XPD)	141
Table 5.7	Axial Ratio, AR Bandwidth and GPS Coverage Performance of the Antenna With and Without DGS under Planar and Bending Conditions	144
Table 5.8	3-dB Axial Ratio Beamwidth (ARBW) Performance of the Antenna With and Without DGS under Planar and Bending Conditions	146
Table 5.9	Summary of the Measured GPS Performance Validation for Antenna With DGS and Without DGS	155
Table 5.10	Comparative Evaluation of Circularly Polarized Textile Antenna with Respect to Bending Validation	156

LIST OF FIGURES

Figures	Title	Page
Figure 1.1	Various Wearable Applications and Technologies	1
Figure 1.2	Excerpt of Radio Spectrum Allocation in Malaysia for GPS-L1 from MCMC	2
Figure 2.1	The Relationship Between the Applied and Internal Electric Fields	16
Figure 2.2	Parallel Plate Measurement Technique	19
Figure 2.3	Transmission/Reflected Line Measurement Technique	20
Figure 2.4	Free-space Measurement Technique	20
Figure 2.5	Open-ended Coaxial Probe Measurement Setup	21
Figure 2.6	Samples of Conductive Textiles	23
Figure 2.7	Antenna Being Worn at a) shoulder b) front and c) back	25
Figure 2.8	Bending Orientation of E-plane and H-plane	26
Figure 2.9	Antenna Bent based on Radius for Curved Surface	27
Figure 2.10	Antenna Bent Curvature based on Angle, θ	27
Figure 2.11	Textile Antenna with a) Circular Arc-shaped Parasitic Patch and Meta surface Element	29
Figure 2.12	Textile Antenna with DGS using a) U-slot b) Modified Ground	31
Figure 2.13	GPS Frequency Bands and the Corresponding Bandwidths	32
Figure 2.14	GPS under GNSSs at Medium Earth Orbit	32
Figure 2.15	GPS Nominal Constellation of 24 Satellites in Six Orbital Planes	32
Figure 2.16	GPS Textile Antenna with Non-textile Conductive Layer a) Denim Substrate and Copper Sheet b) Jeans Substrate and Copper Sheet	34
Figure 2.17	Two Rotation Directions of Wave Travelling Perpendicularly Away from the Observer a) Left Hand Polarization b) Right Hand Polarization	34

Figure 2.18	Electric Field Representation of Elliptical Polarization	35
Figure 2.19	Antenna Measurement Coordinate System	36
Figure 2.20	The Effect of Antenna Beamwidth on Coverage Angle	37
Figure 2.21	Corner Truncation Geometry with a) V and Square-shaped Slits b) Slits and Centre Cross Slot c) Slits in Elliptical Patch d) Irregular Hexadecimal AMC e) Diagonal Slot and AMC	38
Figure 2.22	Slot-based Perturbation a) U-shaped and Centre slot b) Modified E-slot c) L-form Slot d) LI-slotted	39
Figure 2.23	a) Dual-feed configuration b) Single-feed configuration	41
Figure 2.24	Wide AR Beamwidth GPS Antenna a) Asymmetric Structure Patch with an Arc Structure b) Two-pair of Parallel Slots on a Circular Patch c) Asymmetric Slot and Coupled Strip)	42
Figure 2.25	Textile Antenna with Periodic Structures	44
Figure 2.26	Type of Feeds for Microstrip Antennas	46
Figure 2.27	The Simulated and Fabricated Textile Antenna using a) Microstrip Line Feed b) Coaxial Probe Feed	48
Figure 2.28	Comparative Analysis of Surface Current Distribution of Microstrip Feedline and Coaxial Probe Feeding	48
Figure 3.1	Flowchart of Research Works	56
Figure 3.2	Measurement of Substrate Thickness using Digital Thickness Gauge	60
Figure 3.3	Measurement Setup for Dielectric Properties	61
Figure 3.4	Open-ended Coaxial Probe Measurement Illustrating S_{11} Reflection at the Probe-MUT Interface	62
Figure 3.5	Textiles Dielectric Measurement	63
Figure 3.6	Free-space Method Measurement Setup	64
Figure 3.7	Free-space Measurement Setup in MRI	65
Figure 3.8	Free-space Measurement Setup with MUT	65
Figure 3.9	The Process for NRW Method	66
Figure 3.10	Two-Port Transmission Line Model	68
Figure 3.11	Two-Port Transmission Line Model Design	69

Figure 3.12	Two-Port TLM Simulation in CST for Denim, Felt and Tencel Substrate at *h*=0.5 mm in CST	69
Figure 3.13	The Fabricated Transmission Line for Sample 1, Sample 2 and Sample 3 (a) Front View (b) Bottom View	70
Figure 3.14	Measurement Setup for the Conductivity Measurement on TLM	70
Figure 3.15	Geometrical Top View of Rectangular Planar Antenna	72
Figure 3.16	The Configuration of Coaxial Probe-feed Attached to Antenna	73
Figure 3.17	SMA Square Flange Jack Receptacle by Multicomp Pro	74
Figure 3.18	Simulation of Rectangular Microstrip Patch Textile Antenna using CST Software	75
Figure 3.19	SMA Port Excitation	76
Figure 3.20	Local Coordinate System Properties at Bending Reference Point Display	77
Figure 3.21	Cylindrical Bend Setup for E-plane at Angle Bending Display	77
Figure 3.22	E-plane Cylindrical Bending	78
Figure 3.23	H-plane Cylindrical Bending	78
Figure 3.24	Simulated Antenna in E-plane Bending	78
Figure 3.25	Simulated Antenna in H-plane Bending	79
Figure 3.26	Antenna Prototype Development by 3D Printer	80
Figure 3.27	Development of Fabricated Antenna without Feed	80
Figure 3.28	Development of Fabricated Antenna with Feed	81
Figure 3.29	S-parameter Measurement Setup using Vector Network Analyzer	82
Figure 3.30	OTA Measurement System Diagram in Anechoic Chamber	83
Figure 3.31	Measurement Setup for Anechoic Chamber	84
Figure 4.1	Two-Port TLM for the Measurement of Return Loss (S_{11}) and Transmission Loss (S_{21}) of a) Denim b) Felt and c) Tencel at h = 0.5 mm and Further Iterated for h = 1.0 mm, 1.5 mm, 2.0 mm, 2.5 mm, 3.0 mm, 3.5 mm, 4.0 mm	89

Figure 4.2	S_{11} and S_{21} Performance Plots for Fabric of Rogers 5880, denim, felt and Tencel	91
Figure 4.3	Merged Plot of S_{11} and S_{21} Performance for Denim, Felt, Tencel and Rogers 5880	92
Figure 4.4	S_{11} and S_{21} versus Conductivity Plot	92
Figure 4.5	Refinement Plot of S_{21} versus Conductivity Plot	93
Figure 4.6	Actual and Calculated Values of Conductivity of Rogers 5880, Felt, Tencel and Denim	94
Figure 4.7	Simulated and Measured Data of S_{21} for S1, S2 and S3	96
Figure 4.8	Simulated and Measured Plot of the Attenuation Constant, α and Conductivity, σ for S1, S2 and S3	96
Figure 4.9	Effects of Corner Truncation Length to S_{11} Performance	98
Figure 4.10	Effects of Corner Truncation Length to S_{11} and AR Performance	99
Figure 4.11	Effects of Horizontal and Vertical Slot Length to the S_{11} Performance	99
Figure 4.12	Effects of Horizontal and Vertical Slot Length to the S_{11} and AR Performance	100
Figure 4.13	Design Evolution of Stage 1, Stage 2, Stage 3 and Stage 4	103
Figure 4.14	Proposed Antenna Structure	104
Figure 4.15	Return Loss of S_{11} from Stage 1 to Stage 4 of the Evolved Design	104
Figure 4.16	Surface Current Distribution at (a) ω = 0° (b) ω = 90° (c) ω = 180° (d) ω = 270°	105
Figure 4.17	The Fabricated Antenna (a) Radiating Plane (b) Ground Plane	106
Figure 4.18	S_{11} Measurement Setup for the Dual L-shaped Slotted Antenna Prototype	106
Figure 4.19	Far-field Measurement in the Anechoic Chamber	107
Figure 4.20	Simulated and Measured Return Loss (S_{11}) of the Proposed Antenna	107
Figure 4.21	Simulated and Measured Radiation Patterns of the	108

	Proposed Antenna (a) *x-z* plane (b) *y-z* plane	
Figure 4.22	Simulated and Measured Axial Ratio of the Proposed Antenna	109
Figure 4.23	Simulated and Measured RHCP and LHCP Gain at (a) *x-z* plane b) *y-z* plane	110
Figure 4.24	Simulated and Measured RHCP and LHCP Gain Curves of the Proposed Antenna at (a) *x-z* plane (b) *y-z* plane	110
Figure 4.25	Simulated and Measured AR Beamwidth of the Proposed Antenna at *x-z* and *y-z* plane	111
Figure 4.26	Measured AR Beamwidth in the Principle and Diagonal Planes versus Amplitude Ratio	112
Figure 4.27	Measured AR Beamwidth in the Principle and Diagonal Planes versus Phase Difference	112
Figure 5.1	Step-by-step Evolution of the DGS-integrated Design of the Proposed Antenna	118
Figure 5.2	Transparent Configuration of the Radiating Patch and its Corresponding Ground Plane	118
Figure 5.3	Return Loss of the Proposed Antenna at Different DGS Design Steps	119
Figure 5.4	Axial Ratio of the Proposed Antenna at Different DGS Design Steps	120
Figure 5.5	Fabricated Prototype of the Proposed DGS-integrated Antenna with Dimensional Layouts of a) Top Layer and b) Bottom Layer	121
Figure 5.6	Current Distribution on Radiating Patch at φ =0° a) without DGS b) with DGS	123
Figure 5.7	Current Distribution on Ground Plane at φ =0° a) without DGS b) with DGS	123
Figure 5.8	Co-polarization and Cross-polarization LHCP level at θ = 90° of φ =0°	124
Figure 5.9	Simulated Bending Configurations of the Proposed Antenna Under a) E-plane and b) H-plane Bending using CST	125

Figure 5.10	Bending Geometry under a) E-plane and b) H-plane on Cylindrical Foam	126
Figure 5.11	Measurement Setup under E-plane Bending a) Impedance Measurement using VNA b) Radiation and Polarization Measurement in the Anechoic Chamber	126
Figure 5.12	Measurement Setup under H-plane Bending a) Impedance Measurement using VNA b) Radiation and Polarization Measurement in the Anechoic Chamber	127
Figure 5.13	Comparison of the Simulated and Measured S_{11} Performance with and Without DGS under a) Planar b) E-plane Bending c) H-plane Bending	128
Figure 5.14	Summary of S_{11} Performance on Simulated and Measured S_{11} Performance with and Without DGS under Planar, E-plane Bending and H-plane Bending	129
Figure 5.15	Graph Impedance vs Frequency for Series RLC Resonance Circuit	131
Figure 5.16	The Simulated Z-parameters (Real/Imaginary Part) for Antenna a) Without DGS b) With DGS	132
Figure 5.17	Comparison of the Simulated Radiation Pattern Performance with and Without DGS under a) Planar b) E-plane Bending c) H-plane Bending	134
Figure 5.18	Comparison of the Measured Radiation Pattern Performance with and Without DGS under a) Planar b) E-plane Bending c) H-plane Bending	135
Figure 5.19	Comparison of the Simulated RHCP/LHCP Performance with and Without DGS under a) Planar b) E-plane Bending c) H-plane Bending	138
Figure 5.20	Comparison of the Measured RHCP/LHCP Performance with and With DGS under a) Planar b) E-plane Bending c) H-plane Bending	139
Figure 5.21	Comparison of the Simulated 3-dB Axial Ratio under Planar, E-plane Bending and H-plane Bending a) Without DGS b) With DGS	142

Figure 5.22	Comparison of the Measured 3-dB Axial Ratio under Planar, E-plane Bending and H-plane Bending a) Without DGS b) With DGS	143
Figure 5.23	Measured 3-dB ARBW under Planar at Phi=0° and Phi=90° With and Without DGS	148
Figure 5.24	Measured 3-dB ARBW under E-plane Bending at Phi=0° and Phi=90° With and Without DGS	148
Figure 5.25	Measured 3-dB ARBW under H-plane Bending at Phi=0° and Phi=90° With and Without DGS	149
Figure 5.26	Comparison of the Measured 3-dB Axial Ratio Beamwidth under Planar, E-plane and H-plane Bending with and Without DGS at a) Phi=0° and b) Phi=90°	150

LIST OF SYMBOLS

Symbols

α	Attenuation Constant (Np/m)
β	Phase Constant (rad/m)
γ	Propagation Constant ($\gamma = \alpha + j\beta$)
Γ	Reflection Coefficient
ε_0	Permittivity of Free Space (Vacuum Permittivity)
ε_r'	Real Part of Relative Permittivity (Dielectric Constant)
ε_r''	Imaginary Part of Relative Permittivity (Dielectric Loss Component)
θ	Elevation Angle (Polar Angle in Spherical Coordinates)
φ	Azimuth Angle (Spherical Coordinate System)
ρ	Electrical Resistivity ($\Omega \cdot m$)
ω	Angular Frequency ($\omega = 2\pi f$)
Q	Quality Factor
R_s	Surface Resistivity (Ω/sq.)
σ	Electrical Conductivity (S/m)
$\tan \delta$	Loss Tangent (Dielectric Loss Factor)

LIST OF ABBREVIATIONS

Abbreviations

AMC	Artificial Magnetic Conductor
AR	Axial Ratio
ARBW	Axial Ratio Beamwidth
ARC	Antenna Research Centre
AUT	Antenna Under Test
BLE	Bluetooth Low Energy
CP	Circular Polarization
CST	Computer Simulation Technology (CST Microwave Studio)
DGS	Defected Ground Structure
EBG	Electromagnetic Band Gap
FBR	Front-to-Back Ratio
GLONASS	Global Navigation Satellite System (Russia)
GNSS	Global Navigation Satellite System
GPS	Global Positioning System
HIS	High Impedance Surface
IoT	Internet of Things
ISM	Industrial, Scientific and Medical Band
LEO	Low Earth Orbit
LHCP	Left-Hand Circular Polarization

MCMC	Malaysian Communications and Multimedia Commission
MEO	Medium Earth Orbit
MRI	Microwave Research Institute
MTS	Metasurface
MUT	Material Under Test
NRW	Nicolson–Ross–Weir Method
PTFE	Polytetrafluoroethylene
RF	Radio Frequency
RFID	Radio Frequency Identification
RHCP	Right-Hand Circular Polarization
SCL	Short Circuit Line
SMA	SubMiniature Version A Connector
TLM	Transmission Line Method
VNA	Vector Network Analyzer
VSWR	Voltage Standing Wave Ratio
WBAN	Wireless Body Area Network
WLAN	Wireless Local Area Network
XPD	Cross-Polarization Discrimination

CHAPTER 1
INTRODUCTION

1.1 Research Background

In the evolving domain of wireless communication systems, wearable technology has emerged as a highly dynamic and promising field of study and development. Wearable devices provide instantaneous data acquisition, seamless human–machine interaction, and continuous wireless connectivity across diverse applications including healthcare monitoring, sports training, military communication, and personal safety, where real-time tracking and feedback are critical as illustrated in Figure 1.1. At the core of these wearable systems, the antenna functions as the primary interface between the electronic device and its surrounding wireless environment, facilitating the efficient signal transmission and reception.

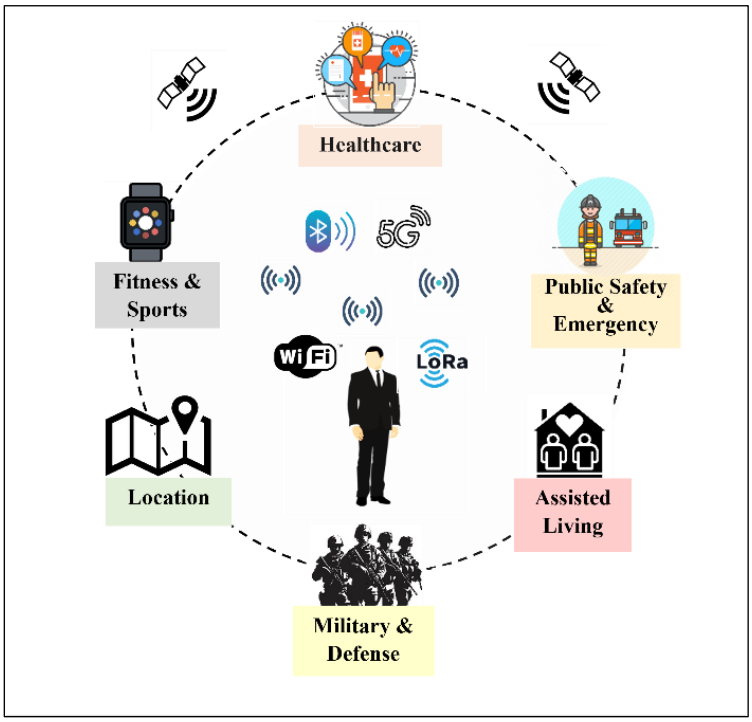

Figure 1.1 Various Wearable Applications and Technologies

In contrast to conventional antennas that are mounted to solid structures, wearable antennas must possess flexibility, lightweight structure, a low profile configuration, and compatibility with textile integration (Marterer et al., 2024; Paracha

et al., 2019; Mahfuz et al., 2022). Furthermore, they are required to maintain reliable electromagnetic performance under various forms of mechanical deformations, including bending, stretching, and compression which commonly occur during daily human activities. These constraints introduce unique challenges in the areas of antenna design, material selection, fabrication methods, and performance validation, thereby necessitating specialized design approaches tailored for wearable and body-centric communication systems.

A crucial aspect in numerous wearable applications is accurate positioning and navigation, especially via the Global Positioning System (GPS). GPS delivers precise location and temporal data that is essential for outdoor navigation, emergency tracking, fall detection, and several body-centric Internet of Things (IoT) applications. The GPS-L1 frequency (1.575 GHz) is the most prevalent operational band, providing global coverage and compatibility with the majority of commercial GPS receiver as seen in Figure 1.2 (Malaysian Communications and Multimedia Commission, 2022).

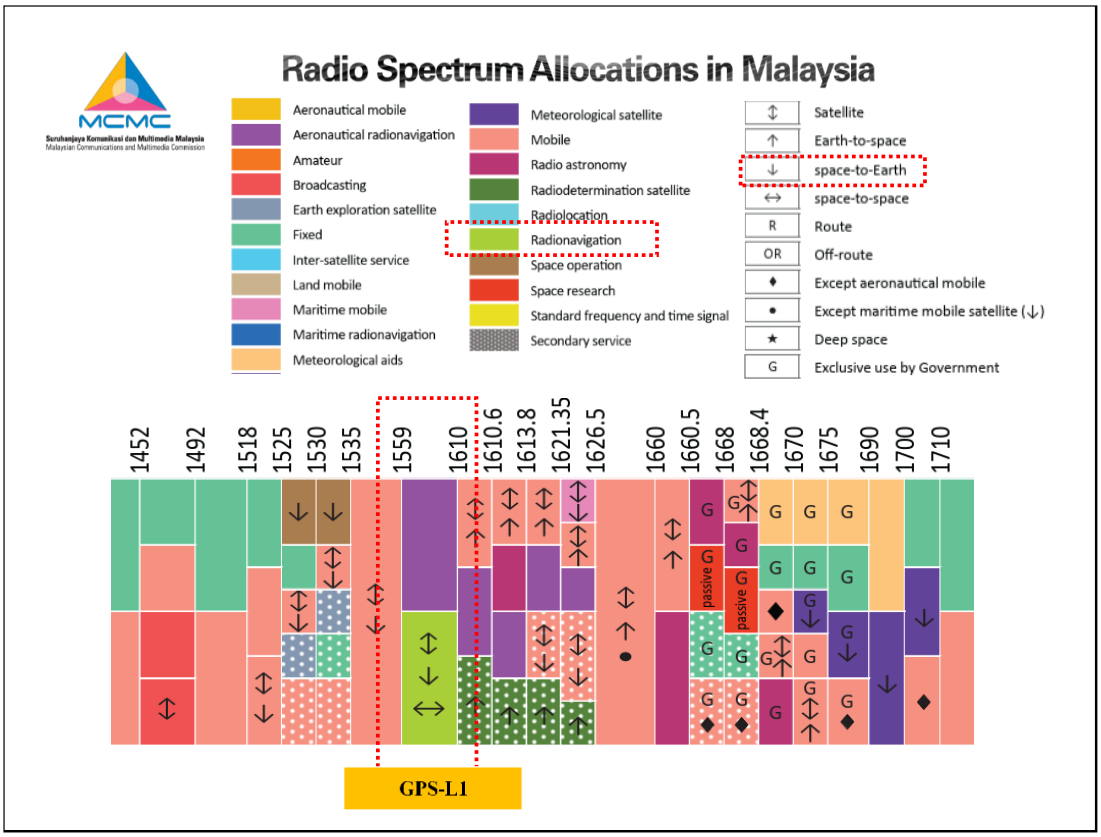

Figure 1.2 Excerpt of Radio Spectrum Allocation in Malaysia for GPS-L1 from MCMC (Malaysian Communications and Multimedia Commission, 2022).

Significantly, GPS signals are transmitted employing right-hand circular polarization (RHCP) and for optimal signal reception, the wearable antenna must demonstrate circular polarization (CP). Compared to linearly polarized antenna, circularly polarized antenna offer significant advantages, such as reduced polarization mismatch, enhanced resistance to multipath fading, and superior orientation independence, all of which are crucial in body-worn applications where antenna orientation frequently varies due to movement. Despite these benefits, most of the existing textile-based antenna designs predominantly adopt linear polarization, primarily due to their simple design structure and ease of production. Besides that, a wearable GPS antenna should also maintain adequate reception over a wide angular of 120° coverage. This requirement is particularly important for wearable systems because the antenna orientation is continuously affected by body movement, clothing placement and deformation. Therefore, evaluating circular polarization only at the broadside direction may not sufficiently represent the practical coverage capability of a wearable GPS antenna. The axial-ratio beamwidth is consequently an important performance parameter because it indicates the angular range over which the antenna preserves acceptable CP.

Achieving circular polarization in wearable textile antennas remains technically challenging due to the intrinsic properties of textile substrates. Textile materials typically exhibit anisotropy, relatively high dielectric loss, and mechanical compressibility, influencing surface current distribution, mode purity, and impedance matching (Loss et al., 2020; Marterer et al., 2024). Moreover, attaining circular polarization necessitates the activation of two orthogonal modes with identical amplitude and a 90-degree phase difference; a condition challenging to achieve in flexible, single-layer structures without intricate disturbances (Zhang et al., 2019).

Various techniques have been reported to generate circular polarization in microstrip and wearable antennas, including corner truncation, diagonal slots, L-shaped slots, parasitic elements, multi-feed arrangements and defective ground structures. Multi-feed configurations can provide accurate control of the orthogonal modes required for circular polarization, but they normally require additional feeding networks, phase-shifting structures and larger implementation areas. Single-feed techniques offer simpler fabrication and integration, although they often provide limited axial-ratio bandwidth or angular circular polarization coverage. In addition, some reported wearable antennas remain dependent on rigid substrate layers, metallic

conductors or relatively complex multilayer structures, which reduce their suitability for fully textile implementation.

To mitigate these issues, several design techniques must be implemented in the geometrical structures of planar patch antennas. Some approaches that are suitable for wearable antenna designs must be identified to produce a low-profile and single-feed architecture suitable for textile integration. However, the design of wearable antennas extends beyond only attaining circular polarization. In practice, these antennas are perpetually exposed to bending, twisting, and folding due to user movement. Such deformations can alter the current trajectories, modify the resonant frequency, constrict the impedance and AR bandwidths, and diminish radiation efficiency (Baudh et al., 2024). The consequences are particularly evident in GPS applications, where a minor frequency shift can significantly degrade signal reception quality (Ilyas et al., 2020).

Consequently, guaranteeing resilient antenna performance amid mechanical deformation is as crucial as attaining the requisite electromagnetic characteristics under optimal conditions. Therefore, a Defected Ground Structure (DGS) technique is proposed in this research to solve the frequency detuning issue. However, conventional method of implementing DGS results in significant iterative trial-and-error process in obtaining the final antenna design. In this thesis, a new strategy of placing the DGS element is applied to ensure that the iterative process can be reduced and good CP performance can be achieved.

Material selection, particularly substrate selection, is a critical aspect of a textile-based wearable antenna design. The electromagnetic properties of textile materials, such as relative permittivity, loss tangent, thickness, and electrical conductivity directly influence antenna performance. However, many previous studies have employed textile substrates without thorough characterization or optimization of their dielectric properties and thickness (Abd Rahman et al., 2018; Abd Rahman et al., 2019), leading to inconsistencies between simulated and measured outcomes. Although methods such as current-voltage (I-V) curve and two-port transmission line technique have been employed to measure textile conductivity, their applicability across diverse textile materials remains limited (Abd Rahman et al., 2019). Therefore, precise characterization of textile substrates, particularly in terms of thickness and electrical conductivity, is crucial for ensuring consistent and reliable antenna performance. In this work, the Transmission Line Method is used to extract the effective dielectric

characteristics of selected textile materials, hence guiding the material selection process for the antenna design.

This thesis proposes the design, development, and assessment of a fully textile, circularly polarized wearable antenna for GPS-L1 applications, addressing key gaps identified in the literature. The research commences with a systematic characterization of textile substrates to identify suitable materials based on dielectric performance. A single-layer patch antenna is built and optimized to achieve circular polarization at 1.575 GHz. The antenna is assessed in both flat and bent states to verify mechanical durability. Ultimately, a DGS is incorporated into the design to improve impedance and axial ratio bandwidths, particularly during deformation. The antenna's performance is verified using both full-wave simulations and experimental measurements, affirming its appropriateness for practical wearable GPS applications.

1.2 Problem Statement

For GPS-L1 wearable operation, the antenna must operate at 1.575 GHz with acceptable impedance matching, right-hand circular polarization, axial ratio not exceeding 3 dB, sufficient impedance and axial-ratio bandwidth, wide axial-ratio beamwidth for satellite reception over different elevation angles, and stable performance under bending deformation. These requirements are particularly important for wearable applications because the antenna is subjected to body movement, orientation variation, curvature, and possible frequency detuning during practical use. Although significant progress has been made in textile antenna research, several fundamental challenges remain unresolved in satisfying the electromagnetic and mechanical requirements of GPS-L1 wearable operation. Accordingly, the research problems in this thesis are formulated based on three key limitations that remain insufficiently addressed in existing textile antenna studies:

a) Insufficient Electromagnetic Characterization of Textile Materials

Although textile materials have been increasingly adopted in wearable antenna design, their electromagnetic properties are often treated using nominal material parameters. This approach is inadequate because textile substrates and conductive fabrics are inherently non-rigid, porous, compressible, and structurally non-uniform. Existing characterization approaches are commonly limited to isolated material

measurements, such as dielectric probing or DC conductivity assessment using an I–V probe. While these methods provide useful fundamental information, they do not fully describe the microwave-frequency behaviour of textile materials under practical guided-wave conditions. For conductive textiles, the RF current distribution is influenced by skin effect, finite conductivity, surface roughness, and ohmic loss. These effects are frequency-dependent and can directly contribute to transmission loss, particularly when the material is used as a radiating patch, ground plane, or transmission structure. Therefore, conductivity values obtained from low-frequency or DC-based measurements alone may not sufficiently represent the actual electromagnetic loss mechanisms occurring at the antenna operating frequency.

Furthermore, the influence of material thickness on electromagnetic response is not always systematically examined, despite its direct relevance to textile antenna design. In microstrip-based wearable antennas, substrate thickness affects effective permittivity, fringing fields, guided wavelength, impedance bandwidth, and modal stability. Similarly, conductive layer thickness and surface profile influence current confinement and conductor loss. Although the transmission line method (TLM) is commonly used to evaluate transmission characteristics, existing TLM-based textile studies often focus on material loss or conductivity behaviour at a fixed thickness, without systematically examining how transmission behaviour varies with substrate thickness. This limits the ability to identify an optimum thickness that provides low transmission loss and stable electromagnetic performance for antenna implementation. Therefore, the absence of systematic frequency- and thickness-dependent characterization may lead to inaccurate material modelling and contribute to discrepancies between simulated and measured antenna performance.

b) Limited Analysis of Wide Axial-Ratio Beamwidth for GPS Wearable Antenna Reception

Circularly polarized wearable antennas for GPS applications are commonly evaluated in terms of impedance bandwidth, axial-ratio bandwidth, gain, radiation pattern, and bending performance. However, many existing studies still focus primarily on antenna performance at broadside direction or under limited angular observation. The limitation becomes more critical when the antenna is used under body-worn conditions. In practical wearable operation, the antenna may be tilted, bent, or

positioned away from the ideal broadside orientation. At the same time, GPS satellites may appear at relatively low elevation angles, causing the received signal to arrive obliquely rather than directly normal to the antenna surface. If the circular polarization quality deteriorates rapidly away from broadside, the antenna may experience polarization mismatch, reduced satellite reception reliability, and unstable coverage performance. Although previous works have reported circularly polarized textile and wearable antennas, the analysis of wide axial-ratio beamwidth remains relatively limited compared with conventional bandwidth and gain analysis. In many cases, the reported 3-dB axial-ratio beamwidth is narrow, not systematically evaluated across multiple planes, or not clearly related to wearable GPS reception scenarios involving orientation variation and low satellite elevation. As a result, the ability of the antenna to sustain circular polarization over a wide coverage angle remains insufficiently addressed.

c) Limited Circular Polarization Robustness under Bending and Narrowband Operation

Although circularly polarized wearable antennas have been widely investigated for GPS applications, maintaining stable circular polarization under practical bending conditions remains a significant challenge. Many reported designs demonstrate acceptable impedance matching and axial-ratio performance under planar conditions; however, their performance often becomes less stable when the antenna is bent or worn on the human body. This limitation is critical because wearable antennas are not used in a fixed flat condition, but are continuously exposed to curvature, body movement, orientation changes, and substrate deformation. Bending changes the physical geometry of the antenna, alters the current distribution on the radiating patch and ground plane, and modifies the effective electromagnetic path length. As a result, the resonant frequency may shift away from the intended GPS-L1 band, while the impedance bandwidth and axial-ratio bandwidth may degrade. For circularly polarized antennas, this effect is more critical because CP operation requires a balanced excitation of two orthogonal modes with approximately equal amplitude and 90° phase difference. Any bending-induced disturbance to this modal balance can increase the axial ratio and reduce polarization purity. Furthermore, narrowband circularly polarized operation limits the antenna's tolerance to frequency detuning. Even if the antenna achieves good

axial ratio under planar conditions, a small shift caused by bending may move the operating frequency outside the 3-dB axial-ratio bandwidth. This can result in degradation of right-hand circular polarization, increased left-hand circular polarization component, higher polarization mismatch, and reduced GPS reception reliability.

1.3 Research Objectives

The research objectives are formulated to address the problem statements outlined in the preceding section. This study aims to accomplish the following objectives:

a) To characterize and analyze textile materials in terms of thickness, dielectric properties, and electrical conductivity using Transmission Line Method (TLM)

b) To design and develop a circularly-polarized (CP) wearable textile antenna for Global Positioning System (GPS) L1 operation at 1.575 GHz.

c) To integrate a bandwidth enhancement technique on the circularly polarized (CP) wearable textile antenna for operation under bending conditions.

d) To validate the performance of the circularly-polarized (CP) wearable textile antenna through lab measurement.

1.4 Scope of Thesis

This research is focused on the design, development, and performance evaluation of circularly polarized wearable textile antennas for GPS applications, with particular attention to the effects of textile substrate properties and structural modifications.

The study begins with the characterization of various textile materials commonly used in wearable antenna applications. The primary objective is to investigate the influence of substrate thickness and dielectric properties in relation to electrical conductivity on the transmission performance of textile materials using the transmission line method. Based on this analysis, the most suitable textile substrate will be identified and proposed for integration into the antenna design.

In the next stage, the research focuses on the development of circularly polarized wearable antennas operating at the GPS-L1 frequency band (1.575 GHz). The antenna is designed on textile material using suitable conductive material. A single-fed, slot-loaded and corner-truncated patch configuration is implemented, in which parametric studies are conducted to optimize the truncation dimension and slot geometries for achieving circular polarization with a low axial ratio. The antenna is modelled and simulated using a 3D full-wave electromagnetic simulator (CST Microwave Studio) to analyze the return loss, bandwidth, gain, directivity, radiation pattern, axial ratio metrics, and surface currents. The proposed antenna is fabricated and its performance is validated through vector network analyzer (VNA) measurements and radiation testing at the Anechoic Chamber in Antenna Research Centre, Universiti Teknologi MARA (UiTM) Shah Alam. To assess robustness under realistic wearable conditions, the antenna is evaluated in both flat and bent states using simulation and experimental validation.

The scope of the study is further extended to include the integration of a DGS into the antenna design to enhance both impedance bandwidth and axial ratio (AR) bandwidth. The impact of the DGS on key antenna performance parameters, including polarization purity, bandwidth enhancement, and tolerance to mechanical bending, is thoroughly re-evaluated through full-wave electromagnetic simulations and experimental measurements. Simulated and measured results are systematically compared to verify the effectiveness and reliability of the enhanced antenna configuration.

1.5 Thesis Organization

This thesis is organized into six chapters, each systematically arranged to address the research objectives and problem statements outlined earlier. The content of each chapter is summarized as follows:

Chapter one introduces the background and motivation of the study, focusing on the need for reliable and robust wearable antenna solutions for GPS applications. This chapter outlines the problem statements, research objectives, scope of the study, significance of the research, and the structure of the thesis.

Chapter two presents a comprehensive review of existing literature related to wearable textile antennas, including a detailed discussion on textile substrate properties,

polarization techniques, and GPS-specific requirements. It also covers circular polarization principles, bandwidth enhancement methods, bending effects, and prior work involving Defected Ground Structures (DGS) and slot-loaded designs. Gaps in current research are identified to justify the novelty and contribution of this study.

Chapter three explains the research methodology adopted throughout the work. It describes the selection and characterization of textile and conductive materials, with particular focus on the transmission line method for evaluating transmission behaviour. The chapter also outlines the antenna design workflow, simulation setup using CST Microwave Studio, fabrication techniques, and measurement procedures used for performance validation.

Chapter four focuses on the design and development of a circularly polarized wearable textile antenna operating at the GPS-L1 frequency of 1.575 GHz. The antenna employs a single-feed, slot-loaded, and truncated patch configuration. Parametric studies are conducted to optimize the slot geometries and truncation dimensions for achieving circular polarization with low axial ratio. The antenna is evaluated under both flat and bent configurations to assess its robustness in wearable scenarios.

Chapter five details the integration of a DGS into the circularly polarized antenna to improve impedance bandwidth, axial ratio bandwidth, and performance under bending. The effects of the DGS on polarization purity and mechanical resilience are analyzed through simulation and experimental validation. Simulated and measured results are compared to confirm the effectiveness and reliability of the enhanced design.

Chapter six concludes the thesis by summarizing the key findings and research contributions. It highlights the outcomes of the antenna development, DGS implementation, and material characterization. Recommendations for future research directions are also presented to guide the continuation of work in wearable antenna technology.

CHAPTER 2
LITERATURE REVIEW

2.1 Introduction

This chapter provides a comprehensive review of wearable textile antenna technologies with emphasis on their application in GPS systems. It begins by introducing the fundamentals of wearable technology and its applications, followed by a discussion on textile antenna materials and their electromagnetic characterization, including the dielectric properties of textile substrates and the electrical behaviour of conductive fabrics. The impact of on-body operation on antenna performance is then examined, highlighting key challenges such as bending effects and bandwidth degradation, together with commonly adopted bandwidth improvement methods for wearable environments. Building on this foundation, the chapter reviews the design considerations for wearable textile antennas intended for GPS applications, with particular focus on circular polarization generation, enhancement techniques, and feeding strategies. This is followed by a synthesis of the existing research context to identify the key limitations and research gaps addressed in this study. The chapter concludes with a summary of the main findings from the literature review.

2.2 Wearable Technology and Applications

Wearable technology refers to electronic systems that are integrated into or worn on the human body to enable continuous sensing, communication, and interaction with digital platforms. Current wearable ecosystems span healthcare monitoring, fitness and sports analytics, occupational safety, the Internet of Things (IoT), navigation support, and military or emergency-response communications (Sreemathy et al., 2022; Rafiq et al.,2024) A typical wearable system comprises multiple functional components, including sensors, processing units, power sources, and wireless communication modules. Within this architecture, the wearable antenna constitutes a key component of wearable technology, as it enables wireless connectivity between on-body electronic devices and the surrounding communication environment across multiple platforms such as Wireless Local Area Networks (WLAN), Wireless Body Area Networks

(WBAN), Bluetooth Low Energy (BLE), and Global Navigation Satellite Systems (GNSS), and many more.

According to the literature, there are two main categories of wearable antennas namely textile and non-textile antennas. Textile antennas inherently provide flexible and lightweight solutions that can be easily integrated inside garments by partially or fully utilizing textile materials for both the conductive elements and the supporting dielectric substrates (Le et al., 2024; Varma et al., 2023) In contrast, the non-textile antennas do not employ textile items for the fabrication of the antenna's conductive and non-conductive parts. However, the wide range of textile materials available for wearable applications exhibits significant variation in electromagnetic, mechanical, and structural properties. These include relative permittivity, loss tangent, thickness, porosity, and moisture sensitivity which directly affect key antenna performance parameters. Therefore, systematic material characterization is necessary to accurately determine the electrical properties of candidate textiles and to enable informed material selection for reliable antenna performance under realistic wearable conditions.

Unlike conventional antennas that operate in free-space or fixed installations, wearable antennas are required to function near to the human body under dynamic and non-ideal conditions. Extensive studies have shown that wearable antenna performance is strongly influenced by body proximity, tissue absorption, posture variation, and changes in placement locations such as the chest, shoulder, wrist, or arm.(Kim et al., 2025; Hashim et al., 2022). In practical scenarios, these factors collectively lead to gain attenuation, frequency detuning, radiation pattern distortion and polarization degradation. Such performance instability is particularly critical for wearable antenna applications that demand continuous and reliable communication under movement, including location tracking, emergency response systems, and navigation services.

While many studies report promising performance for wearable antennas, the evaluation is often limited to a selected set of metrics. As a result, application-driven requirements such as wide beamwidth coverage, polarization purity, and robustness under on-body conditions are not always fully addressed. This challenge is particularly evident in navigation-oriented wearable systems. For example, GNSS/GPS-based wearables require stable polarization characteristics and wide beamwidth coverage due to frequent changes in user orientation and signal arrival over a broad range of elevation angles (Ray et al., 2019; Reddy & Sheila, 2023). Although some designs perform well under ideal or static conditions, practical wearable operation involves bending,

compression, and close interaction with the human body, all of which can significantly alter antenna behavior (Song & Rahmat-Samii, 2019). Consequently, improvements in individual metrics such as gain, impedance matching, or compactness may come at the expense of essential wearable requirements, including comfort, thickness limitations, mechanical flexibility, and stability under deformation.

Therefore, this study is motivated by the need for wearable antenna designs that emphasize robust and consistent performance under realistic body-centric conditions. In addressing this need, the study focuses on performance parameters that are critical to real-world operation, with particular emphasis on antenna performance under wearable textile constraints.

2.3 Textile Antenna Materials and Characterization

Textile materials are a core enabling element in wearable antenna systems, as their dielectric properties and physical dimensions directly govern antenna resonance, bandwidth, and radiation behaviour. Common textile substrates such as felt, denim, polyester, cotton, Tencel, fleece fabrics are typically selected based on mechanical comfort, availability, and manufacturability (Manikandran et al.,2024; Rafiq et al., 2024 Tsolis et al., 2023). In antenna design, however, parameters such as substrate thickness and effective permittivity play a decisive role in determining the resonant frequency and impedance behaviour of planar antennas, particularly at microwave frequencies (Malik et al.,2020; R. Wang et al., 2025).

Existing studies on textile antennas report that satisfactory antenna performance can be achieved using commercially available fabrics with nominal thickness values specified by manufacturers. Many works demonstrate acceptable impedance matching and radiation characteristics by adopting these manufactured textile thicknesses and subsequently adjusting antenna geometry to achieve resonance at the desired frequency band (Singh et al.,2025; Varma et al., 2023; Baudh et al., 2024). These findings suggest that wearable textile antennas can be realised using off-the-shelf materials without extensive evaluation or modification of the substrate.

However, this practice raises concern as the thickness of textile substrates used in many reported designs is dictated by manufacturing or comfort considerations rather than electromagnetic design principles. Manufacturer-specified thickness values reported in textile datasheets are primarily defined for mechanical and thermal

characterisation in accordance with textile standards, and are not specified with respect to antenna resonance or electromagnetic performance requirements, as outlined within the scope of ASTM textile standards (ASTM, n.d.). As a result, antenna designs often rely on geometric modifications or iterative tuning to compensate for non-optimal substrate thickness, making the underlying relationship between substrate thickness, effective permittivity, and resonant frequency not being explicitly examined. This approach limits insight into how textile material thickness fundamentally influences antenna behaviour (Md. Pazil et al, 2023).

In wearable textile antenna, selecting a fabric substrate and adopting a nominal thickness without electromagnetic justification can cause the antenna resonance to become highly sensitive to fabrication tolerances and deformation during wear. For applications such as GPS where the operating band is narrow and polarization performance is critical, even small deviations in effective thickness can result in frequency detuning and performance degradation (Kellomki, 2012). As a result, without proper material characterization, antenna designs become less predictable and difficult to reproduce across different textile batches.

Recent studies show that accurate electromagnetic modelling of textile antennas requires frequency-dependent characterization of both conductive and dielectric properties rather than reliance on nominal datasheet values. Abd Rahman et al. (2019) demonstrated that conventional DC-based conductivity measurements do not adequately represent microwave behaviour, as frequency effects, dielectric losses, and substrate interactions significantly influence extracted conductivity values. Their transmission-line-based validation from 0.5 to 5 GHz confirmed that inaccurate conductivity modelling can lead to substantial degradation in antenna impedance matching and radiation performance. In parallel, Abd Rahman, Yamada, Zulkipli, and Nordin (Year) reported that newly developed textile material exhibit structural inhomogeneity, anisotropy, and internal air gaps that directly affect the extracted effective permittivity, with dielectric properties varying according to textile construction and measurement configuration. Although these studies advanced RF-based material characterization techniques, they did not systematically quantify how variations in textile thickness translate into resonant frequency sensitivity or resonance stability in wearable microwave antennas. Consequently, the direct analytical linkage between textile thickness tolerance, effective permittivity deviation, and resonance predictability remains insufficiently established in current literature.

Therefore, this study addresses the need for systematic material characterization and substrate selection that explicitly consider the influence of textile thickness on antenna resonance and performance. By evaluating textile materials with respect to their effective dielectric behaviour and thickness-dependent electromagnetic response, this work establishes systematic foundation for wearable antenna design. This approach allows the antenna geometry to be designed using physically meaningful material parameters thus improving resonance accuracy and antenna performance.

2.4 Electromagnetic Properties in Textile Materials

In recent years, the electromagnetic properties of textile materials have been widely used in the development of textile-based electronics such as wearable antennas for body-centric wireless systems (J.C Wang et al., 2016), RFID and NFC-based identification tags (Tekcon et al, 2022), textile-based sensing platforms for physiological monitoring (Stopa et al., 2014), and microwave-absorbing fabrics for electromagnetic interference (EMI) shielding applications (Suhaina Singh et al., 2025). A material's response to electromagnetic fields is determined by its constitutive parameters, which include relative permittivity (ε), relative permeability (μ), and conductivity (σ). These parameters define the penetration of electromagnetic fields into the material at a given frequency and are determined by Maxwell's equations (Chen et al., 2004). The next subsections will present the dielectric properties and the conductive textile material used to develop the wearable textile antenna. Since the textile materials used in this work are non-magnetic and exhibit relative permeability close to unity ($\mu r \approx 1$), permeability effects are considered negligible (except for ferromagnetic material); hence are not discussed further (Brodie et al.,2015).

2.4.1 Dielectric Properties of Textile Substrate

One important parameter in the design of textile-based electronics is the dielectric relative permittivity. Permittivity is a complex value that generally depends on frequency, temperature and moisture. Many studies show that the performance and size of electronic devices depend strongly on the dielectric properties of electrically insulating materials (Yamada, 2022). For textile patch antennas, higher dielectric constants allow smaller antenna sizes, while lower dielectric constants provide higher

gain and wider bandwidth (Salvadore et al., 2012; Balanis, 2016). Dielectrics are electrical insulators that become polarized when an external electric field is applied. In contrast to conductors, dielectric do not support electron flow but respond internally through polarization, leading to the storage and dissipation of electrical energy and enabling a wide range of electronic applications. An applied electric field causes polarization in a dielectric material due to generation of an opposing internal electric field that reduces the net electric field within the dielectric, as illustrated in Figure 2.1 below (Yamada, 2022):

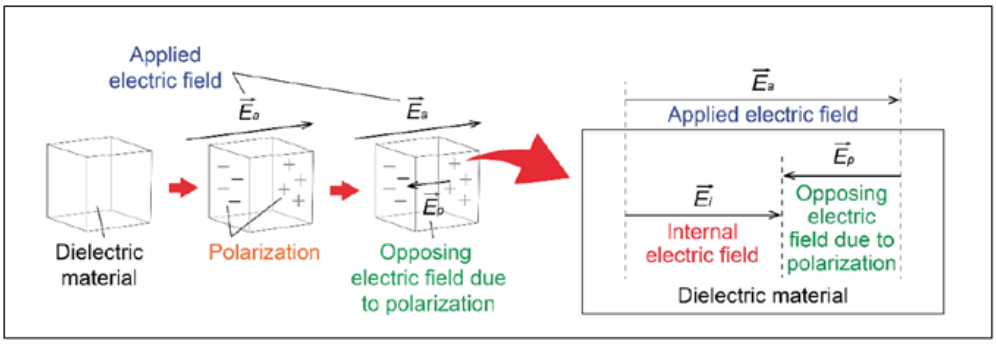

Figure 2.1 The Relationship Between the Applied and Internal Electric Fields (Yamada, 2022)

The strength of the internal electric field can be denoted by relative permittivity (ε_r) and is usually expressed in complex value parameter with ε is the permittivity:

$$\varepsilon = \varepsilon_0 \varepsilon_r = \varepsilon_0 (\varepsilon'_r - j\varepsilon''_r) \tag{2.1}$$

where ε_0 denotes the permittivity of vacuum, with a value of 8.854×10^{-12} F/m, meanwhile ε_r' and ε_r'' represent the real and imaginary parts of the relative permittivity, respectively. The real part, known as the dielectric constant, describes the material's ability to store electrical energy, while the imaginary part represents dielectric loss due to polarization. The loss tangent ($tan\ \delta$), defined as the ratio of ε_r'' to ε_r', is commonly used to assess dielectric material performance with a small $tan\ \delta$ indicates low loss (large storage capacity), whereas a large $tan\ \delta$ indicates high loss (lossy dielectric with limited energy storing capability) (Yamada, 2022).

In general, textile materials have a low dielectric constant, usually between 1 and 2 due to porosity nature and air content, which lowers the relative permittivity (Salvadore et al., 2012). This low dielectric constant reduces surface wave losses related

to guided wave propagation, thereby increasing spatial wave radiation and antenna impedance bandwidth. However, a lower substrate permittivity may also shift the antenna resonance frequency upward, while still allowing antennas with high gain and acceptable efficiency. Table 2.1 shows the dielectric properties of different non-conductive textile materials.

Table 2.1
Dielectric Properties of Non-Conductive Textile (Ouyang et al., 2008)

Nonconductive Textile	**ε_r'**	**tan δ**
Cordura®	1.90	0.0098
Cotton	1.60	0.0400
100% Polyester	1.90	0.0045
Quartzel® Fabric	1.95	0.0004
Cordura/Lycra	1.50	0.0093

Since textile materials usually exhibit a narrow range of relative permittivity values, variations in substrate thickness become the main factor that influences antenna bandwidth, input impedance, and resonance frequency. For a given relative permittivity, the substrate thickness can be selected to increase the bandwidth of a planar antenna. However, the choice of dielectric thickness involves a trade-off between antenna efficiency and bandwidth. The relationship between bandwidth *(BW)* and the antenna quality factor, Q follows $BW \sim 1/Q$, where Q depends on radiation, conduction Ohmic, surface wave, and dielectric losses (Salvadore et al., 2012).

A thorough understanding of the electromagnetic properties of materials is essential for effective antenna design (Mukai & Suh, 2020). Multiple criteria must be considered because several characteristics of textile materials directly influence antenna behaviour. Electrically conductive textiles are widely available and have been successfully used as radiating elements. In contrast, conventional textile fabrics are often used as antenna substrates, but limited information is available on their electromagnetic properties. Several dielectric characterization techniques have been reported in the literature to determine the electromagnetic properties of textile materials used in wearable antenna applications.

The selection of a suitable technique for measuring the electromagnetic properties of antenna materials depends on several technical and practical factors. These include the operating frequency range, the expected values of relative permittivity and permeability, and the level of accuracy required for reliable antenna design. The

physical characteristics and form of the material, such as uniformity and whether it is a solid or thin sheet, also influence method suitability. In addition, practical considerations such as sample size, whether the method is destructive or non-destructive, contact requirements, temperature sensitivity, and overall cost play an important role in determining the most appropriate measurement approach (Keysight Technologies, 2020)

Dielectric characterization methods can be divided into two main types namely resonant and non-resonant methods. In resonant methods, the dielectric properties of a material are obtained by observing how the material changes the resonant frequency and quality factor of a resonant structure. These methods usually provide high accuracy and are therefore suitable for materials with low dielectric loss. However, resonant methods can only measure dielectric properties at a single frequency or at a few specific frequencies. In addition, the physical size of the resonant structure limits their use to certain microwave frequency ranges. Since the presence of the material shifts the resonant frequency, the measured dielectric properties are often obtained at a frequency that is slightly different from the intended operating frequency.

Non-resonant methods, in contrast, allow dielectric properties to be measured over a wide frequency range. These methods work by relating the electrical response of a non-resonant structure to the dielectric properties of the material placed on or within it. Although the accuracy is generally lower than that of resonant methods, non-resonant techniques provide valuable information on how dielectric properties vary with frequency (Yamada, 2022).

While resonant and waveguide methods offer high accuracy at discrete frequencies, they often require rigid or precisely machined samples, limiting their applicability to wearable textiles. In contrast, non-destructive techniques such as coaxial probe and free-space methods are more suitable for textile materials, as they can accommodate material flexibility and porosity. However, these methods are sensitive to factors such as surface contact, compression, and sample uniformity, which must be carefully controlled to ensure reliable parameter extraction.

The following reviews some of the most versatile dielectric characterization methods for textile material from recent literature. Commonly adopted approaches include parallel plate, transmission/reflected line method, , free-space characterization and open-ended coaxial probe measurements. The parallel-plate method is a commonly used technique for dielectric characterization at low frequencies, typically below 1 GHz.

In this method, the material sample is placed between two flat electrodes, and its capacitance and loss are measured using an LCR meter as seen in Figure 2.2. From these measurements, the real part of the relative permittivity is calculated based on the sample thickness and electrode area. For materials with very low electrical conductivity, the measured loss is directly related to the loss tangent, allowing the imaginary part of the permittivity to be determined.

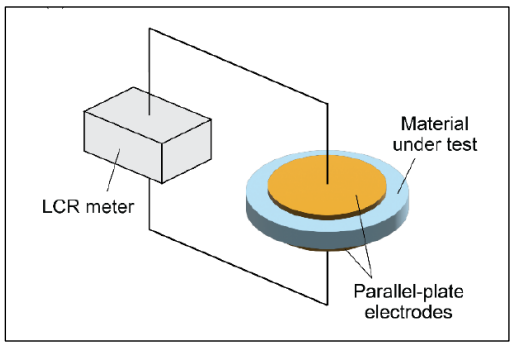

Figure 2.2: Parallel Plate Measurement Technique (Yamada, 2022)

A major advantage of the parallel-plate method is its simplicity whereby the sample preparation is straightforward, and materials with different thicknesses can be measured without damaging the sample by adjusting the electrode spacing. However, a key limitation of this method is electrode polarization, which occurs due to charge build-up at the interface between the sample and electrodes. This effect can distort the measured response, especially at low frequencies. The issue is more pronounced for materials with high moisture content, such as cotton fabrics, and may result in unrealistically high permittivity values.

Figure 2.3 shows the transmission/reflection line method measures the dielectric properties of a material by placing the sample inside a waveguide or coaxial line and measuring the reflected and transmitted signals using a vector network analyzer. These measured signals are directly related to the material's permittivity and permeability and are processed using software embedded in the VNA (Keysight Technologies, 2020). To ensure accurate results, the sample must be carefully prepared so that it fits tightly inside the measurement structure. Accurate measurement also requires strong electric fields within the sample. Calibration is carried out using standard reference conditions such as open, short, or matched loads to improve measurement accuracy. The disadvantage of this technique is that frequencies above 10 GHz are usually immeasurable, due to parasitic losses at higher frequencies (Brodie et al., 2015)

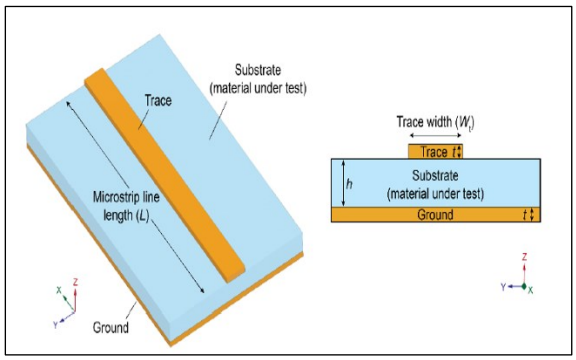

Figure 2.3: Transmission/Reflected Line Measurement Technique (Yamada, 2022)

Free-space measurement is used to characterize materials over a wide frequency range and under harsh or high-temperature conditions. As seen in Figure 2.4, the method requires a large, flat sample placed between two antennas facing each other and connected to a network analyzer. Before measurement, the system is calibrated to ensure accuracy. Several calibration approaches are available, and among them, the line-reflect-line method generally provides the best calibration performance. After calibration, measurements are first taken with an empty sample holder placed between the antennas. The material under test is then positioned on the holder, and the measurement is repeated. By comparing these two measurements, the effect of the sample holder can be removed, allowing the electromagnetic properties of the material to be accurately extracted (Rohde and Schwarz, n.d).

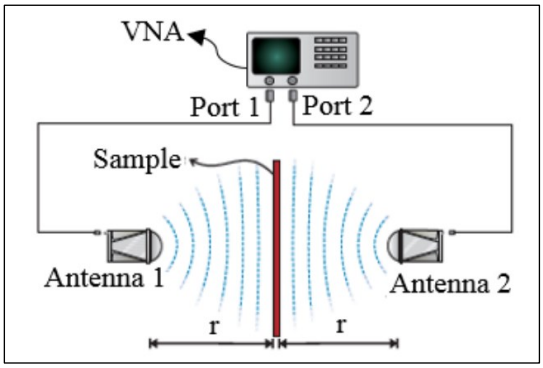

Figure 2.4: Free-space Measurement Technique (Zable et al., 2021)

The real and imaginary parts of the complex permittivity and permeability can be obtained from measured S-parameters (S_{11}, S_{12}, S_{21}, and S_{22}) using several established conversion methods. Common approaches include the Nicholson–Ross–Weir (NRW) method, the NIST iterative method, non-iterative techniques, and the short-circuit line (SCL) method (Zable et al., 2021) The free-space method has been

used by Bakar et al. (2004) to measure the dielectric properties of Kevlar textile composites. Similarly, Kapilevich et al. (2012) reported dielectric characterization of common textile substrates such as denim, wool, satin, Stokinet, and leather. In both studies, the measured relative permittivity values ranged from 2.17 to 4.05. The results also showed that the measured permittivity varies with the angle of incidence, mainly due to non-uniform thickness, surface roughness, and the textured structure of textile materials (Salvadore et al., 2012).

Figure 2.5 shows an open-ended coaxial probe measurement system typically includes a vector network analyzer, a coaxial probe, connecting cables, a probe holder, and data-processing software (Zable et al., 2021). The method works by measuring the reflection coefficient at the open end of the probe when it is placed in contact with the material under test (MUT). This reflection occurs at the boundary between the probe and the material due to the difference in the electrical properties, and the measured response is then used to determine the dielectric properties of the material.

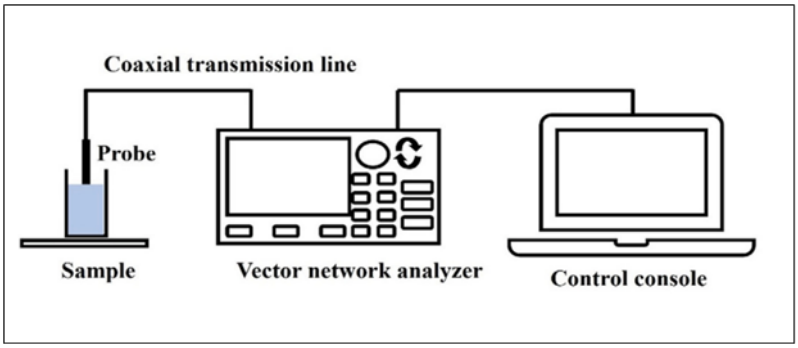

Figure 2.5 Open-ended Coaxial Probe Measurement Setup (S. Chen et al., 2025)

In this approach, calibration is first performed by placing standard references, including an open, a short, and a reference liquid, at the probe tip. The reference liquid must have well-known dielectric properties, and commonly used liquids include water, saline, and methanol. After calibration, the material under test is measured by placing the probe directly into a liquid or by gently touching it to the flat surface of a solid or powder sample. The dielectric probe technique determines the dielectric properties of a material by analyzing the amplitude and phase of the signal reflected from the open end of the coaxial probe when it is in contact with the sample. The probe tip detects changes in the reflected signal, which depend on the electromagnetic properties of the material. The measured S-parameters are then processed using software to extract the dielectric parameters (Keysight Technologies, 2020)

One common challenge of this technique is achieving good contact between the probe and the sample surface. Poor contact can create air gaps, which lead to inaccurate reflection measurements. Therefore, the surface of solid samples must be prepared carefully to ensure proper and consistent contact with the probe (Gioia et al., 2018)

2.4.2 Electrical Properties of Conductive Textile

Conductive textiles are widely used as radiating elements and ground planes in wearable antennas due to the flexibility and ease of integration with garments. These materials can be evaluated in terms of their resistivity, conductivity, deformability, weather-proof, tensile strength, and their integration with flexible materials (Ali et al., 2020). As textiles are planar materials, their electrical behaviour may be quantified by the surface resistivity, R_s demonstrating current flow along a thin sheet (Ferreira et al., 2017). This parameter determines the surface current distribution and directly influences radiation efficiency, gain, and polarization purity. The surface resistivity can be expressed as the ratio of the DC voltage drop per unit length to the surface current per unit width and expressed in Ohm/square (Ω/sq.) (Salvadore et al., 2012). For the antenna design, the relevant parameter is the conductivity of the textile, σ, which unit is Siemens per meter (*S/m*). It is related to the surface resistivity, *Rs*, by Equation (2.2), where *t* is the thickness of the textile:

$$\sigma = \frac{1}{R_s t} \tag{2.2}$$

Conductive textiles used in wearable antenna applications can be broadly categorized based on how electrical conductivity is introduced into the textile structure including metal-coated fabrics, conductive fibre–based fabrics, conductive yarn or thread-embedded textiles and printed conductive textile structures. Metal-coated fabrics, in which a thin metallic layer is deposited onto a conventional textile substrate, are the most widely used and include in commercially available materials such as Shieldit Super, Zelt, Tafetta and Flectron as seen in Figure 2.6 (Manikandan et al., 2024). Conductive fibre–based fabrics incorporate intrinsically conductive fibres or filaments directly into the weave or knit, with examples including silver or stainless-steel fibre woven fabrics. Conductive yarn or thread-embedded textiles employ silver-

coated or stainless-steel conductive threads stitched or embroidered into non-conductive fabrics, such as Shieldex® conductive threads (Tsolis et al., 2023). Printed conductive textile structures rely on conductive inks deposited onto textile substrates, with commercially available options including DuPont™ silver inks designed for flexible electronics (Stoppa & Chiolerio, 2014).

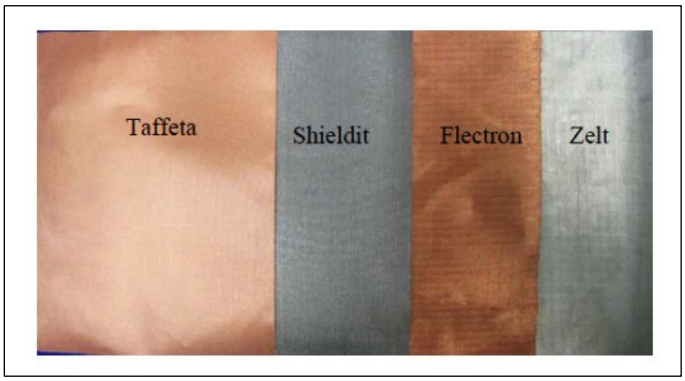

Figure 2.6 Samples of Conductive Textiles (Ashyap et al., 2025)

To minimise ohmic losses and improve radiation efficiency, conductive textiles should have low and uniform surface resistance (Salvadore et al., 2012). In practice, textile structures contain inherent discontinuities that can disturb surface current flow. Discontinuities aligned with the current direction have little impact, whereas those that obstruct current flow increase effective resistance and degrade performance. When conductive textiles are cut to form antenna geometries, the impact of cutting depends on how conductivity is implemented in the fabric. Metal-coated fabrics behave most like continuous metal sheets as when cleanly cut, the conductive layer remains continuous within the antenna area and current disruption is mainly confined to the edges.

For antenna fabrication, reliable integration of the conductive textile with the dielectric substrate is critical. Heat-activated adhesive for metal-coated fabrics such as Shieldit Super allow direct and repeatable attachment, simplifying fabrication via ironing activation (Ali et al., 2020), whereas non-adhesive textiles require external bonding that introduces additional dielectric layers and air gaps, leading to resonance shifts and increased losses. Table 2.2 shows several electrical properties of conductive textiles used in wearable antenna design.

Table 2.2
Electrical Properties of Conductive Textiles (R. Wang et al, 2025)

References	Conductive Textile	Conductiviy (S/m)	Thickness (mm)
Abdulmalek et al, 2016	Shieldit Super	1.18×10^5	0.17
Ahmad et al. (2024)	Shieldex	5.0×10^5	0.1
Tetik et al. (2018)	Polyester Taffeta	2.5×10^5	0.03
Sabapathy et al. (2017)	Zelt	/	/
Vallozi et at.(2010)	Flectron®	/	/

2.5 Textile Antenna Performance for On-Body Application

In practical wearable scenarios, textile antennas operate near to the human body and are subjected to continuous body movement. Human-body proximity introduces significant electromagnetic loading to wearable antennas due to the lossy and high-permittivity characteristics of biological tissues (Kim et al., 2025). As a result, on-body placement significantly affects key antenna parameters, including resonant frequency, bandwidth, radiation efficiency, radiation pattern, and gain, leading to performance variations when the antenna operates in close proximity to the human body (N. H. A. Rahman et al., 2019; Sharma et al., 2024; M. H. A. Rahman et al., 2025). Beyond electromagnetic loading caused by human-body proximity, wearable textile antennas are also subjected to continuous mechanical deformation during normal use. Among these, bending represents one of the most dominant and unavoidable factors influencing antenna performance, making on-body evaluation a critical requirement for assessing real usability. The ability of an antenna to maintain stable performance under bending therefore serves as an important indicator of its suitability for wearable applications.

2.5.1 Effects of Bending on Textile Antenna Performance

In wearable applications, textile antennas are commonly subjected to bending at various body positions, including the arm, wrist, chest, shoulder, and thigh, depending on garment placement and user activity as seen in Figure 2.7. Each position imposes a distinct curvature profile, resulting in different levels of mechanical deformation and electromagnetic disturbance. For example, antennas placed on the arm or wrist typically experience high curvature due to smaller body radii, whereas placement on the torso or chest generally results in low bending with larger radii. These position-dependent bending conditions significantly influence antenna performance by modifying the

effective electrical length and surface current distribution as reported by Ferreira et al. (2017). In this work, the antenna performance at the chest is the most stable with minimal frequency deviation followed by the arm and subsequently wrist position. Similarly, Mao et al. (2020) reported that placing the antenna on the arm caused significant structural deformation, leading to an approximate 1 dB gain reduction and an 8% decrease in efficiency. These conditions are due to the increasing bending severity associated with differences in curvature.

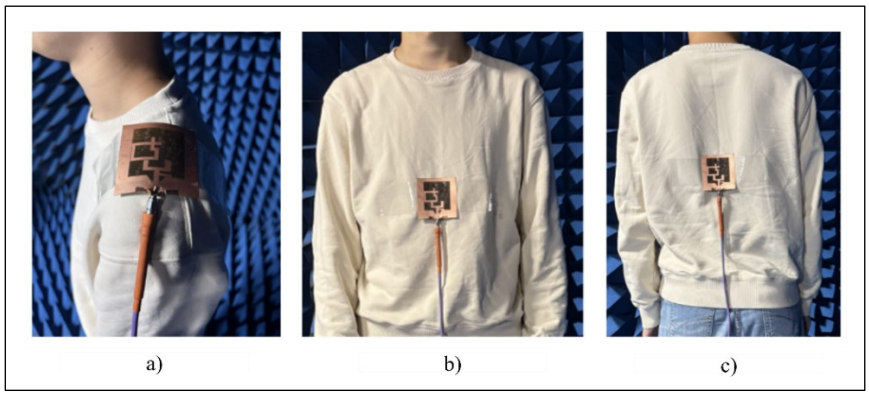

Figure 2.7 Antenna Being Worn at a) shoulder b) front and c) back (Deng et al.,2025)

Bending and mechanical deformation alter the electromagnetic behavior of wearable textile antennas as these geometric changes disrupt the intended current distribution, leading to variations in the resonant characteristics of the antenna. As a result, bending commonly causes resonant frequency detuning and degradation of impedance matching, which can reduce the effective operational bandwidth under on-body conditions (Zaidi et al.,2022). Besides that, bending has a significant impact on circular polarization (CP) performance. The deformation disturbs the amplitude and phase balance between the orthogonal modes required for CP generation, resulting in a substantial degradation of polarization purity. The work by Baudh et al. (2024) demonstrates that, while the antenna continues to cover the intended operating band with relatively stable gain under bending conditions, both impedance and AR bandwitdth are influenced by the bending. This observation is further supported by Sayem et al. (2022), who reported that bending the antenna on a human phantom leads to a degradation of AR performance.

In addition to curvature severity, previous studies have emphasized that the bending orientation relative to the antenna geometry commonly evaluated in the E-plane and H-plane (as seen in Figure 2.8), plays a significant role in determining performance

degradation. Bending along the E-plane generally causes more severe disruption to surface current distribution and resonant behaviour, as it directly affects the dominant current flow on the radiating element. In contrast, H-plane bending often results in comparatively low or stable performance variation, although noticeable changes in radiation pattern symmetry may still occur as reported by Adam et al. (2021). In this work, the angle of the radiation pattern was shifted about 30° for *X*-axis bending, while it maintained the same direction during the *Y*-axis bending. These findings highlight that antenna performance under bending is not only dependent on curvature magnitude but also on the direction of deformation relative to the antenna's principal radiation planes.

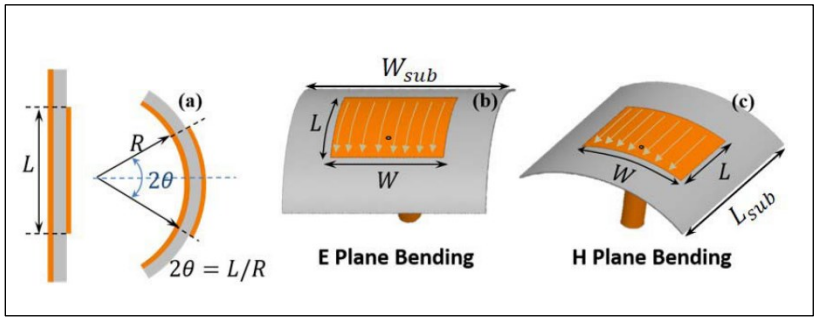

Figure 2.8 Bending Orientation of E-plane and H-plane (Song & Rahmat Samii, 2018)

To systematically evaluate bending effects, existing studies commonly characterize deformation using either bending radius or bending angle. Bending radius is widely adopted to represent curvature severity as shown in Figure 2.9. Reported results generally indicate that larger bending radii produce minimal performance degradation, while high curvature (low radii) leads to more pronounced detuning and efficiency reduction (Anbalagan et al., 2020). Alternatively, bending angles are employed as a characterization metric, as illustrated in Figure 2.10, particularly when antennas are conformed to cylindrical or curved supports. Under low-degree bending, the antenna undergoes minimal geometric deformation while high-degree bending represents a critical stress condition which severely impacts electromagnetic behaviour (Ferreira et al, 2017). Both approaches enable systematic assessment of antenna robustness under deformation and allow comparison of results across different antenna designs.

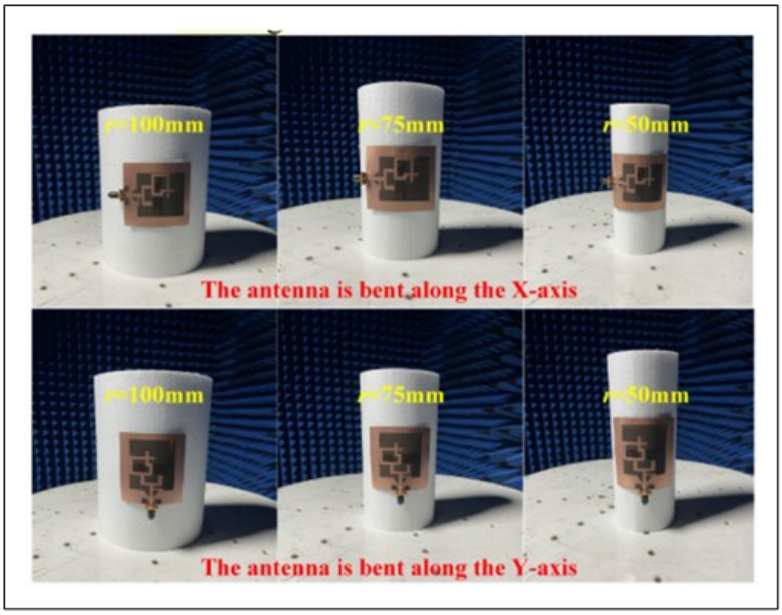

Figure 2.9: Antenna Bent based on Radius for Curved Surface (Deng et al., 2025)

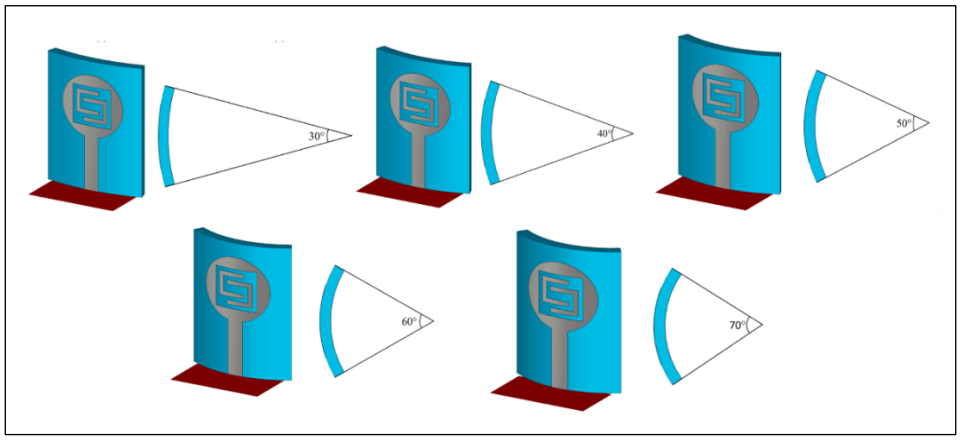

Figure 2.10: Antenna Bent Curvature based on Angle, θ (H.M.A. Rahman, 2025)

In order to provide insight into the significance of bending on the functionality of patch antennas, the work by Song & Rahmat-Samii (2018) adopted the approach in which the patch antenna dimensions are fixed to those of the planar configuration, and bending is subsequently applied without altering the physical dimensions of the patch. As a result, the observed performance variations can be attributed purely to mechanical deformation, providing a realistic representation of wearable operating conditions where antennas are bent by the human body rather than redesigned for curved geometries.

2.5.2 Bandwidth Enhancement Technique

Bandwidth enhancement is a critical requirement for textile wearable circularly polarized GPS antennas to ensure reliable performance under realistic on-body conditions, particularly to compensate for frequency detuning caused by bending and deformation (R. Wang et al., 2025). When selecting a bandwidth enhancement technique for a textile wearable CP-GPS antenna, priority must be given to approaches that offer high overall merit under practical on-body conditions. Techniques requiring increased substrate thickness, multilayer stacking, or complex feeding networks are unsuitable due to reduced flexibility and fabrication complexity. An effective solution should simultaneously enhance impedance and axial-ratio bandwidth, suppress cross-polarization for CP purity, and maintain a low-profile with mechanically compliant structure.

Several bandwidth enhancement techniques have been reported for circularly polarized wearable textile GPS antennas, including slot-loaded patch designs, parasitic or stacked elements, perturbation-based methods, and metasurface-inspired ground-plane structures. Although all these techniques can broaden antenna bandwidth, they operate through different electromagnetic mechanisms and impose different design trade-offs. Slot-loaded techniques, such as U-slots, L-slots, and cross-slots, enhance bandwidth by introducing additional resonant modes and can support single-feed circular polarization. Their main advantage is that bandwidth enhancement can be achieved without adding a separate layer. However, the slot dimensions and positions are highly sensitive to fabrication tolerances because small geometrical deviations may alter the modal frequency separation, impedance matching, and axial-ratio response. This sensitivity is especially important for textile antennas, in which cutting, bonding, and material deformation are less precisely controlled than in rigid printed-circuit substrates.

Parasitic and stacked element approaches provide strong bandwidth enhancement through electromagnetic coupling and multi-resonant behaviour. This is supported by the work of Singh & Verma (2021) who employed a circularly polarized L-strip fed slotted textile antenna with parasitic elements. The work reported a wide impedance bandwidth of 89.16% covering 2.3 – 6.0 GHz, along with a 3-dB AR bandwidth of 47.55% over 2.34 – 3.80 GHz and 12.60% over 5.20 – 5.90 GHz. These results demonstrate the strong bandwidth potential of coupled resonators. Nevertheless,

the large percentage bandwidths should not be compared directly with GPS-L1 antenna performance without considering differences in operating frequency, electrical size, substrate configuration, and intended application. Moreover, parasitic and stacked configurations generally increase antenna thickness, stiffness, and alignment requirements, as illustrated in Figure 2.11(a). Although such configurations may be appropriate where bandwidth is the dominant requirement, they are less attractive for fully textile wearable antennas in which flexibility, comfort, low profile, and fabrication repeatability are equally important.

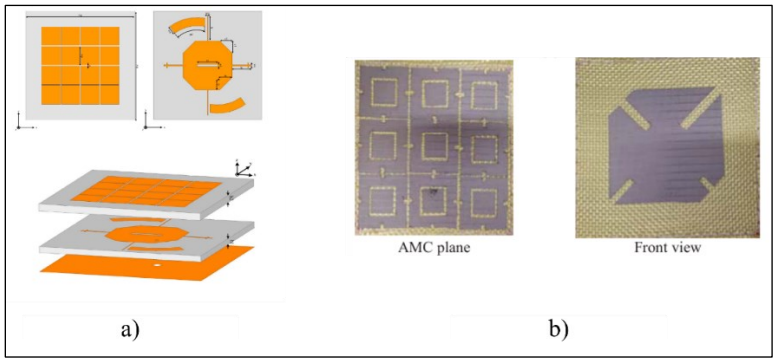

Figure 2.11 Textile Antenna with a) Circular Arc-shaped Parasitic Patch and Metasurface Element (Peng et al., 2023) b) 3x3 AMC (Hussin et al., 2018)

Perturbation-based techniques, such as corner truncation, provide a simpler and lower-profile method of generating circular polarization. The perturbation splits two initially degenerate orthogonal patch modes so that approximately equal amplitudes and a 90° phase difference can be produced at the required frequency. However, corner truncation mainly establishes the CP condition near a specific frequency and does not necessarily provide a wide impedance or axial-ratio bandwidth. Its performance is also sensitive to changes in effective permittivity, substrate thickness, and bending curvature because these factors alter the frequency separation and phase relationship of the two orthogonal modes. Therefore, corner truncation is structurally suitable for textile antennas, but an additional current-path or ground-plane modification may be required when wider CP bandwidth and deformation robustness are targeted.

Metasurface-based techniques, including artificial magnetic conductors and electromagnetic bandgap structures, are effective in improving bandwidth, polarization stability, and front-to-back ratio by suppressing surface waves and backward radiation. The antenna proposed by Kim et al. (2025) of CP all-textile antenna using a metasurface and slot-patterned ground was experimentally validated, achieving a measured

impedance bandwidth of 36.3%, a 3-dB axial ratio bandwidth (ARBW) of 18%, a peak gain of 6.39 dBic, and a radiation efficiency of 64.7%. These findings demonstrate that metasurface loading can provide simultaneous improvements in several antenna characteristics rather than bandwidth alone. Nevertheless, periodic unit cells require accurate dimensional control and consistent spacing, while the additional patterned layer may increase the overall thickness and reduce mechanical compliance, as illustrated in Figure 2.11(b). Consequently, metasurface-based antennas may provide superior isolation and gain, but this improvement is obtained at the expense of greater fabrication complexity, additional material layers, and increased sensitivity to misalignment during bending.

A defected ground structure (DGS) is a ground-plane modification technique in which intentional slots or defects are introduced to perturb the surface current distribution and modify the effective electromagnetic behaviour of an antenna. Through the creation of localized inductive–capacitive effects, DGS alters the input impedance and enables additional resonant modes, which have been widely reported to enhance impedance bandwidth, stabilize circular polarization, and suppress cross-polarized radiation (Guha et al., 2005) in microstrip antennas. Previous study by Hakim et al. (2020) presented DGS was used along with a stub slot configuration to design a dual-band microstrip patch antenna (28 GHz and 45 GHz) for providing wide bandwidth and high gain. Similarly, the work demonstrated by Zaidi et al. (2022) shows the bandwidth improvements from 4% to 12% even under bending conditions.

However, the reported DGS studies were conducted using different frequencies, materials, antenna geometries, and performance objectives. The results therefore establish the general capability of the DGS to modify ground-current behaviour, but they do not directly demonstrate its effectiveness for a fully textile circularly polarized GPS-L1 antenna. In addition, introducing slots into the ground plane may produce unintended trade-offs, including increased backward radiation, altered radiation patterns, reduced front-to-back ratio, and changes in polarization purity if the DGS dimensions or positions are not carefully optimized. The DGS must therefore be designed outside or with limited interference to the dominant radiator-current region so that bandwidth enhancement does not substantially degrade the wide axial-ratio beamwidth or increase body-directed radiation.

Compared with stacked patches, thick substrates, parasitic elements, and periodic metasurfaces, the DGS offers the advantage of maintaining a single-layer, low-

profile, and mechanically compliant antenna structure as shown in Figure 2.12. Its suitability does not arise merely from its ability to increase impedance bandwidth, but from its potential to modify the impedance and modal behaviour without introducing a separate rigid or multilayer structure. Nevertheless, the literature provides limited evidence of DGS designs that simultaneously evaluate impedance bandwidth, axial-ratio bandwidth, axial-ratio beamwidth, RHCP gain, polarization discrimination, and performance under both E-plane and H-plane bending.

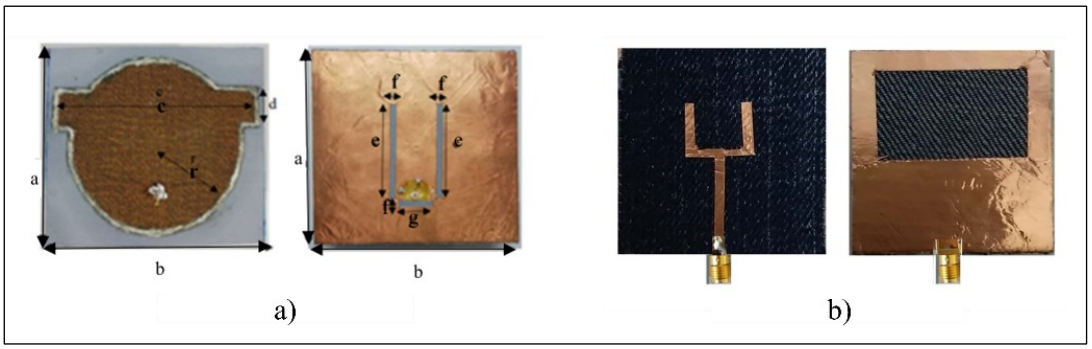

Figure 2.12 Textile Antenna with DGS using a) U-slot (Zaidi et al.,2022) b) Modified Ground (Yadav et al.,2019)

2.6 Design of Wearable Textile Antenna for GPS Application

The Global Positioning System (GPS) represents the most widely implemented Global Navigation Satellite Systems (GNSS) operates across three primary L-band frequencies with the civilian GPS-L1 signal centered at 1.575 GHz as illustrated in Figure 2.13. This system operates in Medium Earth Orbit (MEO) at an altitude of approximately 20,200 km as seen in Figure 2.14 providing global positioning and timing services by determining the receiver position and clock bias through trilateration using signals from a minimum of four visible satellites. As shown in Figure 2.15, there are 24 satellites constellations in GPS distributed across six orbital planes (equally spaced 60 degrees apart) with 4 in each plane, thereby providing between five and eight satellites visible from most locations on the earth (Sheikh et al., 2025; Fouda, 2004).

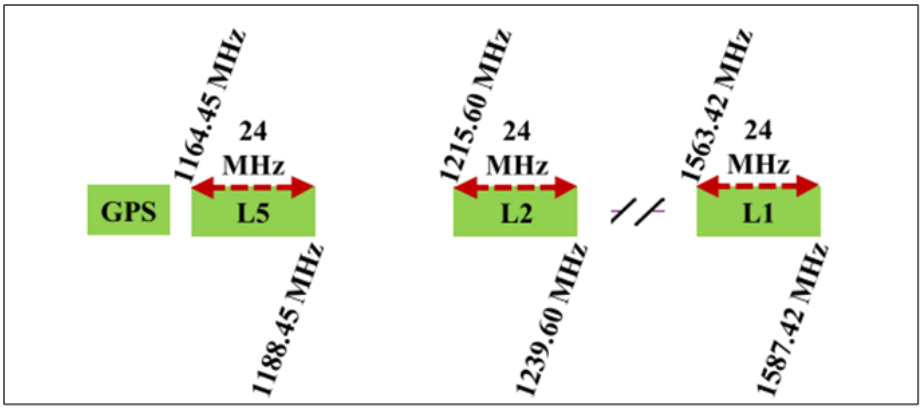

Figure 2.13: GPS Frequency Bands and the Corresponding Bandwidths (Sheikh et al., 2025)

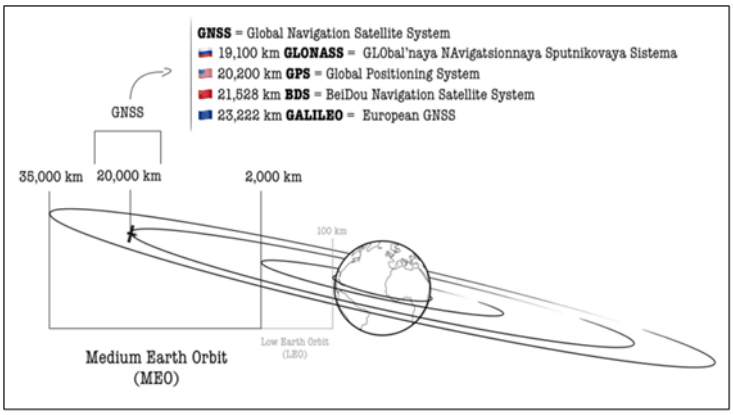

Figure 2.14: GPS under GNSS at Medium Earth Orbit (Deepsecurity, 2024)

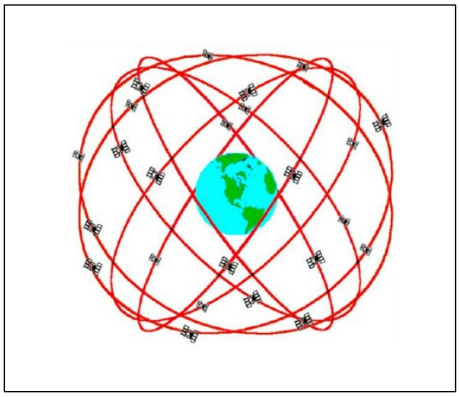

Figure 2.15: GPS nominal constellation of 24 satellites in six orbital planes (Fouda, 2004)

Previous studies have demonstrated diverse applications of GPS wearable textile antennas. Vornholt et al. (2015) proposed a wearable textile GPS antenna integrated with a GPS module and a covered by an additional water proof layer protective clothing as a jacket. The work by Sabapathy et al. (2017) demonstrated the use of a

wearable GPS antenna in a body-worn positioning and tracking system with an operational range of up to 1.0 km, aimed at location monitoring of patients and elderly individuals. Anbalagan et al. (2023) investigated the integration of a GPS module and an embroidered textile antenna within an intelligent wearable system to support location tracking and border alerts in marine environments. GPS antennas are not limited to standalone navigation and can be integrated with other wireless bands to support multi-functional wearable systems. Joshi et al. (2020) integrated a wearable textile GPS antenna with a WLAN system to support outdoor and indoor wireless localization, respectively, for location tracking applications. Pal et al. (2023) demonstrated a military beret incorporating a dual-functional wearable antenna operating in the GPS-L1 and RFID ISM bands with reduced SAR for positioning applications.

Most GPS antenna applications employ planar patch antennas which are attractive due to low profile, simple structure, ease of integration, and compatibility with textile substrates. Several works have explored such configurations in wearable implementations. For instance, Budiastuti et al. (2020) and Gil et al. (2017) reported wearable microstrip patch antenna fabricated using jeans. Zaidi et al. (2022) presented a planar wearable antenna employing a self-developed electro-textile with polyester substrate for tracking applications. Additionally, the use of silver-plated nylon yarn and cotton in the square patch antenna structure was demonstrated by Gil et al. (2017), while Shakhirul et al. (2015) integrated felt and Shieldit conductive fabric in a rectangular microstrip patch antenna design.

While most of GPS wearable antenna studies employ textile substrates, many recent designs (as shown in Figure 2.16) do not constitute fully textile configurations as rigid or non-textile conductive layers such as copper sheets are still incorporated (Budiastuti et al., 2020; Ilyas et al., 2020; Tekneci et al., 2025). Although copper conductors can be mechanically bent, the usage in wearable antennas is often associated with limited durability and long-term reliability under repeated bending, washing, and daily wear. As a result, such hybrid implementations may not fully meet the practical requirements of sustainable and robust wearable GPS applications.

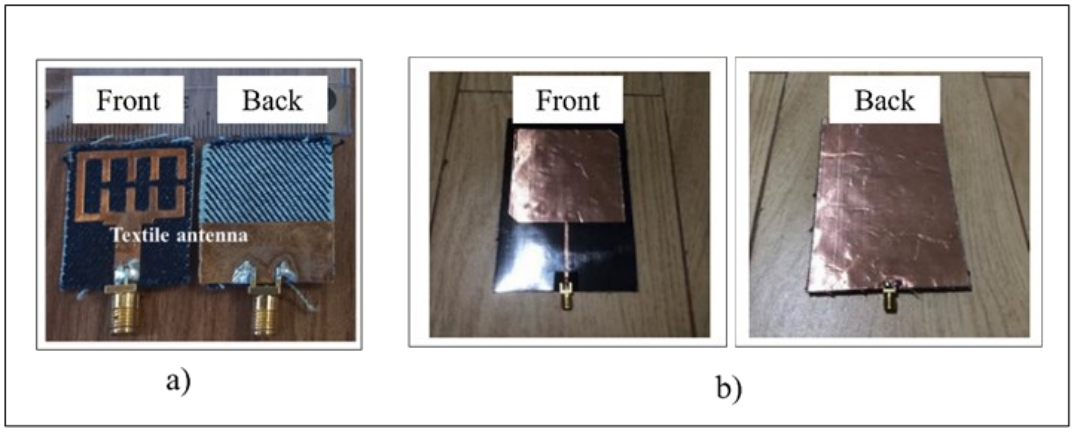

Figure 2.16: GPS Textile Antenna with Non-textile Conductive Layer a) Denim Substrate and Copper Sheet (Tekneci et al., 2025) b) Jeans Substrate and Copper Sheet (Budiastuti et al., 2020)

Antenna polarization refers to the orientation of the electric field of the radiated electromagnetic wave with respect to the Earth's surface. Depending on the trajectory of the electric field vector during propagation, the polarization can be classified as linear, elliptical, or circular. In circularly polarized antenna systems, the direction of rotation of the electric field vector must be considered. According to the right-hand rule, when the wave propagates away from the observer, a counterclockwise rotation corresponds to right-hand circular polarization (RHCP), while a clockwise rotation indicates left-hand circular polarization (LHCP) as shown in Figure 2.17. When the antenna is circularly polarized, either LHCP or RHCP gain is remarkably greater than the other indicating the purity of the circular polarization (Kaivanto et al., 2014). An equal gain values of LHCP and RHCP indicate the wave is propagated in linearly polarized.

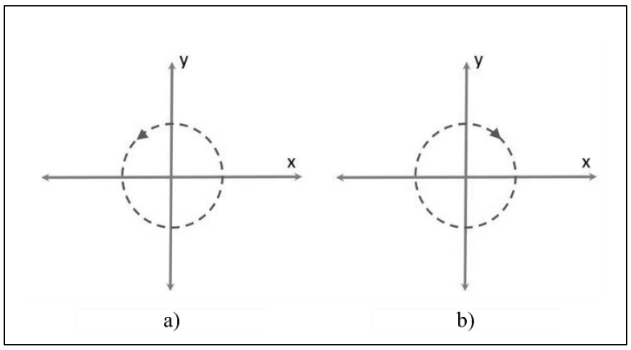

Figure 2.17 Two Rotation Directions of Wave Travelling Perpendicularly Away from the Observer a) Left Hand Polarization b) Right Hand Polarization (Kanvanto et al., 2014)

For GPS antenna design, the signals are transmitted from satellites in right-hand circularly polarized (RHCP) to minimize polarization mismatch and mitigate Faraday rotation during ionospheric propagation (Zhong et al, 2019). CP generation ensures the polarization state in which the electric field vector rotates with constant magnitude, produced by two orthogonal field components of equal amplitude and a quadrature phase difference. The quality of circular polarization is commonly evaluated using the axial ratio (AR), with values below 3 dB indicating acceptable CP performance. Axial ratio can be defined either as the ratio between RHCP and LHCP electric fields or by the means of absolute value gains of the antenna as follows:

$$AR = 20\log\left(\frac{|E_{RHCP}|+|E_{LHCP}|}{|E_{RHCP}|-|E_{LHCP}|}\right) = 20\,log\left(\frac{\sqrt{G}_{RHCP}+\sqrt{G}_{LHCP}}{\sqrt{G}_{RHCP}-\sqrt{G}_{LHCP}}\right) \quad (2.3)$$

Figure 2.18 shows the illustration of axial ratio of the two axes of the ellipse (major to minor) traced by the tip of the electric field vector in the polarization plane. If the tip of the electric field vector traces a perfect circle, the minor and major axes of the ellipse are equal and the AR = 1 (or alternatively 0 dB). As the value increases, the polarization turns elliptical and keeps flattening until it turns to a perfectly linear polarization at infinity. To ensure circularly polarized operation, axial ratio needs to be measured over the desired bandwidth and coverage angle. Figure 2.19 shows the space coordinate system of a patch antenna, in which θ is the elevation angle between the z-axis and xy-plane and φ is the azimuth angle at xy-plane.

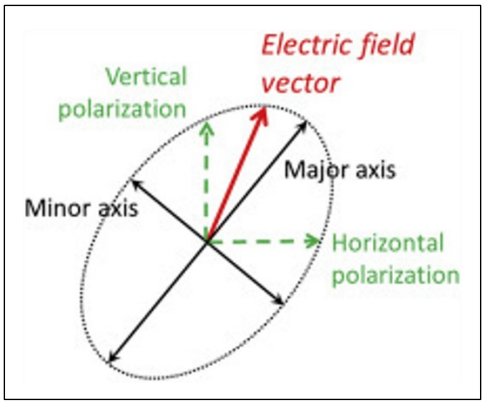

Figure 2.18 Electric Field Representation of Elliptical Polarization (Narbudowicz, 2021)

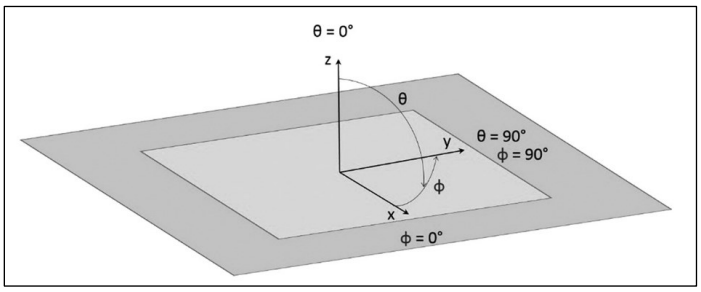

Figure 2.19 Antenna Measurement Coordinate System (Kaivanto et al., 2014)

In practical antenna implementations, achieving a consistently low AR over the entire hemispherical radiation region is very challenging. This is due to the fact that axial ratio tends to degrade towards the edges of antenna beam. Therefore, changes in antenna shape following the wearable situations may accordingly affect the purity of circular polarization and its handedness. Typical AR data are provided for the boresight, i.e., the direction for which the radiation pattern has maximum. This direction is expected to have the best (lowest) AR, with deterioration (i.e., increase) of AR for directions away from the boresight. (Narbudowicz, 2021). Following this, a satisfactory CP behaviour must be maintained not only at boresight but also over a wide angular region for a reliable satellite visibility.

In practical GPS receiver design, a minimum axial-ratio beamwidth (ARBW) of approximately 120° is often regarded as desirable to ensure sufficient sky coverage, particularly for low-elevation satellite reception (Wang et al., 2018; Zhai et al., 2022; Zhong et al., 2019). Figure 2.20 shows the effect of antenna beamwidth on coverage angles in regard to satellite visibility. A narrow-beam antenna restricts the effective coverage to a limited elevation range, resulting in reduced satellite availability. In contrast, a wide-beam antenna provides broader hemispherical coverage, enabling reliable reception from satellites across a wider range of elevation angles and improving positioning robustness in dynamic or obstructed environments.

In addition to wide beamwidth, adequate axial-ratio bandwidth is required to maintain polarization purity across the GPS-L1 band. This requirement is particularly critical for wearable textile antennas, where bending, deformation, and material variability can introduce frequency detuning and degrade circular polarization performance (Yang et al., 2020; Le et al., 2024).

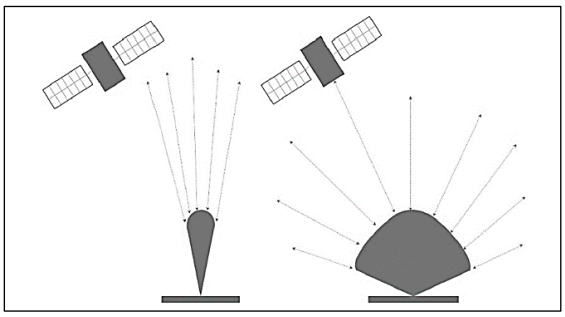

Figure 2.20 The effect of antenna beam-width on coverage angle (Kaivanto et al., 2014)

2.6.1 Circular Polarization Generation Techniques in Antenna Design

Following the requirements outlined for GPS applications, this subsection focuses on the antenna design literatures employed to realize circular polarization in wearable textile antennas**.** Circular polarization (CP) is a fundamental requirement design for GPS antennas, as GPS satellites transmit right-hand circularly polarized (RHCP) signals to mitigate polarization mismatch caused by signal reflection and multipath effects. It is well established that CP can be achieved when two orthogonal resonant modes of equal amplitude are excited with a 90° phase difference. This CP generation can be accomplished by adjusting the physical dimensions of the patch and using either single, dual or more feeds (Balanis, 2005). In practical antenna design, the quality of circular polarization is commonly evaluated using the axial ratio (AR), where an AR value of 3 dB or less is generally accepted as the condition for effective CP operation. The frequency range over which the AR remains below 3 dB defines the axial-ratio bandwidth. For GPS applications, achieving a low AR only at the boresight is not sufficient. Since GPS satellites are distributed over a wide range of elevation angles, the antenna must maintain circular polarization across a broad angular region. Therefore, a minimum axial-ratio beamwidth (ARBW) of about 120° is typically required to ensure reliable reception of RHCP signals from both high- and low-elevation satellites.

Based on these fundamental principles, a substantial body of work on circularly polarized antennas have demonstrated that it can be effectively realized through various geometric and excitation techniques. In Figure 2.21, various CP techniques such as corner truncation, slit insertion, and slot-based perturbations have been widely adopted to achieve CP in single-feed microstrip antennas. In the work by Sreemathy et al.

(2020), a comparative study on textile substrates like washed cotton and denim shows that simple geometries such as corner truncation and V- or square-shaped slits can achieve a good gain of 7.83 dBi and axial ratio of 1.11 dB. However, the design targets a non-GPS application, and critical metrics such as AR bandwidth and beamwidth are not reported, limiting its utility for navigation-focused wearables.

Several CP antennas have been tailored for GPS or GLONASS bands. Rao et al. (2017) demonstrated a compact GPS antenna employs four asymmetric slits, four corner truncations, and a central cross slot to achieve a 45 MHz ARBW and gain above 6 dBic. The study done by Mishra et al. (2020) demonstrated a low-profile CP antenna for GPS -L1, L2, and L5 bands uses paired slits in an elliptical patch, producing a 3-dB ARBW of 20.2 MHz within a 39 MHz bandwidth. Nevertheless, both works omit beamwidth measurements which is critical for ensuring robust CP performance under varying user orientations in wearable scenarios.

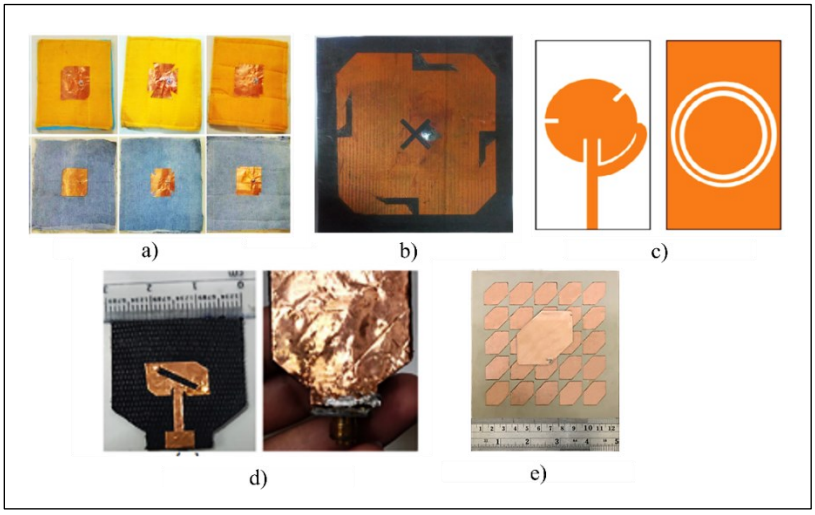

Figure 2.21 Corner Truncation Geometry with a) V and Square-shaped Slits (Sreemathy et al., 2020) b) Slits and Centre Cross Slot (Rao et al., 2017) c) Slits in Elliptical Patch (Mishra et al., 2020) d) Irregular Hexadecimal AMC (Wichaidit et al. (2023) e) Diagonal Slot and AMC (Baudh et al., 2024a)

More sophisticated CP designs aim for enhanced ARBW and gain by integrating Artificial Magnetic Conductor (AMC) surfaces or metastructures. For example, Wichaidit et al. (2023) presents a corner-truncated CP antenna with an irregular hexagonal AMC, achieving 0.7 GHz ARBW and a peak gain of 10.22 dBic. Similarly, Baudh et al. (2024a) utilizes a metasurface-based CP antenna with corner truncation and a diagonal slot, reporting 2.1 GHz ARBW and gain of 8.9 dB. Despite strong performance, these designs use rigid or intricate structures that compromise textile

flexibility and complicate fabrication, making them less practical for fully wearable applications.

Figure 2.22 shows the slot-based perturbations such as U-shaped, E-shaped, I-shaped and L-shaped slots have been extensively employed in microstrip patch antennas to achieve desired electromagnetic characteristics such as impedance matching, bandwidth enhancement, and polarization control. The work by Baudh et al. (2024b) presented a U-shaped and a center slot antenna design to enhance the 3-dB AR on a textile antenna using denim substrate. It achieved a good gain of 5.1 dBi with an enhancement ARBW of 55.17% at 2.45 GHz. Nevertheless, the use of copper tape as the radiating material limits its suitability for fully textile-based applications. A modified E-slot is employed in the work performed by Chavali et al. (2022) to realize the wideband and CP response in a microstrip antenna. Although the design achieved an impedance bandwidth of 38.8%, and a CP bandwidth of 5.3% at GSM and GPS operation, its implementation on a rigid substrate limits the applicability for wearable or conformal antenna system.

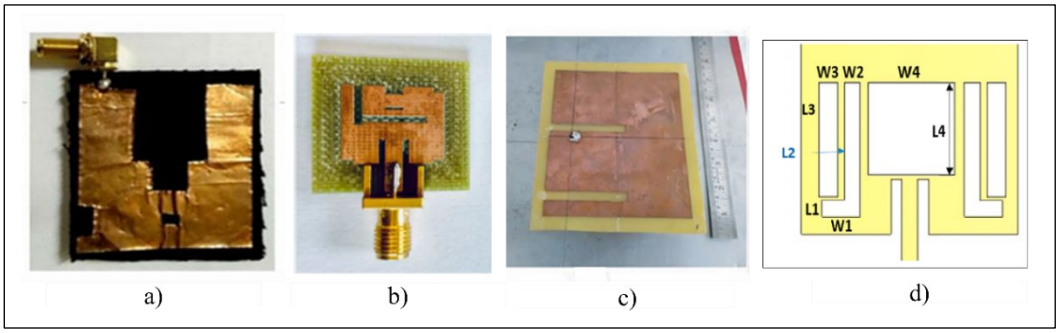

Figure 2.22 Slot-based Perturbation a) U-shaped and Centre slot (Baudh et al., 2024b) b) Modified E-slot (Chavali et al., 2022) c) L-form Slot (Rahsid et al., 2021) d) LI-slotted (Nahas, 2022)

Meanwhile, the combination of L- and I-shaped slots in study by Nahas (2022) yielded high gain up to 11.23 dB and a wide impedance bandwidth of 1.1 GHz for 5G applications. Nonetheless, the study did not address CP and axial ratio metrics as CP was not a design objective. Rashid et al. (2021) designed a compact dual-band antenna integrating an L-form slot, strip-shaped slots, and edge cuts is proposed to achieve multiband operations for medical, wearable, and IoT applications. Although it covered ISM and WBAN bands between 80–150 MHz bandwidth and 3–3.1 dB gains, it is fabricated on a rigid FR-4 substrate thus limiting its flexibility. The study by Subramaniam et al. (2024) investigated variety of textile antenna designs incorporating

dual L-slot and U-slot configuration on jeans substrate to reduce SAR levels while simultaneously enhancing critical antenna parameters relevant to biomedical applications for WBAN applications. While a high simulated gain of 20 dB is reported at 2.4 GHz for both designs, the antennas are not fully textile as it relies on non-textile radiating elements. Another L-slot-based microstrip design by Sureshabu et al. (2020) is used to excite the dual-band and sideband modes, yielding bandwidth between 2.45–3.09 GHz with 5 dB simulated gain using jeans as the substrate. Yet this work remains unvalidated experimentally with no measured results provided.

Other than various of geometric techniques introduced above, a simple way to achieve CP operation is to feed the patch in two orthogonal directions to excite two resonant modes (Ray et al., 2016). Figure 2.23a shows the dual-feed configurations employ two orthogonal feeds driven with a 90° phase difference using hybrid couplers or phase-shifting networks. Prior works report that dual-feed CP textile antennas can achieve superior AR bandwidth and beamwidth with a stable CP performance (Tran et al., 2020; Xu et al., 2025). Despite these advantages, dual-feed designs introduce additional complexity, increased loss, and alignment challenges, making them less attractive for flexible textile fabrication and wearable comfort.

Figure 2.23b shows a simple single feed microstrip antenna structure to realize CP radiation through proper excitation which produces two orthogonal resonant modes of equal amplitude with a 90° phase offset (Moharana & Dwivedy, 2024). Single-feed CP antennas rely on structural perturbations such as truncation, slots, or asymmetry to excite orthogonal modes using a single excitation point (Sahal & Tiwari, 2016; Chowdhury et al., 2019). Studies consistently show that single-feed configurations are favoured in textile antennas due to their simplicity, reduced size, and ease of integration into garments. However, single-feed designs typically offer limited AR bandwidth as it typically relies on a single perturbation or asymmetry to excite two orthogonal modes with a 90° phase difference. Although impedance bandwidth can be improved through various design modifications, such enhancements are often accompanied by trade-off leading to either reduced in antenna gain or insufficient AR bandwidth (Sahal & Tiwari, 2016).

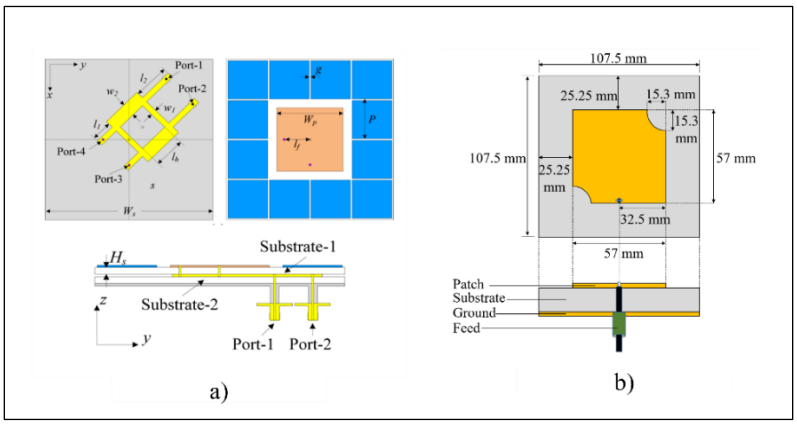

Figure 2.23 a) Dual-feed configuration (Tran et al., 2020)b) Single-feed configuration (Moharana & Dwivedy, 2024)

This limitation is particularly critical for GPS applications, where all three requirements must be satisfied concurrently. Therefore, this research aims to overcome the trade-offs in single-fed CP antenna designs by implementing an optimized design structure that enables simultaneous enhancement of impedance and AR bandwidth, and ARBW while maintaining adequate gain for reliable GPS operation without compromising antenna efficiency or structural simplicity. In this context, the following section reviews and discusses existing circular polarization enhancement techniques particularly on AR bandwidth and ARBW which are critical parameters to achieving robust CP performance in GPS satellite reception.

2.6.2 Circular Polarization Enhancement Techniques

Circular polarization (CP) enhancement techniques have been extensively investigated to improve the robustness and reliability of CP operation in microstrip and wearable textile antennas. In the context of CP antenna design, enhancement does not solely refer to the initial realization of circular polarization at a single operating point, but rather to the improvement of CP quality across both frequency and angular domains. This is commonly quantified through the axial-ratio bandwidth (AR bandwidth), which reflects the frequency range over which the axial ratio remains below 3 dB, and the axial-ratio beamwidth (ARBW), which describes the angular extent of stable CP radiation. While numerous reported studies have demonstrated acceptable axial-ratio performance at the design frequency using various CP generation mechanisms, maintaining wide AR bandwidth and ARBW simultaneously remains a key challenge, particularly for single-feed and low-profile antenna configurations. Consequently, a

range of CP enhancement techniques has been proposed to strengthen orthogonal mode balance, stabilize surface current rotation, and mitigate sensitivity to structural perturbations, forming the basis for the CP design strategies reviewed in this section.

In view of the above requirements, most of the reported GPS antenna designs focused on achieving wide beamwidth to enhance sky coverage and reception robustness. Generally, the fundamental principle is to maintain nearly equal magnitudes of two orthogonal far-field components over a wide angular range, while preserving a 90° phase difference between them (Zhong et al.,2019). To realize such wide-beam characteristics, a variety of design techniques have been explored.

The commonly employed is the geometrical techniques including asymmetric slotting, truncated corners or uneven patch modifications as shown in Figure 2.24. The GPS antenna designed by Zhai et al., (2022) achieved a wide AR beamwidth of 232° and 212.2° in the main plane of $\varphi = 0°$ and $\varphi = 90°$. A gain of 4.09 dBi was attained, nevertheless a narrow AR bandwidth of 20 MHz was reported in the design of asymmetric structure patch with an arc structure. Another work by (Ray et al, 2020) demonstrated a two-pair of parallel slots on a circular patch attained a wide beamwidth of of 228° and 214° at the plane of $\phi = 0°$ and $\phi = 90°$, respectively. Meanwhile, the gain and AR bandwidth achieved for this GPS antenna is 5 dBiC and a 22 MHz respectively.

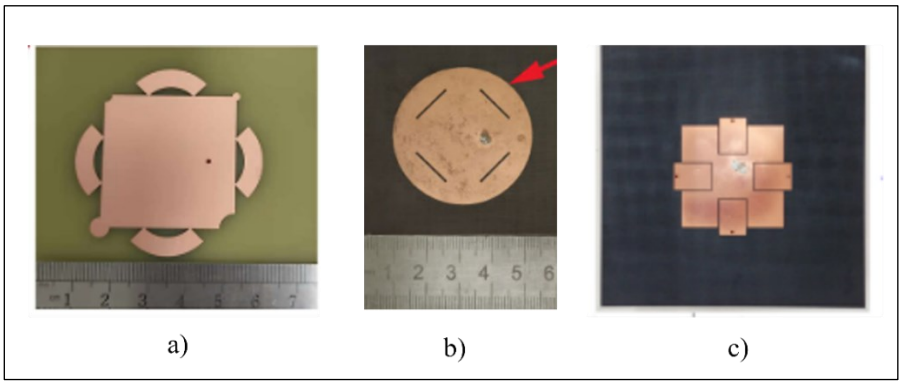

Figure 2.24 Wide AR Beamwidth GPS Antenna a) Asymmetric Structure Patch with an Arc Structure (Zhai et al., 2022) b) Two-pair of Parallel Slots on a Circular Patch (Ray et al., 2020) c) Asymmetric Slot and Coupled Strip (Wang et al.,2018)

Additionally, parasitic elements and coupled strips have been introduced to modify the radiation patterns and extend beamwidth by enabling multi-mode excitation. A study by Jiang et al. (2024) proposes a center-feed CP antenna with four arrow parasitic patches and a slotted ground plane. The results demonstrate an AR beamwidth

of 194°, a peak gain of 5.62 dBi, and an AR bandwidth of 12 MHz.Similiarly, Wang et al. (2018) investigated a square patch design with asymmetric slot and coupled strip attained a wide AR beamwidth of 188°, a gain of 5.4 dBic and AR bandwidth value of 10 MHz. Nevertheless, the findings of the above AR beamwidth techniques show a performance trade-off is observed. When the high attainment of AR beamwidths was demonstrated, the corresponding AR bandwidth remains relatively narrow (typically below 40 MHz). This limitation constrains frequency robustness and tolerance to fabrication inaccuracies which are critical for practical GPS-L1 applications. Furthermore, although moderate to high gains are reported (≈4.09 to 5.4 dBi), these designs are predominantly implemented on rigid substrates, limiting the applicability to wearable and body-centric scenarios.

With regard to AR bandwidth enhancement, various strategies have been employed to improve the excitation and stability of orthogonal modes in CP textile antennas for several applications including WLAN, WBAN, WiMax, X-band, C-band and many more. The work by Yadav et al. (2019) presented a U-shaped radiating patch on jeans substrate with a modified ground of Defected Ground Structure (DGS) technique for WLAN and C-band applications. A wide impedance bandwidth of 60.86% and AR bandwidth of 20.80% (5.1 -5.8 GHz, 7.2-7.8 GHz) were reported along with a peak gain of 5.19 dBi. In addition, another method of widening the AR bandwidth is the addition of parasitic patches near the main radiator. Based on this technique, Peng at al. (2023) presented a pair of parasitic patches to introduce a parasitic mode that can reduce the phase difference at high frequency and thus expand the AR bandwidth. The proposed work achieved an axial ratio bandwidth of 2% (3.34-3.41GHz) and 9.3% (5.52- 6.03GHz) with corresponding peak gains of 7.2dBi and 9.7dBi for WiMax and WBAN applications respectively.

Figure 2.25 shows a more recent technique to enhance the AR bandwidth is by employing a periodic electromagnetic structure, including Artificial Magnetic Conductors (AMCs), Electromagnetic Bandgap (EBG) structures, metasurfaces (MTS), High-Impedance Surfaces (HIS), and metamaterials. These techniques have received significant research interest due to their unique electromagnetic properties (Asyap et al., 2025). In circularly polarized antennas, these structures are commonly utilized to enhance AR bandwidth by providing in-phase reflection that stabilizes the quadrature phase relationship between orthogonal field components across the operating frequency range.

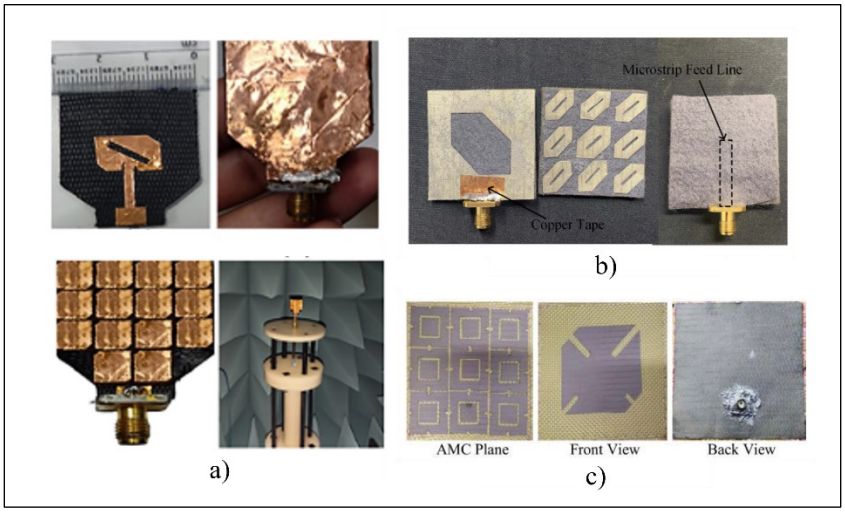

Figure 2.25 Textile Antenna with Periodic Structures a) Baudh et al. (2024) b) Le et al. (2023) c) Joshi et al. (2020)

Studies reported by Le et al. (2024a), Le et al. (2024b) and Baudh et al. (2024) employed metasurface-based configurations in textile antenna designs to achieve a wideband CP. In the work by Le et al.(2024a), a 4x4 MTS layer was implemented on top of the radiator. The MTS also works as polarization converter, which converts the incident wave into orthogonal direction with an equivalent magnitude and a 90° phase different, producing broadband CP radiation of 49.6%. Similarly, Le et al. (2024b) designed a 2x2 array antenna MTS-based with radiators fed by a 90◦ phase difference sequential series- feeding network has successfully attained an AR bandwidth of 47.9%. Meanwhile, Baudh et al. (2024) designed a compact low profile wearable antenna using Cordura fabrics to demonstrate a modified metasurface which offers wide impedance bandwidth (IBW) with high gain of 8.9 dBic and wider AR bandwidth of 21.3% (8.8-10.9 GHz). Nevertheless, these studies above on the AR bandwidth were not targeted at GPS applications and therefore did not consider several performance requirements specific to GPS satellite reception. Meanwhile, the work by Joshi et al. (2020) shows a GPS textile antenna integrated with WBAN application using the Artificial Magnetic Conductor (AMC) consists of a 3 × 3 array of square patch unit cells, where each unit cell is integrated with four square slits and a square ring. The results attained for the AR bandwidth are 141.7° with gain value of 1.98 dBi.

However, this periodic structure in textile antenna designs introduces increased sensitivity to layer alignment and fabrication tolerances, which is particularly challenging in wearable implementations. The electromagnetic performance of

metasurface-based configurations relies on precise periodicity and relative positioning between the radiator and the surface, conditions that are difficult to maintain in textile platforms due to material stretchability, stitching inaccuracies, and deformation under bending. As a result, even minor misalignment or structural distortion can lead to unintended variations in impedance matching and axial-ratio performance, potentially limiting the robustness and repeatability of such designs in practical wearable environments. Moreover, most reported works primarily focus on AR bandwidth and gain, while the AR beamwidth which is an important metric for wearable and GPS-oriented applications is often not reported or evaluated, indicating a notable gap in existing studies.

This research aims to achieve the simultaneous enhancement of axial-ratio bandwidth and axial-ratio beamwidth in a fully textile, wearable GPS antenna, addressing a key challenge in circularly polarized antenna design for body-worn applications. The proposed antenna design emphasizes structural simplicity and mechanical flexibility, ensuring suitability for practical wearable use without reliance on complex geometries or multilayer configurations.

2.6.3 Feeding Techniques

Feeding techniques play a critical role in determining the impedance matching, excitation of resonant modes, and overall radiation performance of an antenna. To ensure it demonstrates good performance, the antenna must be able to supply maximum power transfer from the source; therefore, the suitable feeding technique must be applied to avoid unwanted losses from occurring. There are many available feeding techniques which are available and popular to be integrated into the microstrip antenna such as coaxial probe feeding, microstrip line feeding, aperture coupling, and proximity coupling as shown in Figure 2.26. From these four feeding techniques, it is very important first to understand the design procedure and complexity of feeding techniques used as textile antenna structure is a compressible material which thickness and density might change with low pressures unlike the conventional microstrip antenna (Salvado et al, 2019).

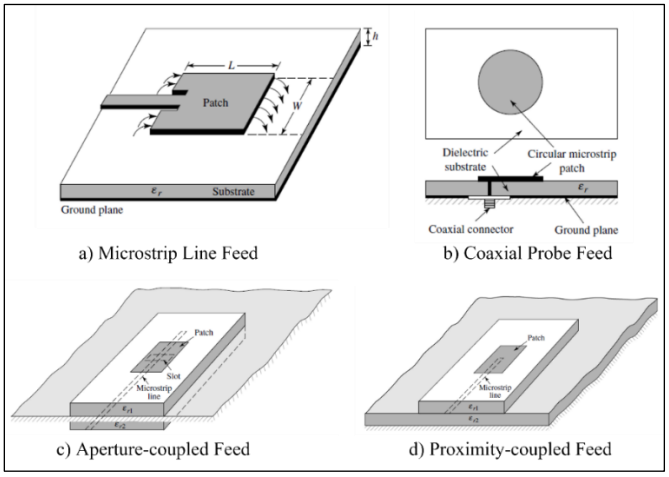

Figure 2.26 Type of Feeds for Microstrip Antennas (Balanis, 2005)

Studies shown that microstrip line feeding is frequently adopted in textile antennas due to its planar nature, ease of integration with the radiating element, simple to match by controlling the inset position and compatibility with low-profile designs (Balanis, 2005). The feed line can be readily implemented using conductive fabric or embroidered traces hence, making it attractive for fully textile-based fabrication. However, the radiation from the microstrip feed line itself can introduce unwanted coupling and asymmetry, which may degrade polarization purity in circularly polarized designs. As the substrate thickness increases, the surface waves and spurious feed radiation increased which limit the bandwidth (typically 2 to 5%) for practical design (Balanis, 2005). Besides that, studies also indicate that microstrip-fed textile antennas are highly sensitive to substrate bending and material inhomogeneity as the feed line impedance and coupling strength depend strongly on the effective dielectric properties and uniformity of the substrate. In wearable implementations, the variations in fabric thickness, and deformation are unavoidable which may alter the feed line characteristic impedance and subsequently leading to impedance mismatch and resonant frequency shift.

For coaxial feed technique, the inner conductor of coaxial connector penetrates the dielectric to the top of the radiator and soldered while the outer conductor is connected to the ground plane of the antenna structure. This feeding method is easy to fabricate and can be placed at any desired position of the patch to obtain the impedance matching while contributes a low spurious radiation effect. As the coaxial connector is rigid, it maintains the fixed electrical references and prevents feed-point deformation for a stable excitation under bending of the textile antenna. However, it has narrow

bandwidth and more challenging to model particularly for thick substrate with $h > 0.02\lambda_0$ (Balanis, 2005).

The aperture coupling consists of two substrates separated by a ground plane. A slot or an aperture is made in the ground plane to couple the patch and the feed line. This coupling aperture is normally employed under the patch centre for symmetry configuration to reduce the cross-polarization for pattern formation and polarization purity (Kumar et al.,2013). This arrangement minimizes the interference of spurious radiation and allows for independent optimization of the feed mechanism and the radiating element by using substrates of different thickness or permittivity. However, it is the most difficult of all four to fabricate and has narrow bandwidth unless multilayer substrates are used. When implemented in textile-based platforms, the alignment between the feed line, coupling aperture, and radiating patch will be critically affected due to deformation and body movement at wearable conditions.

Meanwhile, the proximity coupled feed technique are using two dielectric substrates with the feed line in between both substrates and the radiating patch is on top of the upper substrate. This technique is attractive as it eliminates spurious feed radiation and provides very high bandwidth of about 13% due to the overall increase in the microstrip antenna thickness (Bisht et al.,2014). However, this configuration is less practical for wearable textile antennas as the feedline in a proximity-coupled is subject to bending when the substrate bends and the use of multiple dielectric layers compromises seamless and lightweight integration.

A comparative study on a different feeding technique for textile antennas conducted by Zaidi et al. (2019) demonstrated in Figure 2.27 shows that the coaxial feed technique is more reliable for textile antenna implementations as compared to microstrip feedline. This reliability is due to the stable excitation from the coaxial feed configuration which is inserted directly into the antenna; thereby, reducing input power losses from the feedline. As a result, a higher antenna gain was observed for the coaxial probe feed configuration compared to the microstrip line feed. The findings were also supported by Samat et al. (2020) who showed that the used of coaxial feedline technique resulted a in a 26.1% improvement in return loss and a 6.1% increase in radiation efficiency relative to microstrip feed line configuration. In addition, the authors also reported that microstrip feeding exhibits lower surface current magnitude and weaker current distribution on the radiating patch which is the opposite of coaxial feeding performance. Similarly, a study by Pazil et al. (2021) reported that the coaxial feeding

achieves superior antenna performance in terms of gain and directivity, along with the improved return loss, VSWR, efficiency and FBR when compared to the microstrip line feed.

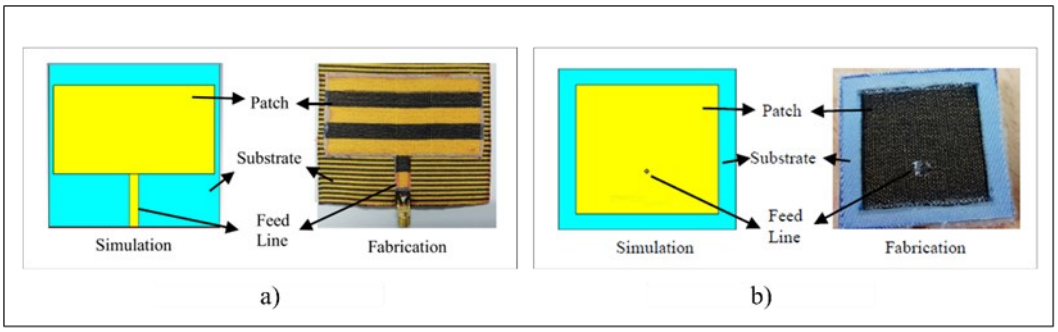

Figure 2.27 The Simulated and Fabricated Textile Antenna using a) Microstrip Line Feed b) Coaxial Probe Feed (Zaidi et al., 2019)

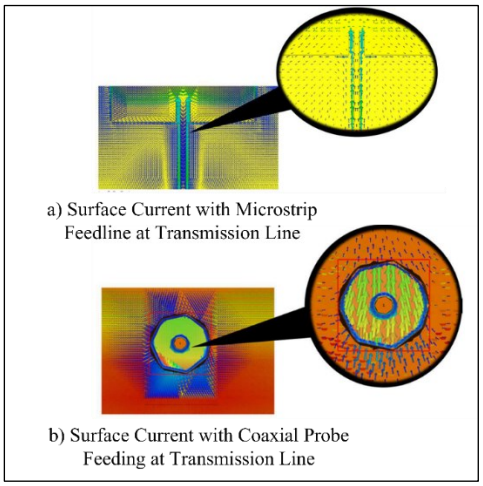

Figure 2.28 Comparative Analysis of Surface Current Distribution of Microstrip Feedline and Coaxial Probe Feeding (Samat et al., 2020)

2.7 Summary of Research Context and Gap from the Existing Wearable Textile Circularly Polarized Antenna Studies for GPS Applications

Table 2.3 summarises the research context and gaps identified from previous studies on wearable textile circularly polarized antennas for GPS applications. The review is organised into four main contexts: textile characterization, bandwidth design for CP-GPS operation, bending robustness, and DGS-based bandwidth enhancement. Existing studies have generally investigated these aspects separately, with limited

consideration of frequency-dependent textile properties, the relationship between substrate parameters and transmission behaviour, the simultaneous achievement of sufficient axial-ratio and impedance bandwidth, circular-polarization stability under bending, and comprehensive DGS validation. These limitations establish the need for an integrated investigation that combines textile material characterization, wideband circular-polarization design, bending analysis, and DGS implementation for reliable GPS-L1 wearable operation.

Table 2.3
Summary of Research Context and Gap from the Existing Wearable Textile Circularly Polarized Antenna Studies for GPS Applications

Context	Characteristic(s)	Research Gap(s)
Textile Characterization	Conductivity measurement using current–voltage method or I–V probe. *(Honavar & Latifi, 2016)* 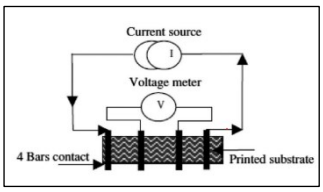	The conductivity evaluation was mainly based on current–voltage behaviour and resistance-to-conductivity conversion. However, frequency-dependent conductivity was not included, which limits its direct applicability to RF antenna design.
	Transmission Line Method (TLM) for electro-textile conductivity evaluation. *(Abd Rahman et al., 2019)* 	The work was mainly limited to lossless substrate and electro-textile evaluation. A direct correlation between substrate thickness, conductivity, and transmission behaviour was not fully established.
Beamwidth Design for CP-GPS Operation	Low-profile circularly polarized GNSS antenna with wide 3-dB axial-ratio beamwidth *(Zhai et al. , 2022)* 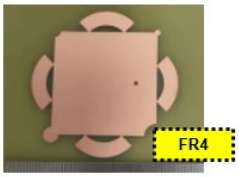	Although high AR beamwidth was achieved, the reported 3-dB axial-ratio bandwidth was relatively low, approximately 20 MHz. This indicates a performance trade-off between AR beamwidth and AR bandwidth.

Bending Robustness on Textile Antenna	Investigation of bending effect on circularly polarized wearable antenna. *(Rizwan et al. 2015)* 	The reported 3-dB AR bandwidth was limited to around 60 MHz. In addition, axial-ratio performance degraded under *yz*-plane bending and shifted toward linear polarization. The GPS coverage potential was not clearly evaluated.
DGS Bandwidth Enhancement Design for Textile Antenna	DGS-based textile antenna with semi-circular slot for IoT applications. *(Singh et al. 2024)* 	The DGS implementation required extensive re-tuning and patch-geometry iterations. In addition, circular-polarization metrics such as AR bandwidth, AR beamwidth, and XPD were not validated
	Bending analysis of electro-textile antenna with bandwidth enhancement. *(Zaidi et al. 2022)* 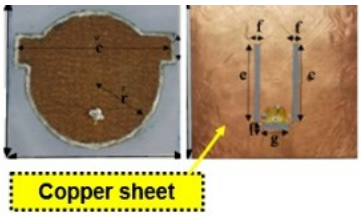	The DGS or bandwidth-enhancement structure was highly coupled to the patch and feed geometry, making the design sensitive to geometrical tolerances and bending. Gain degradation and high back-lobe radiation were also reported. The design was mainly linearly polarized for GPS.

2.8 Summary

This chapter critically reviewed previous studies on wearable textile antennas for GPS-L1 applications, with emphasis on textile material characterization, circular-polarization performance, axial-ratio bandwidth and beamwidth, bandwidth-enhancement techniques, and antenna robustness under bending. The review established that textile antenna performance is strongly influenced by substrate properties, antenna configuration, polarization stability, and mechanical deformation. These factors must therefore be considered collectively in developing a reliable wearable GPS-L1 antenna. Based on the reviewed characterization approaches, the Transmission Line Method (TLM) is selected to evaluate the transmission loss behaviour of textile substrate thickness, while the open-ended coaxial probe and free-

space methods were selected for dielectric characterization. These methods provide the material parameters and transmission characteristics required for subsequent antenna modelling and design. The review also confirmed the importance of circular polarization for GPS reception because it reduces polarization mismatch between the wearable antenna and the satellite signals. However, previously reported circularly polarized textile antennas continue to exhibit limitations in axial-ratio bandwidth, angular circular-polarization coverage, and stability under bending. Therefore, a single-feed configuration combining corner truncation and dual L-shaped slots is selected to realize circular polarization and wide axial-ratio beamwidth. In addition, the review identified the Defected Ground Structure (DGS) as a suitable technique for modifying the ground-current distribution and enhancing bandwidth. Since previous DGS-based textile antenna studies have primarily emphasised impedance improvement, with comparatively limited consideration of circular-polarization stability and bending performance, the DGS is selected for integration and evaluation under planar and bent conditions. These selected techniques form the basis of the research methodology presented in Chapter 3.

CHAPTER 3
RESEARCH METHODOLOGY

3.1 Introduction

This chapter presents the research methodology adopted to systematically design, characterize, fabricate, and validate the proposed wearable textile antenna. The methodology begins with an overview of the overall research workflow presented in Section 3.2, followed by the establishment of textile antenna design requirements and performance specifications in Section 3.3. The procedures used to select and characterize the textile substrate and conductive materials are detailed in Section 3.4. The methods employed to measure dielectric properties and substrate thickness are described in Section 3.5, incorporating both open-ended coaxial probe and free-space measurement techniques to ensure measurement accuracy and cross-verification. The procedure on the measurement of Transmission Line Method (TLM) is presented in Section 3.6. The antenna design procedure, including dimension calculation and the implementation of the probe-feed technique, is discussed in Section 3.7. Electromagnetic simulation procedures under both flat and bending conditions are reported in Section 3.8 to assess antenna performance under realistic wearable scenarios. The fabrication process and measurement procedure of the textile antenna, including return loss and radiation pattern measurements, are presented in Section 3.9. Section 3.10 discusses the legal, ethical, and sustainability considerations relevant to the research. Finally, Section 3.11 summarizes the chapter by consolidating the key methodological steps and explaining how the achievements of the research objectives are supported.

3.2 Flow of Research Work

This research adopts a structured methodology to develop a circularly polarized (CP) wearable textile antenna for GPS-L1 application. Figure 3.1 represents the detailed flowchart to accomplish the research objectives. The process flow begins with reviewing the basic theories of the antenna and the relevant literatures to establish

performance standards for GPS-L1 circular polarization and wearable application constraints.

The fundamental operating mechanisms and performance requirements of the antenna were systematically reviewed and consolidated to define the key design specification (Table 3.1). A wide range of commercial textiles was evaluated, and candidates were selected based on criteria like dielectric constant, loss tangent, and thickness. Only materials that conform to the established standards (Table 3.2) advance to subsequent analysis.

The selected textiles were characterised by the Transmission Line Method (TLM), utilising simulated S-parameters to determine conductivity and evaluate signal transmission efficacy. These values were validated against the requisite performance indicators (Table 3.2). Upon satisfying these criteria, chosen textile was employed in the fabrication of a reference antenna, which were subsequently measured and compared with simulation data to verify consistency.

Subsequent to substrate validation, a circularly polarized textile antenna was constructed and simulated for functionality at 1.575 GHz to meet the design specifications listed (Table 3.3). The design incorporates optimal perturbation techniques to attain circular polarization, with optimization focused on return loss and axial ratio (bandwidth and beamwidth). The optimized design has been fabricated and experimentally verified. Upon confirming that the measured performance adheres to the GPS specifications, the antenna is further assessed under bending conditions to determine its mechanical robustness and electromagnetic stability in wearable contexts.

In the concluding design phase, a Defected Ground Structure (DGS) is implemented to better optimise antenna performance, especially under bent conditions. The CP antenna with DGS is simulated, constructed, and evaluated in both flat and bending configurations. Performance measures are assessed and compared to ensure that the design sustains stability and efficiency throughout mechanical deformation. The process culminates in an extensive data analysis and report documentation, confirming the antenna's technical feasibility and practical applicability for wearable GPS utilization.

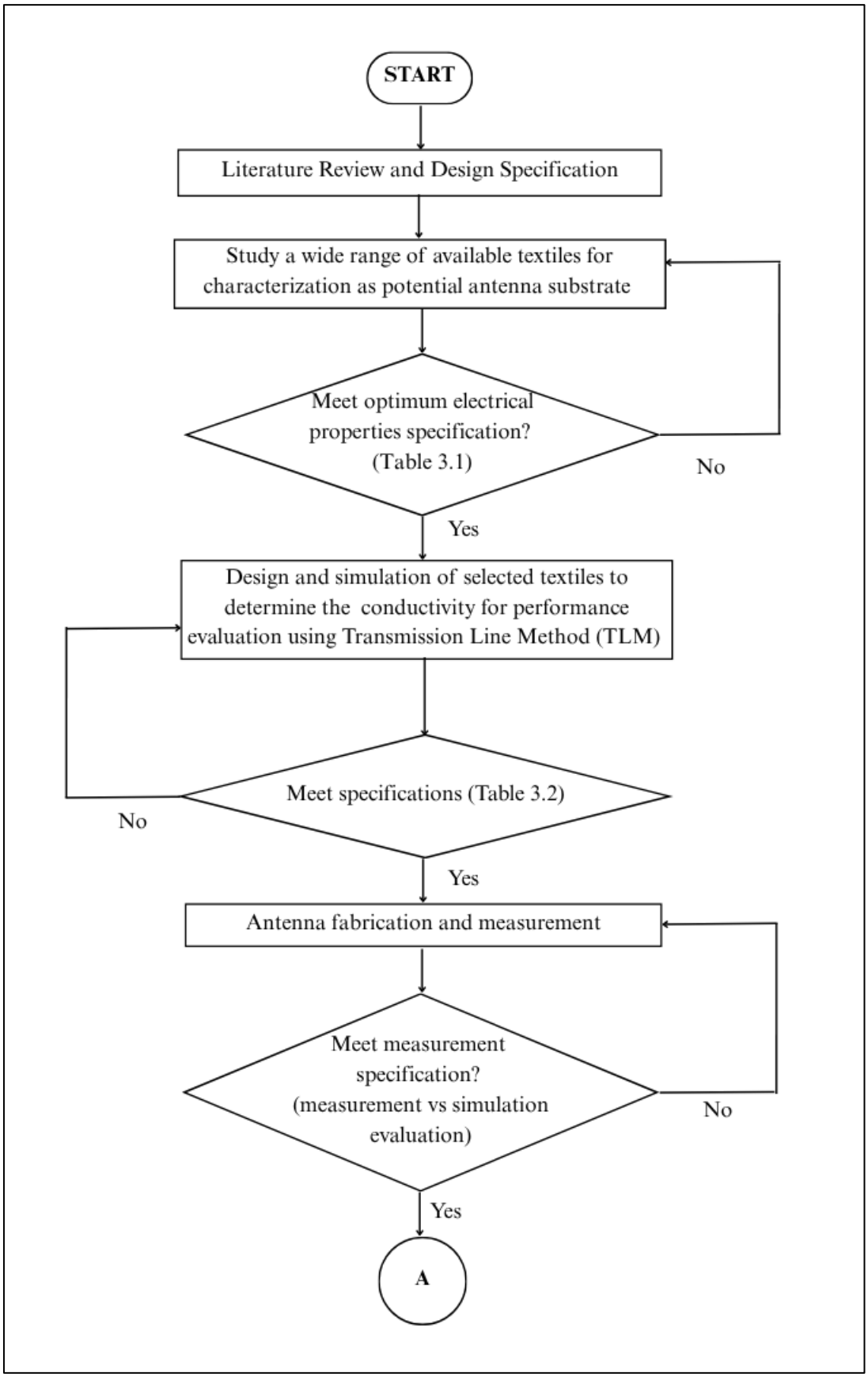
START
Literature Review and Design Specification
Study a wide range of available textiles for characterization as potential antenna substrate
Meet optimum electrical properties specification? (Table 3.1)
No
Yes
Design and simulation of selected textiles to determine the conductivity for performance evaluation using Transmission Line Method (TLM)
Meet specifications (Table 3.2)
No
Yes
Antenna fabrication and measurement
Meet measurement specification? (measurement vs simulation evaluation)
No
Yes
A

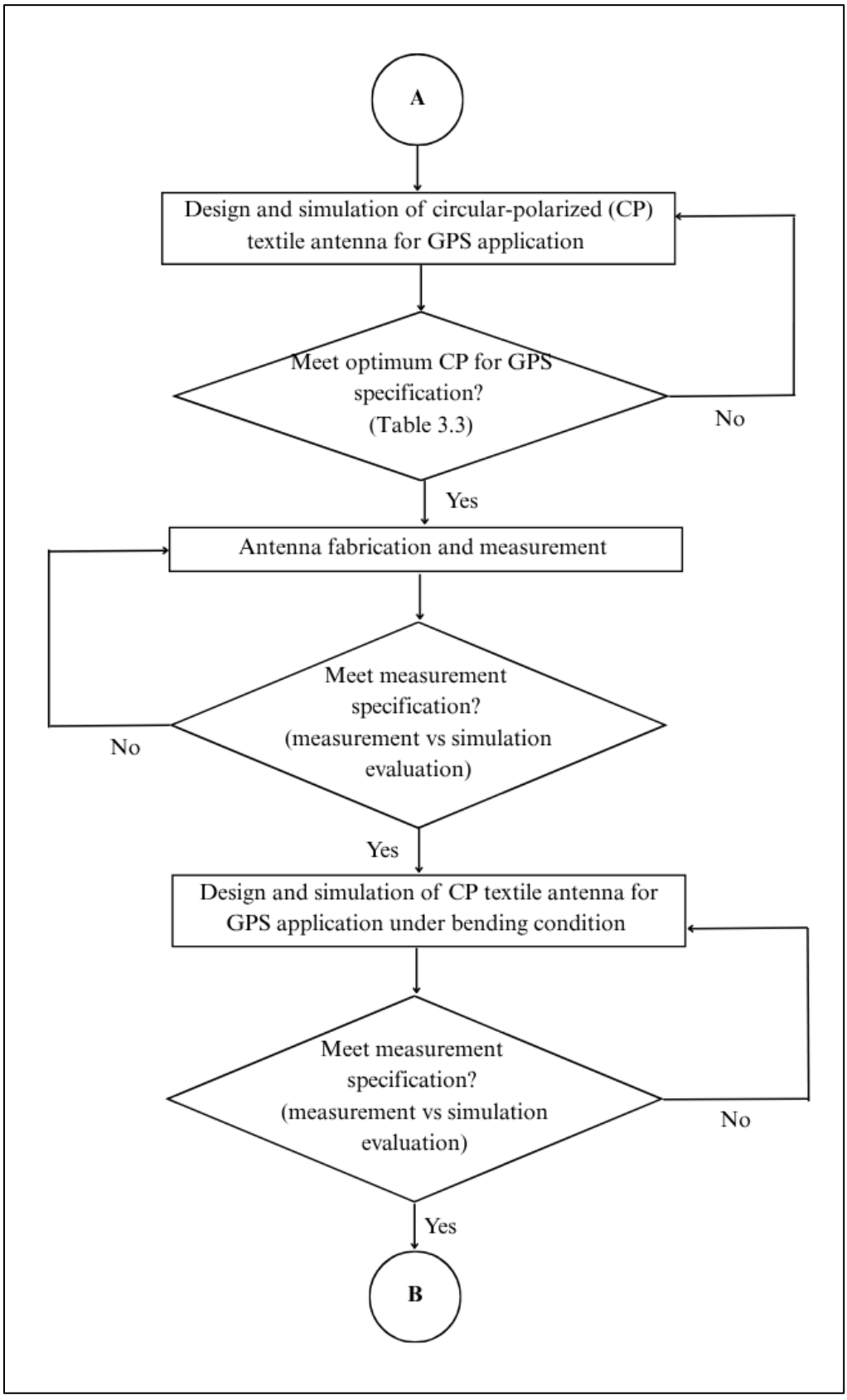
A
Design and simulation of circular-polarized (CP) textile antenna for GPS application
Meet optimum CP for GPS specification? (Table 3.3)
No
Yes
Antenna fabrication and measurement
Meet measurement specification? (measurement vs simulation evaluation)
No
Yes
Design and simulation of CP textile antenna for GPS application under bending condition
Meet measurement specification? (measurement vs simulation evaluation)
No
Yes
B

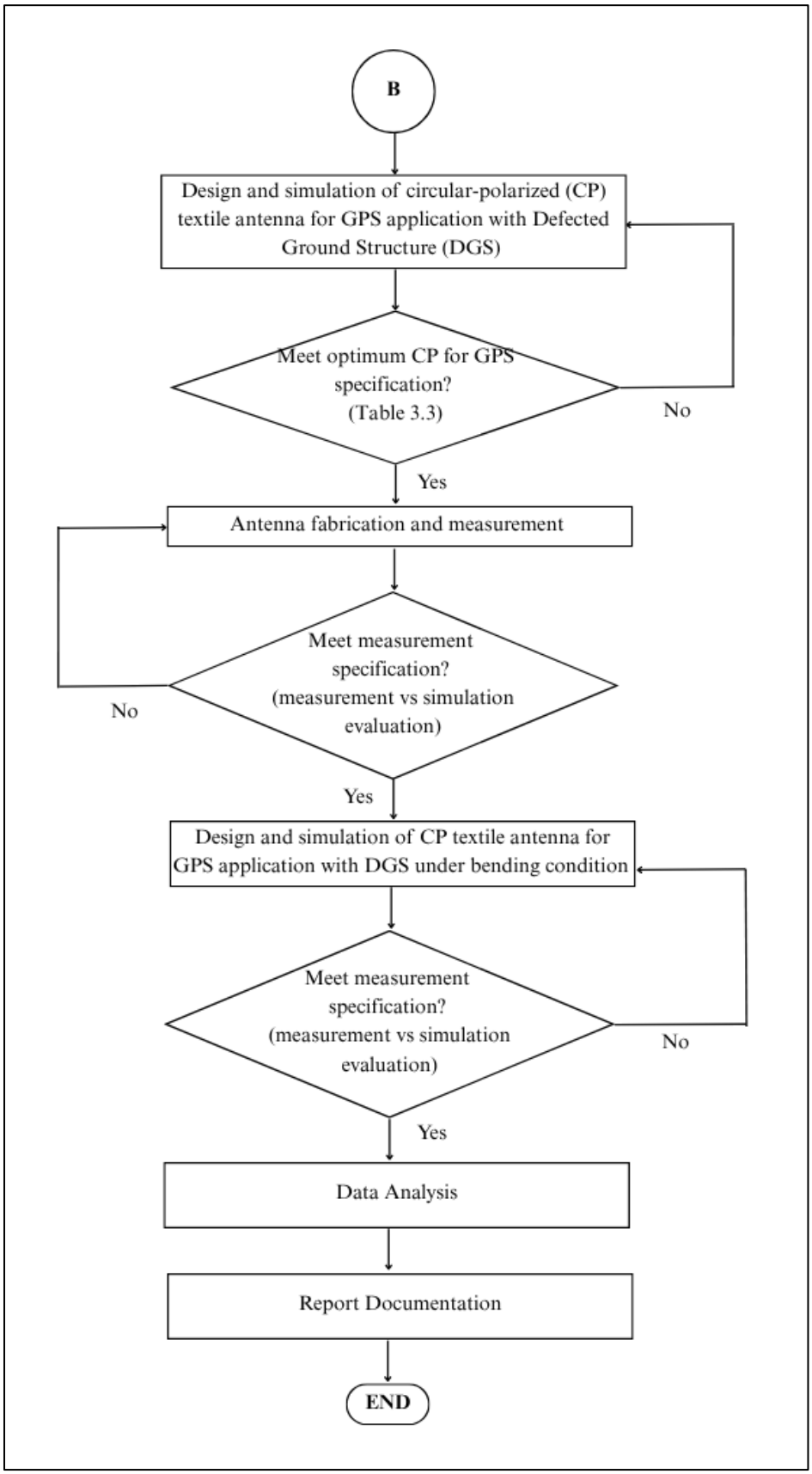

Figure 3.1 Flowchart of Research Works

3.3 Textile Antenna Design Requirements and Performance Specifications

This subsection outlines the key design requirements and performance specifications adopted for the development of the proposed textile antenna intended for wearable GPS-L1 applications.

The physical and electrical properties of the selected textile materials employed in this study are summarized in Table 3.1. In addition, the key technical performance parameters and measurement conditions adopted for conductivity characterization using the Transmission Line Method (TLM) are presented in Table 3.2. Based on these material characteristics and measurement considerations, the target design and performance specifications defined for the proposed wearable textile antenna system are listed in Table 3.3, which serve as the reference benchmarks for the subsequent antenna design and performance evaluation.

Table 3.1
Specification of Textile Antenna Materials

Item	**Parameter**	**Target Specification**
Non-conductive Element	Dielectric Constant, ε_r	1.0 to 2.0
	Loss Tangent, $tan\ \delta$	0.00 to 0.10
	Thickness, h (mm)	0.4 to 3.0
	Number of Textile Variants, n	3
Conductive Element	Thickness, t (mm)	0.1 to 0.5
	Electrical Conductivity, σ (S/m)	$\approx 10^5$

Table 3.2
Simulation Parameters for Conductivity Measurement using Transmission Line Method (TLM)

Parameter	**Target Specification**
Operating Frequency, fr (GHz)	1.575 GHz
Return Loss, S_{11} (dB)	≤ -10 dB
Transmission Loss, S_{21} (dB)	Approaching 0 dB
Attenuation Constant, α	Minimal value
Substrate Thickness Range	0.5 to 4.0 (in 0.5 mm steps)

Table 3.3
Target Specification for the Proposed Antenna Wearable Textile Antenna System

Parameter	**Target Specification**
Operating Frequency, *fr* (GHz)	1.575 GHz
Impedance Bandwidth, *IBW* (MHz)	≥ 51 MHz (GPS-L1 Spectrum:1.559 to 1.610 MHz)
Return Loss, S_{11} (dB)	≤ −10 dB
Radiation Efficiency, η (%)	≥ 50%
Gain, *G* (dB)	≥ 2 dB
Polarization	Circular (Right Hand)
Axial Ratio, *AR* (dB)	≤ 3 dB (within operating band)
Axial Ratio Bandwidth, *ARBW* (MHz)	≥ 30 MHz
Axial Ratio Beamwidth, AR Beamwidth (°)	≥100 degrees

Overall, the material specifications, conductivity measurement parameters, and target antenna performance requirements presented in this section establish a clear and structured design framework for the proposed wearable textile antenna. These specifications ensure that both electromagnetic performance and practical wearable constraints are systematically addressed. The subsequent sections describe how these defined criteria are applied in the antenna design and evaluation procedures.

3.4 Determination of Textile Components

The substrate material selection is crucial to meet the required bandwidth and good antenna efficiency. In this work, felt, Tencel, and denim are chosen as substrates as seen in Table 3.4 and Table 3.5 based on their excellent performance and popularity in the application of wearable textile antenna (Adam et al., 2021; De Cos Gomez et al., 2020a; De Cos Gómez et al., 2020b; Douhi et al., 2023; Ilyas, Budiastuti, & Rahardjo, 2020b; Mahmood et al., 2021; Sharma et al., 2025; Singh & Mishra, 2025; Singh & Verma, 2021; Tekneci et al., 2025; Yang, Liu, & Fan, 2022). The three selected textile variants presents diverse range of category as seen in Table 3.4 and exhibits unique physical and electromagnetic properties including differences in porosity, mechanical stiffness, moisture absorption behaviour and dielectric characteristics. These variations provide a valuable basis for conducting a comparative analysis of how substrate properties influence the key antenna performance metrics.

Table 3.4
Classification of Textile Variants

Textile	Composition	Category	Fibre Origin
Felt	70% wool + 30% viscose	Natural + Regenerated Blend	Animal (wool) + Plant (viscose from wood pulp)
Tencel	100% Lyocell	Regenerated cellulose	Plant-based wood pulp
Denim	100% cotton	Natural (Plant-based)	Cotton plant

For the conductive material, Shieldit Super was selected for the antenna patch due to its excellent combination of electrical conductivity, mechanical flexibility, and ease of integration with textile substrates. It is a commercially available nickel-plated copper fabric that provides low surface resistivity (approximately 0.07 Ω/sq), which is crucial for minimizing conductor losses and ensuring efficient current distribution across the antenna surface. Unlike rigid copper sheets, Shieldit Super maintains electrical performance while remaining soft, conformable, and durable, making it highly suitable for wearable applications. Its adhesive backing further simplifies fabrication by allowing direct lamination onto textile substrates without requiring additional bonding agents or stitching, thereby preserving the antenna's structural and electromagnetic integrity. The material's proven performance in numerous peer-reviewed textile antenna studies further supports its reliability and suitability for this research.

3.5 Measurement of Thickness and Dielectric Properties of Substrate (Non-Conductive Layer)

Firstly, textile characterization was performed for all three textiles namely felt, denim and Tencel to measure the thickness (h). For measuring the thickness of each textile, a digital thickness gauge was used as seen in Figure 3.2. For dielectric measurement, the techniques are commonly divided into contact-based and non-contact approaches. In this work, the dielectric properties are evaluated using two established method namely the open-ended coaxial probe technique and the free-space measurement method. The open-ended coaxial probe method was used as the primary dielectric characterization technique for all candidate textile substrates because it allows direct extraction of complex permittivity and loss tangent using relatively small material

samples. However, since textile materials are porous, compressible, and surface-sensitive, the extracted dielectric properties may be influenced by probe contact pressure, surface roughness, air gaps, and local material non-uniformity. Therefore, the free-space method was included as a complementary measurement technique to verify the dielectric response under non-contact plane-wave propagation conditions.

Table 3.5
Selected Textile Variants and Conductor

Textile Substrate		
Felt	**Tencel**	**Denim**
		
Textile Conductor: Shieldit Super		
Front		**Back (with adhesive)**
		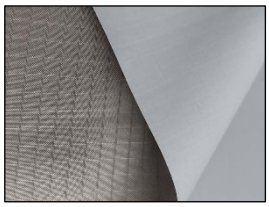

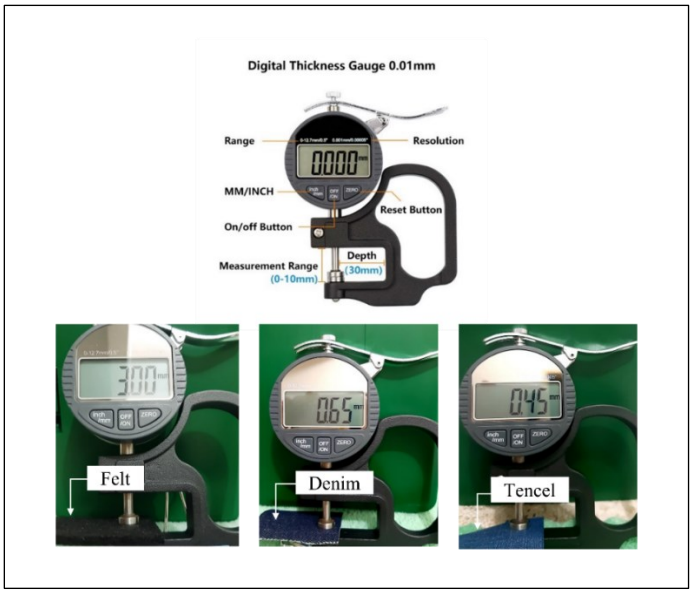

Figure 3.2 Measurement of Substrate Thickness using Digital Thickness Gauge

3.5.1 Open-ended Coaxial Probe Measurement Method

The open-ended coaxial probe method was used to determine the dielectric constant (ε_r) and loss tangent ($tan\ \delta$) via a measurement setup comprised of Keysight N5232A PNA-L Vector Network Analyzer (VNA) connected to a Keysight 85070 dielectric probe kit with data acquisition and material property extraction performed using the Keysight dielectric probe software as illustrated in Figure 3.3. The dielectric probe operates by terminating a coaxial transmission line in an open end, which is placed in direct contact with the material. As seen in Figure 3.4, the fringing electromagnetic fields at the probe tip penetrate the textile sample, and the reflected signal is influenced by the material's dielectric properties and can support a frequency range from 200 MHz to 20 GHz. Prior to measurement, the dielectric probe is calibrated using open, short, and distilled water as the reference liquid at the probe tip to eliminate systematic errors and ensure measurement accuracy.

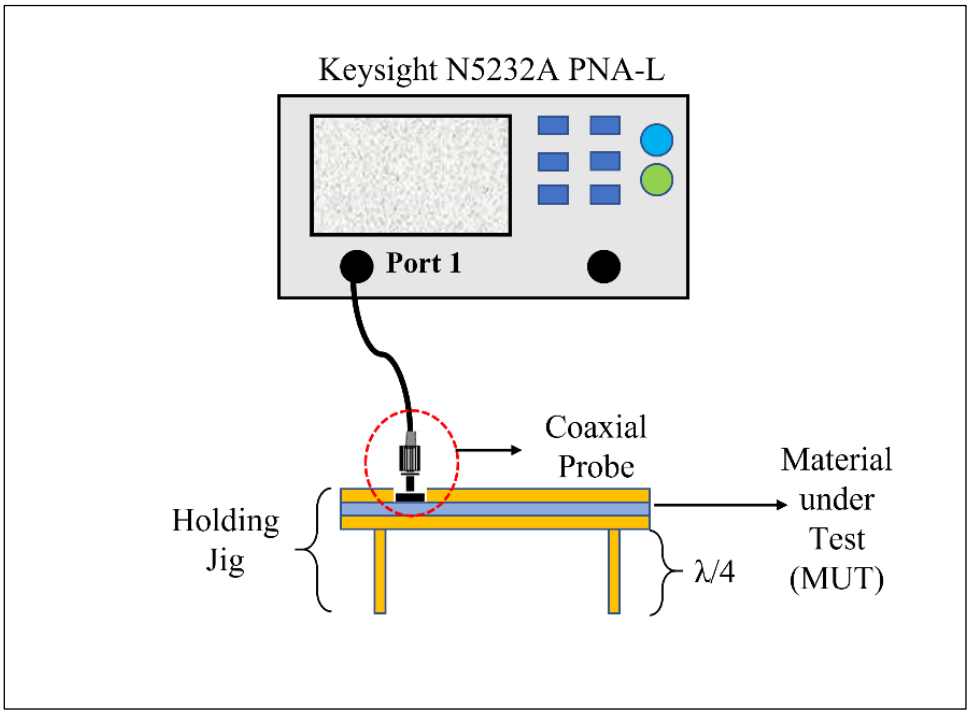

Figure 3.3 Measurement Setup for Dielectric Properties

A customised holding jig was developed to sustain the textile firmness for constant flat surface and most importantly to prevent air gaps between the probe tip and textile surface throughout measurement process. The jig enables adjustment of the sample height according to the operating frequency to minimize multiple reflections from the supporting surface. Accordingly, the separation between the MUT and the desk surface was maintained at greater than one-quarter of the wavelength (λ/4).To ensure the consistency and accuracy of result, the probe was placed on each 9 uniform points made on the jig as seen in Figure 3.5 for every textile sample and subsequently the results are average out. Each measurement was repeated ten times and the results were used to assess measurement repeatability and reliability.

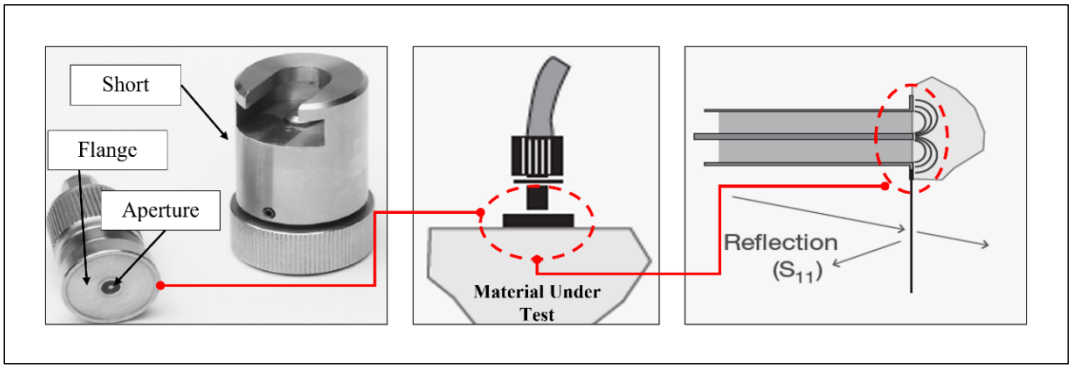

Figure 3.4 Open-ended Coaxial Probe Measurement Illustrating S_{11} Reflection at the Probe-MUT Interface (Keysight)

The VNA was used to measure the complex reflection coefficient (S_{11}) at the probe–material interface over the frequency of 1.575 GHz. This reflection response forms the basis for extracting the dielectric constant (ε_r) and loss tangent (tan δ). To calculate ε_r, the real part of dielectric value, ε' and the imaginary part namely ε'' were obtained from the display of VNA. The complex relative permittivity, ε_r and loss tangent of *tan δ* can be determined from the equations below:

$$\varepsilon_r = \varepsilon' + j\varepsilon'' \tag{3.1}$$

$$\tan\delta = \frac{\varepsilon''}{\varepsilon'} \tag{3.2}$$

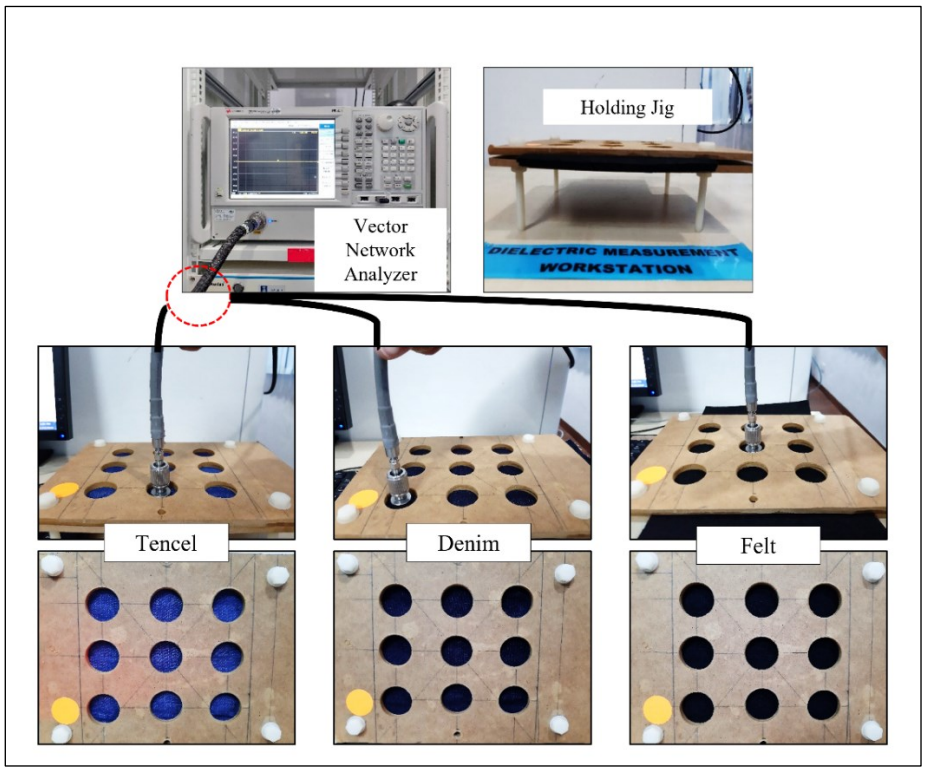

Figure 3.5 Textiles Dielectric Measurement

Based on the measurement performed, the average out results are tabulated in Table 3.6 below for each of textile.

Table 3.6
The Parameter Measured Values of Selected Substrates for Open-ended Coaxial Probe Measurement Method

Substrate	Relative Permittivity ($\mathcal{E}_r$)	Loss Tangent ($tan\ \delta$)	Thickness, h (mm)
Denim	1.1113	0.0669	0.65
Tencel	1.2215	0.0410	0.45
Felt	1.0980	0.0395	3.00

3.5.2 Free Space Measurement Method

A free-space measurement setup comprises a vector network analyser (VNA), a pair of antennas, a sample holder, and dedicated measurement software (as seen in Figures 3.6, 3.7 and 3.8) was performed in Microwave Research Institute (MRI), UiTM Shah Alam. The two antennas function respectively as the transmitting and receiving antennas and both are connected to VNA. Meanwhile, the material under test (MUT) is positioned in between of the two antennas. This configuration enables non-contact

electromagnetic characterization of the MUT by analysing the transmitted and reflected signals, thereby avoiding mechanical loading or deformation of the material during measurement. The VNA was first calibrated using the through-reflect-line (TRL) method using PTFE as the standard reference.

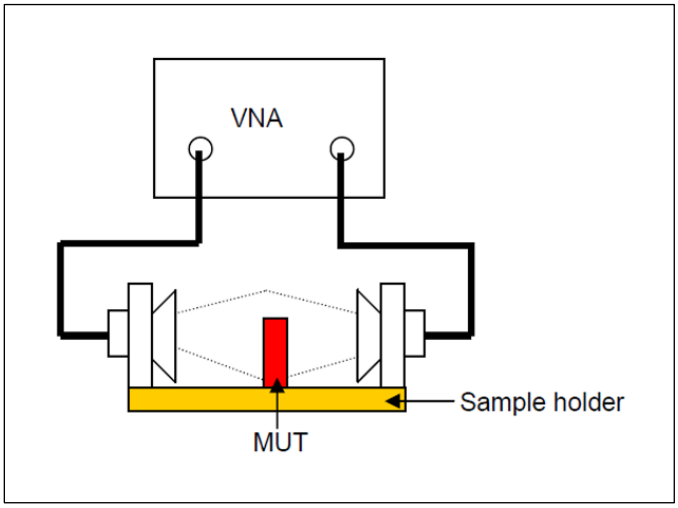

Figure 3.6 Free-space Method Measurement Setup

After calibration was performed, the S-parameters of the empty sample holder were measured and obtained by placing it midway between the two antennas. In Figure 3.8, the MUT was then placed on the sample holder between the two antenna and the s-parameters measurement was performed again. The influence of the sample holder can be cancelled out using the de-embedding functions of the VNA to determine the s-parameter of the MUT. In this method, time domain gating should be applied to ensure no multiple reflections in the sample itself and to eliminate the diffraction of energy from the edge of the antenna. The dielectric properties can be determined by the post processing of the measured reflections and transmission coefficient. The MUT measurement with dimension 10 cm x 10 cm was performed under 10 different thickness from the selected textile and the final values of the dielectric properties been averaged out.

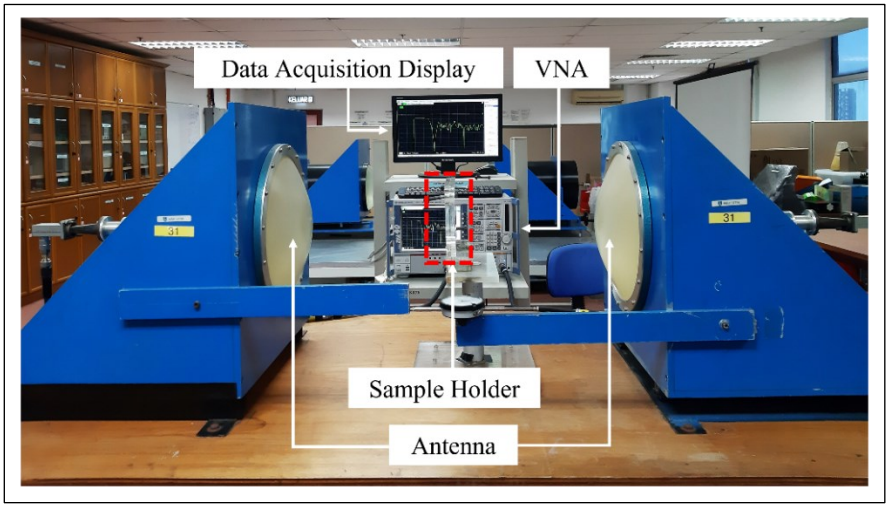

Figure 3.7 Free-space Measurement Setup in MRI

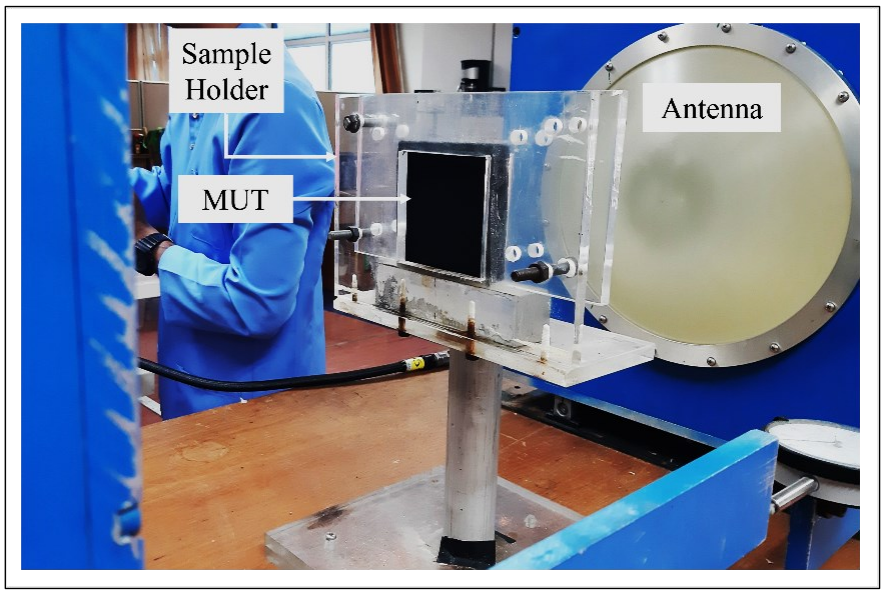

Figure 3.8 Free-space Measurement Setup with MUT

To obtain the dielectric properties from the measured s-parameters, a conversion method called Nicholson-Ross-Weir (NRW) was used. The NRW is a common method used to provide a direct calculation of both permittivity and permeability due to its accuracy and fast speed. The mathematical model of NRW process is shown in Figure 3.9.

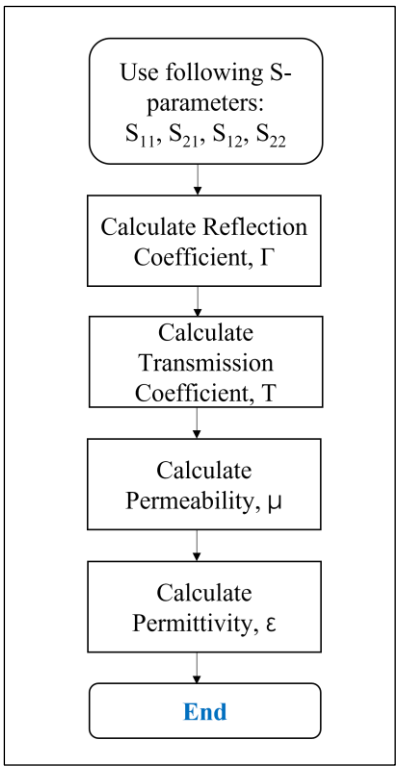

Figure 3.9 The Process for NRW Method

The procedures proposed by NRW method is deduced from the following equations of S_{11} and S_{21} which can obtain directly from the network analyzer:

$$S_{11} = \frac{\Gamma(1 - T^2)}{(1 - \Gamma^2 T^2)} \tag{3.3}$$

$$S_{21} = \frac{T(1 - \Gamma^2)}{1 - \Gamma^2 T^2} \tag{3.4}$$

The reflection coefficient can be deduced from:

$$\Gamma = X \pm \sqrt{X^2 - 1} \tag{3.5}$$

where $|\Gamma 1| < 1$ is required for finding the correct root and in terms of s-parameters.

$$X = \frac{{S_{11}}^2 - {S_{21}}^2 + 1}{2S_{11}} \tag{3.6}$$

The transmission coefficient can be written as:

$$T = \frac{S_{11} + S_{21} - \Gamma}{1 - (S_{11} + S_{21})\Gamma} \tag{3.7}$$

The permeability is given as:

$$\mu_r = \frac{1 + \Gamma_1}{\Lambda(1 - \Gamma)\sqrt{\frac{1}{\lambda^2{}_0} - \frac{1}{\lambda^2{}_c}}} \tag{3.8}$$

where λ_0 is a free space wavelength and λ_c is the cut off wavelength. Given:

$$\frac{1}{\Lambda^2} = \left(\frac{\varepsilon_r * \mu_r}{\lambda^2{}_0} - \frac{1}{\lambda^2{}_c}\right) = -\left(\frac{1}{2\pi L} ln\left(\frac{1}{T}\right)\right)^2 \tag{3.9}$$

The permittivity can be defined as:

$$\varepsilon_r = \frac{\lambda^2{}_0}{\mu_r}\left(\frac{1}{\lambda^2{}_c} - \left[\frac{1}{2\pi L} ln\left(\frac{1}{T}\right)\right]^2\right) \tag{3.10}$$

From the above equation 3.3 to 3.10, the notation is described as below:

L = material length

ε_r = relative permittivity

μ_r =relative permeability

λ_g = wavelength in sample

Based on the measurement performed, the average out results are tabulated in Table 3.7 below for the sample done on felt textile. Felt was selected for this verification stage based on its preliminary suitability for wearable antenna implementation, including its available substrate thickness, mechanical stability, surface uniformity, flexibility, and practical compatibility with antenna fabrication. These characteristics made felt more suitable for reliable free-space measurement because the method requires a relatively flat, stable, and sufficiently large sample to minimize sagging, diffraction, air-gap, and edge-related measurement uncertainties.

From the results, the extracted relative permittivity (ε_r) of the felt fabric is relatively high at approximately 4.5. This elevated value indicates that the effective permittivity of felt is influenced by its porous and non-homogeneous structure. These

characteristics introduce scattering, multiple internal reflections, and non-uniform electrical thickness, which increase the apparent phase delay of the propagating electromagnetic wave.

Table 3.7
The Parameter Measured Values of Selected Substrates for Free-space Measurement Method

Substrate	Relative Permittivity ($\mathcal{E}_r$)	Loss Tangent ($tan\ \delta$)	Thickness, h (mm)
Felt	4.5746	0.02322	3.00

3.6 Transmission Loss Evaluation using Transmission Line Method

To identify the most suitable substrate material for antenna implementation, a Transmission Line Method (TLM) was used to compare the transmission behaviour of the conductive layer across the three textile dielectric substrate (felt, denim and Tencel). The general transmission line characteristics can be represented by γ based on equation 3.11 through the parameters of inductance; L (H/m), resistance; R (Ω/m), capacitance; C (F/m) and conductance; G (S/m) and represented as a two-port transmission line equivalent model as seen in Figure 3.4.

$$\gamma = \sqrt{(R + j\omega L)(G + j\omega C)} \tag{3.11}$$

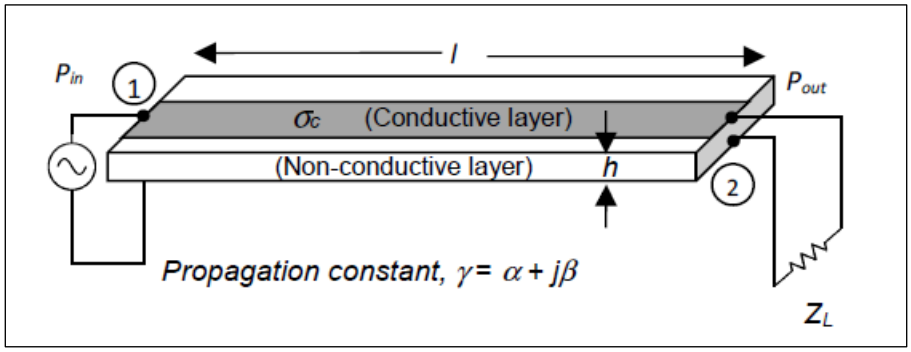

Figure 3.10 Two-Port Transmission Line Model (Abd Rahman, Yamada, & Ahmad, 2019)

In this equivalent model, the conductivity parameter of sigma, σ can be developed from the scattering parameter measurement which represents the transmission loss of the line sample, derived based on equation (3.12) where ε is the

material's relative permittivity, μ is the material's permeability, h is the substrate's thickness and α is the attenuation constant through the S_{21} measurement:

$$\sigma_{calc} = \frac{\omega^3 \varepsilon^2 \mu}{\alpha^2 h^2 (2h^2 + 2\omega^2 \varepsilon \mu)} \tag{3.12}$$

Figure 3.11 shows the two-port TLM in Computer Simulation Technology (CST), with a conductive layer at the top and a non-conductive layer at the bottom. The conductive layer of pure copper with the conductivity, σ of 5.86 x 10^7 S/m and sheet thickness of 0.035 mm is used in this study to develop the two-port transmission line model simulation as shown in Fig 3.12. Based on this approach, the impedance measurement is set at 50 Ω by optimising the width of each substrate for each thickness which varies from 0.5 mm to 4.0 mm in 0.5 mm steps (practical wearable application). The simulated assessment on the return loss and transmission loss parameters are performed for all textiles thicknesses of each material at 1.575 GHz for Global Positioning System (GPS) application. The optimal textile thickness is identified and used further to assess the transmission behaviour performance among all textiles.

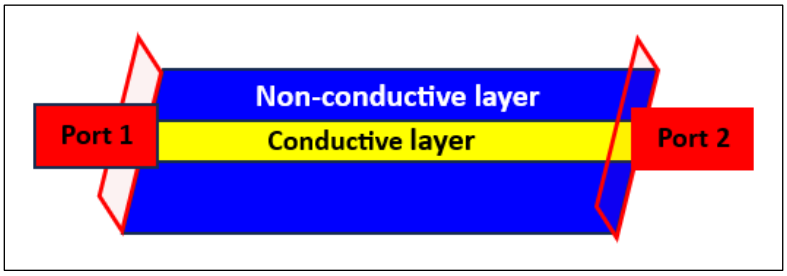

Figure 3.11 Two-Port Transmission Line Model Design

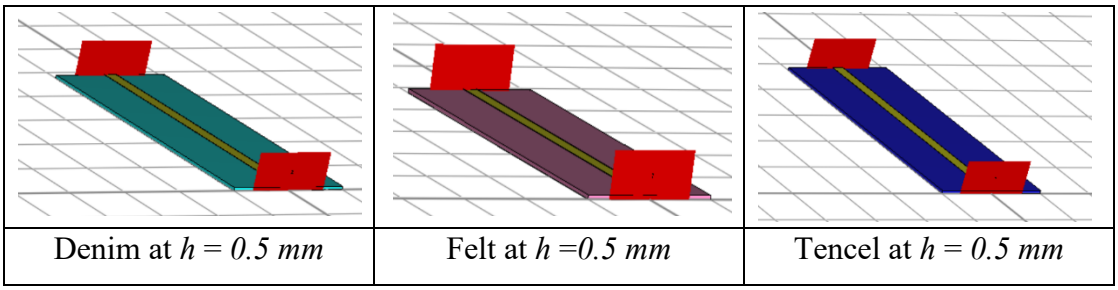

Denim at *h = 0.5 mm*	Felt at *h =0.5 mm*	Tencel at *h = 0.5 mm*

Figure 3.12 Two-Port TLM Simulation in CST for Denim, Felt and Tencel Substrate at *h=0.5 mm* in CST

To validate the TLM for lossy substrate, three samples were fabricated based on the identified optimal performance of textile substrate. Sample 1 (S1) was designed as

a low-loss reference sample made of Copper Pure and Rogers RO5880 (dielectric constant, ε_r = 2.2, *tan* δ = 0.0009). Sample 2 (S2) comprises of Shieldit Super and Rogers RO5880, while Sample 3 (S3) consisted of Shieldit Super and optimal performance textile substrate as shown in Figure 3.13.

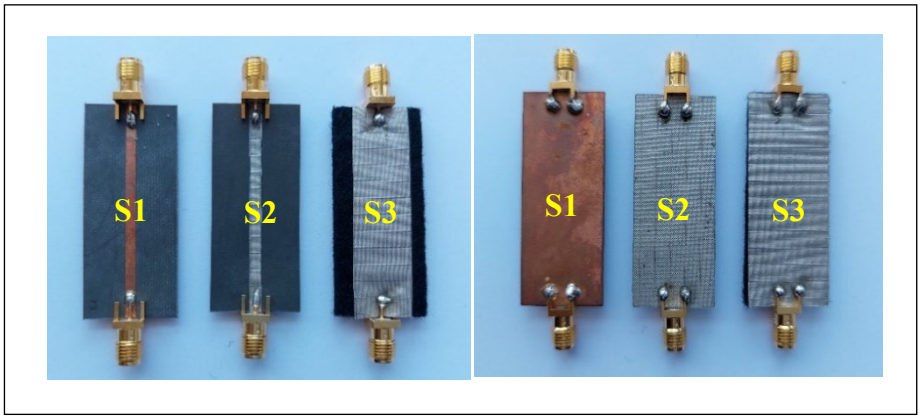

(a) (b)

Figure 3.13 The Fabricated Transmission Line for Sample 1, Sample 2 and Sample 3 (a) Front View (b) Bottom View

Figure 3.14 shows the measurement setup for the proposed two-port strip line technique using Keysight N5234A PNA-L VNA. The impedance measurement was first conducted before the S_{21} measurement to ensure each sample S1, S2 and S3 has the input impedance of 50-ohm to avoid reflection mismatch for a reliable conductivity calculation.

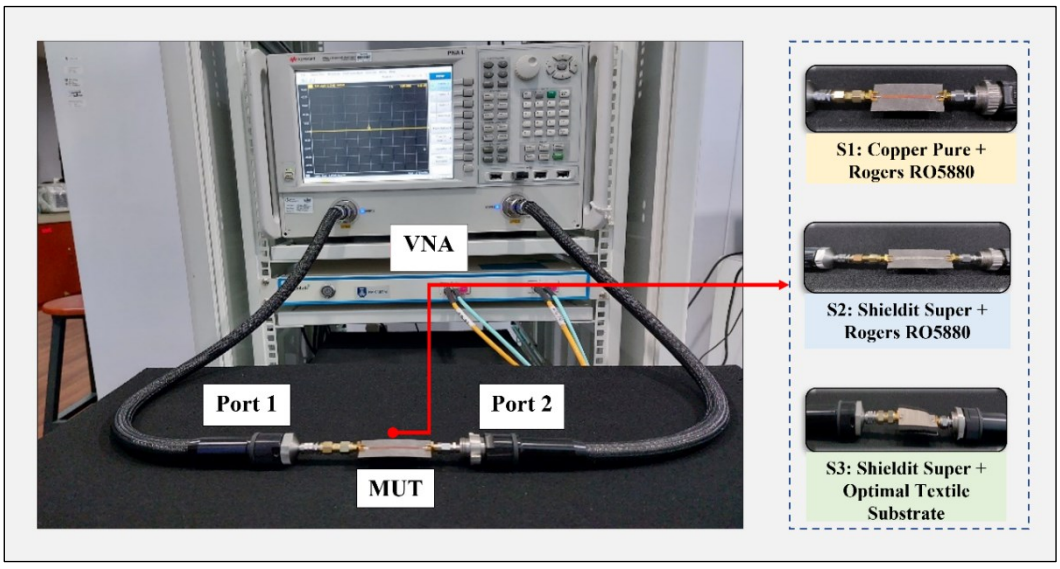

Figure 3.14 Measurement Setup for the Conductivity Measurement on TLM

3.7 Design of Textile Antenna

This study focus on bandwidth enhancement of wearable circular polarization (CP) textile antenna for GPS-L1 applications. The primary considerations for designing this antenna are the ability to support the wearability on body and must operate in Right-Hand Circular Polarization (RHCP) at 1.575 GHz. Therefore, the antenna design process commenced with the selection of a coaxial probe feeding technique, as it offers mechanical robustness and higher reliability under bending and deformation which are critical requirements for wearable textile antennas. Subsequently, the antenna in RHCP at the resonant frequency, f_r was developed via software and hardware (prototype). The software development includes the optimal design of the radiating elements which is able to generate robust RHCP while improving impedance and axial ratio bandwidth under bending conditions. The theoretical calculations for the radiating elements and substrate were first performed to establish the initial antenna dimensions and subsequently simulated using electromagnetic. The antenna design was fabricated and validated during the measurement process.

3.7.1 Calculation of Antenna Dimension

Figure 3.15 shows the typical geometry of a rectangular planar antenna fed by a transmission feed line structure. The radiating patch may take various shapes including squre, rectangular, thin strip (dipole), circular, elliptical, triangular or other configuration. In this work, a rectangular antenna was used due to its ease of analysis and fabrication simplicity (Balanis, 2005). Initially, the radiating patch element was designed to operate at GPS-L1 resonant frequency of 1.575 GHz. The antenna dimensions were calculated based on fundamental antenna theory whereby the resonant behaviour is reflected by the patch width W, patch length L, and relative permitivity ε_r of the dielectric material. The theoretical expressions relate the operating frequency f_r to the free-space wavelength through the speed of light in free space, denoted by c ($c = 3 \times 10^8 m/s$).

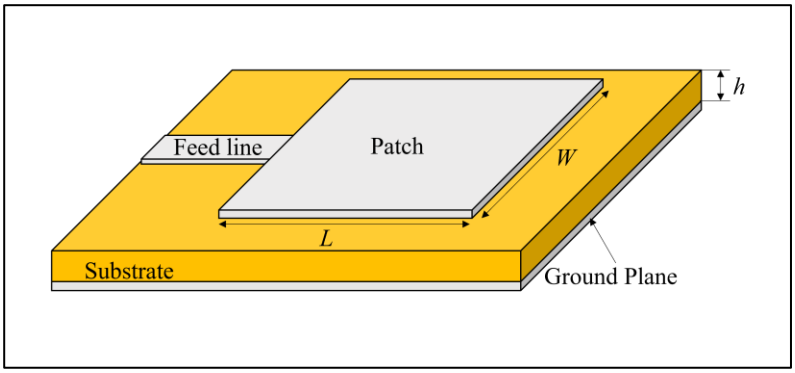

Figure 3.15 Geometrical Top View of Rectangular Planar Antenna

Other key parameters including effective relative dielectric constant ε_{reff} , effective electrical length L_{eff} and the length extension due to fringing fields ΔL were derived using closed-form equations to obtain the physical patch length required for resonance. The substrate length *L,* and width *W,* were chosen to be larger than the corresponding patch dimensions for sufficient space of fringing fields to decay and reducing edge diffraction effects. The substrate thickness *h* was carefully selected to balance bandwidth enhancement and radiation efficiency while mitigating surface wave excitation, which is particularly important for low-permittivity textile substrates.

The related equations derived from rectangular microstrip antenna theory are presented by equations (3.13) to (3.19) below to calculate the patch and substrate dimensions serve as a initial design reference:

Width of patch, *W*

$$W = \frac{c}{2f_r}\sqrt{\frac{\varepsilon_r + 1}{2}} \tag{3.13}$$

Length of patch, *L*

$$L = L_{eff} - 2\Delta L \tag{3.14}$$

$$L_{eff} = \frac{c}{2f_r\sqrt{\varepsilon_{reff}}} \tag{3.15}$$

$$\varepsilon_{reff} = \frac{\varepsilon_r + 1}{2} + \frac{\varepsilon_r - 1}{2}\left[1 + 12\frac{h}{W}\right]^{\frac{1}{2}} \tag{3.16}$$

$$\Delta L = 0.412h\frac{\left(\varepsilon_{reff} + 0.3\right)\left(\frac{W}{h} + +0.264\right)}{\left(\varepsilon_{reff} - 0.258\right)\left(\frac{W}{h} - 0.8\right)} \tag{3.17}$$

As a reference for optimum antenna performance, the substrate dimensions are given by the following equations:

$$W_s = 6h - W \tag{3.18}$$

$$L_s = 6h + L \tag{3.19}$$

3.7.2 Probe-feed Technique

In this work, a coaxial probe feed is adopted due to its structural simplicity, mechanical robustness, and suitability for wearable textile antennas to maintain stable electrical performance under bending, deformation, and repeated handling. Unlike microstrip feed lines, which are more sensitive to bending-induced impedance variations and conductor misalignment, the coaxial probe feed provides a localized and mechanically stable excitation point, thereby improving impedance consistency when the antenna is subjected to bending. In addition, this feeding technique produces low spurious radiation, which is desirable for reducing unwanted coupling with the human body.

The configuration of the coaxial probe feed is illustrated in Figure 3.16. The inner conductor of the coaxial connector is connected to the radiating patch, while the outer conductor is connected to the ground plane. he inner and outer conductors are separated by an insulating dielectric layer made of polytetrafluoroethylene (PTFE) to provide stable electrical insulation.

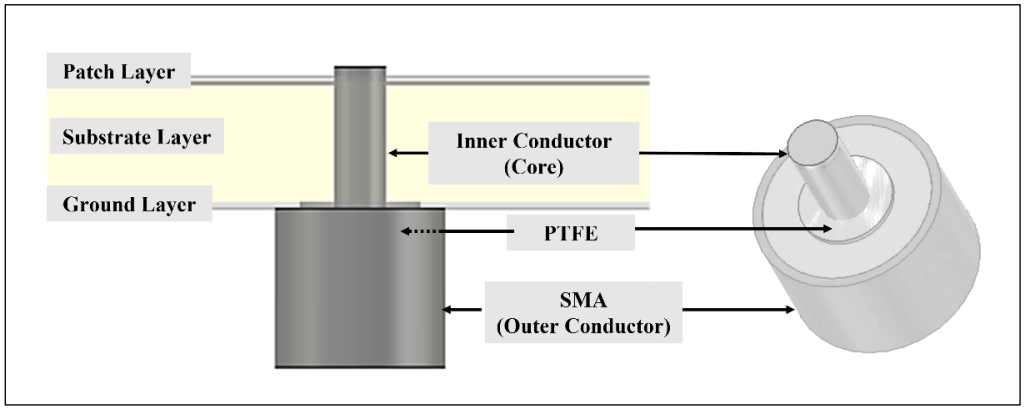

Figure 3.16 The Configuration of Coaxial Probe-feed Attached to Antenna

Figure 3.17 shows a 50 Ω SMA square-flange jack receptacle by Multicomp Pro was employed as the feeding connector. The square-flange structure enables the connector to be firmly fixed to the ground plane, reducing mechanical movement at the feed point and enhancing connection stability. The coaxial probe penetrates the substrate vertically and excites the patch through a localized feed point. To ensure proper electrical connectivity, the PTFE insulation was removed from the core prior to fabrication.

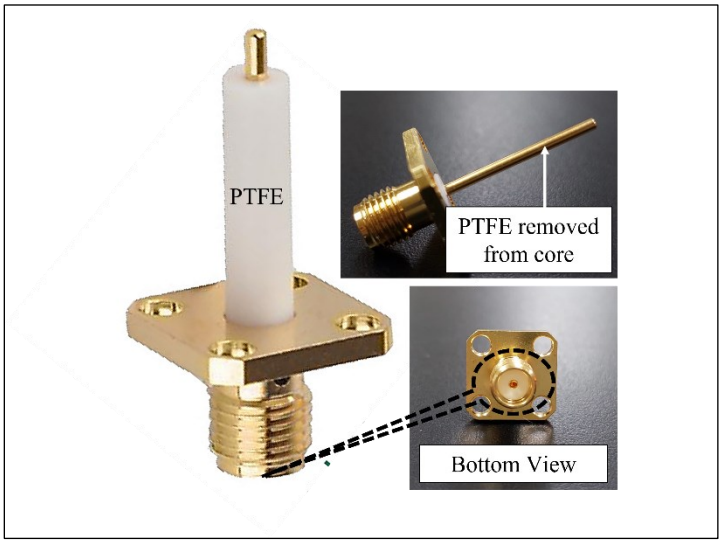

Figure 3.17 SMA Square Flange Jack Receptacle by Multicomp Pro

A standard 50 Ω SMA connector was employed to ensure compatibility with measurement equipment and reliable power delivery with low attenuation. To achieve impedance matching between the antenna and the source, the feed location was positioned near *Lp*/3 and *Wp*/2. Feeding at the patch center was avoided due to the zero electric field resulting in near-zero input impedance. Meanwhile feeding at the patch edge leads to excessively high input impedance because of the maximum electric field. This feed positioning provides an input impedance close to 50 Ω that is effective power transfer for wearable operation.

3.8 Simulation of Textile Antenna

After the design specifications were established, the antenna geometry was implemented and analysed using Computer Simulation Technology (CST). This software was selected due to its user-friendly interface and reliable electromagnetic simulation capability, which makes it suitable for the efficient analysis and design of

antenna structures and related RF components. Among the available CST modules, CST Microwave Studio (CST MWS) was chosen due to its high accuracy in full-wave three-dimensional electromagnetic simulation to evaluate key parameters including return loss, impedance bandwidth, surface current distribution, and radiation characteristics such as gain, beam direction, and beamwidth. For this research, the antenna models were iteratively optimized through simulation until the electrical and radiation target specifications were achieved.

3.8.1 Development of Textile Antenna Model

From Figure 3.18, the initial design stages began with the development of a rectangular microstrip patch antenna as the fundamental radiating structure due to ease of impedance matching and its low geometric complexity for textile implementation. This stage focused on achieving effective impedance matching at the target GPS-L1 frequency of 1.575 GHz by optimizing the patch dimensions and probe feed location based on the calculated antenna dimensions in Section 3.7.2. Once a stable input impedance close to 50 Ω was obtained, the patch geometry was subsequently designed into a square or nearly square configuration. This geometric transition was essential to enable the excitation of two orthogonal resonant modes with comparable amplitudes, thereby providing a suitable foundation for circular polarization generation. By fixing the coaxial probe feed first and progressively evolving the square patch geometry, the design maintained impedance stability while enabling systematic polarization enhancement for GPS wearable operation.

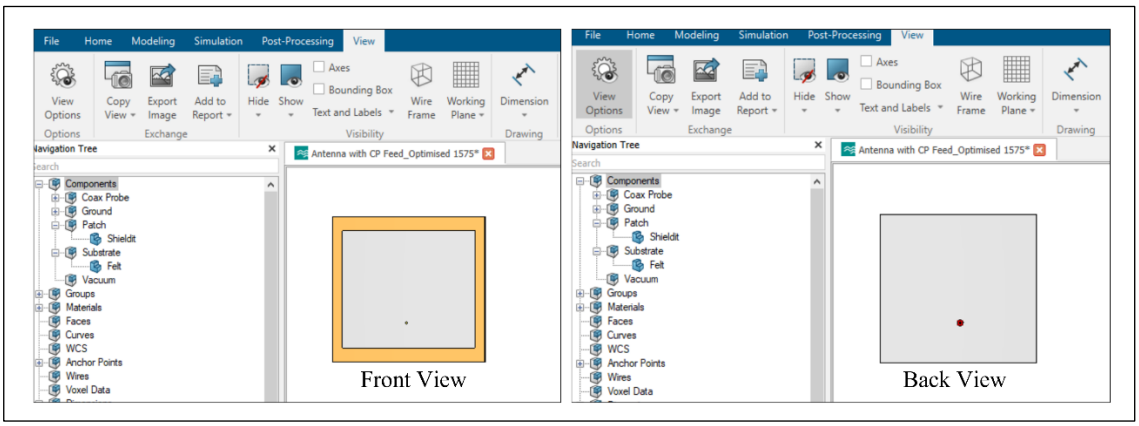

Figure 3.18 Simulation of rectangular microstrip patch textile antenna using CST Software

The SMA coaxial connector was modelled in the simulation to define the port excitation by selecting the physical faces of the inner conductor and the ground plane. In the simulation setup, the port excitation was defined on the back face of the SMA coaxial connector to represent the coaxial feed interface, as shown in Figure 3.19. Following the port excitation, the antenna was optimized and subsequently simulated to achieve the desired key performance parameters with impedance matched close to 50 Ω.

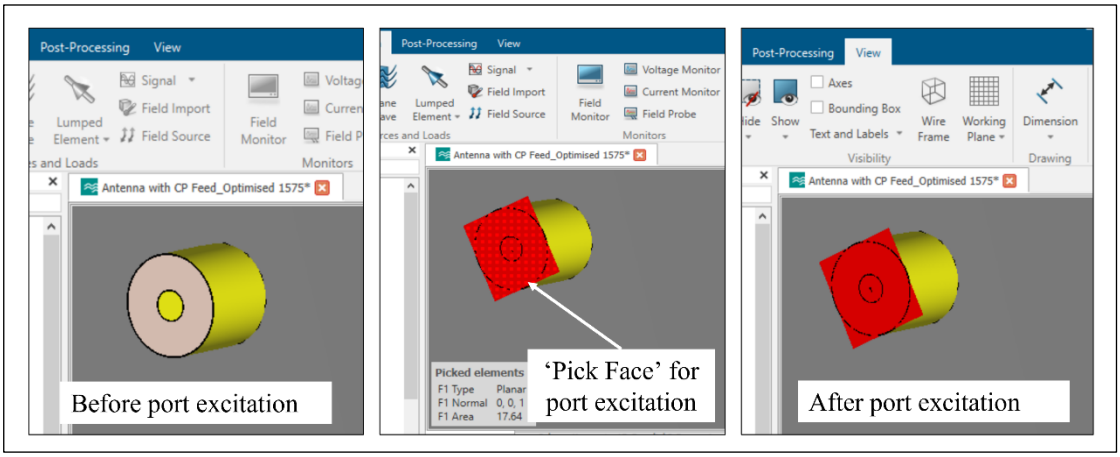

Figure 3.19 SMA Port Excitation

3.8.2 Simulation of Antenna in Bending Conditions

Wearable textile antennas are frequently subjected to bending when integrated into garments or worn on curved parts of the human body, such as the arm, leg, or torso. To realistically evaluate the mechanical deformation effects on antenna performance, bending simulations were carried out by conforming the antenna over a cylindrical surface. During the measurent, a foam structure was used as the supporting medium due to its lightweight nature, low dielectric constant, and minimal electromagnetic interference, allowing the bending effect to be isolated without introducing significant parasitic loading.

The simulated textile antenna was bent over a cylindrical support along both the E-plane and H-plane directions to represent the principal bending orientations encountered in practical wearable scenarios. In wearable applications, the degree of bending experienced by a textile antenna depends on the curvature of the body part on which it is mounted.. To bend the antenna the bending reference point was defined at the probe-feed location by adjusting the local working coordinate system (WCS) in CST

software as shown in Figure 3.20. Within the modelling environment the cylindrical bending function was selected which enabled the options of bending parameters for the antenna structure as seen in Figure 3.21.

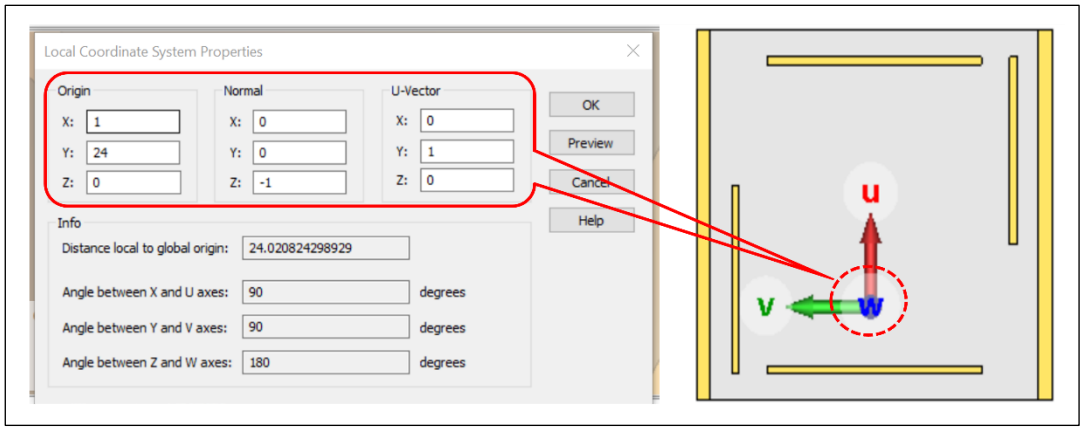

Figure 3.20 Local Coordinate System Properties at Bending Reference Point Display

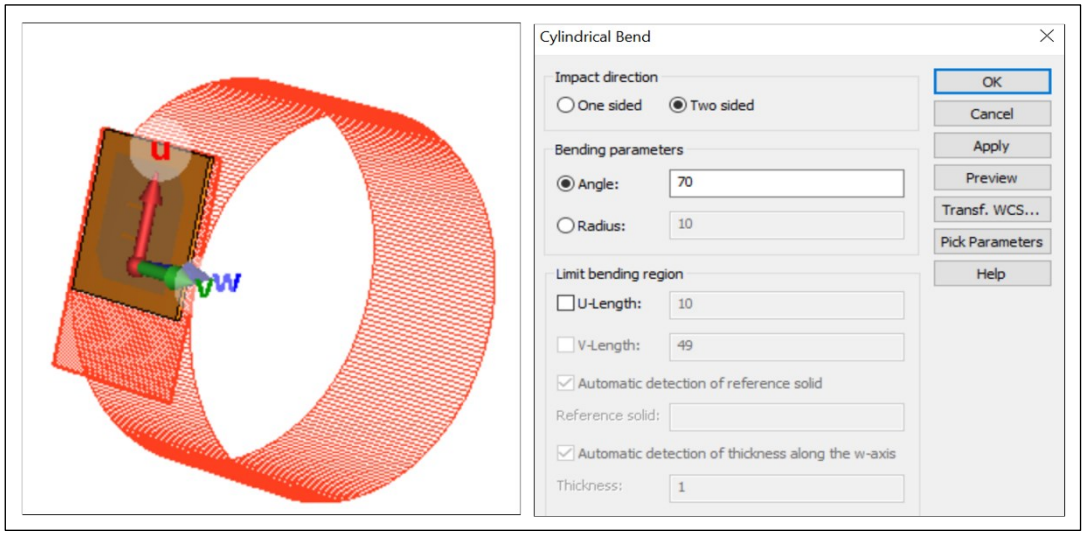

Figure 3.21 Cyclindrical Bend Setup for E-plane at Angle Bending Display

Figure 3.22 and Figure 3.23 shows the E-plane and H-plane cylindrical bending respectively. The bending degree was used as a simulation parameter and was defined by the bending radius of the cylindrical support where smaller radii represent more severe bending conditions.

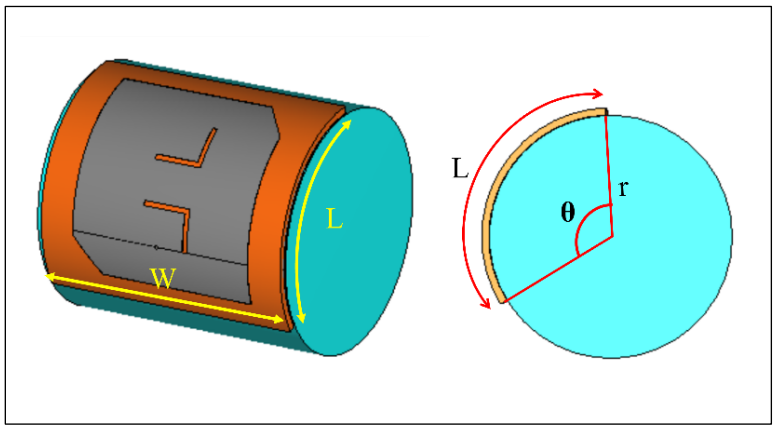

Figure 3.22 E-plane Cylindrical Bending

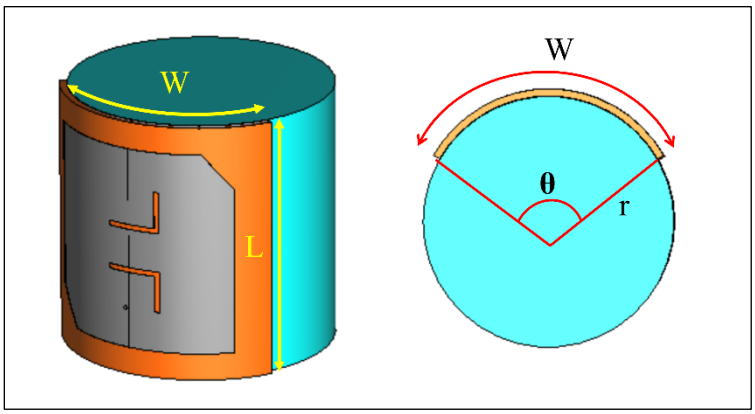

Figure 3.23 H-plane Cylindrical Bending

Figure 3.24 and Figure 3.25 show the simulation of antenna bending in E-plane and H-plane respectively. The results were compared against the flat antenna to determine the performance variation introduced by mechanical bending on wearable condition.

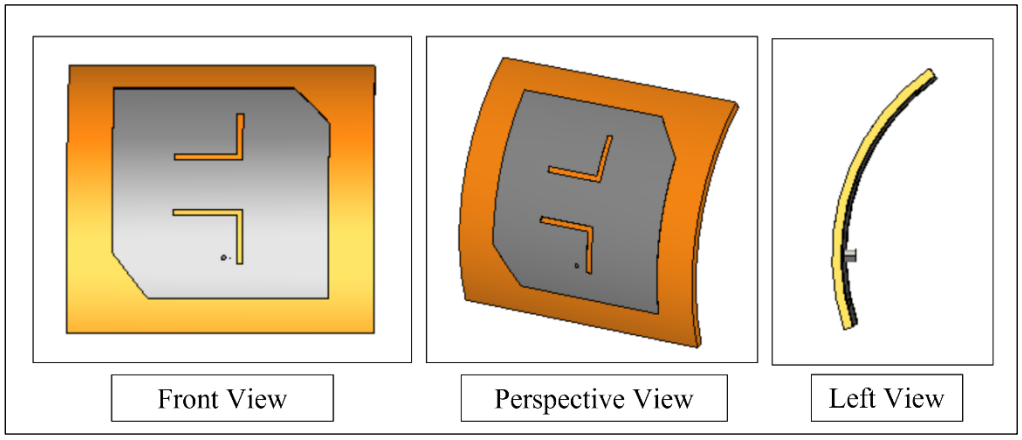

Figure 3.24 Simulated Antenna in E-plane Bending

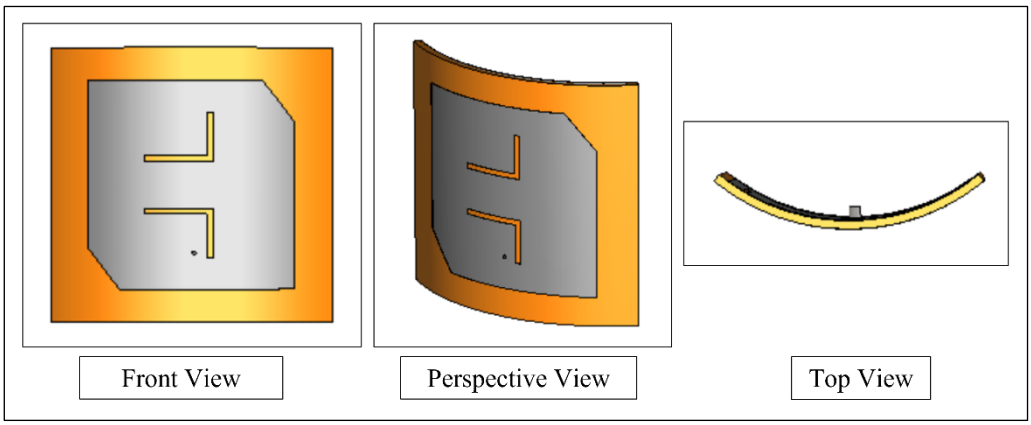

Figure 3.25 Simulated Antenna in H-plane Bending

3.9 Fabrication and Measurement of Textile Antenna

The antenna was fabricated after achieving the optimum design requirements, allowing the experimental evaluation through comparison between simulated and measured performance results. Radiation pattern measurements were then performed in an anechoic chamber to assess the far-field behaviour of the constructed antenna. The procedures for antenna development and measurement are described in the subsections that follow.

3.9.1 Antenna Fabrication and Assembly

The fabrication and assembly procedures focus on the practical implementation of the antenna geometry using textile materials and conductive elements suitable for wearable applications. Since textile substrates and conductive fabrics are flexible and deformable, manual cutting may introduce dimensional errors that can affect the slot geometry, patch shape, ground-plane size, and overall antenna performance. Therefore, three-dimensional (3D) printed moulds were used as fabrication templates to improve cutting accuracy, alignment consistency, and repeatability of the antenna geometry. The moulds, representing the antenna patch and ground plane, were designed using Autodesk Fusion 360 and fabricated using a Creality Ender 3 V2 Neo 3D printer, as illustrated in Figure 3.26. This method helped reduce human error during manual fabrication and ensured that the fabricated prototype closely followed the optimized simulation design.

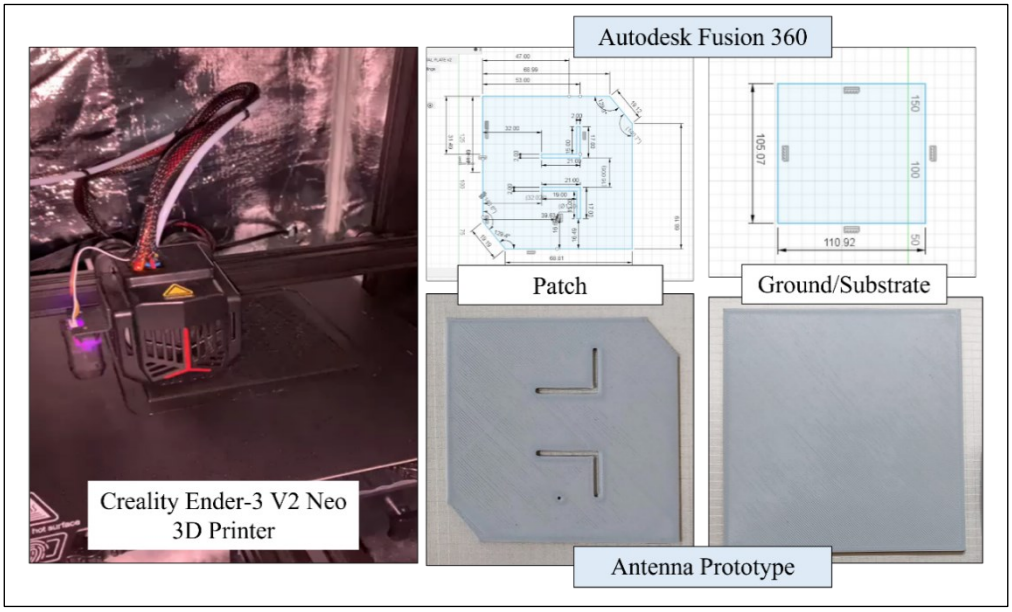

Figure 3.26 Antenna Prototype Development by 3D Printer

From the developed moulds, the conductive textile and dielectric substrate were traced and cut using a precision craft knife to ensure accurate realization of the antenna geometry as shown in Figure 3.27. The cut of radiating patch and ground plane both made from Shieldit Super conductive textile were then bonded to the dielectric substrate by applying heat using a dry hot iron, forming the top and bottom layers of the antenna structure.

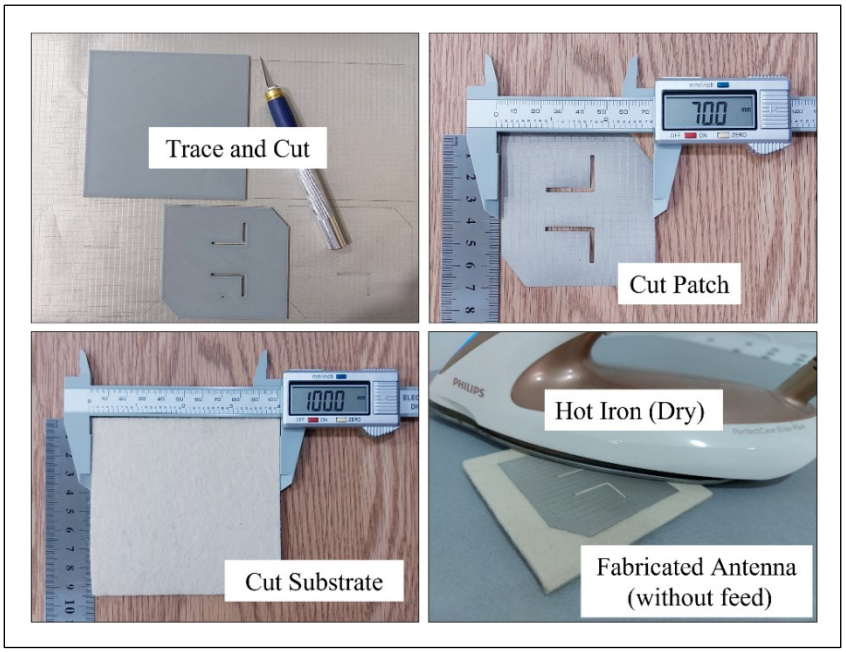

Figure 3. 27 Development of Fabricated Antenna without Feed

Figure 3.28 shows the development of fabricated antenna with feed. To realize the antenna excitation, an SMA probe-fed connector was integrated at the designated feed location from the bottom side of the antenna. A via hole was introduced through the substrate to accommodate the diameter of the SMA inner conductor (core). The polytetrafluoroethylene (PTFE) dielectric surrounding the core was partially removed to expose the signal pin, and the protruding length of the conductor was trimmed to the required height to establish contact with the radiating patch. Subsequently, the exposed core and the SMA flange mount were soldered to the top radiating patch and bottom ground plane, respectively, to ensure reliable electrical continuity between the feed and the antenna structure. Upon completion of the fabrication and feed integration processes, the antenna was prepared for experimental measurement.

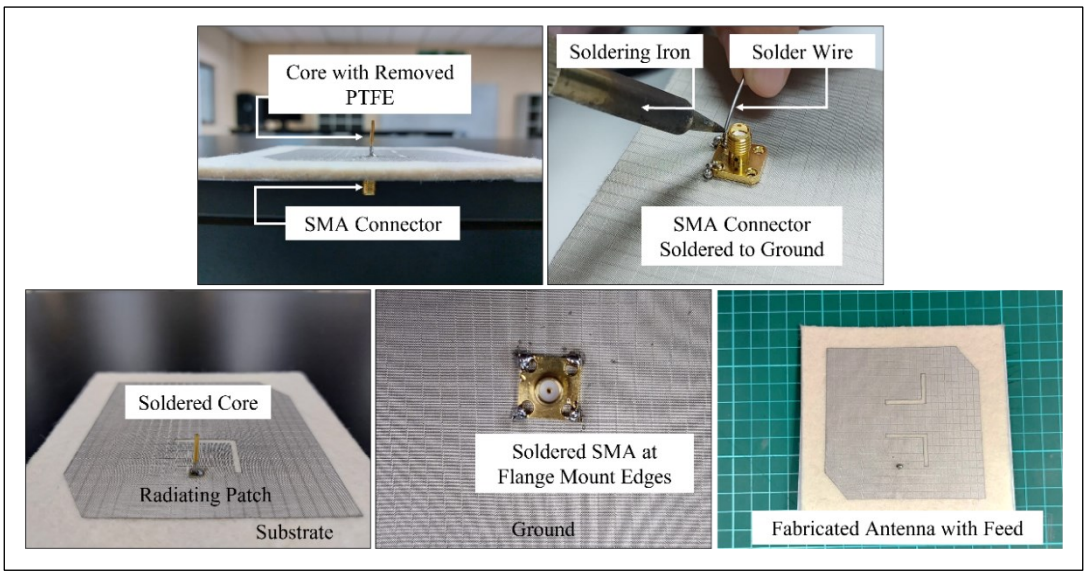

Figure 3.28 Development of Fabricated Antenna with Feed

3.9.2 Return Loss Measurement

A vector network analyzer (VNA) of Keysight Technologies N5234A PNA-L was employed to measure the antenna S-parameters. Prior to measurement, the VNA was calibrated to ensure measurement accuracy and to minimize systematic errors and cable mismatch effects. The calibration procedure was performed using a standard short-open-load (SOL) calibration, in which the short, open, and broadband load standards were sequentially connected to the probe feed cable as illustrated in Figure 3.29.

The Antenna Under Test (AUT) was connected to the VNA through a 50 Ω probe feed cable allowing the acquisition of key antenna parameters, including return loss, VSWR and impedance bandwidth. Measurement data were recorded in Touchstone S1P format for subsequent analysis. Prior to radiation pattern characterization in the anechoic chamber, the return loss and resonant frequency of the fabricated antenna were first verified using the VNA to confirm proper operation at the intended frequency band.

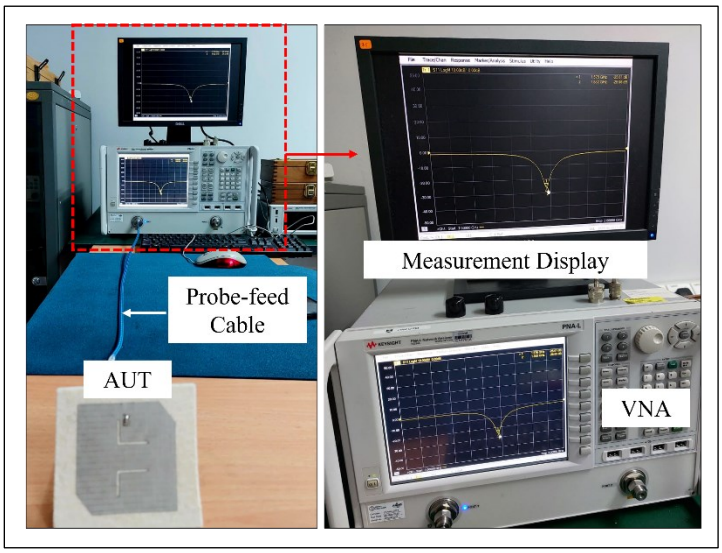

Figure 3.29 S-parameter Measurement Setup using Vector Network Analyzer

3.9.3 Radiation Pattern Measurement

An anechoic chamber of series OTA-500 by Atenlab was employed in this study to characterize the radiation performance of the fabricated antenna, including gain, radiation efficiency, and radiation pattern. Figure 3.30 illustrates the block diagram of the anechoic chamber, depicting the configuration of the radiation pattern measurement process. The chamber has internal dimensions of 5 m (L) × 2.5 m (W) × 2.5 m (H) and supports antenna measurements over an operating frequency range of 800 MHz to 18 GHz for antennas with physical dimensions up to 12 inches. It utilized for over-the-air (OTA) measurements and functions as a shielded environment lined with radio-frequency (RF) absorbing materials. This controlled setup minimizes unwanted reflections and echoes, thereby enabling accurate characterization of antenna radiation behavior under near free-space conditions.

As shown in the figure, the chamber comprises a horn antenna, pyramidal RF absorbers, and the Antenna Under Test (AUT), which is mounted vertically on a probe chamber holder. During measurement, the horn antenna operates as the transmitting antenna, radiating the signal toward the AUT, which acts as the receiving antenna, with a separation distance of 2 m between them. The diagram also indicates the integration of a switch box within the measurement system, which facilitates automated measurement operation, improves measurement speed, and maintains low return loss during high-speed signal switching. Additionally, the communication test unit, network analyzer, and spectrum analyzer are interfaced between the switch box and the control center to support signal generation, acquisition, and data processing (Solidbase Technology, 2025).

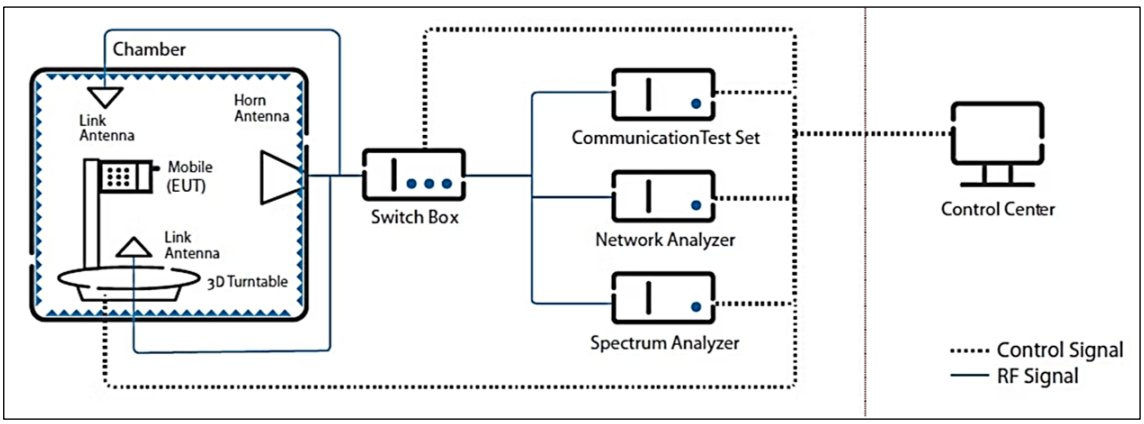

Figure 3.30 OTA Measurement System Diagram in Anechoic Chamber (Solidbase Technology, 2015)

The actual measurement setup in the OTA-500 Atenlab anechoic chamber used to measure the antenna performances regarding the radiation pattern, gain, directivity, and efficiency is shown in Figure 3.31. During measurement, the Antenna Under Test (AUT) was mounted on a three-dimensional (3D) positioner and oriented to face a standard horn antenna at a separation distance of 2 meter. The AUT functioned as the transmitting antenna, while the horn antenna served as the receiving antenna. The anechoic chamber environment was realized by lining all interior surfaces with pyramidal radio-frequency (RF) absorbers to suppress unwanted reflections and approximate free-space conditions.

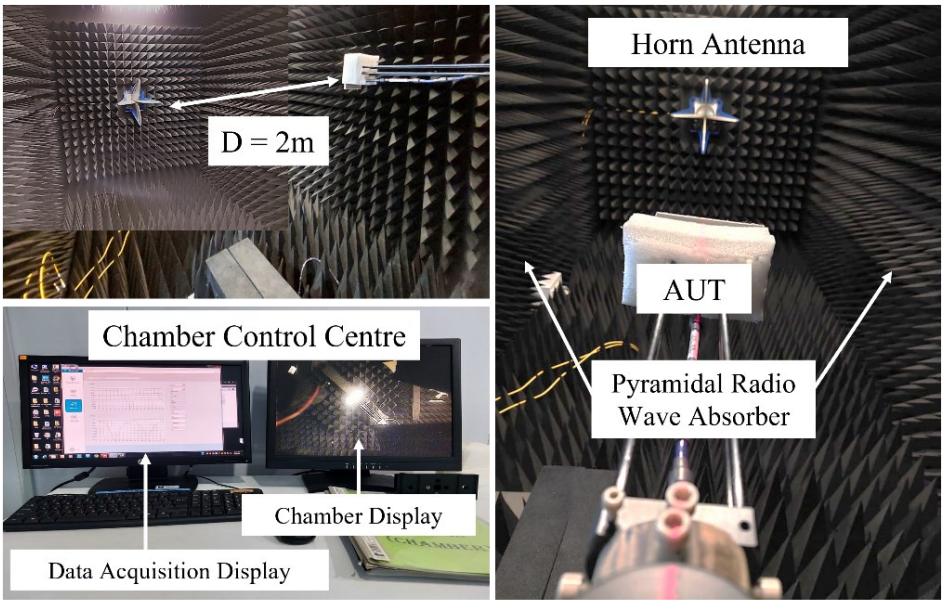

Figure 3.31 Measurement Setup for Anechoic Chamber

3.10 Legal, Ethical and Sustainability Considerations

The methodology adopted in this research was conducted with consideration of legal, ethical, and sustainability aspects relevant to wearable antenna development. From the legal perspective, the proposed antenna was designed for GPS-L1 reception at 1.575 GHz and does not involve active signal transmission. Therefore, the experimental work was limited to controlled laboratory characterization and antenna measurement using standard RF equipment. All measurements were conducted within laboratory and antenna chamber environments to ensure safe and controlled testing conditions. The use of RF instruments, textile materials, conductive fabrics, and fabrication tools followed the laboratory safety procedures and equipment operating guidelines.

From the ethical perspective, this research did not involve human participants, biological samples, personal data collection, or clinical testing. The bending analysis was conducted to represent practical wearable curvature conditions without requiring direct testing on human subjects. As such, issues related to informed consent, privacy, and personal data protection were not applicable. Nevertheless, ethical research practice was maintained by ensuring accurate reporting of measurement procedures, transparent presentation of results, and fair comparison with existing antenna studies.

Sustainability was also considered through the development of a fully textile antenna structure, which supports lightweight, flexible, and wearable integration without requiring rigid or bulky antenna substrates. The material characterization stage allowed the substrate to be selected based on measured electromagnetic suitability, thereby reducing unnecessary trial-and-error fabrication. In addition, the single-layer antenna configuration and DGS integration were implemented without increasing antenna thickness or adding complex multilayer structures, which helps minimize material usage and fabrication complexity. These considerations support a more resource-conscious approach to wearable antenna design while maintaining the required electromagnetic performance for GPS-L1 applications.

3.11 Summary

This chapter has presented the methodological framework used to characterize textile materials and evaluate the suitability for fully textile wearable antenna development. The methodology was structured to address the research objectives by linking material characterization, transmission-loss evaluation, antenna design groundwork such as simulation, fabrication, and measurement validation. Specifically, the transmission-line method was adopted to systematically assess the influence of substrate thickness and material conductivity on return loss, S_{11}, transmission loss, S_{21} and overall electromagnetic performance as further discussed in the subsequent chapter. Meanwhile, the free-space measurement method was also incorporated as a complementary cross-reference technique to verify the dielectric properties obtained from the open-ended coaxial probe measurement under non-contact plane-wave propagation conditions. This approach provides a controlled basis for comparing the candidate textile materials and justifying the substrate configuration used in the subsequent antenna design stage. The use of controlled fabrication procedures, including 3D-printed moulds, also supports dimensional accuracy and repeatability, which are important for reducing simulation-to-measurement discrepancies. To ensure material consistency and reproducibility in the later stages of the research, the felt used in the following antenna development chapter was sourced from RS Components, a recognized engineering supplier that provides traceable and quality-controlled materials for research and prototyping. In the preliminary stage, commercially available felt sourced from Spotlight was used to explore the feasibility of the textile antenna concept.

The subsequent use of RS Components felt does not alter the design intent; rather, it strengthens material traceability, improves dielectric and mechanical consistency, enhances simulation-to-measurement correlation, and facilitates future replication of the research. The methodological decisions made in this chapter collectively support the development of the proposed antenna in the subsequent stages of the research. The antenna design, simulation, fabrication, and measurement procedures described in this chapter further establish a clear pathway for validating the proposed fully textile antenna under planar and bending conditions.

CHAPTER 4
DEVELOPMENT OF CIRCULAR POLARIZED WEARABLE TEXTILE ANTENNA FOR GPS APPLICATION

4.1 Introduction

This chapter firstly presents the simulated analysis of the Transmission Line Method (TLM) as decsribed in the previous chapter to identify the textile material with the best performance. Following this, a prototype of the proposed circularly polarized (CP) wearable textile antenna for GPS-L1 applications is developed using fully textile materials with Shieldit Super employed as the conductive patch and the selected best textile serving as the dielectric substrate. While conventional microstrip CP antennas commonly suffer from narrow axial-ratio bandwidth and limited beamwidth, the proposed design aims to overcome these limitations by integrating perturbation techniques, and optimized feeding mechanisms. The objective of this chapter is to verify the simulated results through anechoic chamber measurements, focusing on key radiation characteristics, including radiation pattern, gain, axial ratio (AR), and front-to-back ratio (FBR). Both principal planes (*x–z* and *y–z*) were analyzed to verify the radiation performance. Additionally, 3-dB axial ratio bandwidth and angular beamwidth were measured to validate the circular polarization purity to confirm the reliability and feasibility of the antenna for wearable GPS systems.

This chapter also provides a comparative assessment of the measured results against simulated data, as well as benchmarking with existing CP antenna designs reported in the literature.

4.2 Transmission Line Method (TLM) Analysis for Dielectric Substrate Selection

When multiple fabrics with varying thicknesses are considered, it is imperative to ensure that the optimized fabric thickness and the correct conductivity value of the radiating element are used as an incorrect conductivity value can significantly affect the efficiency and radiation properties of the antenna (Abd Rahman, Yamada, & Ahmad, 2019). Although increasing the fabrics thickness appear attractive for maximizing the

antenna bandwidth, such an approach can also compromise radiation efficiency (Pazil, Abd Rahman, Ramli, & Awang, 2020).

This sub-chapter presents the systematic analysis adopted for evaluating various textile substrates chosen to represent a range of textile commonly utilized in wearable technologies. The characterization methods has been discussed in Chapter 3 as a basis for substrate selection and dielectric property evaluation, which are subsequently used in the TLM to analyze antenna performance.

4.2.1 Simulated Fabric Thickness and Conductivity Performance Analysis of Dielectric Substrates Selection

As shown in Figure 4.1, a simulated assessment of the return loss and transmission loss parameters was performed for all fabric thicknesses of each material at 1.575 GHz, corresponding to the Global Positioning System (GPS) L1 application. The simulation was carried out by modelling a microstrip transmission line structure on three textile materials; denim, felt and Tencel. For each material, the substrate thickness was parametrically varied from 0.5mm to 4.0 mm to represent a practical range for wearability thicknesses. Two-port waveguide excitation was applied at both ends of the transmission line, enabling the extraction of the scaterring parameters of S_{11} and S_{21} at the operating frequency of 1.575 GHz. The return loss (S_{11})was used to evaluate the impedance matching at the input port while the transmission lost (S_{21}) represented the signal attenuation along the transmision line.

For each thickness variation, the corresponding S_{11} and S_{21} values were recorded and tabulated in Table 4.1. The S_{11} and S_{21} results for each fabric thickness were subsequently plotted and comparatively analysed to determine the most suitable thickness based on impedance matching and transmission-loss performance.

(a) Denim at h = 0.5 mm	Simulated result of return loss (S_{11}) & transmission loss (S_{21})
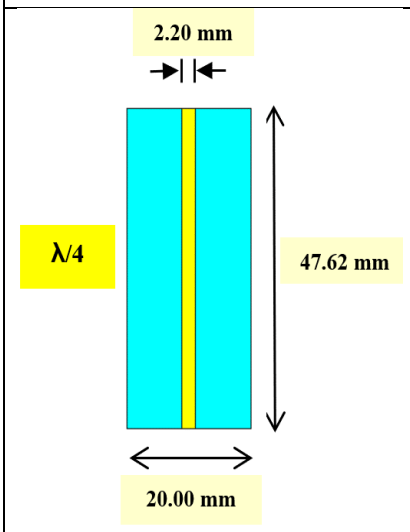	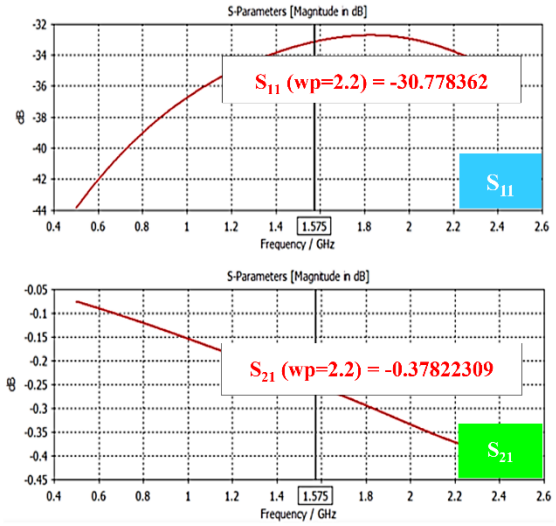
(b) Felt at h =0.5 mm	**Simulated result of return loss (S_{11}) & transmission loss (S_{21})**
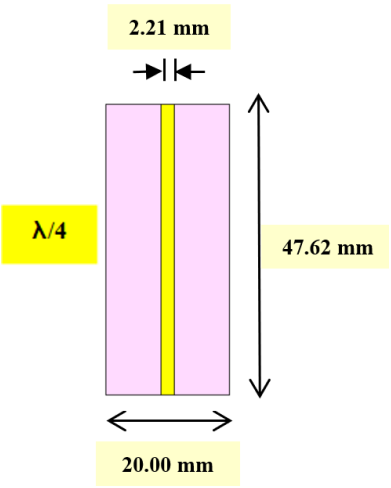	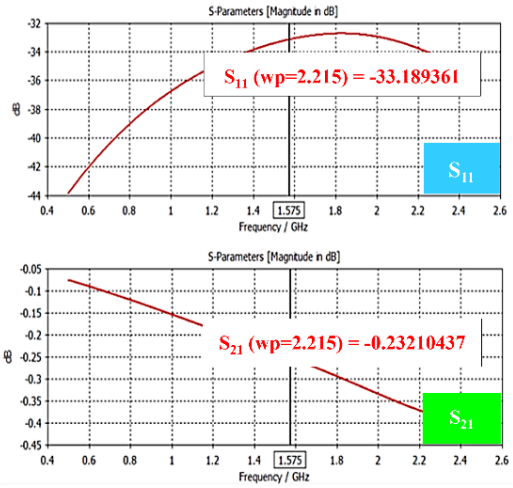
(c) Tencel at h = 0.5 mm	**Simulated result of return loss (S_{11}) & transmission loss (S_{21})**
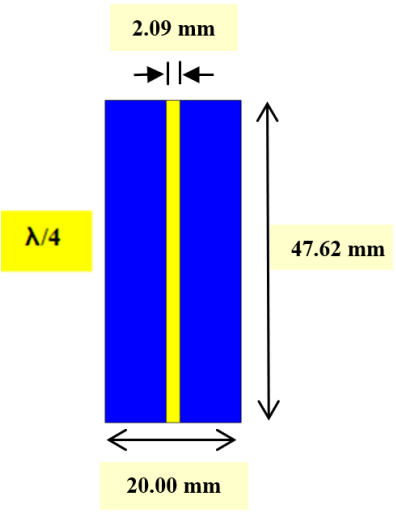	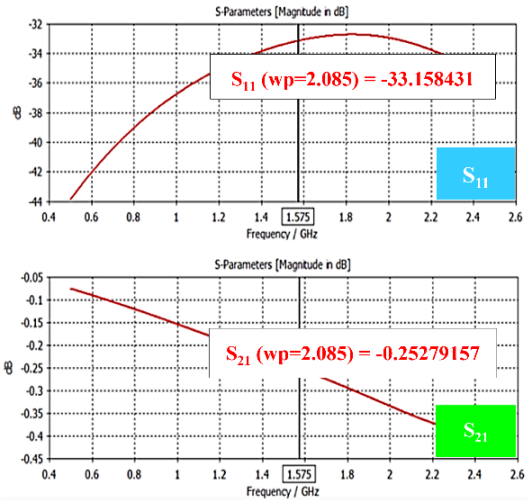

Figure 4.1 Two-Port TLM for the Measurement of Return Loss (S_{11}) and Transmission Loss (S_{21}) of a) Denim b) Felt and c) Tencel at h = 0.5 mm and Further Iterated for h = 1.0 mm, 1.5 mm, 2.0 mm, 2.5 mm, 3.0 mm, 3.5 mm, 4.0 mm

Table 4.1
Fabric Thickness Performance on Return Loss (S_{11}) and Transmission Loss (S_{21}) Parameter

Thickness (mm)	Parameter	Simulated Fabric Performance (dB)		
		Denim	Felt	Tencel
0.5	S_{11}	-30.78	-33.19	-33.16
	S_{21}	-0.3782	-0.2321	-0.2528
1.0	S_{11}	-33.61	-33.03	-32.82
	S_{21}	-0.5889	-0.4261	-0.4264
1.5	S_{11}	-38.49	-53.03	-51.10
	S_{21}	-0.4924	-0.3432	-0.3762
2.0	S_{11}	-35.89	-44.74	-43.67
	S_{21}	-0.4507	-0.3034	-0.3297
2.5	S_{11}	-35.44	-42.75	-42.07
	S_{21}	-0.4317	-0.2891	-0.3127
3.0	S_{11}	-34.41	-38.50	-39.20
	S_{21}	-0.4188	-0.2784	-0.3010
3.5	S_{11}	-32.25	-33.63	-34.78
	S_{21}	-0.4150	-0.2780	-0.2993
4.0	S_{11}	-29.12	-29.20	-30.39
	S_{21}	-0.4246	-0.2975	-0.3170

Figure 4.2 shows S_{11} and S_{21} performance of denim, felt and Tencel fabrics, with Rogers 5880 as the control substrate. The observed trends for all textile materials are consistent with those of the reference Rogers 5880 substrate. However, as expected, the lossy textile materials (denim, felt and Tencel) exhibit significantly higher transmission loss (S_{21}) compared to Rogers 5880. The observed changes in S_{11} are attributed to the geometrical effect of thickness on the textile-loaded transmission line. Variation in *h* changes the *W/h* ratio, distributed capacitance and inductance, characteristic impedance, and input impedance of the transmission line. Consequently, the impedance matching relative to the 50 Ω reference impedance varies with thickness, and the most negative S_{11} does not necessarily occur at the greatest substrate thickness.

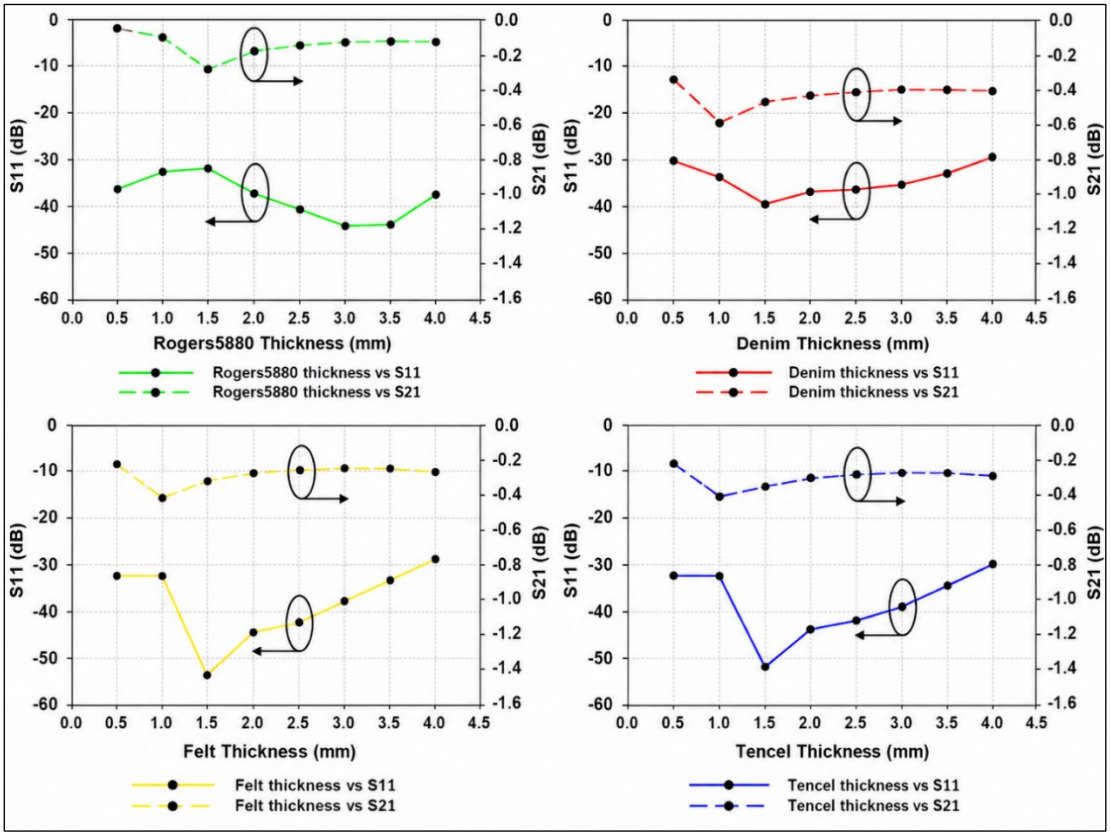

Figure 4.2 S_{11} and S_{21} Performance for Rogers 5880, denim, felt and Tencel

The results presented in Figure 4.2 have been merged into Figure 4.3 to enable a more direct comparison of the S_{11} and S_{21} responses for the investigated substrate materials and thicknesses. Among the investigated textiles, felt generally demonstrates the lowest transmission loss, whereas denim exhibits the highest. The transmission loss behaviour becomes relatively stable between 3.0 and 3.5 mm, indicating that a further increase in thickness provides only a marginal improvement. Although some thicknesses produce more negative individual S_{11} values, the final thickness was not selected solely according to the minimum S_{11}. At 3 mm, felt achieves S_{11}=−38.50 dB and S_{21}=−0.2784 dB, providing satisfactory impedance matching and low transmission loss. Increasing the felt thickness to 3.5 mm changes S_{21} by only 0.0004 dB, from −0.2784 dB to −0.2780 dB, while S_{11} becomes less negative, changing from −38.50 dB to −33.63 dB. The additional thickness therefore provides no meaningful electromagnetic improvement and would increase the antenna profile and structural bulk. Based on the observation of S_{11} and S_{21}, a thickness of 3 mm was selected for the final felt-based antenna as the most appropriate overall trade-off among impedance matching, transmission loss and low-profile single-layer construction.

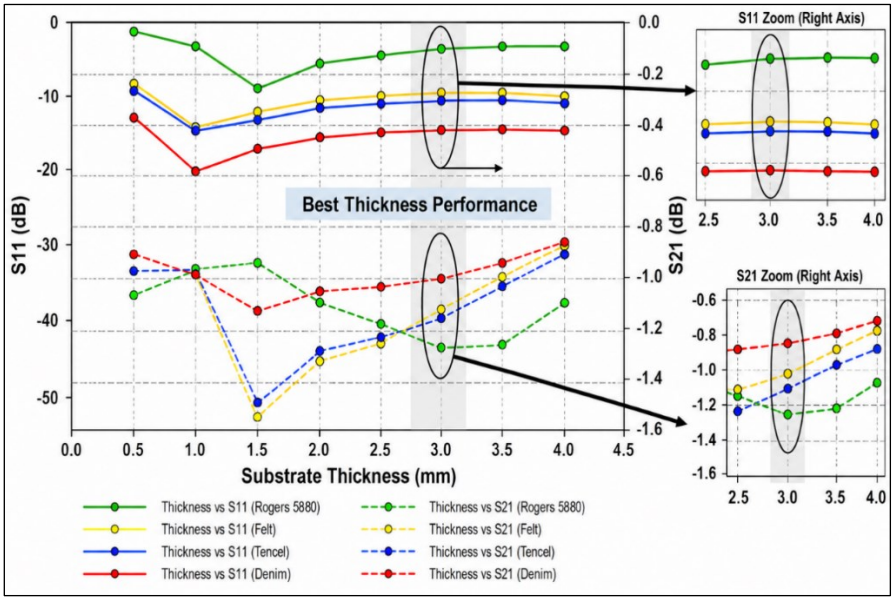

Figure 4.3 Merged Plot of S_{11} and S_{21} Performance for Denim, Felt, Tencel and Rogers 5880

Referring to Figure 4.4, as the conductivity (σ) increases, the S_{21} approaches 0 dB, indicating near loss-free transmission while it degrades significantly with the reduction of σ. This trend demonstrates consistent and comparable performance across all substrates in comparison to the result shown for Rogers 5880. In addition, as S_{21} approaches the loss-free level, a gradual reduction in transmission loss is observed. Reduced transmission loss enhances the radiated power and subsequently improves the antenna efficiency.

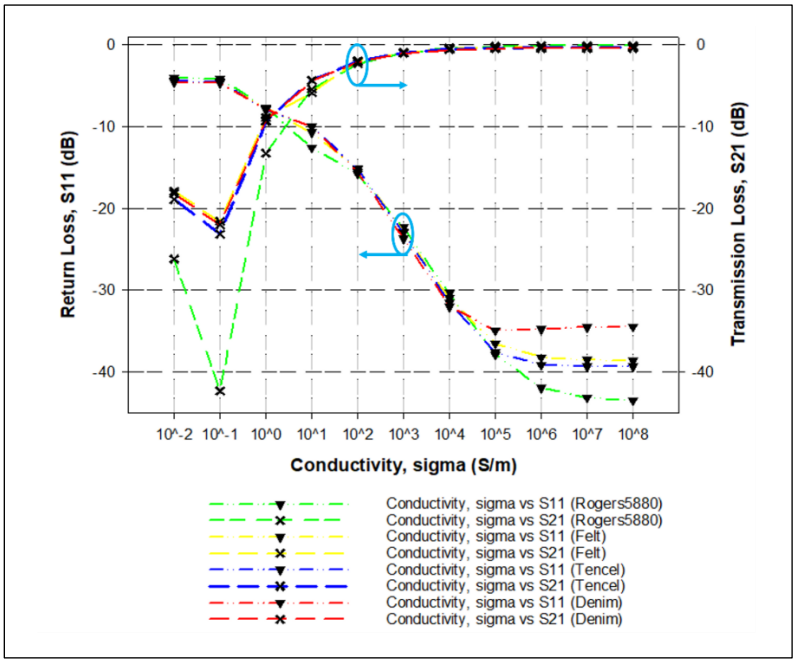

Figure 4.4 S_{11} and S_{21} for Various Conductivity (σ) Values

The same trend is also observed in the S_{11} parameter whereby the higher the magnitude of σ, the higher the return loss value is achieved. A close observation from the same figure shows that the acceptable return loss of -10 dB for all substrates is seen from the conductivity of 10^1 S/m and above. Based on this scenario, these three substrates have the potential to be implemented for textile antenna. This is due to the fact that most of the electro-textiles (e-textiles) such as Shieldit Super, Zelt, or Pure Copper Taffeta fabric (Jais, Malek, Jamlus, & Jusoh, 2012) that is commonly used as a conductive layer in wearable application have the conductivity of 10^5 S/m at minimal. Therefore, based on this observation, it is clear that the antenna will attain an optimal performance when it is designed on a suitable substrate that synergized well with the conductive layer at the optimal magnitude. This statement is supported by a study done in (Vojtech, Blažek, Neruda, & Neru, 2013) showing the effects of radiation efficiency by the increased of conductivity level in logarithmic manner.

Taking the graphical observation into account, a reduced scale version shown in Figure 4.5 is plotted to clearly demonstrate the performance of fabrics distinctively.

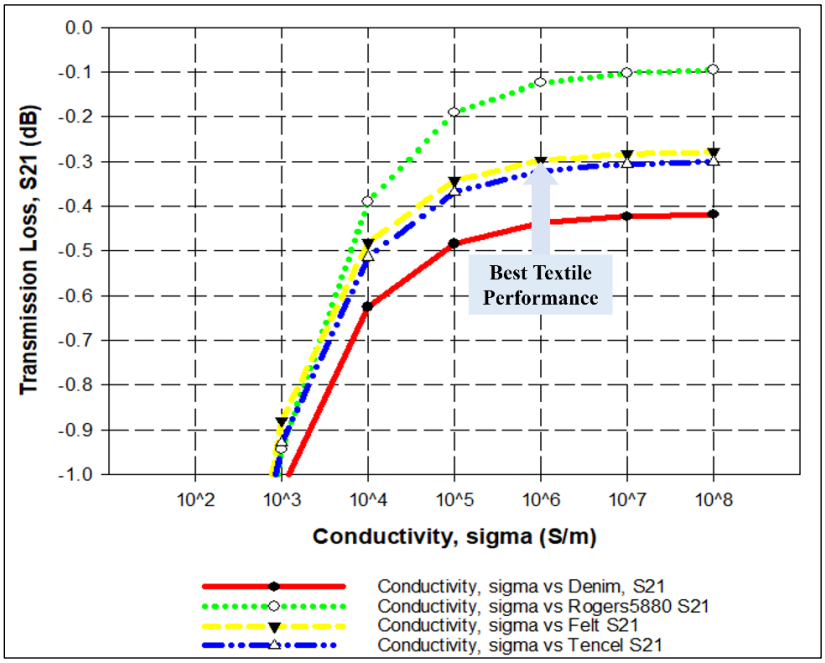

Figure 4.5 Refinement Plot of S_{21} versus Conductivity Plot

It is observed from this plot that felt textile possessed the best fabric performance of all after Rogers 5880, followed by Tencel and lastly denim. As the best fabric thickness is identified at 3 mm, this situation provides an advantage for felt fabrication as it comes in as 3 mm under the manufactured thickness. Therefore, the additional layer which will

further complicate the fabrication process is not required due to the fulfilment to the benchmark set for the best substrate thickness. From this figure, it can also be observed that by applying the conductive layer with σ of at least 10^5 S/m, the transmission loss can be reduced by 0.5 dB for denim while more than 0.4 dB is depicted for felt and Tencel.

Based on the simulated S_{21}, the conductivity value is re-calculated using equation (3.12) from Section 3.6 to validate the accuracy of the proposed two-port transmission line method for fabric characterisation. Figure 4.6 illustrates the actual and calculated conductivity of Rogers 5880, felt, Tencel and denim for conductivity values from $\sigma = 10^{-2}$ (S/m) to $\sigma = 10^9$ (S/m).

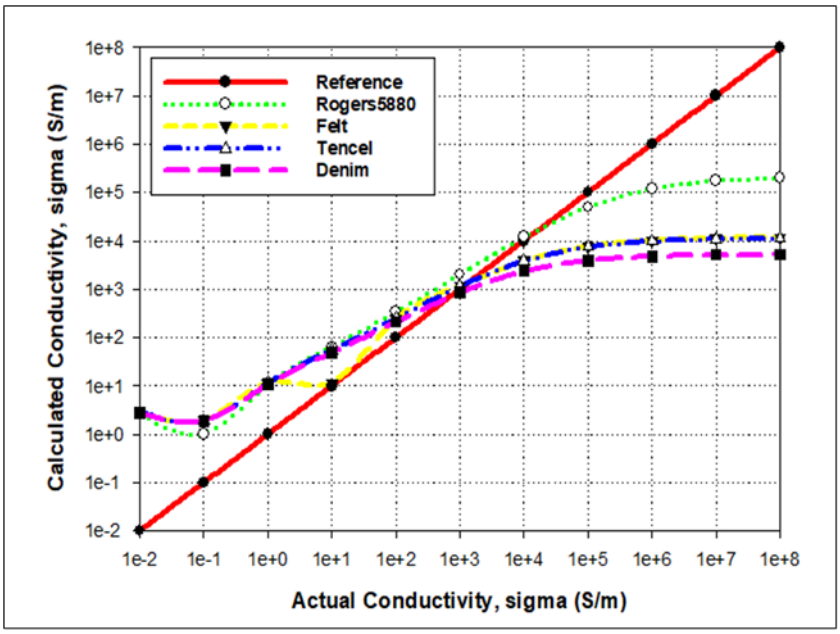

Figure. 4.6 Actual and Calculated Conductivity Values of Rogers 5880, Felt, Tencel and Denim

From observation, the trend of calculated conductivity for fabric samples matched the conductivity of the lossless control sample i.e., Rogers 5880. It can be seen from the graph that the trend of Rogers 5880 has small deviation as compared to the trend shown in reference. This resulted from the influence of low loss tangent (0.0009) in Rogers 5880 which does not affect the signal transmission from port 1 to 2 unlike other fabrics sample which demonstrate significant value of loss tangent and subsequently generate a higher transmission loss. In comparison to the actual conductivity, the fabric samples show a similar trend with the reference until it reaches $\sigma = 10^6$ (S/m) and subsequently shows a stagnant inclination at higher conductivity

region, which agrees very well with the analysis done in (Abd Rahman, Yamada, & Nordin, 2018). This due to a circumstance whereby; when σ is low, the resistance of conductive layer is high due to the effective resistance are derived from both conductive and substrate layer. In contrast, when σ is in the high region, the resistance magnitude for conductive layer is low as the significant resistance is only derived from the substrate layer.

In conclusion, the proposed technique of two-port transmission line is suitable to be used for multiple fabric characterisation of textile antenna having low-to-medium conductivity. Hence, the implementation of fully textile antenna is viable as most of the available conductive textile material demonstrates the conductivity region of 10^5 S/m.

4.2.2 Measured Conductivity Performance Analysis of the Selected Dielectric Substrate

Table 4.2 shows the simulated and the measured data of S_{21} from the two-port TL for S1, S2 and S3, which has been mentioned in Section 3.6. The simulated results for S1 and S2 exhibit a close agreement to the measured S_{21} values as both samples were developed on Rogers5880 with a very low loss tangent 0.0009 as compared to felt with 0.0395. This event leads to a higher σ as the effective resistance is merely from the substrate itself. Hence, S1 validates the aforesaid scenario as pure copper is a good conductor and therefore the resistance is derived from a low-loss substrate giving S1 the highest σ among all as seen in the measured column below.

Table 4.2
Simulated and Measured Data of S1, S2 and S3

Sample No.	Data sheet	Simulated	Measured	
	σ (S/m)	S_{21} (dB)	S_{21} (dB)	σ(S/m)
S1: Reference (Copper Pure + Rogers 5880)	≈10^7	-0.0387	-0.0399	1.7E+07
S2 (Shieldit Super + Rogers 5880)	≈10^5	-0.3302	-0.3394	2.3E+05
S3 (Shieldit Super + felt)	≈10^5	-0.3552	-0.4200	6.0E+03

In addition, the S2 and S3 samples which were developed from Shieldit Super as the conductive layer proven a consistency in result validation for the simulated and measured data using this TL technique. As a low-loss substrate Rogers5880 is used for S2, the accumulated effective resistance is low and indirectly preserved the conductivity

of Shieldit Super. This resulted a σ value for S2 that is in a good agreement to the estimated value of 10^5 S/m. Unlike felt substrate with a higher loss tangent, the σ degrades in S3 due to the rise in the effective resistance from substrate and the conductive layer.

To further validate the effectiveness of this TL measurement technique, the correlation between the attenuation constant, α, and conductivity based on equation (3.14) is analysed and demonstrated in Figure 4.7 and Figure 4.8.

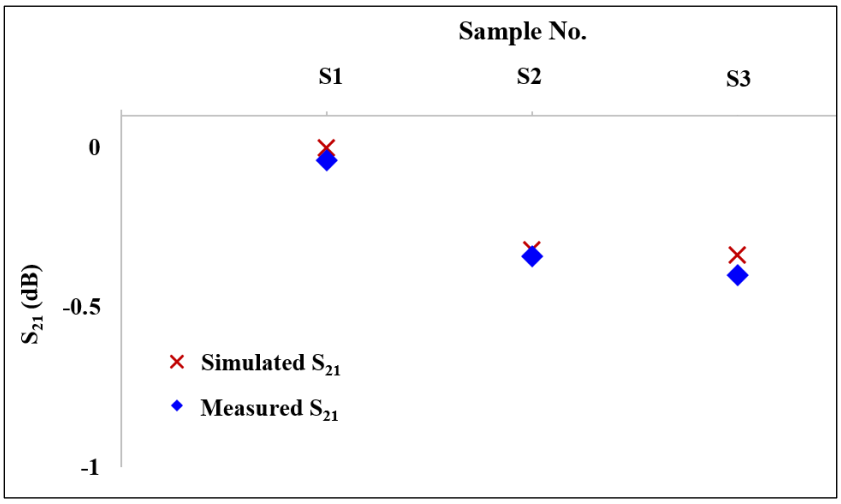

Figure 4.7 Simulated and Measured S_{21} for S1, S2 and S3

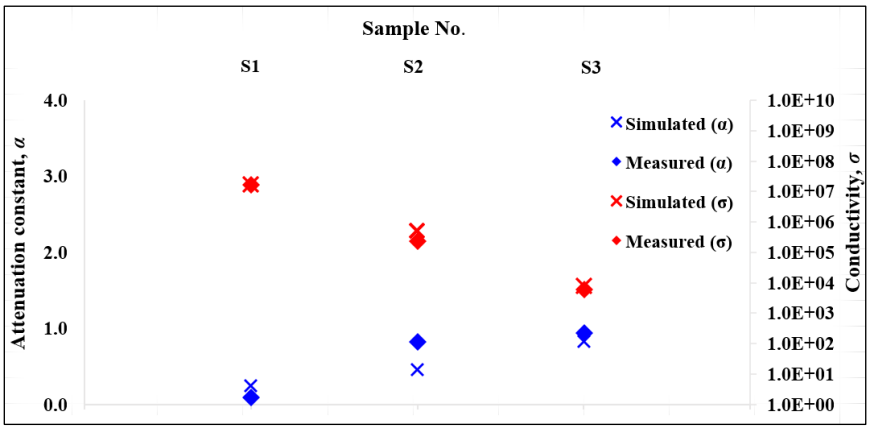

Figure 4.8 Simulated and Measured Plot Attenuation Constant, α and Conductivity, σ for S1, S2 and S3

This equation shows that the higher the σ, the lower the α will be due the signal amplitude depreciation along the TL. This leads to a better σ as proven in graph below with the best performance shown in S1 followed by S2 and S3 samples. Based on the graph, the accuracy of the TL method is validated, specifically when the sample-under-test is fabricated on a low-loss or lossless substrate. When a lossy substrate (felt) is

used, the attenuation constant is as expected, however the σ is less accurate as it is highly affected by other factor such as the absorption of signal by the lossy dielectric.

4.3 Parametric Study of Antenna Design

To investigate the effects of various geometrical parameters on the proposed antenna performance, a parametric study is being employed to optimize the final design. In this design, the circular polarization is achieved by introducing truncated corners and slots towards the radiating patch. Here, three principles parameters, corner truncation (C_t), horizontal slot (S_h) and vertical slot (S_v), have been analyzed and studied.

Based on the literature review, corner truncation was employed to perturb the current distribution of the square patch and initiate the excitation of two near-degenerate orthogonal modes. Here, the top-right and bottom-left corners of the square radiating patch were truncated along the same diagonal to perturb the initially degenerate orthogonal TM_{10} and TM_{01} modes. In combination with the adopted feed position and antenna orientation, this diagonal truncation establishes the amplitude-phase progression required for right-hand circular polarization. However, corner truncation alone provides limited control over the amplitude balance, resonant separation, and phase relationship of the two orthogonal modes. Therefore, asymmetric dual L-shaped slots were introduced to provide additional control of the surface-current distribution and circular-polarization response.

The L-shaped slot was selected because its horizontal and vertical arms are perpendicular to each other and correspond to the two principal current directions of the square radiating patch. Its relatively simple geometry also avoids the additional design variables associated with more complex U- or E-shaped slots, which is beneficial for the fabrication of a fully textile antenna.This geometry enables the slot to perturb and redistribute the surface-current components associated with the TM_{10} and TM_{01} modes. The two interconnected arms also lengthen the effective current paths within a compact patch area, while their dimensions can be controlled through S_h and S_v. Appropriate tuning of these parameters adjusts the resonant-mode separation, relative current amplitudes, and phase relationship required for circular polarization. Although the physical 90° orientation of the L-shaped arms does not itself impose a 90° phase difference, it supports spatially orthogonal current control, while the required quadrature phase relationship is obtained through electromagnetic tuning of the slot

dimensions. The effects of the corner-truncation and slot dimensions are discussed in the following subsections.

4.3.1 Effects of Corner Truncation Dimensions

Figure 4.9 and 4.10 demonstrate the effect of varying corner truncation length (C_t) on S_{11} and AR performance. The graph illustrates that as the corner truncation length (bottom-left and top-right) increases, the S_{11} decreases indicating a better impedance matching. When corners are truncated, it alters and lengthened the effective electrical path of the current and subsequently changed the resonant frequency of the antenna. Among the evaluated configurations, the proposed design with C_t =18.1 mm achieves optimal tuning showing a centred resonance at 1.575 GHz.

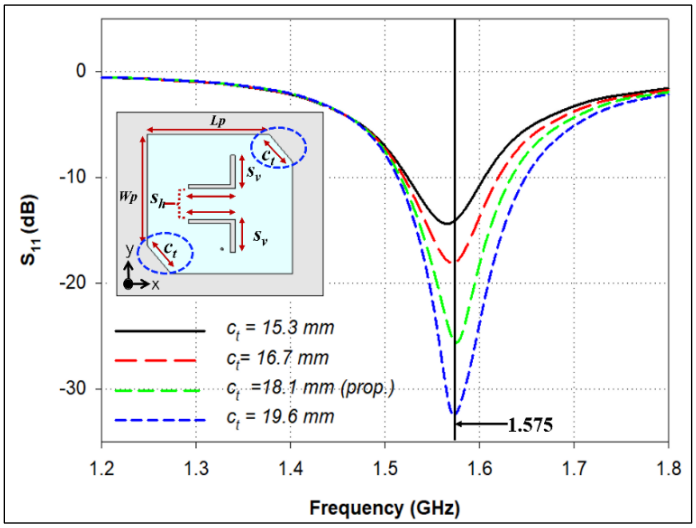

Figure 4.9 Effects of Corner Truncation Length to S_{11} Performance

Figure 4.10 shows the trade-off and correlation between S_{11} and AR performance at 1.575 GHz for varying C_t values. Optimal CP performance is observed around C_t =18.1 mm which aligns perfectly with the optimal bandwidth of S_{11}. Here, the corner truncation acts as perturbation that breaks the symmetry of the patch enabling balance of excitation modes of two orthogonal TM modes in quadrature thereby generating CP. However, insufficient truncation produces inadequate modal perturbation and does not establish the required amplitude and phase relationship. Conversely, excessive truncation reduces the effective radiating area and over-perturbs the two modes, which can disturb their amplitude balance and quadrature phase

relationship. Therefore, C_t=18.1 mm was selected as the best compromise between impedance matching and axial-ratio performance at the GPS-L1 frequency.

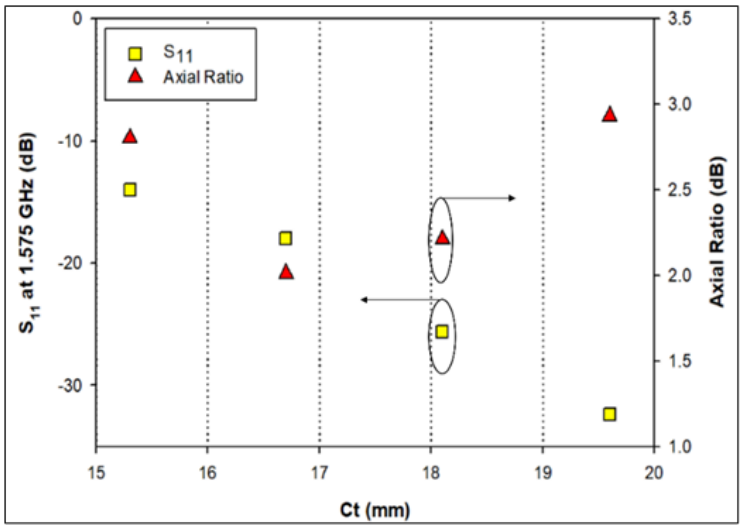

Figure 4.10 Effects of Corner Truncation Length to S_{11} and AR Performance

4.3.2 Effects of Horizontal and Vertical Slot Variation

Figure 4.11 and 4.12 illustrates the effects of varying the horizontal (S_h) and vertical (S_v) slot lengths for S_{11} and AR performance. From the simulation result obtained in Figure 4.11, it can be observed that an increased in both S_h and S_v shift the resonance frequency to a lower value. When slots are introduced and enlarged, it disrupts and lengthen the effective electrical currents path thus lowers the resonant frequency as the antenna appears electrically larger.

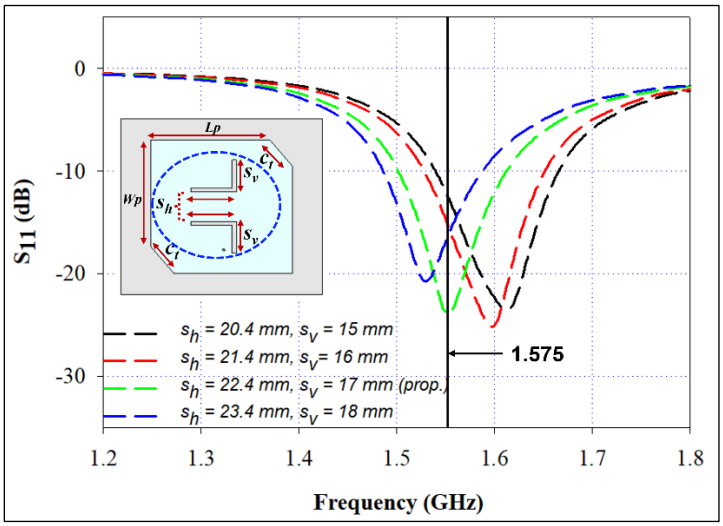

Figure 4.11. Effects of Horizontal and Vertical Slot Length to the S_{11} Performance

Figure 4.12 presents the trade-off between S_{11} and axial-ratio performance at 1.575 GHz for different S_v/S_h ratios. The optimum combined response is obtained at $S_v/S_h \approx 0.75–0.76$, where the antenna achieves an axial ratio below 3 dB together with strong impedance matching. The asymmetric horizontal and vertical slot dimensions create unequal but controllable current-path lengths along the two principal directions of the radiating patch. This perturbation enables the amplitudes and phase relationship of the orthogonal current components to be adjusted towards the conditions required for CP. Ratios outside the optimum range produce excessive geometrical imbalance between the slot arms, which disturbs the modal amplitude balance and phase difference. Consequently, the axial ratio deteriorates even when acceptable impedance matching is retained. The selected S_v/S_h ratio therefore represents a compromise between impedance matching, modal balance, and RHCP performance at the target frequency.

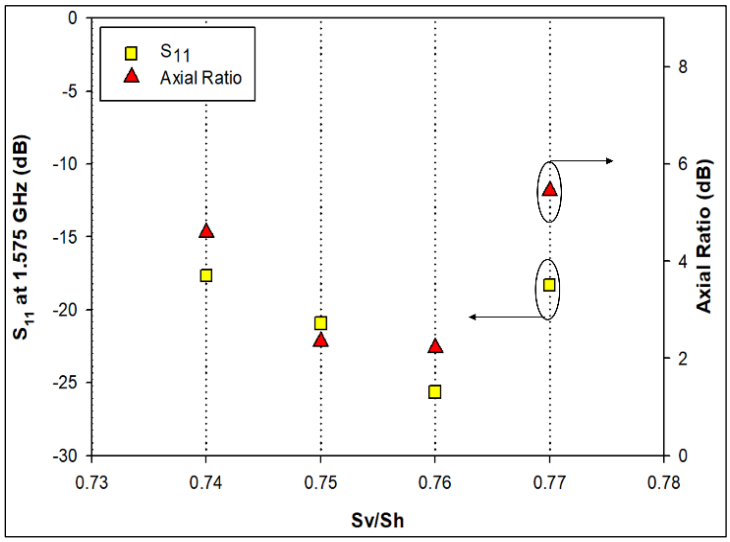

Figure 4.12. Effects of Horizontal and Vertical Slot Length to the S_{11} and AR Performance

In conclusion, the parametric results demonstrate that the minimum S_{11} condition does not necessarily correspond to the minimum axial ratio. The final values of C_t, S_h and S_v were therefore selected based on their integrated performance to maintain impedance matching while producing the modal amplitude balance and approximately 90° phase difference required for RHCP at 1.575 GHz. This integrated selection constitutes the principal design trade-off in the development of the proposed CP antenna.

4.4 Simulation of Dual L-shaped Slotted Antenna with Circular Polarization

This sub-chapter presents the design and simulation of a circularly polarized (CP) wearable textile antenna developed for GPS-L1 applications at 1.575 GHz. Following the establishment of substrate characterization in Section 4.2, the integration of felt with an antenna geometry structure was developed to generate a right-hand circular polarization (RHCP). The design process aims to achieve a wide impedance and axial ratio bandwidth with sufficient beamwidth for a reliable CP signal reception to support the antenna performance in textile-based wearable platforms.

Among various patch geometries, the square (or near square) configuration offers geometric symmetry and ease of perturbation for CP excitation which is highly suitable fundamental structure for polarization conversion techniques. A square patch antenna supports degenerate orthogonal modes (TM_{10} and TM_{01}) that resonate at the same frequency when the patch is perfectly symmetrical. This modal degeneracy is a prerequisite for achieving circular polarization with 90° phase difference between the modes. By using simple perturbations such as corner truncation, slots, or asymmetric feed placements, a straightforward implementation of CP can be achieved.

To maintain a compact, low-profile, and wearability structure, a single-feed configuration was selected over more complex dual-feed or hybrid-fed systems. While dual-feed methods provide more control over mode excitation, this method is bulky and impractical for textile integration. In contrast, the single-feed approach simplifies fabrication and reduces parasitic effects. The feed point was adjusted parametrically during simulation to achieve a return loss better than –10 dB at the center frequency of 1.575 GHz. This feed location was also chosen to avoid strong excitation of higher-order modes and to ensure that the dominant modes could effectively couple through the perturbation features to generate RHCP. The following section will be describing in details on CP design based on the above configurations.

4.4.1 Evolution from Linearly Polarized to Circular Polarized Antenna

Circular polarization (CP) was achieved in microstrip patch antennas by exciting two orthogonal resonant modes of equal amplitude with a 90° phase difference. In this work, a single-feed square patch was modified using structural perturbations to generate right-hand circular polarization (RHCP) suitable for GPS-L1 applications. To realize

CP in a compact and wearable-friendly configuration, two perturbation techniques were employed namely corner truncation and dual-L shaped slots via 4 stages as shown in Figure 4.13. The corner truncations were made on the top-right corner and bottom-left corner to excite the generation of RHCP. This perturbation technique introduces a deliberate imbalance in the patch geometry producing the required 90° phase shift between the two orthogonal modes. The truncation also helps to suppress unwanted linear polarization components therefore enhancing the purity of RHCP.

The asymmetric dual L-shaped slots were progressively developed on the radiating patch to disturb the initially dominant linear surface current distribution. By creating unequal current paths along the patch, the slots assist in elongating the current path and producing the required phase shift for circular polarization generation. This controlled perturbation supports the excitation and coupling of the orthogonal TM_{10} and TM_{01} modes, with comparable field amplitudes and the necessary quadrature phase relationship. The detailed verification of this current rotation mechanism is provided in Section 4.4.2 through the surface current distribution analysis at different phase angles. The placement and orientation of the L-shaped slots are therefore critical, as they must operate in conjunction with the corner truncation technique to achieve stable circular polarization. This approach enables robust CP generation without requiring a complex feeding network or dual-port configuration, thereby preserving both the electrical performance and mechanical simplicity of the fully textile antenna design. The dimensions of the final antenna design are presented in Table 4.3.

Table 4.3
Dimensions of the Proposed Antenna

Description	**Parameter**	**Dimension (mm)**
Patch length	L_p	57.2
Patch width	W_p	59.1
Substrate length	L_s	94.0
Substrate width	W_s	100.0
Ground length	L_g	94.0
Ground width	W_g	100.0
Height (Shieldit Super)	h_1	0.17
Height (Felt)	h_2	3.0
Truncated corner length	C_t	18.1
Vertical Slot Length	S_V	22.4
Horizontal slot length	S_h	17.0
Overall antenna height	-	3.0 + 0.17 +0.17 =3.34

To initiate the 4 stages, a fundamental square patch is designed to achieve the desired operating frequency at 1.575 GHz. A rectangular ground plane of Shieldit Super with the dimension of 94 × 100 mm^2 is fed using a 50 Ω coaxial probe. Referring to Figure 4.13, the antenna design is first presented as linearly polarized in Stage 1 due to the Axial Ratio (AR) value exceeding 3 dB. To achieve the Right-Hand Circular Polarization (RHCP), an excitation of two orthogonal modes with a 90° phase difference is required to generate a circular polarization characteristic. Hence, as seen in Stage 2, the antenna is modified by truncating the top-right and bottom-left corners. Although RHCP is achieved with an axial ratio (AR) below 3 dB, the value remains close to the threshold, indicating that further design optimization is necessary to ensure stable performance under wearable conditions.

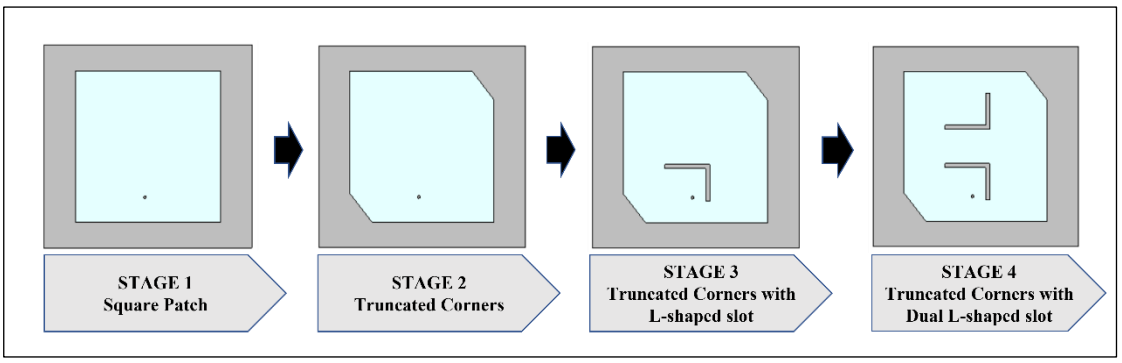

Figure 4.13 Design Evolution of Stage 1, Stage 2, Stage 3 and Stage 4

An L-slot is further introduced to the antenna as a second tuning to adjust the mode amplitude and phase balance to achieve lower the AR, as seen in Stage 3. Here, the L-slot is employed near the probe-fed where the current density is highest with the dimension of the horizontal slot is longer than the vertical slot. Nevertheless, this single L-slot introduction has altered the surface electric field distribution at Stage 3 and subsequently changed the antenna operation characteristic in linearly polarized mode. Another mirrored L-slot is added to the design for Stage 4 to improve the magnitude ratio (E_x/E_y) between the horizontal and vertical electric fields with 90° phase difference. The final slot addition to the design subsequently demonstrates an improved AR value that concludes the process of generating circular polarization of right-handed characteristics as seen in the final design of Figure 4.14. The return loss (S_{11}) from Stage 1 to Stage 4 of the evolved design is shown in Figure 4.15.

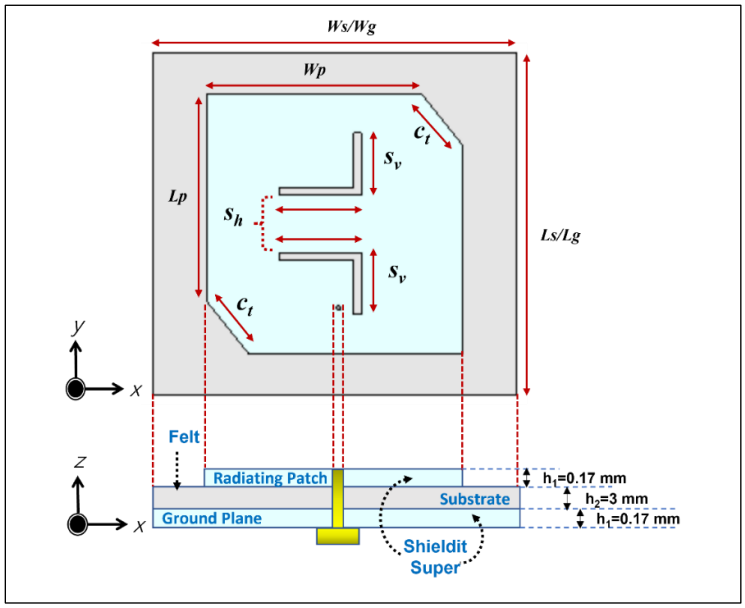

Figure 4.14 Proposed Antenna Structure

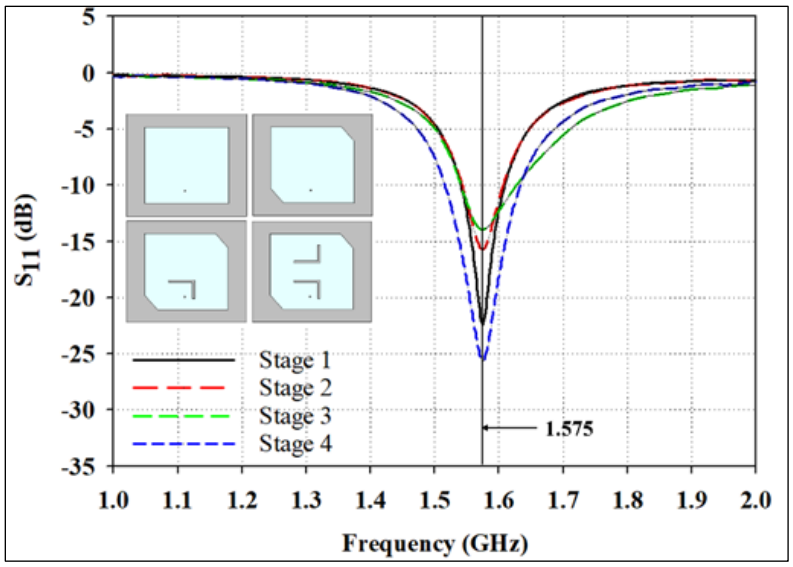

Figure 4.15 Return Loss of S_{11} from Stage 1 to Stage 4 of the Evolved Design

4.4.2 Surface Current Distribution Analysis for Circular Polarization Verification

To gain an insight into CP radiation characteristic, the simulated surface current distribution is studied. Circular polarization is characterized by the rotation of current vectors in a circular behaviour (right-hand or left-hand orientation) as the electromagnetic wave propagates (Wichaidit et al., 2024). The orientation of the surface current vector is shown at four different phases, ω of 90° apart (0°, 90°, 180° and 270°).

Figure 4.16(a) to 4.16(d) shows the surface current distribution changes with the variation from 0° to 270° of feeding phases. In Figure 4.16(a), the dominant current vectors are presented in +*x*-direction at 0° phase, whereas, at 90° phase, the dominant current vectors are in the +*y*-direction as seen in Figure 4.16(b). Meanwhile, a strong horizontal current component towards the left is visible for 180° phase shown in Figure 4.16(c) and subsequently an inclination of dominant current orientated vertically downwards in the phase of 270° viewed in Figure 4.16(d). The result shows that the current distribution at 0° and 180° stages has equal magnitude but is distributed in the opposite phase. Nevertheless, when the change in feeding phases from 180° to 270° occurred, the dominant current vectors are at the opposite of 0° and 90° phases, respectively. From these observations, the phase progressions demonstrate that the surface current vectors are rotating counter clockwise, depicting a valid RHCP operation with the beam radiated along +*z*-direction.

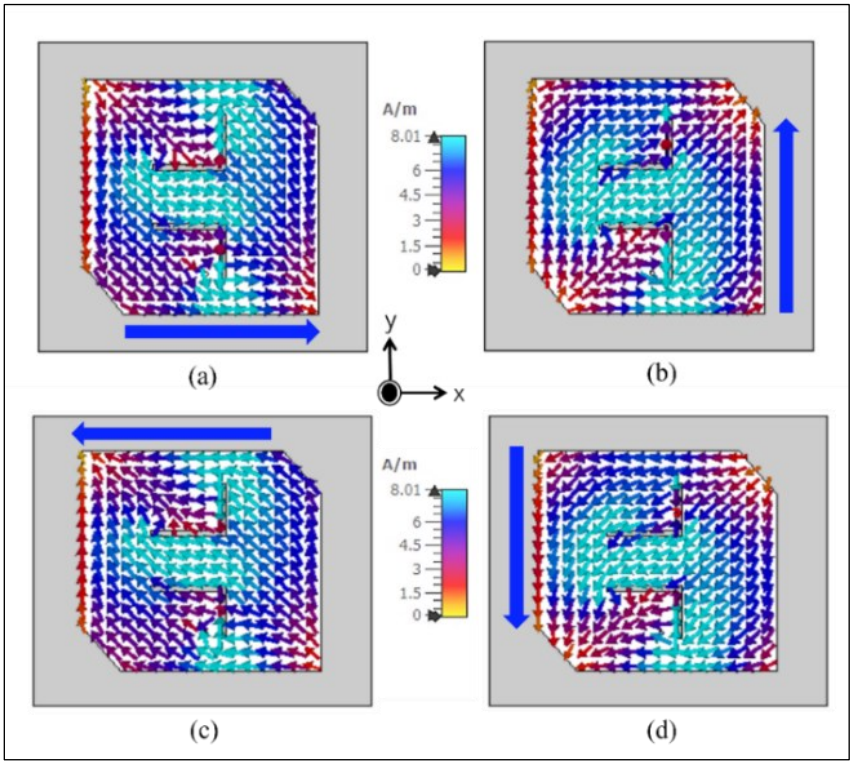

Figure 4.16 Surface Current Distribution at (a) ω = 0° (b) ω = 90° (c) ω = 180° (d) ω = 270°

4.5 Antenna Fabrication and Measurement

To conclude the simulation and optimization process, the finalized antenna design was fabricated to demonstrate its real-world implementation in wearable

application as shown in Figure 4.17. The manual fabrication process was done precisely and accurately to replicate of the simulated structure of textile antenna for a reliable performance validation during measurement. Figure 4.18 shows the fabricated antenna was measured for the impedance matching performance before the measurement was done in the anechoic chamber for antenna radiation performance as seen in Figure 4.19.

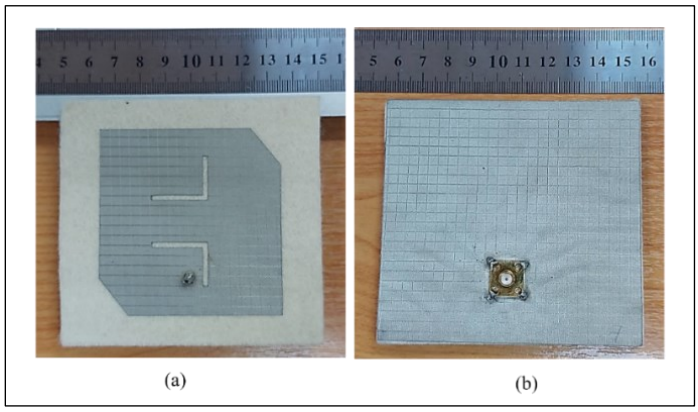

Figure 4.17 The Fabricated Antenna (a) Radiating Plane (b) Ground Plane

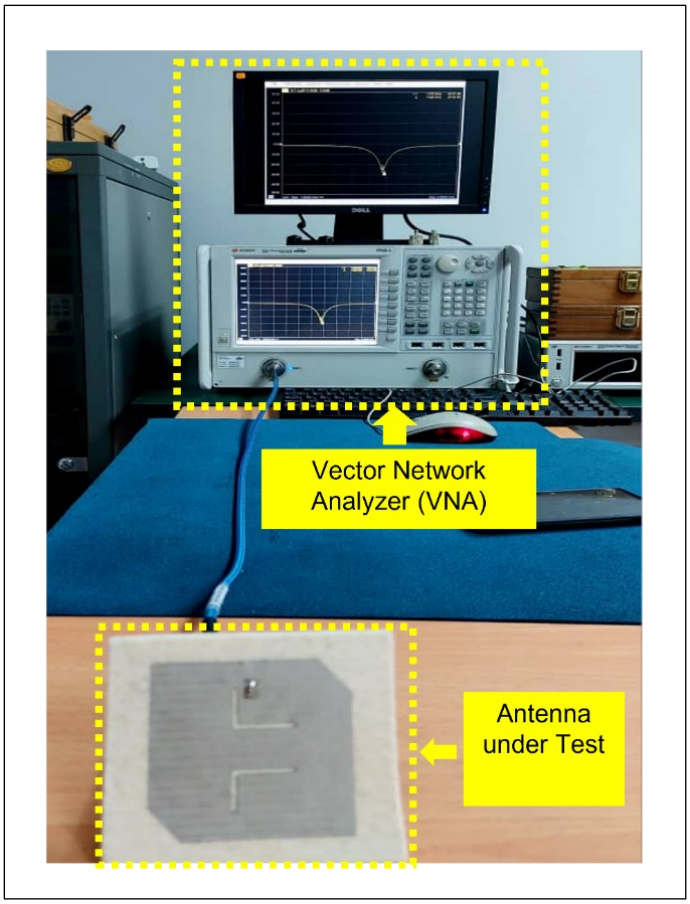

Figure 4.18 S_{11} Measurement Setup for the Dual L-shaped Slotted Antenna Prototype

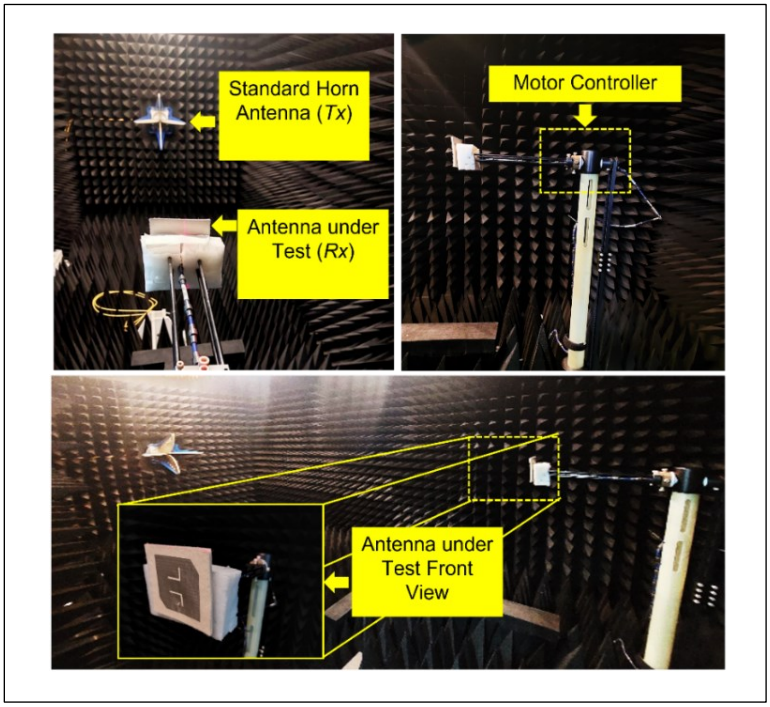

Figure 4.19 Far-field measurement in the anechoic chamber

4.6 Performance Analysis of Simulated and Measured Key Parameters of Circular Polarization Antenna

Figure 4.20 shows the simulated and the measured S_{11} of the proposed antenna. A comparison from this figure shows a good agreement was apparent between simulation and measurement results. The measured and simulated frequency bandwidths for both $S_{11} < -10$ dB is 108 MHz (1.525–1.630 GHz) and 116 MHz (1.517–1.633 GHz), respectively with a slight frequency shift from 1.575 GHz in simulation to 1.582 GHz in the measurement result.

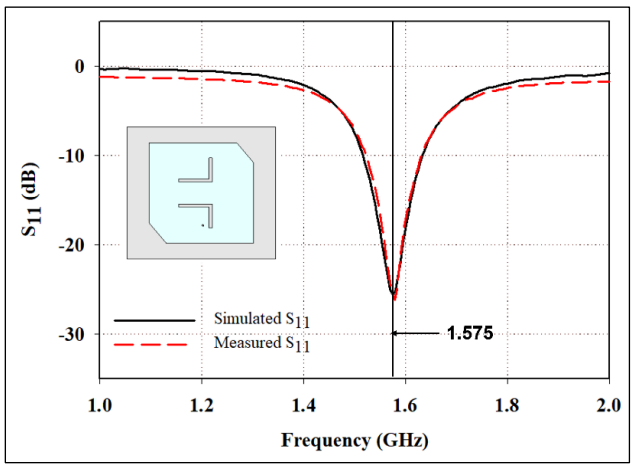

Figure 4.20 Simulated and Measured Return Loss (S_{11}) of the Proposed Antenna

According to Malaysian Communications and Multimedia Commission (MCMC) spectrum plan, the bandwidth for GPS-L1 bandwidth is allocated from 1.559 to 1.610 GHz (Malaysian Communications and Multimedia Commission, 2022). As such, this antenna design met the specifications and adhered to the requirements for GPS applications by the regulatory body in Malaysia.

The radiation patterns at 1.575 GHz of the proposed antenna shows a good concurrence with each other in the two principal planes (*x*–*z* and *y*–*z*) as shown in Figure 4.21(a) and Figure 4.21(b), respectively. From Figure 4.21(a), a unidirectional pattern is demonstrated with Half-Power Beamwidth (HPBW) radiating from 76.3° –79.4° for the simulated value and 76.5°– 78.6° for the measured value. The maximum gain manifested at *x*-*z* plane is 3.32 dB and 3.96 dB for the simulation and measurement result, respectively. For *y*-*z* plane in Figure 4.21(b), the gain achieved is 3.31 dB for the simulation result and 3.73 dB for the measurement result. It can be observed that both values of gain in the measurement result are slightly higher than the simulated value. This is due to a narrower beamwidth being demonstrated in the measurement values resulting from the radiated energy concentration in the boresight direction.

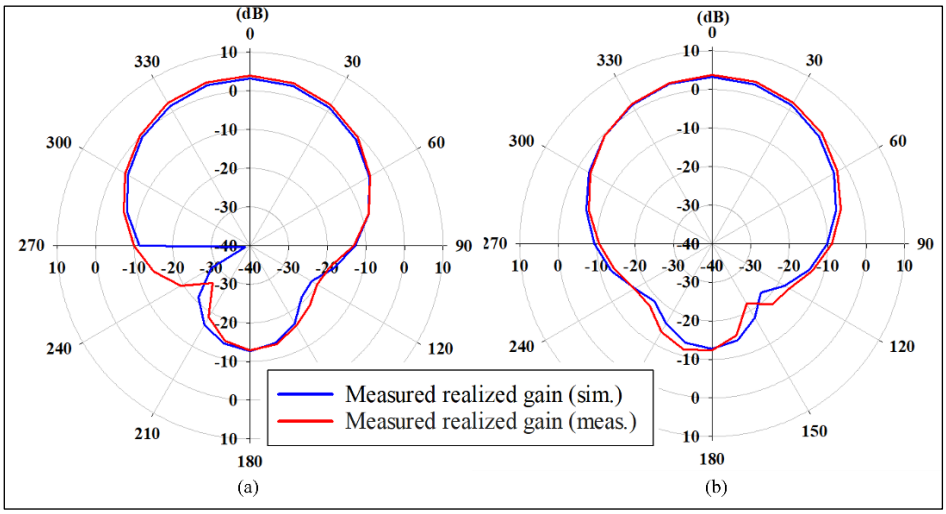

Figure 4.21 Simulated and Measured Radiation Patterns of the Proposed Antenna (a) *x*-*z* plane (b) *y*-*z* plane

Meanwhile, to investigate the amount of energy reflected, which depicts low back radiation to the body for wearable suitability, a front-to-back ratio (FBR) parameter must be analyzed (Rajavel & Goshal, 2023). As illustrated in Figure 4.21(a), the *x*-*z* plane demonstrates an FBR value of 19.42 dB for the simulated value and 16.86 dB for the measurement result. On the other hand, the simulated and measured values

of *y*-*z* plane as shown in Figure 4.21(b) resulted in 19.41 dB and 16.17 dB respectively. The difference between these FBR values for the simulated and measurement approach may be due to the experimental tolerance in the alignment setup during the measurement. In general, the measured FBR values of both planes indicate a good performance for the on-body application as the FBR percentage demonstrates more than 97.58% of power radiated in forward direction for both principal planes.

Figure 4.22 shows the 3-dB AR bandwidth of the simulated and measured result. The simulated AR bandwidth demonstrates a result of 24 MHz (1.560 – 1.584 GHz) with an AR value of 2.21 dB while the measured AR bandwidth shows the performance of 36 MHz (1.555 – 1.591 GHz) with an AR of 2.38 dB. The observed expansion in the measured AR bandwidth may attributed by minor fabrication tolerances, particularly in the slot dimensions and truncated corners. Besides that, the highly sensitive nature of CP may also enhanced the excitation of the orthogonal balance moded. With slight deformation in textile structure due to conformability structure, a deviation between the simulation and measurement results were expected. However, the measured results confirm that the proposed antenna maintains robust circular polarization characteristics with a wider AR operational bandwidth and demonstrates practical suitability for GPS-L1 wearable applications.

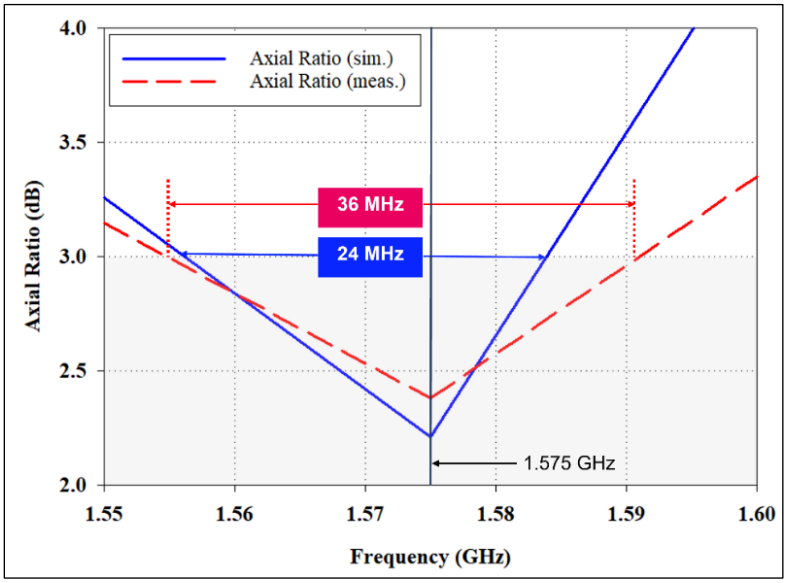

Figure 4.22 Simulated and Measured Axial Ratio of the Proposed Antenna

To validate the dominance of polarization for the proposed antenna, the gain plots of RHCP and LHCP are assessed accordingly. Based on the radiation patterns as illustrated in Figure 4.23, it can be observed that the co-polarization gain of RHCP dominates LHCP gain for both the *x-z* and *y-z* planes. In these planes, the magnitude of the RHCP gain of 3.86 dB and 3.64 dB observed are significantly higher than the LHCP gain of -12.04 dB and -12.77 dB. Given this outcome, the antenna demonstrates the desired polarization as the RHCP gain is remarkably different by more than 15 dB, as seen in Figure 4.24. Therefore, the result from these co-polarized and cross-polarized levels indicates that the RHCP properties have been successfully acquired in both planes and attained a good cross-polarization ratio. Comparing the simulated and the measured results, the RHCP gain for both approaches demonstrate a good agreement. Nevertheless, a deteriorated gain is observed slightly in LHCP gain, which may affect the CP purity and degrade the AR value towards linear polarization.

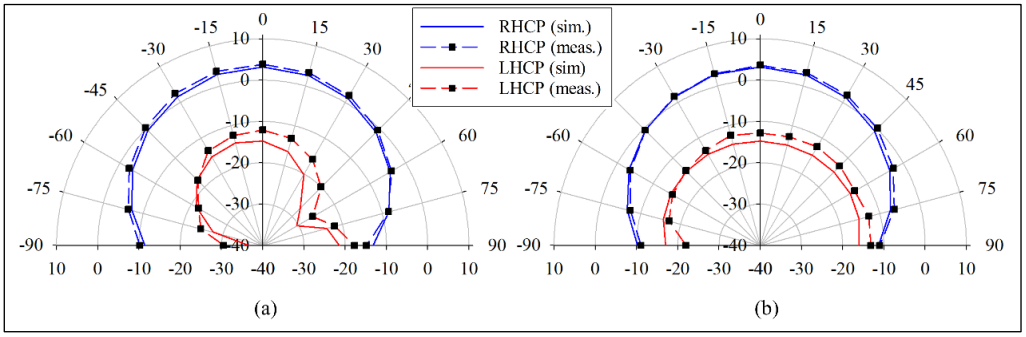

Figure 4.23 Simulated and Measured RHCP and LHCP Gain at (a) *x-z* plane (b) *y-z* plane

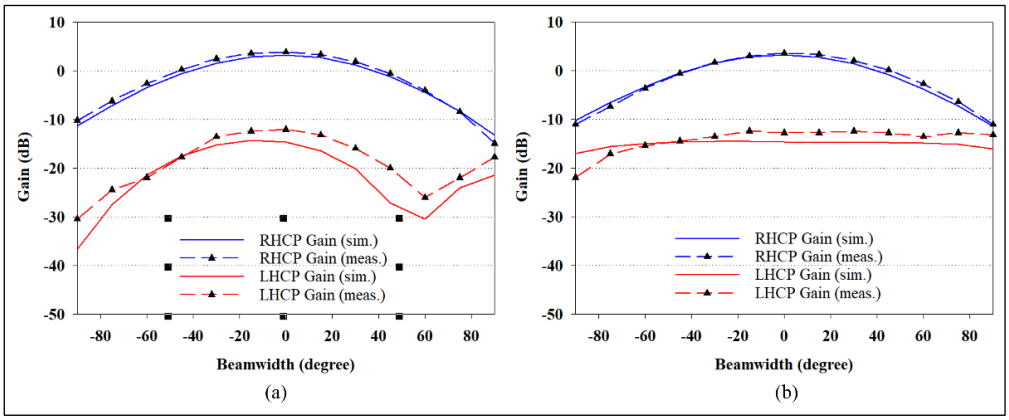

Figure 4.24 Simulated and Measured RHCP and LHCP Gain Curves of the Proposed Antenna at (a) *x-z* plane (b) *y-z* plane

For a practical GPS operation, a width angle of 120° beamwidth is required to cover at least four satellites for accurate 3D positioning at latitude, longitude and altitude. Moreover, the antenna can receive a stable signal although the satellites are positioned at a low elevation angle (Elsikh et al., 2019). Figure 4.25 shows the simulated and measured 3-dB AR beamwidth of the proposed antenna at *x*-*z* and *y*-*z* plane. The measured beamwidth demonstrates 150° (-90° to 60°) at Phi=0° and 135° (-75° to 60°) at Phi=90°. From observation, the beamwidth of the measurement is slightly wider than the simulation result. This could be due to the angle misplacement that introduced asymmetric excitation and hence skewed the main lobe and increased the beamwidth. The simulation assumptions are not wholly met, leading to differences between simulated and measured results.

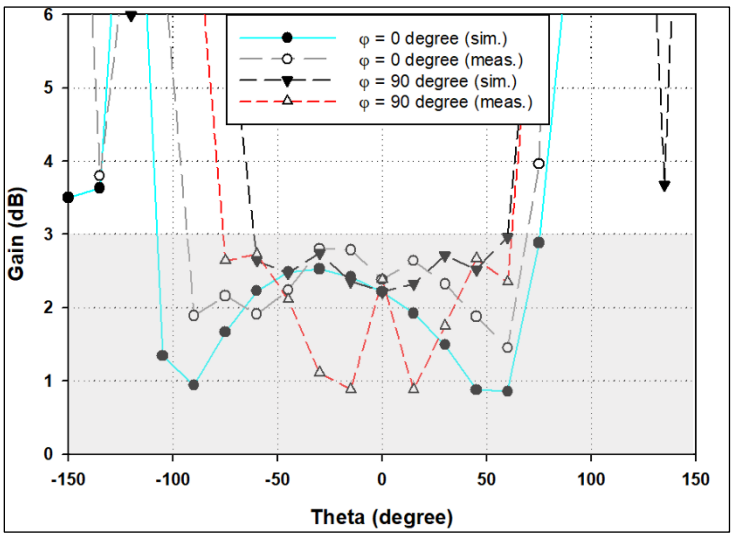

Figure 4.25 Simulated and Measured AR Beamwidth of the Proposed Antenna at *x*-*z* and *y*-*z* plane

The antenna structure shows that the mirrored L-slots antenna is symmetrical with respect to the *x*-axis but asymmetrical with respect to the *y*-axis. The current distribution will be uniformly distributed along the *x*-axis when the antenna is symmetrical. This condition will result in a wider beamwidth as the energy is spread evenly across a wide angle. Unlike the asymmetrical antenna structure along the *y*-axis, the current distribution will be unevenly distributed especially in the direction in which the L-slots open (the orientation of the arms of the L). As seen on the surface current distribution in previous Figure 4.16, the current peak occurred at the lower arm of L-slot, nearer to the feed point location. This will cause the radiation to be more directional

as the energy intensifies, narrowing the beamwidth in that plane. As a result, the AR beamwidth in the *x-z* plane has a wider angle than in the *y-z* plane.

The amplitude and phase components of the radiated electric fields were also analyzed across different azimuthal planes to assess the CP behaviour and subsequently verify the mode orthogonality of the proposed antenna. Figure 4.26 and Figure 4.27 show the variation of AR, amplitude ratio, and phase difference as a function of the elevation angle (θ) for four azimuthal planes (φ = 0°, 45°, 90°, 135°). The dual-axis plots reveal a clear correlation between axial-ratio minima (< 3 dB) and regions where both amplitude equality and quadrature phase (≈ 90°) are simultaneously achieved.

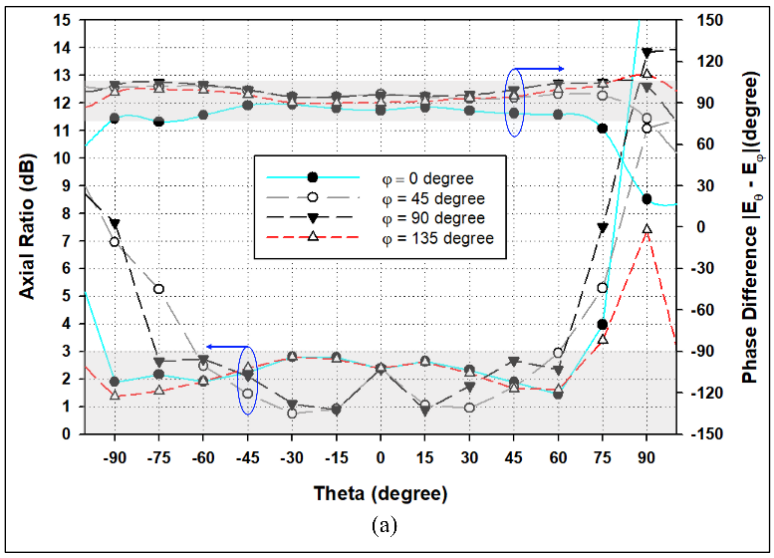

Figure 4.26 Measured AR Beamwidth in the Principle and Diagonal Planes versus Amplitude Ratio

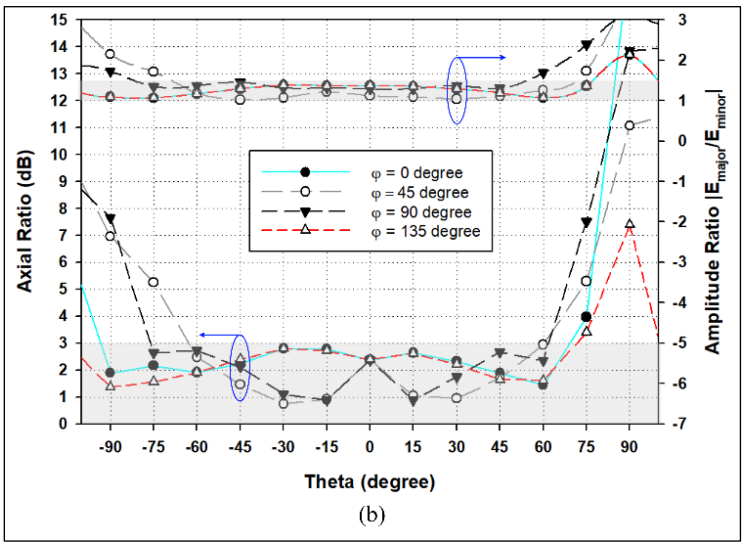

Figure 4.27 Measured AR Beamwidth in the Principle and Diagonal Planes versus Phase Difference

Theoretically, CP is achieved when the orthogonal components (Eθ, Eφ) exhibit both amplitude balance within ±3 dB and a phase difference near + 90° for RHCP. From observations, any departure from perfect quadrature requires even tighter amplitude matching to sustain AR ≤ 3 dB. At broadside (θ ≈ 0°), the components remain nearly equal in magnitude ($|E_\theta|/|E_\varphi| \approx 1$) and maintain a 90° phase separation, producing an AR below 3 dB across φ = 0°–135°. As θ increases toward ±90°, the phase deviates from quadrature in Figure 4.26 and the amplitude ratio drifts beyond 1.4 (i.e., $|E_{major}|/|E_{minor}| \leq 1.414$) in Figure 4.27, causing the AR to degrade. This behavior is attributed to field imbalance arising from asymmetric surface-current distribution and edge-induced diffraction as the observation angle increases.

The φ = 0° and 135° planes maintain better amplitude stability across a wider angular span, which correlates with their broader AR < 3 dB coverage in the main beam. Hence, amplitude equalization is strongest near the broadside direction and gradually deteriorates toward the end-fire region. For φ = 90° and 135° show the most consistent phase behaviour, implying better symmetry of current flow in those azimuths. This indicates that the antenna preserves the correct rotational sense predominantly within the main beam, while the polarization purity deteriorates toward larger angles due to structural asymmetry. In summary, by comparing both figures, regions where amplitude ratio ≈ 1 and phase difference ≈ 90° correspond directly to minimum AR < 3 dB. Where either amplitude or phase deviates, AR rises sharply indicating a transition from circular to elliptical polarization. This agreement confirms that the antenna's measured AR behaviour is physically consistent with its electromagnetic field balance, validating the correctness of both simulation and measurement.

Overall, the differences between the simulated and measured results are mainly attributed to the idealized material and geometrical assumptions applied in the simulation model. In practice, textile-thickness variation, substrate compression, uncertainty in dielectric properties, variation in conductive-fabric conductivity, surface roughness, adhesive-layer effects, and fabrication tolerances can modify the effective current paths and resonant behaviour. Additional differences may arise from the coaxial-feed implementation, connector and cable interactions, antenna alignment, and measurement-system uncertainty. These effects are particularly significant for the axial ratio because circular polarization depends on maintaining comparable amplitudes and an approximately 90° phase difference between the two orthogonal modes. Nevertheless, the overall agreement between the simulated and measured trends verifies

the proposed antenna-design mechanism and demonstrates the practical feasibility of the fully textile antenna for GPS-L1 operation.

To position the achieved performance within the existing state of the art, Table 4.4 compares the proposed antenna with previously reported wide-beam CP antennas for various applications such as ISM, GPS or general GNSS. These applications employed comparable modal-perturbation mechanisms such as asymmetric patch shaping, slot loading, and magnetic dipole excitation that are relevant to ARBW enhancement. However, all designs were implemented on rigid substrates and none on textile antennas. The textile CP GPS antennas primarily focus on bandwidth or AMC-based FBR improvement but not reporting beamwidth characterization.

Table 4.4
Comparative Analysis of the Reported CP Antennas for Wide Beamwidth and Textile GPS Application

Application Band & Authors	**Antenna Structure**	**Substrate**	**Fully Textile**	**Polarization**	**Gain (dB)**	**FBR (dB)**	**3-dB AR Bandwidth (MHz)**	**3-dB ARBW, φ (degree)**	
								0°	90°
Wide Beamwidth CP Antennas									
GNSS (Zhai et al., 2019)	Asymmetric arc-loaded patch	FR-4	No	RHCP	4.09	NR	20	232	212
GPS-L1 (Wang et al., 2018)	Dual asymmetric slot with coupled strips	F4BK350	No	RHCP	5.4	NR	10	188	188
ISM (Ray et al., 2019)	Two pairs diagonal narrow slots	Rogers RT	No	LHCP	3.87	17.7	23	226	198
ISM (Ray et al., 2020)	Two orthogonal parallel slot pairs	Taconic TLP-3	No	LHCP	5	18	22	224	214
Textile CP GPS Antennas									
GPS-L1 (Budiastuti et al., 2020)	Truncated edge with quarter-wave transformer and slot	Jeans	No	RHCP	-3.6	NR	NR	NR	
GPS-L1 (Ilyas et al., 2020)	Truncated side patch with quarter-wave transformer and slot	Felt	No	RHCP	6.3	NR	27	NR	
GPS-L1, ISM (Joshi et al., 2020)	Dual-band AMC backed patch (3x3 cells)	Felt, Kevlar	Yes	RHCP/ LHCP	1.98, 1.94	16.7	141.75	NR	
GPS-L1 (This Work)	Dual L-shaped slotted patch with corner truncation	Felt	Yes	RHCP	3.96	16.9	36	150	135

The proposed dual L-shaped slotted antenna in this paper achieves verified wide-beam RHCP radiation with an average 3-dB ARBW of 143°, full GPS-L1 AR bandwidth coverage, and a high FBR of 16.9 dB in a compact, single-layer, single-feed

configuration. This combination of wide-beam circular polarization, polarization purity, and mechanical conformability establishes it as one of the most effective fully textile antennas for wearable GPS navigation.

4.7 Summary

The study proposed a systematic development and performance evaluation of a circularly polarized (CP) wearable textile antenna designed for GPS-L1 applications. The selection of dielectric substrates from three different textiles was first addressed through Transmission Line Method (TLM) analysis. The transmission loss behaviour effects on fabric thickness ranging from 0.5 mm to 4.0 mm were analyzed to justify the best substrate choice for antenna design implementation. The suitability of felt which was selected as the suitable dielectric substrate were verified via conductivity measurement using TLM approach. To study the influence of geometrical pertubation on circular polarization, a comprehensive parametric study was subsequently conducted on corner truncation and slot parameter. The configurations were systematically varied to examine the effects on resonant frequency, return loss, and axial ratio performance. This analysis provided critical guidelines to design the CP antenna into exciting two orthogonal resonant modes of equal amplitude with a 90° phase difference conditions . The chapter then detailed the evolution of the antenna design from a linearly polarized configuration to a circularly polarized structure. Through surface current distribution analysis, the behavior of surface currents which generated RHCP were analysed and validated. In the final stage, the fabrication and measurement validation of the antenna prototype were subsequently carried out. A comparative analysis between simulated and measured results were presented on the key performance parameters, including axial ratio characteristics on the bandwidth and beamwidth, radiation pattern behavior, and polarization performance of the developed antenna. The close agreement between simulation and measurement were verified hence, confirmed the feasibility of the antenna for wearable GPS applications. In summary, this study has successfully demonstrated a systematic design approach for realizing a fully textile of circularly polarized antenna for wearable implementation.

CHAPTER 5
DEVELOPMENT OF WEARABLE TEXTILE ANTENNA WITH DEFECTED GROUND STRUCTURE

5.1 Introduction

In the preceding chapter, the development of a circularly polarized wearable textile antenna for GPS applications was presented based on the selection of the dielectric substrate, parametric analysis of the patch perturbations, the evolution from linear to circular polarization, and validation through simulation and measurement. While satisfactory circular polarization (CP) performance was achieved under planar conditions, wearable usage introduces bending effects that require thorough evaluation of antenna characteristics, particularly resonant frequency, gain and polarization which are essential for reliable GPS reception.

Based on these observations, Chapter Five presents an improved antenna design aimed at mitigating bending and detuning effects at GPS-L1 application. At the same time, the proposed design must maintain and enhance the dominant right-hand circular polarization (RHCP) characteristics including axial-ratio (AR) bandwidth and axial-ratio beamwidth (ARBW), while suppressing undesired cross-polarized radiation associated with probe-fed configurations on thicker substrates. To overcome these issues in wearable antennas, a defected ground structure (DGS) is introduced to redistribute the ground surface currents and control parasitic currents, thereby enhancing tolerance to mechanical deformation. The design evolution, operating mechanism, and performance of the proposed antenna under both planar and bent conditions with respect to GPS-LI application are discussed in detail in this chapter.

5.2 Antenna Design with Defected Ground Structure (DGS)

The Defected Ground Structure (DGS) is introduced to mitigate frequency detuning effects caused by mechanical deformation of the textile antenna. In wearable applications, bending along the E-plane or H-plane alters the effective current distribution and electrical length of the radiator, which may shift the resonant frequency away from the GPS-L1 band (1.575 GHz). By strategically incorporating a DGS, the

ground current path is redistributed, reducing localized reactive energy concentration and effectively lowering the quality factor (Q-factor) of the antenna.

In this research, a new technique in placing DGS has been introduced. Conventionally, to increase antenna bandwidth, DGS slots are placed under the antenna radiating patch to disturb the ground current distribution and introduce additional inductive–capacitive (LC) effects. This effectively reduces the quality factor (Q-factor) of the antenna and broadens the impedance bandwidth. Positioning the DGS slots directly under the patch would strongly disturb the patch surface current distribution due to the modifications of electromagnetic fields (Elias et al.,2021). Such defects may alter the dominant current paths on the patch resulting in unintended polarization, distortion or narrowing of the radiation beamwidth and degradation of AR performance.

However, in order to preserve the polarizarion characteristics and beamwidth determined by the radiating patch, as a new concept, the DGS slots are intentionally not introduced beneath the patch geometry. In the proposed design, the DGS is strategically positioned on the ground plane outside the projected footprint of the radiating patch, specifically along the outer ground region where the return current density is significant but does not directly contribute to orthogonal mode excitation. By placing the DGS in this peripheral ground area, the structure primarily perturbs the return current path rather than the radiating fields above the patch.

To achieve controlled ground perturbation, a fragmented slot configuration comprising both vertical and horizontal segments is introduced. The vertical segments primarily interrupt longitudinal ground currents, while horizontal segments disturb transverse current components. These interuptions ensures a more uniform redistribution of ground current. The segmented structure behaves as multiple coupled LC perturbations loading is distributed across the ground plane rather than one strong localized defect. As a result, the equivalent inductive–capacitive effect across the ground plane, lowering the Q-factor in a more controlled manner. As the perturbation is distributed and not concentrated beneath the patch, the orthogonal modes generated by the dual L-slots remain balanced. This minimizes amplitude imbalance and phase deviation, thereby preserving axial ratio stability.

Overall, this placement strategy ensures that bandwidth enhancement and polarization preservation are achieved simultaneously without mutual degradation while maintaining polarization integrity. The detailed geometrical evolution of this DGS configuration is discussed in the following subsection.

5.2.1 DGS Design Parameters and Evolution

Figure 5.1 illustrates the progressive evolution of the DGS introduced to enhance impedance matching and CP performance. In this work, as the DGS is intentionally positioned outside the region directly beneath the radiating patch as discussed earlier, the available perturbation area is inherently limited as shown in Figure 5.2. Therefore, simple rectangular slots are employed as the ground-plane defects. In addition to accommodating the area constraint, the rectangular slot geometry also offers ease of fabrication on textile substrates while minimizing edge complexity and dimensional inaccuracies.

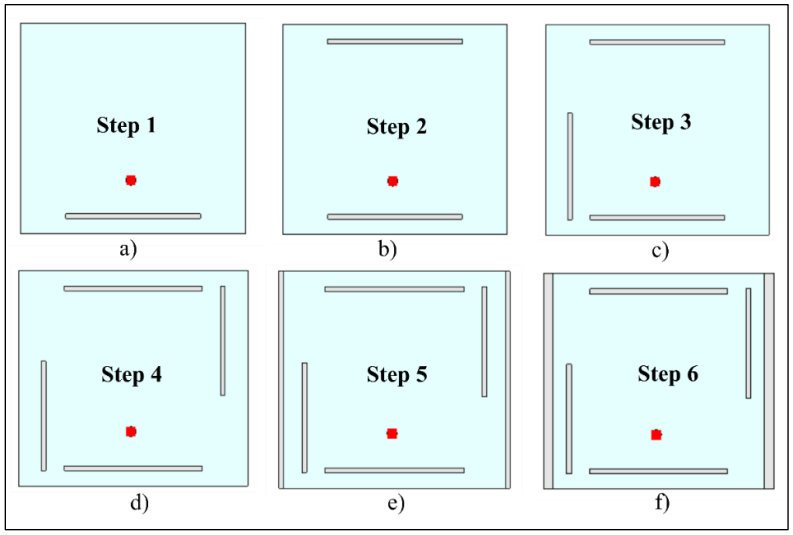

Figure 5.1 Step-by-step Evolution of the DGS-integrated Design of the Proposed Antenna

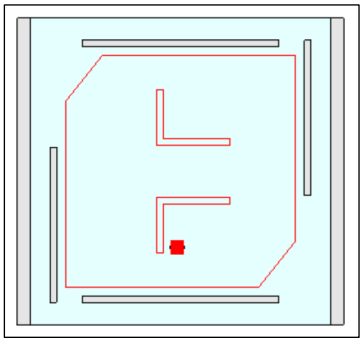

Figure 5.2 Transparent Configuration of the Radiating Patch and its Corresponding Ground Plane

Figure 5.3 shows the return loss performance of the proposed antenna at each stage of the DGS development. In reference to Figure 5.1, during Step 1, a single horizontal slot is introduced in the ground plane near the feed, as this region exhibits the highest ground current density and strongest coupling with the excitation source (Prajapati et al., 2025). This configuration achieves stable resonance at 1.575 GHz with good impedance matching of −35.37 dB. However, the AR remains relatively high at 1.5625 dB, indicating degraded circular polarization purity. This limitation motivates the introduction of an additional slot that restores geometrical symmetry to the ground plane. In Step 2, a second horizontal slot is added symmetrically mirrored to the antenna's central axis to balance ground current distribution and improve impedance matching. This results in improved matching to −40.24 dB at 1.578 GHz and a reduced AR to 1.4196 dB. Despite this improvement, the resonant frequency shifts to higher frequency with a slight enhancement in polarization purity.

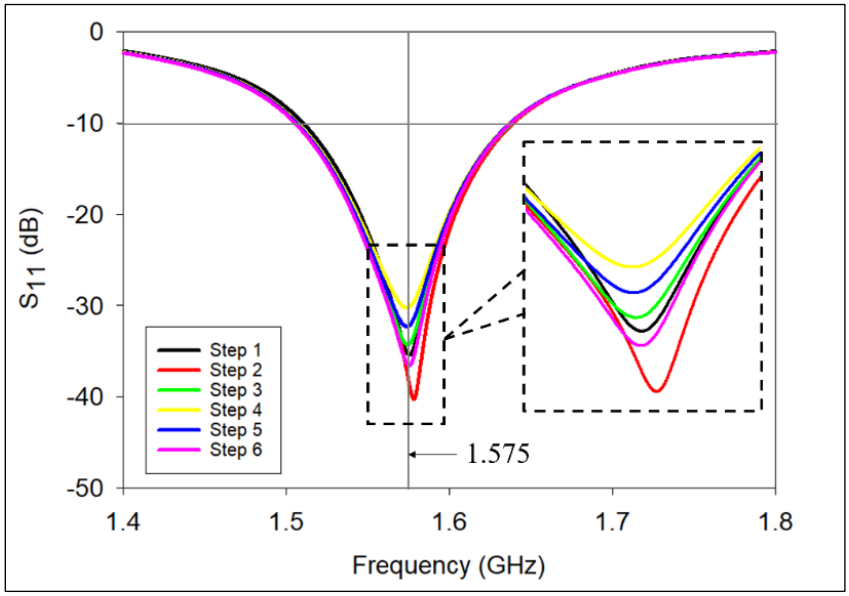

Figure 5.3 Return Loss of the Proposed Antenna at Different DGS Design Steps

In Step 3, a vertical slot is introduced to support the orthogonal surface current component required for CP. The resonant frequency shifts marginally to 1.574 GHz while the AR slightly increases to 1.4239 dB, indicating that the balance between orthogonal modes remains suboptimal and requires further refinement of the ground perturbation. In Step 4, an additional vertical slot is added to increase the effective electrical length in the orthogonal direction. However, excessive ground perturbation degrades the impedance matching to −30.26 dB and increases AR to 1.5459 dB.

In Step 5, the design strategy shifts to introducing left–right ground perturbations to regulate the transverse surface current distribution rather than further increasing longitudinal slots. This approach improves modal balance and reduces the AR to 1.252 while maintaining resonance at 1.574 GHz and acceptable impedance matching at −32.32 dB. Nevertheless, further optimization is required to achieve the GPS-L1 resonant frequency and lower AR for wearable purpose. Finally, Step 6 refines the left–right ground perturbations to achieve optimal balance between the orthogonal current components. This final configuration yields resonance at 1.575 GHz with improved impedance matching of −36.55 dB and a significantly reduced AR of 0.8630 confirming effective CP suitable for GPS-L1 wearable applications.

As the DGS is progressively introduced and refined from Step 1 to Step 6, a clear improvement in impedance matching is observed in Figure 5.3, with the resonant frequency consistently maintained around the GPS-L1 band. The reflection coefficient deepens notably after the initial DGS perturbations indicating enhanced coupling and effective control of the ground current distribution.

Simultaneously, Figure 5.4 shows the AR response demonstrates a systematic reduction at the operating frequency demonstrating the gradual improvement in CP purity. In particular, the later design steps yield a lower minimum AR and a smoother frequency variation demonstrating a significant and a more balanced excitation of the orthogonal modes required for RHCP operation. This trend demonstrates that the DGS modifications are successfully implemented to enable simultaneous optimization of impedance matching, polarization characteristics and bandwidth enhancement while maintaining the resonant frequency.

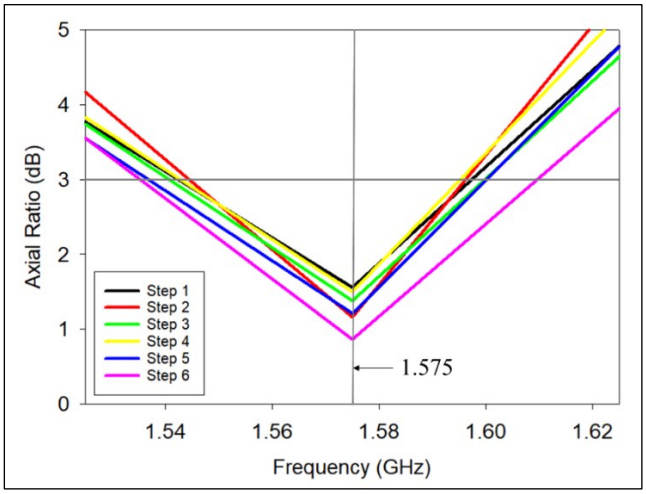

Figure 5.4 Axial Ratio of the Proposed Antenna at Different DGS Design Steps

Figure 5.5 shows the fabricated prototype of the proposed DGS-integrated textile antenna including the dimensional layouts of the top layer (radiating patch) and the bottom layer (ground plane). The patch antenna design and dimensions, incorporating dual L-shaped slot pertubations, remained identical to those presented in the previous chapter (without DGS). The ground plane incorporates a fragmented DGS slot arrangement designed to modify the return current distribution, enhance impedance and AR bandwidth, while suppressesing cross-polarization radiation to improve polarization purity for GPS-L1 wearable operation. The antenna parameters and dimensions are summarized in Table 5.1.

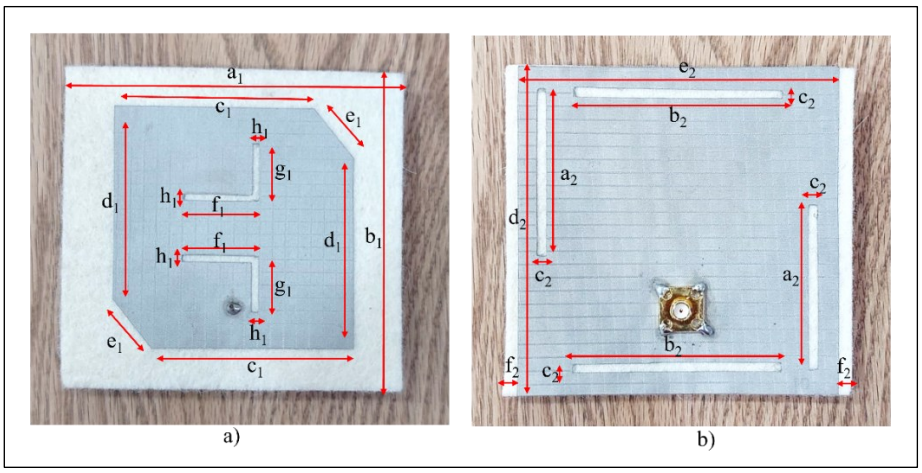

Figure 5.5 Fabricated Prototype of the Proposed DGS-integrated Antenna with Dimensional Layouts of a) Top Layer and b) Bottom Layer

Table 5.1
Parameters and Dimensions of the Proposed DGS-integrated Antenna

Radiating Patch								
Parameter	a_1	b_1	c_1	d_1	e_1	f_1	g_1	h_1
Dimension (mm)	100	94	59	57	18	22	17	2
Ground Plane								
Parameter	a_2	b_2	c_2	d_2	e_2	f_2		
Dimension (mm)	47	60	2	94	92	4		

Table 5.2 compares the simulated and measured performance of the antenna with and without the DGS under planar conditions. The introduction of the DGS improves impedance matching and robustness, resulting in 33.3% increase in measured −10 dB impedance bandwidth and 13.6% in simulated bandwidth. The antenna gain shows modest improvement for a single layer configuration, with improvements of 0.55 dB in simulation and 0.02 dB in measurement. This shows that DGS does not degrade

the radiation strength. Meanwhile, the antenna efficiency shows an improvement of 11.7% and 7.4% for simulation and measured values, respectively demonstrating a reduced loss.

Table 5.2
Comparison of Simulated and Measured Antenna With and Without DGS

Performance Parameter	**Planar Antenna at 1.575 GHz**			
	Antenna without DGS		Antenna with DGS	
	Simulated	Measured	Simulated	Measured
S_{11} (dB)	-25.63	-25.66	-36.55	-23.14
Impedance Bandwidth (MHz)	110 (1.52-1.63)	105 (1.525-1.630)	125 (1.51-1.635)	140 (1.515-1.655)
Gain (dBi)	3.31	3.96	3.86	3.98
Efficiency (%)	34.9	37.76	39	40.55
AR (dB)	2.21	2.38	0.86	0.99
AR Bandwidth (MHz)	28 (1.556-1.584)	36 (1.555-1.591)	72 (1.535-1.639)	139 (1.483-1.622)

More importantly, the DGS significantly enhances CP performance whereby the AR is reduced by approximately 61% in both simulation and measurement. The ARBW increases by approximately 157% in simulation and 286% in measurement after incorporating the DGS. As shown in Figure 5.4 earlier, the AR at the GPS-L1 frequency is gradually reduced while the slope of the AR response around resonance becomes noticeably flatter. This behaviour indicates improved amplitude balance and phase consistency between the orthogonal surface current modes required for CP which allow the AR less than 3-dB condition to be maintained over a wider frequency range.

5.2.2 Surface Current Distribution Analysis

Figure 5.6 compares the surface current distribution of the antenna with DGS and without DGS on radiating patch at 1.575 GHz. Both figures are presented on an identical scale ranging from 0 to 8 A/m. Referring to Figure 5.6, the patch surface current distributions before and after introducing the DGS exhibit a consistent rotational pattern which indicates that the dominant orthogonal modes responsible for RHCP radiation are preserved. The similarity in current magnitude and direction confirms that the DGS does not significantly perturb the patch radiation mechanism. As seen in Figure 5.6b), the current magnitudes exhibits a more uniform spatial distribution across the patch surface with high-current regions (red/orange) are less concentrated in one area

as in Figure 5.6a). The improved uniformity helps to prevent local current dominance that contributes to cross-polarized radiation and support the polarization purity.

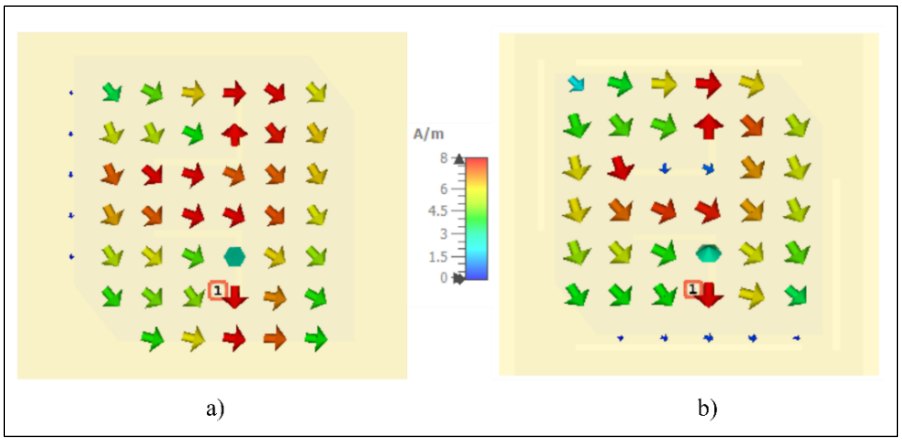

Figure 5.6 Current Distribution on Radiating Patch at φ =0° a) without DGS b) with DGS

Meanwhile, the comparison of the surface current distribution of the antenna with DGS and without DGS on ground plane are illustrated in Figure 5.7. Without DGS, large red regions indicate high current density hot spots is observed near the feed and central ground region as seen in Figure 5.7a). With DGS, the return current is redistributed across a wider ground area and forced to follow the DGS slot boundaries with the strong currents appear along the top and bottom slots as depicted in Figure 5.7b). This elongated return current paths and phase dispersion due to DGS have reduces localized current loops that are out of phase with the intended circularly polarized radiation. As a result, undesired cross-polarized components are suppressed and led to improved polarization purity and cross-polarization discrimination.

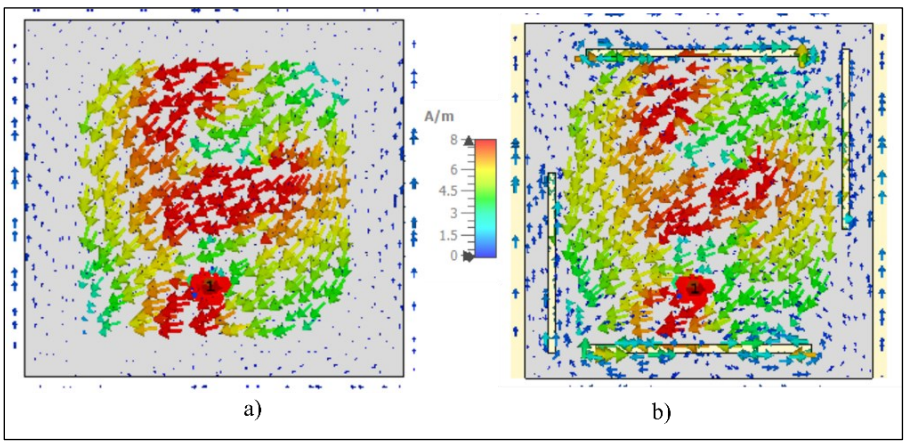

Figure 5.7 Current Distribution on Ground Plane at φ =0° a) without DGS b) with DGS

To further validate the suppression of cross-polarization inferred from the surface current analysis, the co-polarized (RHCP) and cross-polarized (LHCP) radiation patterns evaluated in the φ = 0° plane are examined. As shown in Figure 5.8, the RHCP gain with and without the DGS remains largely unchanged across the main beam region which demonstrates the dominant radiating mode of the patch is preserved. In contrast, the LHCP component exhibits a significant reduction when the DGS is introduced, with an improvement of approximately 7.68 dB observed near boresight which demonstrates the effective polarization purity enhancement.

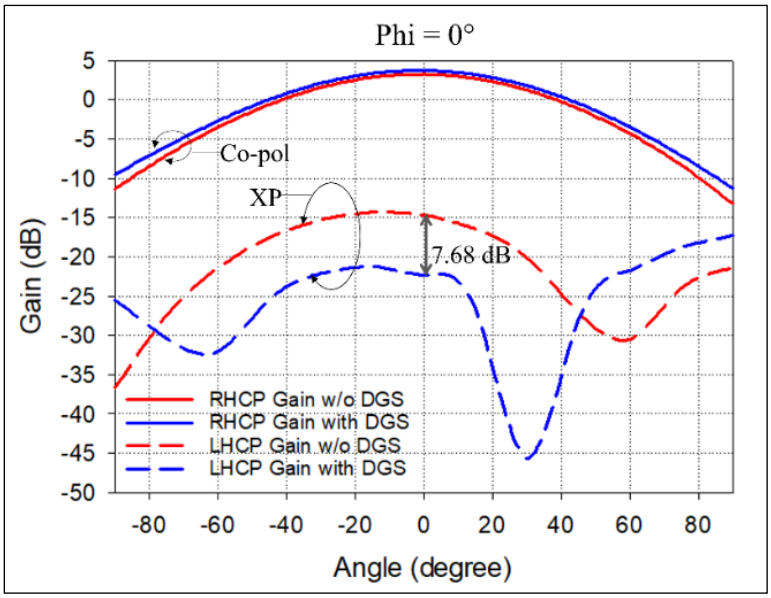

Figure 5.8 Co-polarization and Cross-polarization LHCP level at θ = ±90° of φ =0°

5.3 Effects of Bending on Antenna Performance

In practical wearable applications, the antennas are subjected to mechanical deformation caused by body movement and surface curvature which can alter their electromagnetic characteristics. This section investigates the effects of bending on the performance of the proposed DGS-integrated antenna. The antenna is evaluated under E-plane and H-plane bending conditions through both simulation and measurement. Key performance parameters including impedance matching, realized gain, radiation pattern, circular polarization characteristics (RHCP and LHCP), AR, AR bandwidth and ARBW are systematically analyzed and compared with the planar configuration to assess the robustness of the proposed design under wearable deformation.

5.3.1 Simulation and Measurement Setup of Bending Analysis

Figure 5.9 shows the simulated bending configurations of the proposed wearable textile antenna under a) E-plane bending and b) H-plane bending using CST. In the E-plane bending case, the antenna is bent along a_1 (refer to Figure 5.9a), meanwhile for the H-plane bending case, the antenna is bent along b_1(refer to Figure 5.9b). The perspective and sectional views illustrate the bending orientation and radius used to evaluate the antenna's robustness under wearable deformation.

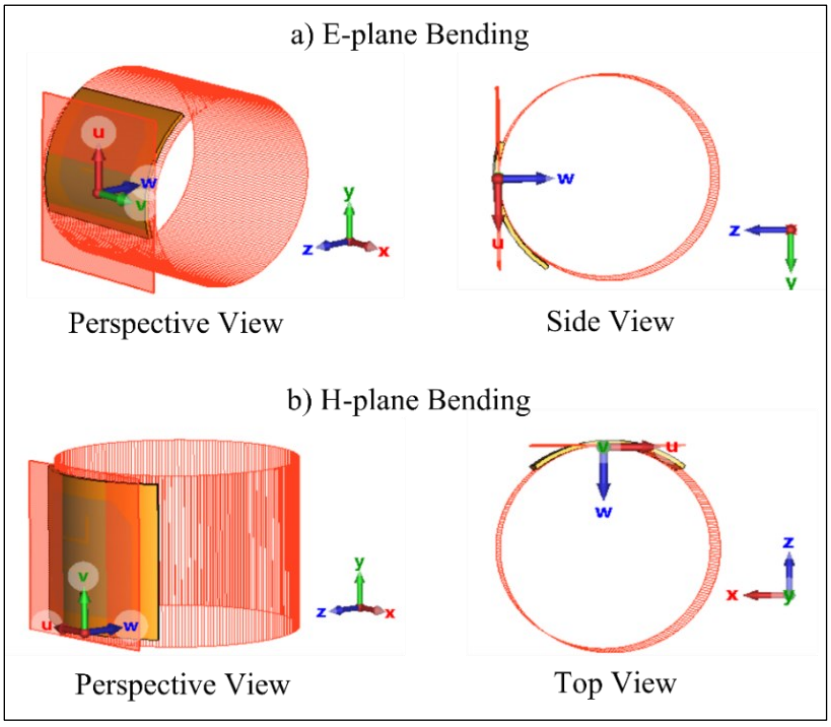

Figure 5.9 Simulated Bending Configurations of the Proposed Antenna Under a) E-plane and b) H-plane Bending using CST

Figure 5.10 shows the bending geometry modelled as a circular arc of radius, r = 72 mm. The subtended angle, θ is calculated using Equation (5.1) and the corresponding bent arc length, s is determined from Equation (5.2) where θ is expressed in radians. For b_1 = 94 mm (E-plane bent), the bending angle is approximately 82° yielding an arc length of approximately 102.5 mm. When a_1=100 mm (H-plane bent), the bending angle increases to approximately 88° corresponding to an arc length of 110.6 mm. The selected radius emulates limb radii such as the upper arm which are common wearable mounting locations.

$$\theta = 2\ sin^{-1}(\frac{c}{2r}) \tag{5.1}$$

$$s = r\theta \tag{5.2}$$

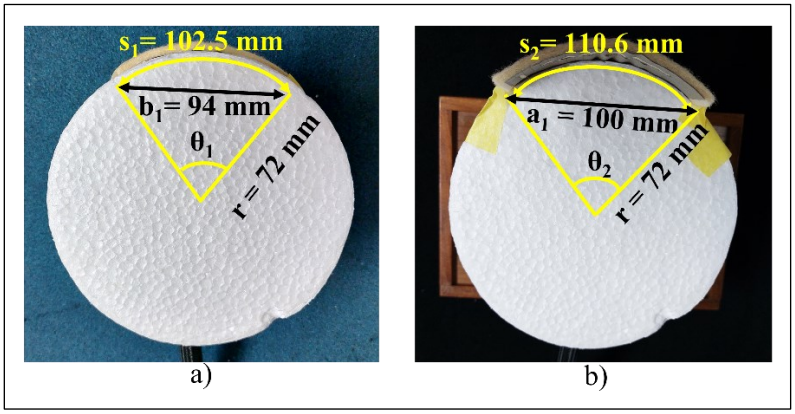

Figure 5.10 Bending Geometry under a) E-plane and b) H-plane on Cylindrical Foam

Figures 5.11 and 5.12 illustrate the experimental setups used to evaluate the antenna performance under the E-plane and H-plane bending conditions, respectively. The antenna prototype is wrapped around a cylindrical foam structure to provide a consistent curvature and emulate realistic wearable deformation. For each bending configuration, impedance measurements are conducted using a Vector Network Analyzer (VNA), while radiation and polarization characteristics are measured in an anechoic chamber to ensure far-field conditions and minimize environmental interference.

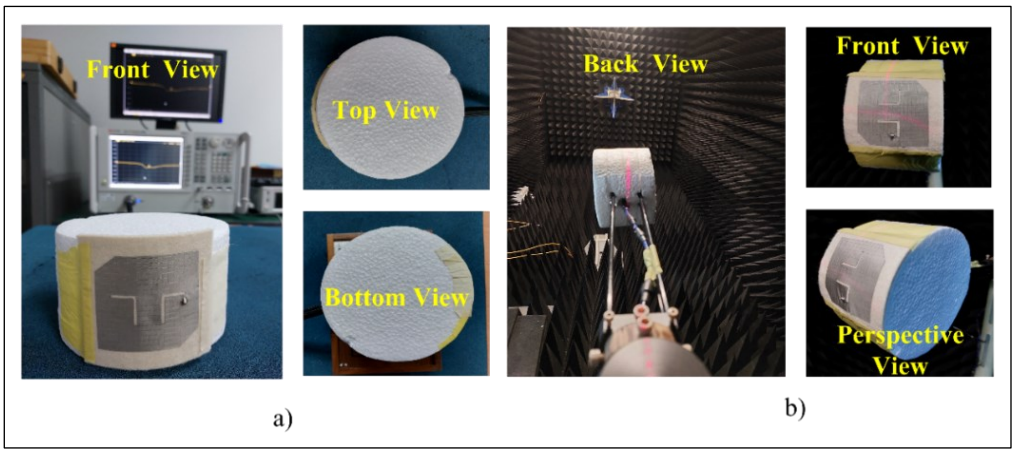

Figure 5.11 Measurement Setup under E-plane Bending a) Impedance Measurement using VNA b) Radiation and Polarization Measurement in the Anechoic Chamber

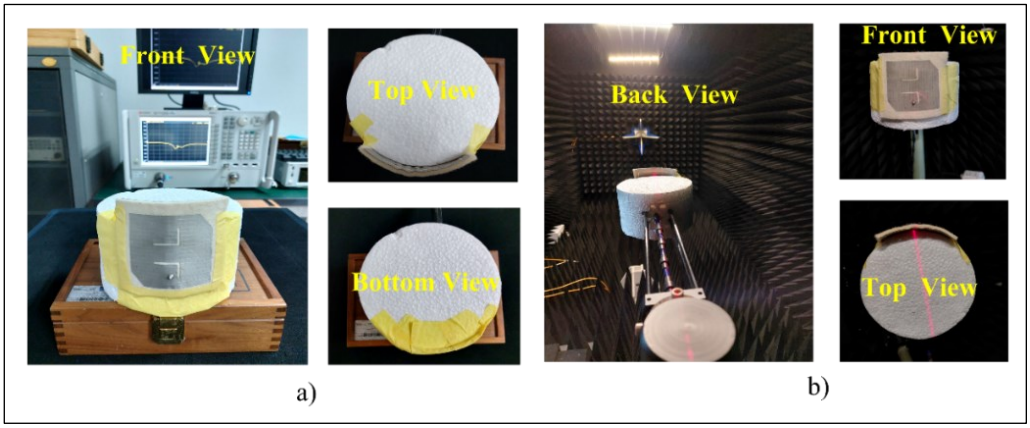

Figure 5.12 Measurement Setup under H-plane Bending a) Impedance Measurement using VNA b) Radiation and Polarization Measurement in the Anechoic Chamber

5.3.2 Return Loss (S_{11}) Analysis

Figure 5.13 compares the simulated and measured reflection coefficients of the antenna with and without DGS under planar (undeformed condition), E-plane bending, and H-plane bending conditions. In all cases, the operating resonance is maintained close to the GPS-L1 frequency of 1.575 GHz showing good frequency stability under mechanical deformation. Generally, the introduction of the DGS results has improved the impedance matching, as evidenced by deeper S_{11} and a more stable impedance response particularly under E-plane bending where deformation effects are more significant. The DGS interrupts the conventional ground-current path and causes the current to propagate around the defected regions. This increases the effective current-path length and introduces additional inductive and capacitive loading into the antenna structure. The resulting ground-plane perturbation produces a closely coupled resonant response that combines with the original patch resonance, thereby extending the frequency range over which satisfactory impedance matching is maintained. This mechanism explains the wider impedance bandwidth observed for the DGS-integrated antenna under both planar and bent conditions. In contrast, the antenna without DGS exhibits noticeable degradation in matching depth and increased sensitivity to bending. Figure 5.14 illustrates the comparison of the simulated and measured return loss of the proposed antenna under planar, E-plane bending, and H-plane bending conditions, with and without the DGS.

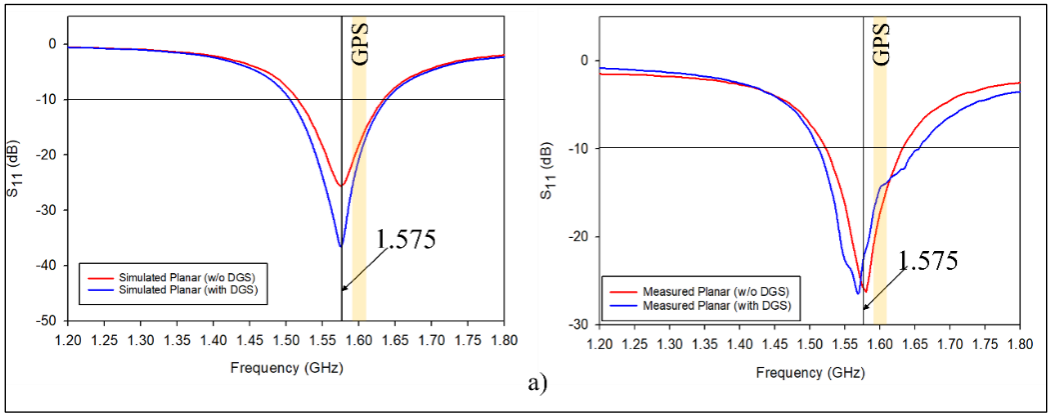

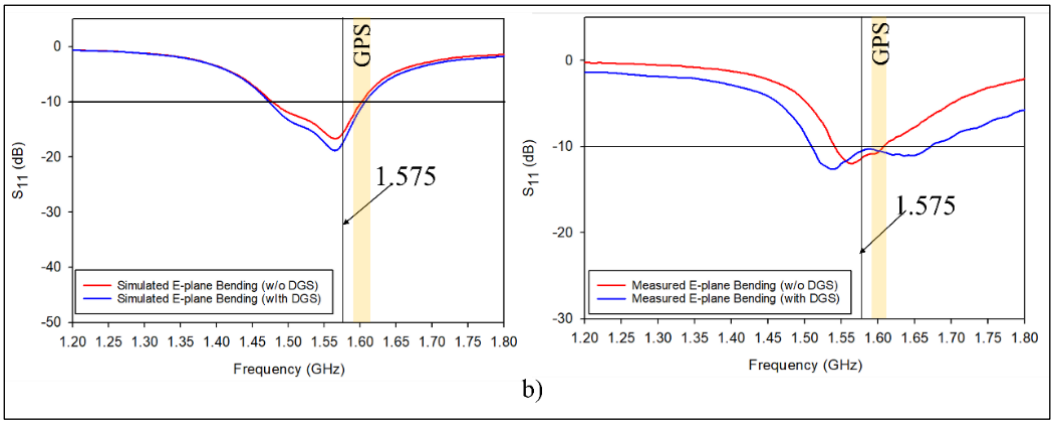

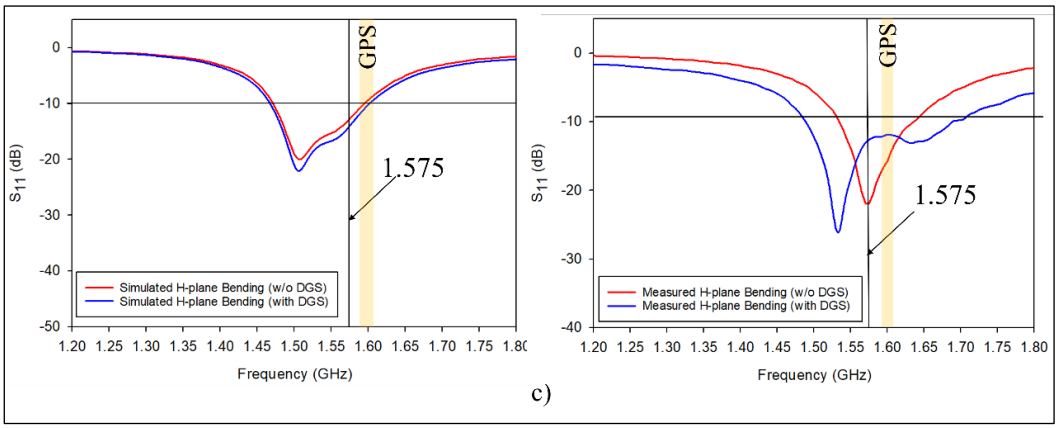

Figure 5.13 Comparison of the Simulated and Measured S_{11} Performance With and Without DGS under a) Planar b) E-plane Bending c) H-plane Bending

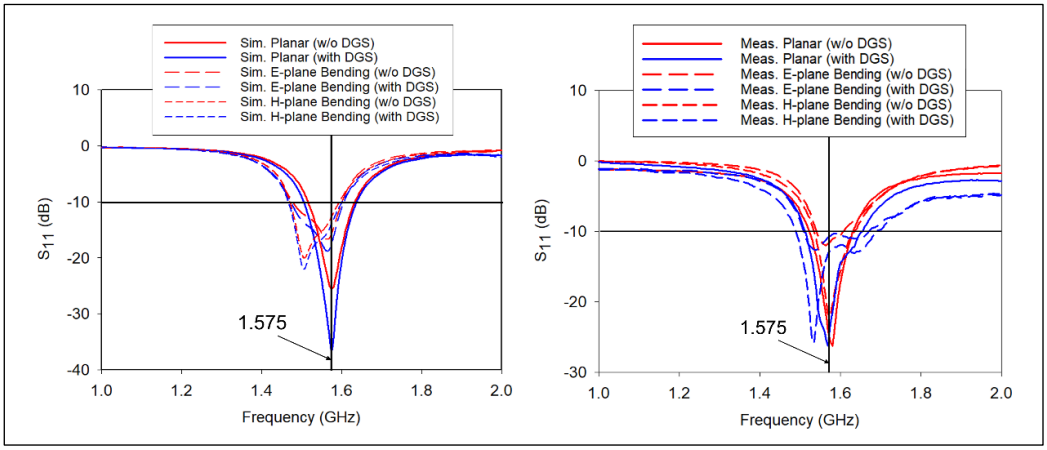

Figure 5.14 Summary of S_{11} Performance on Simulated and Measured S_{11} Performance With and Without DGS under Planar, E-plane Bending and H-plane Bending

To provide better analysis of DGS effect on resonant frequency, Table 5.3 presents a quantitative comparison of simulated and measured S_{11} resonant frequency detuning and GPS bandwidth coverage under planar, E-plane bending, and H-plane bending condition. The overall results demonstrate that while bending inevitably introduces frequency variation due to changes in effective electrical length and substrate deformation, the DGS improves practical bandwidth stability and ensures consistent GPS-L1 coverage, validating its effectiveness in maintaining operational reliability under wearable conditions. The DGS introduces additional electromagnetic loading into the antenna structure. The elongated and redistributed ground-current path changes the input impedance and produces a secondary resonant contribution close to the original patch resonance. The interaction between these closely spaced resonant responses extends the frequency range over which the input impedance remains matched to the feed. Consequently, the DGS broadens the impedance bandwidth and provides a greater tolerance to the frequency detuning caused by bending.

When the antenna is bent, its effective electrical length, patch-to-ground spacing and fringing-field distribution are modified. These effects shift the resonant frequency and may degrade the impedance match. However, the broader matched response produced by the DGS enables the GPS-L1 frequency to remain within the −10-dB impedance bandwidth under both planar and bent conditions. Therefore, the principal role of the DGS is not to eliminate bending-induced detuning, but to provide sufficient impedance-bandwidth margin so that the antenna remains operational after deformation.

The results tabulated in Table 5.3 above can be further explained by the impedance-frequency relationship for series resonance graph. As shown in Figure 5.15, the inductive and capacitive reactances cancel at resonance resulting in optimal impedance matching. In the present design, mechanical bending under E-plane and H-plane alter the effective electrical length of the antenna (Zaidi et al., 2020). The deformation perturbs the distributed reactive components of the antenna by modifying the effective capacitance related to fringing fields and effective inductace related to surface current paths. As a result, the LC resonance balance is disturb causing a shift in the resonant frequency.

Table 5.3
Comparison of Simulated and Measured S_{11}, Detuning, Impedance and GPS Bandwidth Coverage under Planar, E-plane Bending and H-plane Bending With and Without DGS

Simulated S_{11}, Percentage Detuning and GPS Coverage				
Antenna Structure	Parameter	Planar	E-plane	H-plane
Without DGS	Frequency (GHz)	1.575	1.565	1.505
	Percentage Detuning (%)	0	0.64	4.44
	Impedance Bandwidth (MHz)	110	120	115
	Frequency Range (GHz)	1.52-1.63	1.48-1.60	1.475-1.59
	GPS Bandwidth Coverage (%)	100	80.4	60.8
With DGS	Frequency (GHz)	1.575	1.565	1.505
	Percentage Detuning (%)	0	0.64	4.44
	Impedance Bandwidth (MHz)	125	130	130
	Frequency Range (GHz)	1.51-1.635	1.475-1.605	1.47-1.60
	GPS Bandwidth Coverage (%)	100	90.2	80.4
Measured S_{11}, Percentage Detuning and GPS Coverage				
Antenna Structure	Parameter	Planar	E-plane	H-plane
Without DGS	Frequency (GHz)	1.580	1.56	1.575
	Percentage Detuning (%)	0.32	0.95	0
	Impedance Bandwidth (MHz)	105	60	100
	Frequency Range (GHz)	1.525-1.63	1.545-1605	1.535-1.635
	GPS Bandwidth Coverage (%)	100	90.2	100
With DGS	Frequency (GHz)	1.57	1.54	1.535
	Percentage Detuning (%)	0.32	2.22	2.54
	Impedance Bandwidth (MHz)	140	160	195
	Frequency Range (GHz)	1.515-1.655	1.51-1.67	1.49-1.685
	GPS Bandwidth Coverage (%)	100	100	100

The introduction of the DGS provides an effective distributed balance LC perturbation by elongating the ground current paths via longer slots which develops the inductive effect. Meanwhile, the introducing of localized capacitive coupling via the etched narrow slots of 2 mm width provides stronger electric field across the gap as seen in Figure 5.7b). This reactive compensation subsequently restores the condition of $X_C \approx X_L$ which explains the observed preservation of the resonant frequency near 1.575 GHz and the improved impedance matching under planar and bent conditions. With less than 3% of detuning experienced for measurement value, the DGS is proven to reduce the mechanical deformation sensitivity to bending-induced detuning. This results are consistent with the demonstrated reflection coefficient trends observed in Figure 5.13 and Figure 5.14.

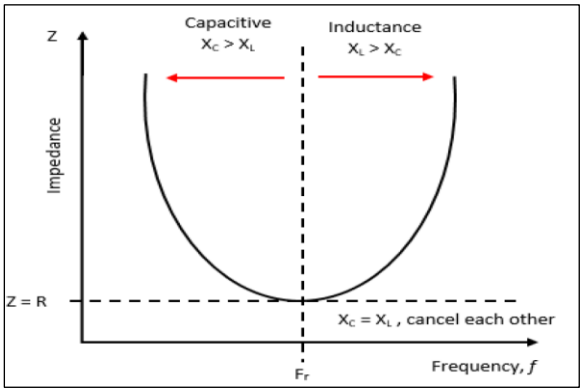

Figure 5.15: Graph Impedance vs Frequency for Series RLC Resonance Circuit (Zaidi et. al, 2021)

The relationship between bandwidth (BW), center frequency (F_c), and Q-factor is defined in Equation (5.3), where bandwidth is inversely proportional to Q. In addition, Q is directly proportional to the reactive component X at resonance and inversely proportional to the resistive component R, as described in Equation (5.4). Therefore, any modification to the reactive loading alters the balance between stored and dissipated energy, ultimately affecting the impedance bandwidth.

$$BW = \frac{F_C}{Q} \tag{5.3}$$

$$Q = \frac{X}{R} = \frac{Xc}{R} or \frac{X_L}{R} \tag{5.4}$$

The observed bandwidth enhancement can be justified through the current density distribution and its influence on the effective quality factor. In a conventional solid ground plane, the return current tends to form high-density localized loops near the feed region and along the patch edges. These concentrated current paths are associated with stronger near-field confinement and increased reactive energy storage which is reflected by X according to quality factor expression in Equation (5.3). As X increases, the stored reactive energy becomes more dominant relative to the dissipated energy, resulting in a higher Q factor but a lower bandwidth. In contrast, with the introduction of the DGS, discontinuities are created in the ground plane that redistribute and re-route the return current. Instead of allowing strong current crowding, the DGS spreads and fragments the surface current distribution, thereby reducing localized field confinement and subsequently reduced the reactive energy storage represented by X in Equation (5.4). As the reactive dominance is reduced, the reactance-to-resistance ratio decreases, leading to a lower effective Q factor. A reduction in Q directly results in an expansion of impedance bandwidth, therefore broadens the −10 dB bandwidth and improves frequency tolerance under bending conditions.

The simulated Z-parameter plots in Figure 5.16 further validate the effective quality factor introduced by the DGS. At 1.575 GHz, the DGS configuration exhibits an imaginary impedance of approximately −1.37 Ω compared to −5.22 Ω without DGS. Based on the relation in Equation (5.3), the estimated Q reduces from approximately 0.103 (without DGS) to 0.0277 (with DGS), representing a 73% reduction. Since bandwidth is inversely proportional to Q, this substantial decrease in resonance selectivity explains the enhanced impedance bandwidth observed in the DGS configuration.

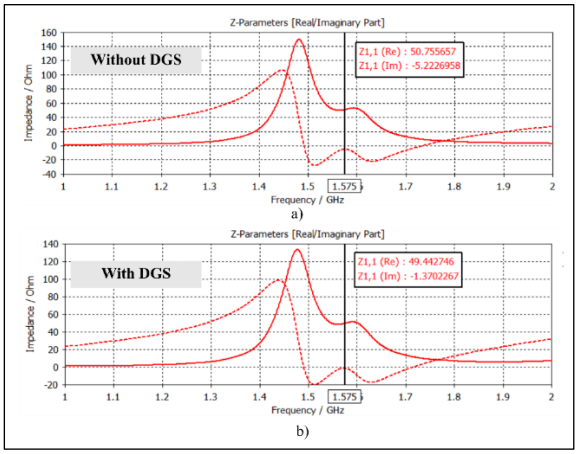

Figure 5.16 The Simulated Z-parameters (Real/Imaginary Part) for Antenna a) Without DGS b) With DGS

5.3.3 Gain and Radiation Pattern Analysis

Figures 5.17 and 5.18 present the simulated and measured radiation patterns of the proposed antenna with and without DGS under planar, E-plane bending, and H-plane bending conditions for φ = 0° and φ = 90°. Overall, good qualitative agreement is observed between simulation and measurement, particularly in terms of main-lobe direction and back-lobe behaviour. In both results, the antenna incorporating the DGS consistently exhibits reduced back-lobe radiation compared to the antenna without DGS design which indicate an improvement in front-to-back ratio (FBR)(Ullah et al.,2020). While the simulated patterns show more symmetric and deeper back-lobe suppression, the measured patterns exhibit slightly elevated back-lobe levels and minor asymmetries, which are attributed to practical measurement factors such as feed-cable radiation, textile material non-uniformity, fabrication and imperfect alignment. These discrepancies are more evident under E-plane bending where mechanical deformation introduces additional current redistribution which is not fully captured in the ideal simulation environment. Nevertheless, the measured results confirm the same trend predicted by simulation and demonstrates that the DGS effectively confines ground return currents and mitigates bending degradation of radiation performance, thereby preserving a higher FBR under realistic wearable conditions.

Table 5.4 validates the simulated and measured gain and FBR performance of the antenna with and without DGS at φ = 0° and φ = 90° under planar and bending conditions. Under planar configuration at φ = 0°, the simulated gain increases from 3.31 dBi to 3.86 dBi. This improvement is attained by the inductive–capacitive loading of DGS, which increases the effective surface impedance and suppresses surface-wave propagation (Elias et al., 2021). However, the measured gain shows only a marginal increase from 3.96 dBi to 3.98 dBi due to practical losses during measurement and textile irregularities which limit the gain enhancement. At φ = 90°, the simulated gain also improves by 0.55 dB confirming uniform efficiency enhancement under ideal conditions. Nevertheless the measured gain decreases by 0.47 dB, which may be attributed by minor rotational misalignment which affect radiation levels in specific angle cut. Besides that, the decreases is also due to the redistribution of current intensity between principal planes as more power is radiated towards φ = 0°.

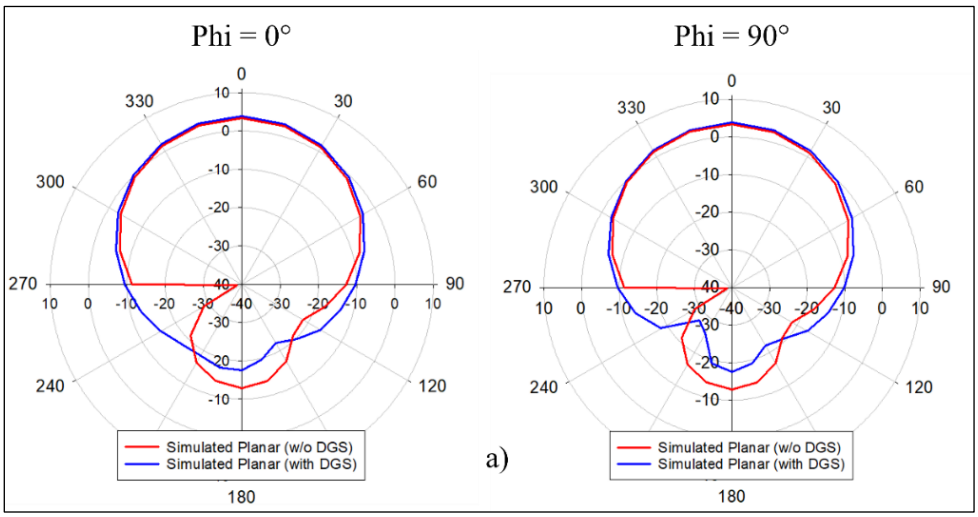

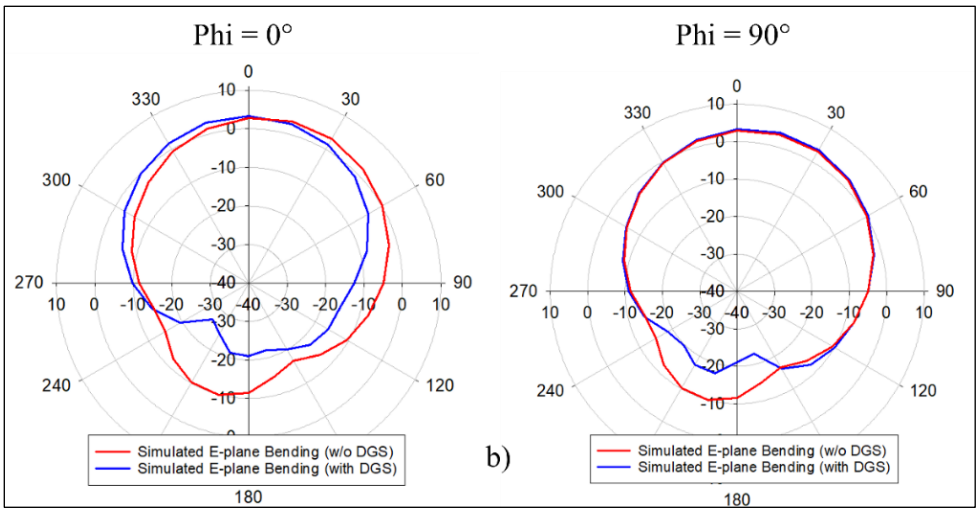

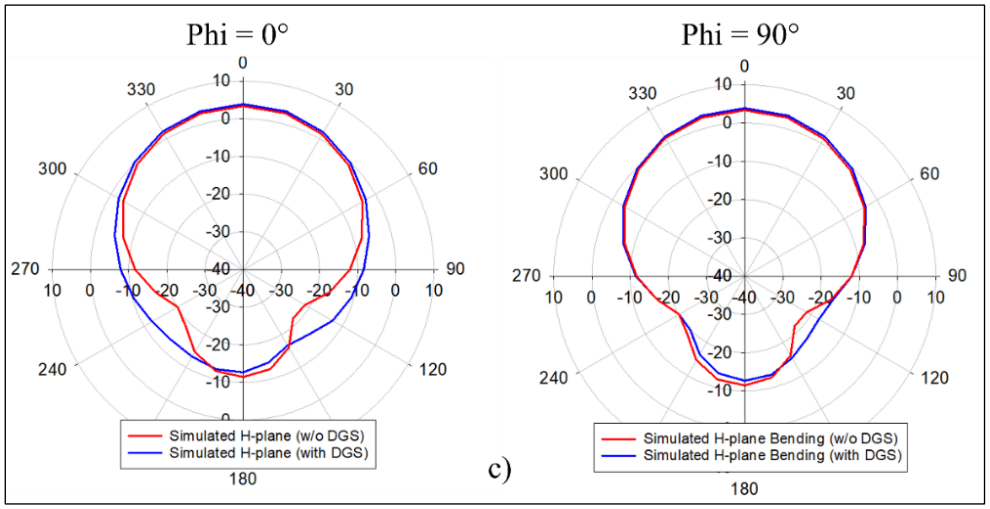

Figure 5.17 Comparison of the Simulated Radiation Pattern Performance With and Without DGS under a) Planar b) E-plane Bending c) H-plane Bending

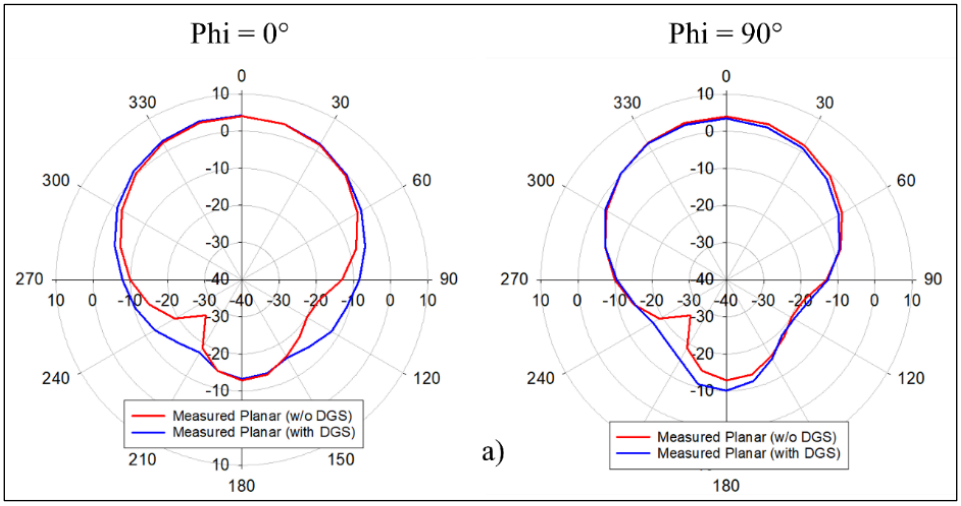

Figure 5.18 Comparison of the Measured Radiation Pattern Performance With and Without DGS under a) Planar b) E-plane Bending c) H-plane Bending

Under E-plane bending at φ = 0°, the simulated gain increases by 0.45 dB while the measured gain improves significantly by 0.97 dB. Bending normally distorts current paths and enhances back radiation but the DGS mitigates this by forcing return currents to detour around etched slots to reduce edge current intensity. At φ = 90°, a minor reduction is observed which reflects the transverse current imbalance due to deformation. For H-plane bending at φ = 0°, simulated and measured gains increase by 0.54 dB and 0.44 dB, respectively. At φ = 90°, the measured gain increases slightly, confirming radiation robustness under this deformation mode.

The FBR results further highlight the significant implementation of the DGS. Under planar conditions, the simulated FBR increases by 4.96 dB due to reduced back radiation, achieved through surface-wave suppression and increased ground-plane impedance. The measured planar improvement is modest because the antenna without DGS already exhibits acceptable directional control. The most significant improvement occurs under E-plane bending, where simulated and measured FBR increase by 10.01 dB and 7.92 dB, respectively. The DGS modifies the return current path under bending and prevents current concentration at the curved ground edge and thereby suppressing backlobe radiation. Under H-plane bending, simulated and measured FBR improve by 1.87 dB and 2.85 dB, respectively, confirming consistent backlobe suppression through enhanced surface-current confinement.

Table 5.4
Gain and Front-to-Back Ratio (FBR) Performance of the Antenna With and Without DGS at φ =0° and φ =90° under Planar and Bending Conditions

Antenna Condition	**Gain (dBi) at φ =0°**			
	Antenna without DGS		Antenna with DGS	
	Simulated	Measured	Simulated	Measured
Planar	3.31	3.96	3.86	3.98
Bend E-plane	2.88	2.74	3.33	3.71
Bend H-plane	3.32	2.86	3.86	3.3
Antenna Condition	**Gain (dBi) at φ =90°**			
	Antenna without DGS		Antenna with DGS	
	Simulated	Measured	Simulated	Measured
Planar	3.31	3.96	3.86	3.49
Bend E-plane	2.88	2.74	3.33	2.56
Bend H-plane	3.32	2.86	3.86	2.90
Antenna Condition	**Front-to-Back Ratio (FBR) at Principal Plane (dB)**			
	Antenna without DGS		Antenna with DGS	
	Simulated	Measured	Simulated	Measured
Planar	16.08	16.86	21.44	17.12
Bend E-plane	14.39	11.59	24.4	19.51
Bend H-plane	14.74	10.41	16.61	13.26

5.3.4 RHCP and LHCP Performance Analysis

Figures 5.19 and 5.20 compare the simulated and measured RHCP/LHCP radiation characteristics of the antenna with and without DGS under planar, E-plane bending, and H-plane bending conditions for φ = 0° and φ = 90°. In both simulation and measurement, the antenna incorporating the DGS exhibits dominant RHCP radiation in the forward direction, while the LHCP component is consistently suppressed. This demonstrates improved polarization purity and enhanced cross-polarization discrimination (Ray et al., 2020). Without DGS, bending particularly along the E-plane introduces noticeable distortion in the circular polarization characteristics due to elevated LHCP levels and reduced RHCP–LHCP separation. In contrast to DGS, the design maintains stronger RHCP dominance and better LHCP suppression under deformation which indicates improved robustness of CP for wearable operation. Generally, the RHCP/LHCP radiation results demonstrate that the proposed DGS enhances polarization purity and preserves RHCP dominance under mechanical deformation for a robust CP performance for wearable GPS applications.

Table 5.5 further supports the radiation pattern observations by providing a quantitative comparison of the RHCP/LHCP gain and cross-polarization discrimination (XPD) performance with and without DGS under planar and bending conditions. At φ = 0°, the measured RHCP gain shows consistent improvement with the introduction of the DGS under planar condition, E-plane bending, and H-plane bending. Similar enhancement trends are observed at φ = 90°, where the measured RHCP gain under E-plane and H-plane bending improves by 0.97 dB and 0.5 dB, respectively. In parallel, the LHCP component is generally reduced with the DGS, with suppression levels reaching up to 8.15 dB in the planar case and 6.71 dB under H-plane bending at φ = 0°. These results indicate that the DGS effectively preserves dominant RHCP radiation while suppressing undesired LHCP components, thereby enhancing polarization purity and robustness under mechanical deformation. The strong RHCP retention under severe bending confirms the suitability of the proposed design for reliable wearable GPS operation.

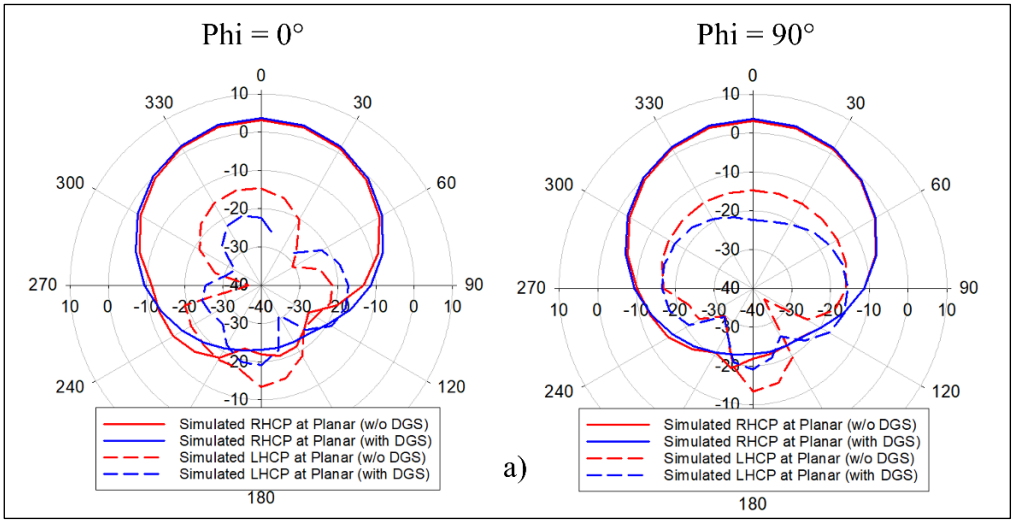

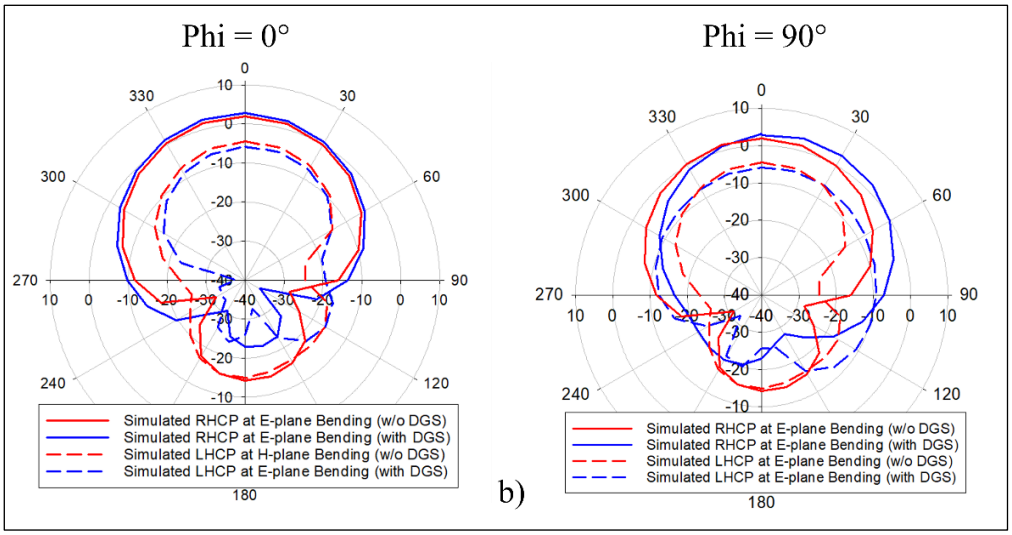

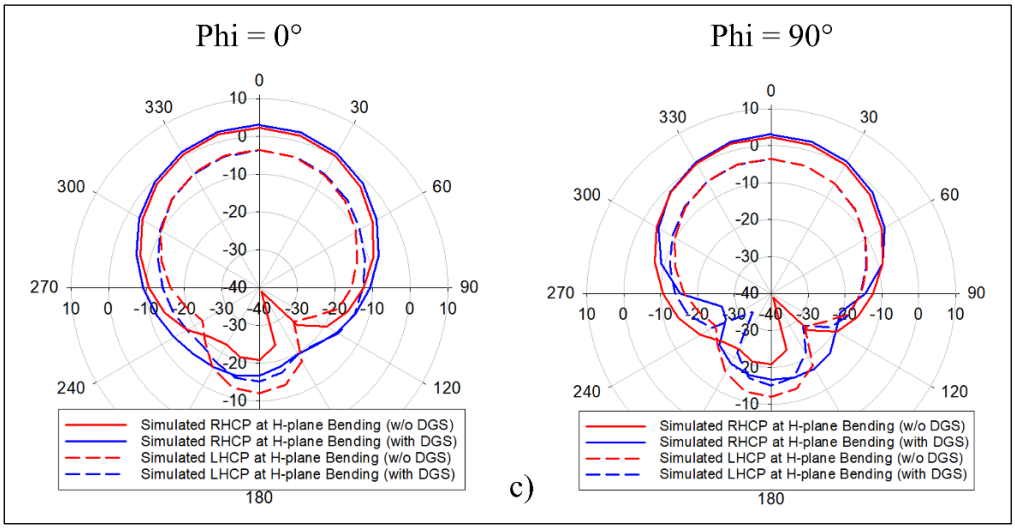

Figure 5.19 Comparison of the Simulated RHCP/LHCP Performance With and Without DGS under a) Planar b) E-plane Bending c) H-plane Bending

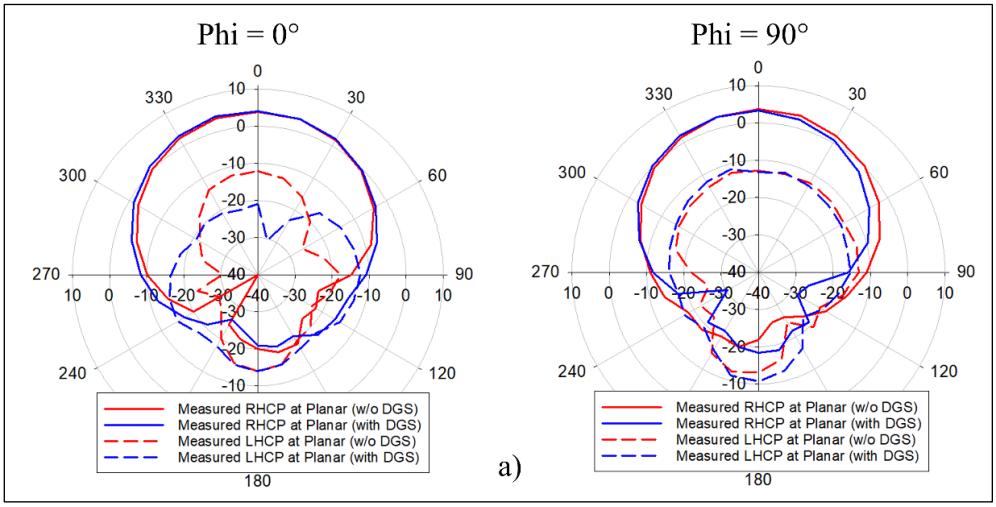

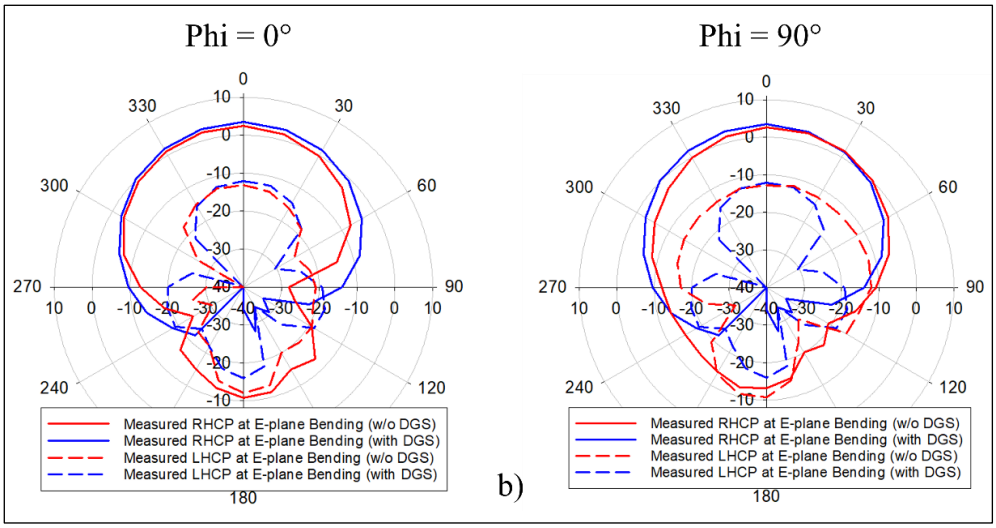

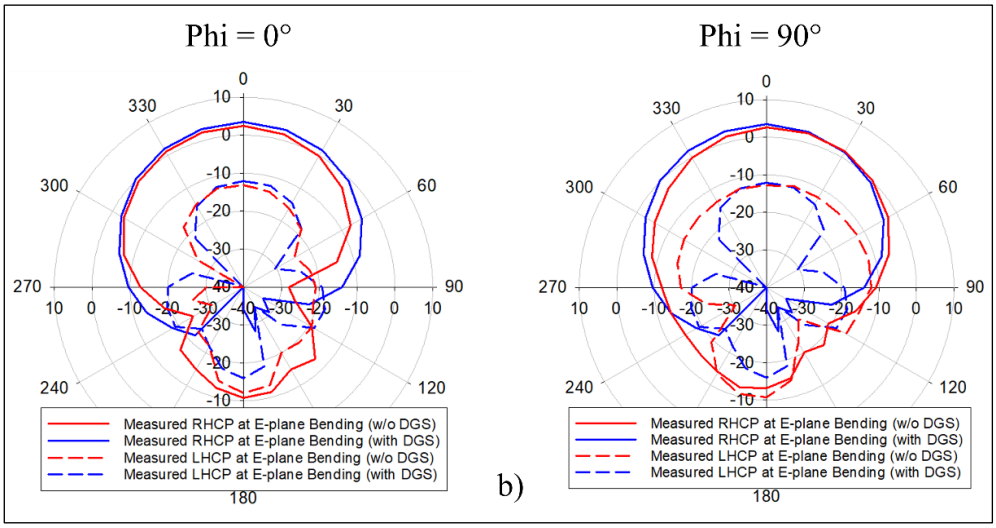

Figure 5.20 Comparison of the Measured RHCP/LHCP Performance With and With DGS under a) Planar b) E-plane Bending c) H-plane Bending

The observation in XPD results of planar antenna for simulated increases from 17.92 dB to 26.09 dB, corresponding to a 8.17 dB improvement. Similarly, the measured XPD improves from 15.90 dB to 24.88 dB, demonstrating an excellent CP discrimination of XPD > 20 dB (Li et al., 2025). This substantial increment validate that the DGS effectively suppresses the undesired LHCP component while maintaining the dominant RHCP radiation at planar condition. Meanwhile, the improvement remains evident under E-plane bending. The simulated XPD increases from 6.47 dB to 8.52 dB, while the measured XPD shows a marginal change from 15.63 dB to 15.62 dB. This minor deviation demonstrates that the DGS maintains polarization stability even under structural deformation. Importantly, all measured XPD for DGS design antenna remains above 15 dB, which is generally classified as good performance with strong polarization purity for reliable GPS-L1 circular polarization performance (Hassan & Nizam Uddin, 2025).

Table 5.5
RHCP/LHCP Gain Performance Comparison for the Antenna With and Without DGS at φ = 0° and φ = 90° under Planar and Bending Conditions

Antenna Condition	**Gain (dBi) at φ=0°**							
	Antenna without DGS				Antenna with DGS			
	Simulated		Measured		Simulated		Measured	
	RHCP	LHCP	RHCP	LHCP	RHCP	LHCP	RHCP	LHCP
Planar	3.25	-14.67	3.86	-12.04	3.74	-22.35	3.97	-20.92
Bend E-plane	2.00	-4.47	2.48	-13.15	2.77	-5.75	3.58	-12.04
Bend H-plane	2.32	-3.54	1.79	-8.18	3.01	-3.64	3.23	-14.89
Antenna Condition	**Gain (dBi) at φ =90°**							
	Antenna without DGS				Antenna with DGS			
	Simulated		Measured		Simulated		Measured	
	RHCP	LHCP	RHCP	LHCP	RHCP	LHCP	RHCP	LHCP
Planar	3.25	-14.67	3.64	-12.77	3.73	-22.35	3.40	-13.15
Bend E-plane	2.00	-4.47	2.61	-12.77	2.77	-5.78	3.58	-12.04
Bend H-plane	2.32	-3.54	2.73	-12.04	3.01	-3.64	3.23	-14.89
Antenna Condition	**Cross-Polarization Discrimination (dB) at φ=0°**			
	Antenna without DGS		Antenna with DGS	
	Simulated	Measured	Simulated	Measured
Planar	17.92	15.90	26.09	24.88
Bend E-plane	6.47	15.63	8.52	15.62
Bend H-plane	5.85	9.97	6.65	18.12

More significant improvement is observed under H-plane bending. The simulated XPD increases from 5.85 dB to 6.65 dB. However, in measurement, the XPD improves significantly from 9.97 dB to 18.12 dB, representing an 8.15 dB enhancement. This large measured improvement indicates that the DGS effectively redistributes

ground-plane surface currents under curvature by reducing phase-misaligned current loops that would otherwise contribute to cross-polarized radiation. As H-plane bending directly perturbs the current path orthogonal to the CP mode, the DGS plays a critical role in stabilizing the orthogonal mode balance required for circular polarization. From a critical perspective, the percentage improvements are more remarkable in measurement than in simulation particularly under H-plane bending. This suggests that the DGS provides additional practical stabilization effects that may not be fully captured in idealized simulation models, especially considering current redistribution under bending condition. These results strengthens the practical significance of the DGS for wearable GPS applications.

Overall, the data demonstrate that the incorporation of the DGS enhances XPD by approximately 9 dB in planar conditions and up to 8.15 dB under H-plane bending in measurement. This level of polarization discrimination is considered excellent for wearable circularly polarized textile antennas and demonstrates effective suppression of undesired LHCP components. A review of recent DGS-based antenna designs reveals in Table 5.6 that while high cross-polarization discrimination of >20 dB has been achieved in rigid microstrip configurations, no study has systematically evaluated polarization purity under mechanical bending conditions particularly for textile antenna.

Table 5.6
Previous Studies of DGS-based Antenna on Cross-Polarization Discrimination (XPD)

Authors & Year	Antenna Type	DGS Design	XPD (dB)	Bending Evaluation
Naik et al., 2023	Rigid	DGS-based circular using CMA	10 – 15	-
Kumar & Guha, 2020	Rigid	Asymmetric-arc DGS	18 - 20	-
Khandelwal et al., 2014	Rigid	Circular-shaped DGS	35	-

5.3.5 Axial Ratio (AR) Bandwidth Analysis

Figure 5.21 demonstrates the simulated 3-dB axial ratio (AR) performance under planar, E-plane bending, and H-plane bending conditions for both configurations of without DGS and with DGS. In the absence of DGS, bending significantly degrades circular polarization performance, where the AR at 1.575 GHz increases to approximately 8–10 dB under E- and H-plane deformation which exceeds the 3-dB CP

threshold. This indicates severe imbalance in the amplitude and phase of the two orthogonal modes when the antenna is mechanically distorted. In contrast, the DGS configuration exhibits improved polarization stability under both bending conditions as observed by the reduced AR values. Although the simulated AR under bending remains above 3 dB, the degradation magnitude is visibly lower in DGS configuration compared to the antenna without DGS design demonstrating the mitigation of modal imbalance in DGS.

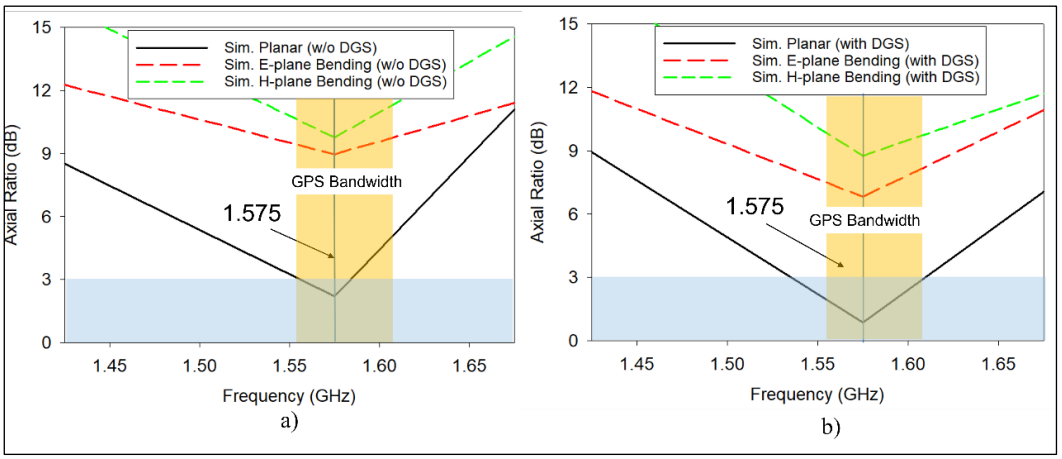

Figure 5.21 Comparison of the Simulated 3-dB Axial Ratio under Planar, E-plane Bending and H-plane Bending a) Without DGS b)With DGS

Figure 5.22 describes the measured 3-dB axial ratio (AR) performance of the antenna under planar, E-plane bending, and H-plane bending conditions for DGS and without DGS configurations. For the antenna without DGS, bending significantly affects polarization purity, particularly in the E-plane, where the AR approaches the 3-dB threshold within the GPS band. The AR bandwidth is substantially reduced under deformation proving that mechanical bending disturbs the amplitude and phase balance between the orthogonal modes responsible for circular polarization. In contrast, the antenna incorporating the DGS maintains AR values below 3 dB at 1.575 GHz under both E-plane and H-plane bending conditions. Although a reduction in AR bandwidth is still observed compared to the planar case, the DGS configuration preserves a wider effective CP bandwidth and exhibits improved stability within the highlighted GPS operating region.

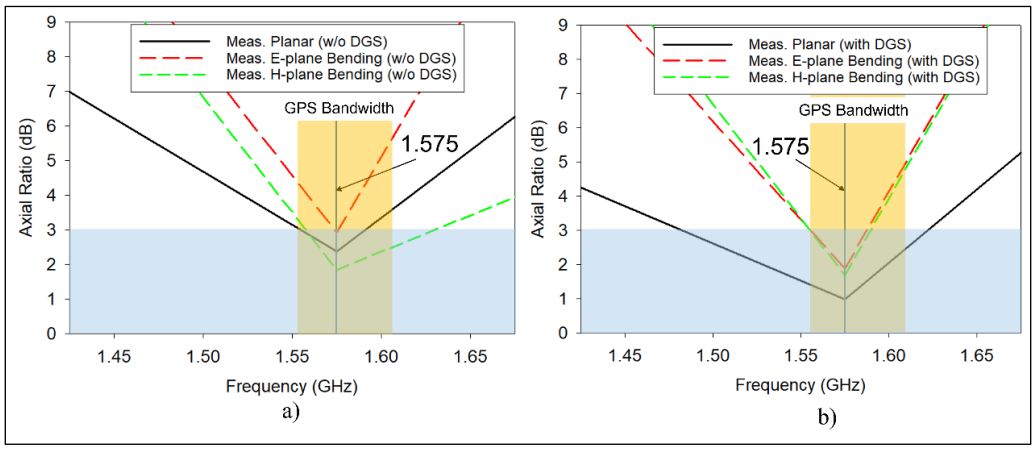

Figure 5.22 Comparison of the Measured 3-dB Axial Ratio under Planar, E-plane Bending and H-plane Bending a) Without DGS b)With DGS

Based on the quantitative data presented in Table 5.7, the incorporation of the DGS significantly demonstrate enhancement to circular polarization (CP) performance under planar conditions and improves robustness under bending. In the planar state, the measured 3-dB AR bandwidth increases to an expansion of approximately 286% while the minimum AR improves to 1.39 dB reduction. Simulation result also shows a similar trend, with bandwidth increasing by about 212%. This confirms that the DGS modifies the reactive current distribution on the ground plane while efftcively tuning the reactive loading due to the etched slots associated with orthogonal modes. This adjustment further widen the frequency region that satisfies the CP condition of AR $\leq$ 3 dB. Importantly, the DGS configuration fully covers the Malaysian GPS band regulated by MCMC (1.559–1.610 GHz) under planar conditions, ensuring polarization purity across the entire operational bandwidth.

Under bending, the antenna without DGS exhibits severe CP degradation, particularly in the E-plane, where the measured AR bandwidth reduces by approximately 83% which limits the effective GPS coverage. In contrast, the DGS maintains a 32 MHz AR bandwidth under E-plane bending, preserving AR below 3 dB at 1.575 GHz and sustaining usable CP performance within the GPS band. Although simulated AR under bending exceeds 3 dB, the measured results remain below 3 dB for both E- and H-plane cases. This difference is attributed to practical wearable effects not fully modeled in simulation, such as non-uniform curvature, textile deformation and misalignment which can slightly retune the amplitude and phase balance toward improved quadrature.

Table 5.7
Axial Ratio, AR Bandwidth and GPS Coverage Performance of the Antenna With and Without DGS under Planar and Bending Conditions

Antenna Condition	Parameter	Type of Antenna			
		Antenna without DGS		Antenna with DGS	
		Simulated	Measured	Simulated	Measured
Planar	3-dB AR (dB)	2.21	2.38	0.86	0.99
	AR Bandwidth (MHz)	24	36	75	139
	AR Freq. Range (MHz)	1.560-1.584	1.555-1.591	1.535-1.610	1.483- 1.622
	GPS Freq. Coverage (%)	47%	62.7%	100%	100%
Bend E-plane	3-dB AR (dB)	8.96	2.92	6.83	1.88
	AR Bandwidth (MHz)	Above 3-dB	6	Above 3-dB	32
	AR Freq. Range (MHz)	-	1.573-1.579	-	1.555-1.587
	GPS Freq. Coverage (%)	0	11.8%	0	54.9%
Bend H-plane	3-dB AR (dB)	9.76	1.84	8.75	1.68
	AR Bandwidth (MHz)	Above 3-dB	79	Above 3-dB	34
	AR Freq. Range (MHz)	-	1.557-1.636	-	1.555-1.589
	GPS Freq. Coverage (%)	0	100%	0	58.8%

The comparative analysis confirms that the proposed DGS does not merely broaden the planar axial-ratio bandwidth but also mitigates polarization degradation under mechanical bending. The axial-ratio-bandwidth improvement is associated with the ability of the DGS to maintain the required amplitude balance and phase quadrature between the two orthogonal modes over a wider frequency range. Without the DGS, the optimum modal relationship may occur only within a relatively narrow frequency interval. Away from this interval, either the modal amplitudes become unequal or the phase difference deviates from 90∘, causing the axial ratio to exceed 3 dB.

The DGS redistributes the ground current and modifies the electromagnetic coupling associated with both modes. This introduces an additional degree of tuning that brings the modal responses closer together and reduces the rate at which their amplitude and phase relationship deteriorates with frequency. Consequently, the 3-dB axial-ratio condition is maintained over a wider frequency range. The broadened axial-ratio bandwidth also improves bending robustness. Although bending shifts the modal frequencies and alters the field distribution, the wider circular-polarization operating range increases the probability that the GPS-L1 frequency remains within the 3-dB

axial-ratio bandwidth. Therefore, the DGS provides circular-polarization bandwidth margin against deformation-induced frequency shifting. Despite the expected increase in AR under deformation, the DGS configuration preserves meaningful GPS frequency coverage and maintains superior CP performance relative to the conventional structure which further validates its suitability for wearable GPS-L1 operation.

5.3.6 Axial Ratio 3-dB Beamwidth (ARBW) Analysis

Table 5.8 shows the comparison of ARBW ≤ 3 dB between the antenna with and without DGS under planar, E-plane bending, and H-plane bending conditions at φ = 0°, 45°, 90°, and 135°. Under the measured planar configuration, the incorporation of the DGS results in a reduction of ARBW from 150° to 135° at φ = 0° (10% reduction), from 120° to 90° at φ = 45° (25% reduction), from 135° to 75° at φ = 90° (44.4% reduction), and from 165° to 75° at φ = 135° (54.5% reduction). These reductions which represent the narrowing in the principal and diagonal planes reflects the polarization confinement due to the redistribution of the return current path in DGS. As the localized highly intensity current is reduced, a more uniform CP radiation region will be formed rather than excessive angular spreading.

Under H-plane bending, the measured ARBW decreases by 12.5% at φ = 0°, 28.6% at φ = 45°, 30% at φ = 135° and remain unchanged at 90° (0% variation). This indicates that the DGS maintains relatively stable orthogonal mode balance (less than 30% variations) under H-plane curvature as bending along this plane minimally disturbs the effective electrical lengths of the two CP modes. In contrast, under E-plane bending, the ARBW exhibits plane-dependent variation with the incorporation of the DGS. At φ = 45°, the ARBW decreases by 36.4% and 40% reduction at φ = 135° . However, a different trend is observed at φ = 90°, where the ARBW increases by a 20% indicating an improvement with the DGS. The stronger sensitivity under E-plane curvature arises because this bending direction directly alters the perturbation slot geometry and the effective length (Zaidi et al., 2022). Since circular polarization is achieved through near-degenerate orthogonal modes with precise phase quadrature, even slight geometrical distortion degrades the AR. Consequently, the angular region satisfying the 3-dB AR criterion becomes narrower in certain azimuthal planes leading to reduced AR beamwidth.

Table 5.8
3-dB Axial Ratio Beamwidth (ARBW) Performance of the Antenna With and Without DGS under Planar and Bending Conditions

Antenna Condition	Phi Angle (°)	Antenna Without DGS		Antenna With DGS	
		Simulated(°)	Measured(°)	Simulated(°)	Measured(°)
Planar	0	180	150	150	135
	45	90	120	105	90
	90	120	135	90	75
	135	45	165	90	75
Bend E-plane	0	Above 3-dB	150	Above 3-dB	150
	45		165		105
	90		75		90
	135		150		90
Bend H-plane	0	Above 3-dB	120	Above 3-dB	105
	45		105		75
	90		90		90
	135		150		105

From an electromagnetic perspective, the DGS modifies the ground plane's equivalent inductive–capacitive characteristics, which can be expressed conceptually through the quality factor relationship from Equation (5.3) and Equation (5.4) where reduced reactive energy storage (X) leads to broader impedance bandwidth but also tighter polarization confinement. Thus, the observed ARBW reduction (10–55% in planar case and 12–36% in bending cases) reflects refined polarization control due to the supression of undesired orthogonal polarization while stabilizing the amplitude and phase relationship between the CP generating modes. Importantly, despite the ARBW reduction, the antenna still maintains the AR less than 3-dB and more than 100° coverage at $\varphi = 0°$ under planar condition which is acceptable for hemispherical GPS-L1 reception.

It is noteworthy that under both E-plane and H-plane bending configurations, the simulation results indicate the AR remains above 3 dB across all angular cuts, suggesting the absence of a valid CP region. However, the measured results demonstrate the presence of finite AR beamwidth values under the same bending conditions. This apparent discrepancy can be explained by considering the differences between idealized simulation modeling and practical textile deformation behavior. In CST simulation, bending is modeled as a perfectly uniform cylindrical curvature applied to a homogeneous material with constant permittivity and conductivity. Under such ideal conditions, the structural symmetry of the antenna is uniformly distorted leading to a significant imbalance between the orthogonal CP modes. Since CP requires both

amplitude equality and precise 90° phase quadrature, even slight difference for both in simulation due to bending can cause the AR to exceed the 3 dB threshold entirely.

In contrast, during practical measurement, the textile substrate does not undergo perfectly uniform curvature. Localized compression and stretching occur non-uniformly across the patch and ground plane. These micro-scale mechanical variations can partially compensate for modal imbalance by introducing slight asymmetrical current redistribution that restores near-quadrature phase in certain angular directions. As a result, localized angular regions satisfying AR ≤ 3 dB may still exist in measurement, even though the ideal simulation predicts complete CP collapse. Overall, the measured presence of AR beamwidth under bending does not contradict the simulation trend; instead, it highlights the sensitivity of CP performance to realistic textile deformation effects. Importantly, the general trend of AR degradation under bending remains consistent between simulation and measurement, validating the physical interpretation.

Figures 5.23, 5.24 and 5.25 show the measured 3-dB ARBW at Phi=0° and Phi=90° with and without DGS under planar, E-plane and H-plane bending respectively. These plots illustrate clearly the angular spread of circular polarization stability over the elevation angle (θ), corresponding to the upper hemisphere coverage relevant for satellite sky visibility. Under planar condition as shown in Figure 5.23, the antenna exhibits a wider 3-dB ARBW for the antenna without DGS as compared to the antenna with DGS for both Phi=0° and Phi=90. This shows that the DGS does not significantly expand the AR beamwidth although it effectively improved the AR and impedance bandwidth. A slight asymmetry region spans is observed between the negative and positive θ with the AR minimum occurs near the broadside for the antenna with and without DGS. Although minor angular asymmetry is observed, the 3-dB AR beamwidth remains sufficiently wide for GPS sky coverage.

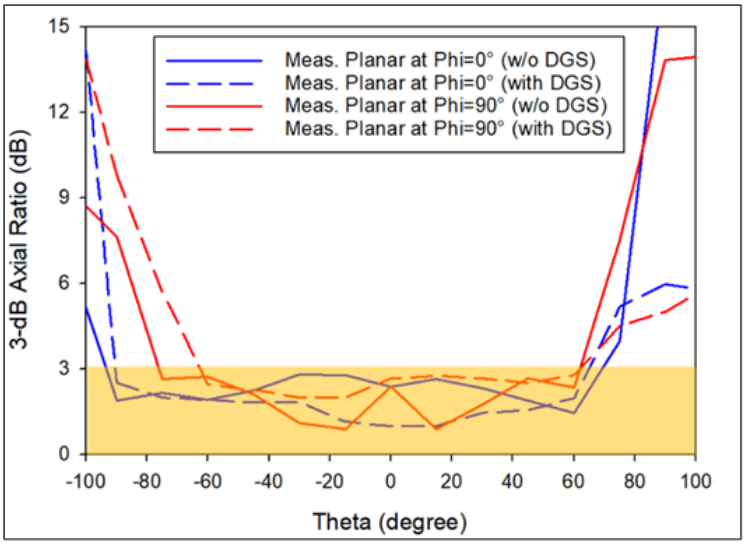

Figure 5.23 Measured 3-dB ARBW under Planar at Phi=0° and Phi=90° With and Without DGS

Under E-plane bending shown in Figure 5.24, the AR beamwidth reduces compared to the planar condition due to the effective electrical length changes causing the frequency shiftts and phase quadrature deviation. Nevertheless, the incorporation of DGS for Phi=0° and Phi=90 slightly enhanced beamwidth symmetry by producing a more uniform AR distribution over the elevation angle via the redistribution of ground return current.

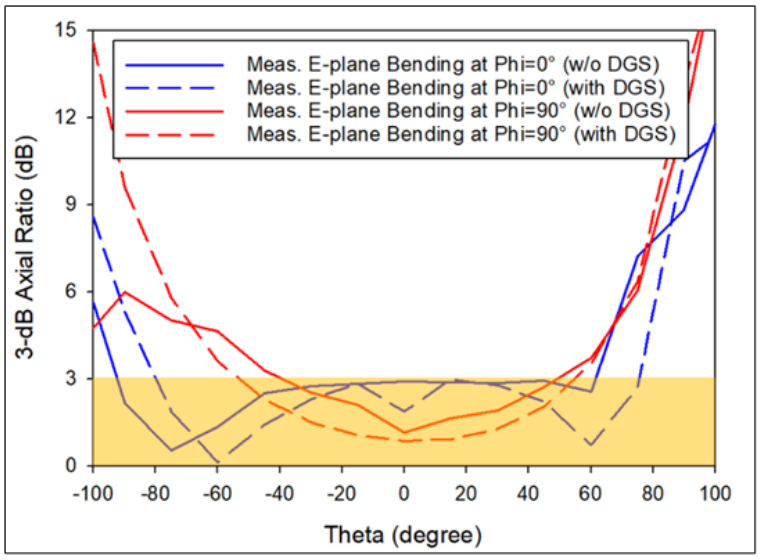

Figure 5.24 Measured 3-dB ARBW under E-plane Bending at Phi=0° and Phi=90° With and Without DGS

In comparison to E-plane bending, H-plane bending produces more significant AR beamwidth reduction and slight angular imbalance for both Phi=0° and Phi=90 as shown in Figure 5.25. This indicates that H-plane deformation introduces greater

disruption to the orthogonal modal current distribution and radiation symmetry leading to the integrated phase deviation and amplitude imbalance that reduce angular circular polarization stability. While the DGS lowers the effective *Q*-factor and mitigates phase sensitivity near resonance, it cannot fully counteract the differential resonance shift between the two orthogonal currents and angular radiation imbalance introduced by mechanical curvature. In particular, H-plane bending interacts more strongly with the dominant slot-oriented current compared to E-plane bending leading to greater AR beamwidth degradation.

Figure 5.26 provides a comprehensive comparison of the measured 3-dB AR beamwidth under planar, E-plane, and H-plane conditions. The planar configuration exhibits the widest angular CP coverage, while E-plane bending introduces moderate beamwidth reduction. In contrast, H-plane bending produces the most significant ARBW degradation across both Phi=0° and Phi=90°. From a GPS perspective, maintaining a wide AR beamwidth is essential for reliable satellite reception across varying elevation angles. The results indicate that while the antenna maintains acceptable CP near broadside under bending, H-plane deformation represents the more critical scenario for sky coverage preservation in wearable applications.

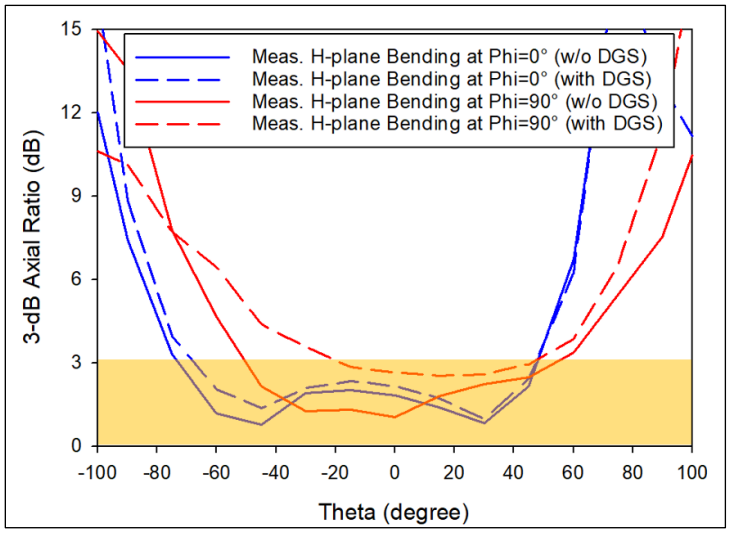

Figure 5.25 Measured 3-dB ARBW under H-plane Bending at Phi=0° and Phi=90° With and Without DGS

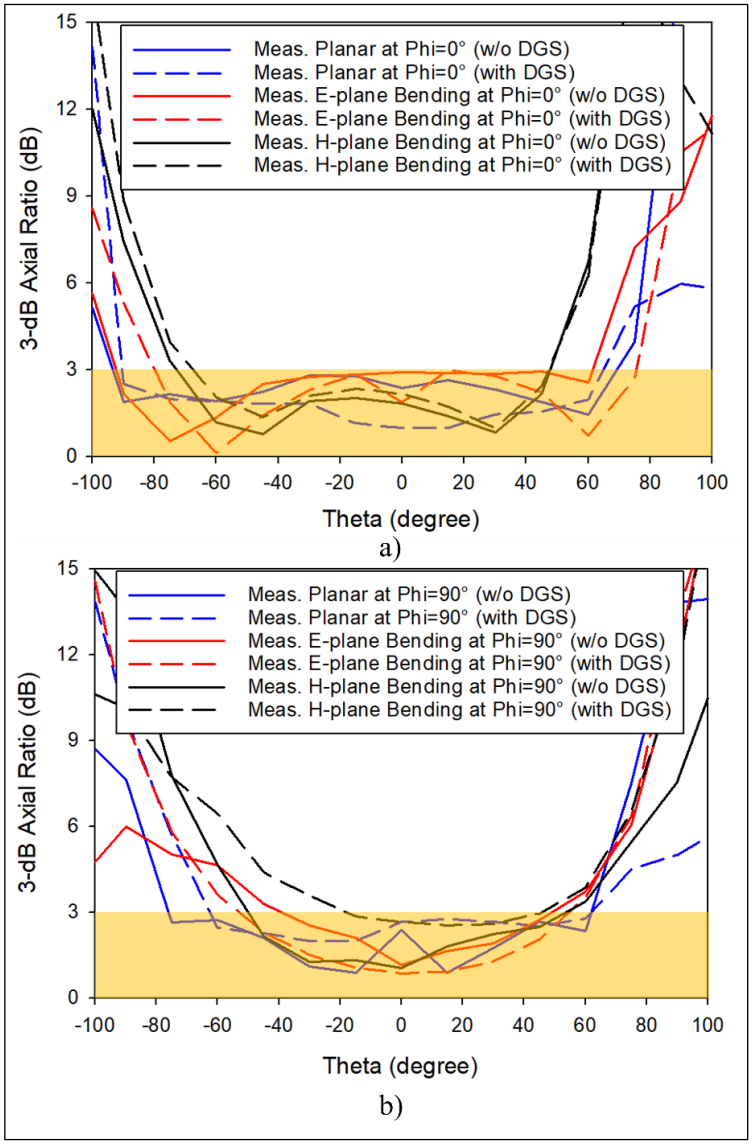

Figure 5.26 Comparison of the Measured 3-dB Axial Ratio Beamwidth under Planar, E-plane and H-plane Bending With and Without DGS at a) Phi=0° and b) Phi=90°

5.3.7 Overall Effect of DGS under Bending and Simulation-Measurement Discrepancies

The overall results shown in Sections 5.3.1 to 5.36 demonstrated that the DGS improved the electromagnetic robustness of the proposed antenna under both E-plane and H-plane bending. Mechanical bending modifies the effective current-path length, local substrate thickness, field distribution, and coupling between the orthogonal modes responsible for circular polarization. Without the DGS, these changes caused greater variation in impedance matching, axial-ratio performance, and radiation characteristics. The introduction of the DGS redistributed the ground-plane current and provided

additional control of the antenna reactance and modal coupling, thereby reducing the sensitivity of the antenna to deformation.

Under bending, the DGS produced substantial improvements in impedance bandwidth. The measured bandwidth increased from 140 MHz to 160 MHz under E-plane bending and to 195 MHz under H-plane bending. This indicates that the DGS compensated for part of the impedance variation introduced by the change in antenna curvature. The slot configuration altered the effective inductive and capacitive behaviour of the ground plane, allowing the input impedance to remain better matched over a wider frequency range despite the geometrical deformation.

The circular polarization performance was also more stable after the DGS was introduced. Bending can disturb the amplitude equality and approximately 90° phase difference between the two orthogonal modes, resulting in an increased axial ratio or a shift in the axial-ratio operating band. The DGS reduced this sensitivity by modifying the ground-current distribution and strengthening the coupling conditions required for circular polarization. Consequently, the antenna maintained a lower axial ratio and a wider axial-ratio bandwidth around the GPS-L1 frequency under the investigated bending conditions. This demonstrates that the DGS improved not only impedance robustness but also the frequency-domain stability of circular polarization during deformation.

The RHCP gain was similarly improved under bending, with the most significant enhancement of up to approximately 80% observed under H-plane bending. This improvement indicates that the DGS assisted in preserving the desired RHCP radiation component when the antenna geometry was deformed. At the same time, the undesired LHCP component was suppressed, resulting in improved polarization discrimination. The gain enhancement under bending can therefore be attributed not merely to an increase in total radiation, but to the redistribution of the radiated power towards the desired RHCP component.

The axial-ratio beamwidth results further demonstrate that the wide angular circular-polarization coverage was largely retained under bending. Most of the evaluated principal-plane axial-ratio beamwidths remained at or above 120°, although a minimum beamwidth of approximately 105° was observed in one plane. The reduction in that particular plane may be associated with the asymmetrical current redistribution caused by the bending direction. Nevertheless, the antenna continued to provide wide angular CP coverage under deformation. Therefore, the principal benefit of the DGS

was not necessarily an increase in every axial-ratio beamwidth value, but the preservation of wide beamwidth while simultaneously improving the axial-ratio level, axial-ratio bandwidth, RHCP gain, and bending robustness. This result indicates that the DGS mitigated the trade-off between frequency-domain CP enhancement and angular CP coverage.

Differences were observed between the simulated and measured results under both E-plane and H-plane bending, particularly in the resonant-frequency positions, bandwidth boundaries, axial-ratio minima, gain levels, and axial-ratio beamwidths. These discrepancies may be attributed to variations in the actual bending radius, uneven curvature, local textile compression, wrinkles, and changes in substrate thickness during measurement. In contrast, the simulation model assumed a uniform and precisely defined bending geometry. Variations in textile dielectric properties, conductive-fabric surface roughness and finite conductivity, adhesive-layer non-uniformity, fabrication tolerances, connector losses, and cable movement may also have contributed to the measured deviations.

The axial-ratio and axial-ratio-beamwidth discrepancies are particularly sensitive to these uncertainties because circular polarization depends on a precise amplitude and phase relationship between the two orthogonal modes. Small changes in curvature, slot dimensions, or material properties can therefore alter both the frequency range and angular range over which the axial ratio remains below 3 dB. Similarly, differences in measured RHCP gain may arise from conductor and connector losses, bending-fixture interactions, and angular misalignment during radiation-pattern measurements. Despite these discrepancies, the simulation and measurement results show consistent overall trends, confirming that the DGS improved impedance bandwidth, circular-polarization stability, RHCP gain, and deformation robustness while maintaining wide axial-ratio beamwidth under bending.

5.4 Specific Absorption Rate (SAR) in Wearable Antenna

Wearable antennas operate close to the human body, where electromagnetic interaction between the antenna and biological tissue may affect both antenna performance and user exposure. The human body is a lossy dielectric medium; therefore, part of the electromagnetic energy directed towards the body may be absorbed and converted into heat. Specific absorption rate (SAR), is commonly used to quantify

the rate at which radio-frequency electromagnetic energy is absorbed per unit mass of biological tissue. SAR is expressed in watts per kilogram and can be defined as:

$$SAR = \frac{\sigma |E|^2}{\rho} \tag{5.3}$$

where σ is the electrical conductivity of the tissue in S/m, E is electric-field magnitude within the tissue in V/m, and ρ is the tissue mass density in kg/m^3.

Based on the obtained results, a higher antenna gain does not necessarily correspond to a higher specific absorption rate (SAR), since antenna gain is a far-field parameter that describes the ability of an antenna to radiate power in a specified direction. In contrast, SAR is primarily governed by the near-field electric-field distribution induced within biological tissue. An antenna may therefore exhibit increased forward gain while producing a lower SAR when a greater proportion of the accepted power is directed away from the human body. Conversely, an antenna with relatively low gain may still produce a high localized SAR if strong near-field coupling or electric-field concentration occurs within the adjacent tissue. This relationship has been demonstrated in previous wearable-antenna studies. For example, Saha et al. (2021) introduced an artificial magnetic conductor (AMC) behind a wearable antenna to suppress radiation towards the human body. The resulting design achieved a gain of 7.47 dB while reducing SAR by approximately 90% compared with the antenna without the AMC structure. These findings demonstrate that gain enhancement and SAR reduction may occur simultaneously when the antenna backing structure redirects electromagnetic radiation away from the body.

For the proposed antenna, the measured high FBR indicates effective suppression of backward radiation in the far-field region. The increase in RHCP gain under bending should therefore be interpreted as an improvement in the desired forward circularly polarized radiation rather than an indication of increased electromagnetic-energy absorption by the wearer. In particular, the improvement in RHCP gain, together with the suppression of the undesired LHCP component, indicates that a greater proportion of the accepted power contributes to the required polarization and radiation direction. The DGS also modifies the ground-plane current distribution and may influence the amount of electromagnetic energy radiated towards the rear region. However, unlike a continuous AMC or EBG backing structure, the DGS contains

apertures within the ground plane. Consequently, its influence on near-field penetration towards the body cannot be evaluated solely from the measured gain and front-to-back ratio.

It should also be recognised that the proposed GPS-L1 antenna is intended primarily for passive signal reception. Therefore, the associated human-exposure consideration is substantially lower than that of an actively transmitting wearable antenna. Nevertheless, SAR evaluation would remain relevant if the proposed antenna were subsequently integrated with an active transmitter or a bidirectional wearable communication system. As direct SAR simulation and measurement were beyond the scope of the present investigation, the high FBR and improved forward RHCP gain are considered qualitative indicators of greater proportion of the energy directed away from the body. Further quantitative evaluation may be undertaken using a multilayer human-body model, a clearly specified input power, realistic antenna-to-body separation, and both planar and bent antenna configurations.

5.5 Checklist for GPS Application and Comparison with Existing Works

Table 5.9 consolidates the measured GPS-L1 validation results under planar and bending conditions. It is observed that impedance matching and S_{11} bandwidth requirements are consistently satisfied for all configurations, indicating stable resonance within the GPS band. The introduction of the DGS significantly enhances planar circular polarization performance, achieving full compliance (*/*) in AR bandwidth while maintaining strong RHCP dominance (≥10 dB) and wide AR beamwidth (>120°).

The '*average*' status for the DGS antenna design under bending shows that the 3-dB AR band still covers more than half of GPS reference bandwidth including 1.575 GHz. Under the E-plane bending antenna without DGS, a minimal coverage of less than 50% demonstrates a reduction in the 3-dB AR which minimize the tolerance to detuning. Both scenarios demonstrate that the CP is preserved at the operating frequency but with a reduced polarization bandwidth tolerance. Technically, this scenario only affects the robustness and not the functionality of GPS operation.

Table 5.9
Summary of the Measured GPS Performance Validation for Antenna With DGS and Without DGS

Parameter	Requirement	With DGS			Without DGS		
		Planar	E-plane Bending	H-plane Bending	Planar	E-plane Bending	H-plane Bending
		Meet Requirement?					
S_{11} Freq. Detuning	Within GPS Bandwidth Coverage (1.551 to 1.610 MHz)	Yes	Yes	Yes	Yes	Yes	Yes
S_{11} Bandwidth		Yes	Yes	Yes	Yes	Yes	Yes
AR Bandwidth		Yes	Average (>50%)	Average (>50%)	Yes	Minimal (<50%)	Yes
RHCP Dominance	≥ 10 dB	Yes	Yes	Yes	Yes	Yes	No
AR Beamwidth	≥ 120° at boresight	Yes	Yes	No	Yes	Yes	Yes
GPS Operational Status		/	/	/	/	/	X

**Status Indicator (/ = Full compliance, X=Non-compliance)*

In contrast, a non-compliant condition (X) observed for the antenna without DGS under H-plane bending resulted from the insufficient RHCP dominance (<10 dB). Due to this, the LHCP component may becomes significant which results in degraded polarization discrimination. Although the antenna does not switch to LHCP, the increased ellipticity reduces effective RHCP coupling to the satellite signal and increases polarization mismatch loss. Nevertheless, in reflective wearable environments, multipath propagation can introduce polarization reversal whereby reflected RHCP signals are converted into LHCP components. Therefore, strong RHCP dominance is a fundamental requirement for reliable GPS reception to preserve polarization selectivity to minimizes polarization mismatch loss, and enhances resistance to multipath interference.

Table 5.10 presents a comparative evaluation of recent circularly polarized textile antennas with respect to operating band, polarization behavior, structural complexity, and bending robustness. From Table 5.10, it is evident that early textile CP designs such as Rizwan et al. (2015) relied primarily on slot perturbation with partial ground modification. Although the structure was single-layer and simple, axial-ratio degradation and gain reduction were observed under yz-plane bending, indicating insufficient modal stability during deformation. Yadav et al. (2019) incorporated DGS into a CP textile antenna and achieved wide axial-ratio bandwidth. However, bending validation was not conducted, and the antenna was not designed for GPS-L1 operation.

As shown in Table 5.10, the absence of mechanical evaluation limits the design's suitability for wearable satellite applications. Joshi et al. (2020) validated GPS circular polarization under bending using an AMC-backed textile antenna, although the multilayer reflector increased structural complexity compared with a single-layer design.

Table 5.10
Comparative Evaluation of Circularly Polarized Textile Antenna with Respect to Bending Validation

Parameter	**Authors & Year**				
	Rizwan et al. (2015)	Yadav et al. (2019)	Joshi et al. (2020)	Zaidi et al. (2022)	**This work*
Antenna Type	Textile (denim + copper tape)	Textile (jeans + copper tape)	Fully textile (Felt, Kevlar, Shieldit Super)	Fully Textile (polyester + electro-textile)	Fully Textile (felt+ Shieldit Super)
Operating Band	2.4 GHz ISM/ WBAN	WLAN/ C-band	GPS-L1 / 2.45 GHz	GPS-L1	GPS-L1
Polarization	CP	CP	CP (dual sense)	LP	CP
Antenna Techniques	Diagonal slotted + partial/slotted ground	U-shaped patch + ground DGS	Truncated-corner CP patch + AMC reflector	U-shaped patch + ground DGS	Dual L-shaped slotted + DGS-integrated
Gain (dB)	2.25	5.19	1.98/1.94	1.45	3.98
Impedance Bandwidth (MHz)	160	4200	440/185	226	125
AR Bandwidth (MHz)	60	700 & 600	141.75	NR	139
3-dB AR	≤3 dB	≤ 3 dB	≤ 3 dB	NR	0.99
AR Beamwidth (°)	218	NR	NR	NR	135
XPD (dB)	NR	NR	NR	NR	24
Bending Evaluation	Yes (*xz* & *yz* planes , meas.)	No	Yes (*x*- and *y*-axis, sim.)	Yes (E- & H-plane, meas.)	Yes (E- & H-plane, meas.)
Performance Under Bending	AR degrades in *yz*-bending to LP , gain & efficiency reduced	NR	Reduced bandwidth to 72% (upper arm)	Higher back radiation, gain & directivity reduced	Preserved CP metrics and GPS operation
Structural Complexity	Single layer	Single layer	Multilayer	Single layer	Single layer

*NR – Not Reported

Zaidi et al. (2022) investigated a fully textile antenna with DGS for GPS-L1 and performed bending analysis. The DGS effectively improved impedance bandwidth and reduced frequency detuning. Nevertheless, the antenna was linearly polarized, and polarization robustness under bending was not addressed. In contrast, as summarized in Table 5.10, the proposed work uniquely integrates:

- Circular polarization (RHCP)
- GPS-L1 operation
- Fragmented symmetric DGS for distributed ground current control
- Single-layer fully textile structure
- Systematic E-plane and H-plane bending validation

Most importantly, the proposed antenna preserves axial-ratio bandwidth (139 MHz), maintains AR beamwidth (135°), and achieves 24 dB XPD while exhibiting stable performance under bending.

5.6 Summary

Chapter 5 presents the development and validation of the proposed wearable textile antenna incorporating a Defected Ground Structure (DGS) for enhanced circular polarization and GPS-L1 performance. The chapter begins with the systematic evolution of the DGS design, where key geometrical parameters are optimized to improve impedance matching, axial-ratio bandwidth, and polarization purity. Surface current distribution analysis reveals that the DGS disrupts continuous ground return paths, redistributes current flow, and reduces localized reactive energy concentration. This lowers the effective *Q*-factor and moderates phase sensitivity near resonance, thereby stabilizing the orthogonal CP generating current components required to maintain phase quadrature and amplitude balance. The effects of mechanical deformation are then comprehensively investigated under E-plane and H-plane bending conditions. Both simulated and measured results are presented for S_{11}, gain, radiation pattern, RHCP/LHCP characteristics, AR bandwidth, and ARBW. The results confirm that the planar configuration achieves the widest AR beamwidth due to preserved orthogonal current balance and radiation symmetry. The findings also reveal that bending introduces amplitude imbalance and phase deviation, particularly under H-

plane curvature leading to a narrower effective polarization coverage. Nevertheless, the antenna maintains acceptable impedance bandwidth, RHCP dominance, and CP stability within the operational region. Finally, GPS performance validation confirms that the proposed DGS-based design satisfies key operational requirements, including frequency coverage within the GPS-L1 band (1.551–1.610 GHz), adequate AR bandwidth, strong RHCP dominance (≥10 dB), and sufficient hemispherical coverage for satellite reception. Although slight reductions in ARBW are observed under bending, the antenna remains operationally viable for wearable GPS applications. Overall, the chapter demonstrates that the DGS effectively enhances polarization robustness and performance stability without compromising practical usability at wearable application.

CHAPTER 6
CONCLUSION

6.1 Conclusion

This research established a systematic framework for the development of a fully textile circularly polarized wearable antenna for GPS-L1 applications. The study progressed from the analytical evaluation of textile substrate performance, through the realization of circular polarization using corner truncation and mirrored dual L-shaped slots, to the modification of ground-plane electromagnetic behaviour using an integrated Defected Ground Structure (DGS). The overall aim was to achieve wide angular circular-polarization coverage, adequate impedance and axial-ratio bandwidths across the GPS-L1 band, acceptable radiation performance and stable operation under mechanical deformation.

The characterization-driven approach was important because textile materials cannot be assumed to behave like conventional rigid and homogeneous substrates. Textile substrates are porous, compressible and structurally non-uniform, while conductive textiles exhibit finite conductivity, surface roughness and fabrication-dependent electrical behaviour. These characteristics can directly influence resonance, impedance matching, attenuation, radiation efficiency and simulation–measurement agreement. Accordingly, denim, felt and Tencel were evaluated using a transmission-line-based analytical model at 1.575 GHz. The effects of substrate thickness from 0.5 mm to 4.0 mm and conductor conductivity were systematically investigated in terms of reflection coefficient, transmission loss and conductivity-related behaviour. The results identified 3 mm felt as providing the most optimized electromagnetic performance among the investigated textile substrates at the GPS-L1 frequency. By selecting the substrate through systematic electromagnetic evaluation rather than relying solely on nominal material properties, the antenna was developed using a more representative model of the fabricated textile structure. This contributed to the overall agreement observed between simulation and measurement. The broader significance of this characterization stage is that material evaluation should form an integral part of wearable textile antenna development. In textile structures, uncertainty in substrate thickness, dielectric behaviour and conductive performance can propagate into later

stages of the design and produce resonant-frequency shifts, impedance mismatch, gain reduction and circular-polarization degradation. Therefore, the characterization-driven approach used in this research reduces design uncertainty and strengthens the reliability of the antenna development process.

Following the material evaluation, circular polarization was realized through the coordinated integration of corner truncation and mirrored dual L-shaped slots. The purpose of these perturbations was to excite two near-degenerate orthogonal resonant modes with approximately equal amplitudes and an approximately 90° phase difference. Parametric investigations of slot length, slot width and perturbation position were conducted to identify the configuration that minimized axial ratio while maintaining acceptable impedance matching. The optimized non-DGS antenna achieved an axial-ratio bandwidth of approximately 36 MHz and a minimum axial ratio of 2.38 dB. It also produced a front-to-back ratio of approximately 16.9 dB and a gain of approximately 3.96 dBi. Wide axial-ratio beamwidths were achieved across the principal and diagonal observation planes, namely approximately 150° at Phi=0°, 135° at Phi=90°, 120° at Phi=45° and 165° at Phi=135°. The significance of the dual L-shaped slot configuration is therefore not limited to the generation of circular polarization at broadside. Its more important contribution is the achievement of wide angular circular polarization coverage. This is particularly relevant to wearable GPS reception because the relative orientation between the antenna and the satellites is continuously affected by human movement, clothing position and body curvature. A broadside axial ratio alone would not sufficiently describe the practical coverage capability of the antenna. The wide axial-ratio beamwidth achieved in this study demonstrates that a single-feed, single-layer and fully textile antenna can maintain circular polarization over a broad angular region while preserving a structurally simple configuration. Although the corner-truncated dual L-shaped slotted antenna achieved satisfactory circular-polarization performance, further improvement was required in impedance bandwidth, axial-ratio bandwidth and polarization purity, particularly to provide a greater operating margin under deformation.

An integrated DGS was therefore introduced on the ground plane outside the patch footprint. The DGS geometry was systematically developed to redistribute the ground return current, reduce strong localized current concentration and modify the reactive field behaviour of the antenna. The incorporation of the DGS increased the measured impedance bandwidth from 105 MHz to 140 MHz, representing an

improvement of approximately 33%. The axial-ratio bandwidth increased by approximately 286%, while the minimum axial ratio improved from 2.38 dB to 0.99 dB. Cross-polarization discrimination increased to 24.88 dB, indicating improved polarization purity. These improvements demonstrate that the DGS did not function merely as an impedance-matching feature. The more significant role was to modify the ground-current paths and stabilize the electromagnetic interaction between the two orthogonal circular-polarization modes. Here, the contribution of the DGS lies in its ability to complement the primary circular-polarization mechanism created by the patch perturbations while enhancing frequency-domain polarization stability.

Nevertheless, the findings also reveal that improvement in axial-ratio bandwidth does not directly produce a corresponding improvement in axial-ratio beamwidth in every observation plane. The DGS broadened the frequency range over which circular polarization was maintained and improved polarization discrimination, but the modified ground-current distribution also affected the angular composition of the radiated fields. This demonstrates a trade-off between frequency-domain circular-polarization stability and angular circular-polarization coverage. Therefore, the DGS contribution should be interpreted as improving the robustness and operational margin of the antenna, while recognising that axial-ratio beamwidth remains dependent on the integrated patch and ground current distributions.

Mechanical deformation analysis was subsequently performed under E-plane and H-plane bending conditions using a bending radius representative of upper-arm curvature. The antenna maintained acceptable impedance and circular-polarization performance under both bending orientations. Although moderate resonant-frequency detuning and axial-ratio variation were observed, the proposed antenna maintained an axial ratio of 3 dB or below within the required GPS-L1 operating region. Under bending, the axial-ratio beamwidth varied from approximately 75° to 150° across the investigated principal and diagonal planes, demonstrating that useful angular circular-polarization coverage was retained under body-representative curvature. The bending investigation also demonstrated that the two bending orientations produced different electromagnetic effects. E-plane bending predominantly changed the effective electrical length and altered the field distribution across the antenna. H-plane bending produced a stronger disturbance to the relative phase of the orthogonal modes because of its relationship with the slot orientation and surface-current paths. Despite these changes, the DGS configuration exhibited reduced sensitivity to deformation compared with the

corresponding non-DGS antenna, supporting the conclusion that distributed ground-current control contributes to polarization stability under mechanical stress.

However, the reduction in axial-ratio beamwidth observed in certain bent conditions demonstrates an inherent trade-off between flexibility and electromagnetic structural stability. The mechanical flexibility of textile materials enables the antenna to conform to the body, but deformation also changes the antenna geometry, current path and orthogonal modal relationship. Therefore, flexibility cannot be considered independently from polarization stability. In practical wearable design, sufficient conformability must be achieved without excessively disturbing the electromagnetic structure required for circular polarization.

A further trade-off concerns bandwidth and planar compactness. The proposed antenna is compact in terms of its low-profile, single-layer and structurally simple implementation. However, its planar dimensions remain comparable to those of a conventional half-wavelength patch, and the antenna was not aggressively miniaturized. Greater footprint reduction could improve physical compactness, but it would likely increase stored reactive energy and quality factor, which may reduce impedance bandwidth, axial-ratio bandwidth, radiation efficiency and angular circular-polarization coverage. The adopted antenna dimensions therefore represent a deliberate balance between wearable integration, bandwidth, radiation performance and circular-polarization stability rather than a design focused solely on minimum physical size.

The use of a 3 mm textile substrate also reflects a related design compromise. Increasing substrate thickness can improve impedance bandwidth by enhancing fringing fields, but excessive thickness may promote surface-wave excitation, unwanted radiation, impedance instability and radiation-pattern distortion. The selected thickness therefore provided a balance between bandwidth enhancement, low-profile construction, textile flexibility and stable circular-polarization performance.

All investigated antenna configurations were fabricated using fully textile materials and experimentally validated. Good agreement was obtained between simulation and measurement in terms of resonant frequency, impedance bandwidth, axial-ratio bandwidth, gain and radiation characteristics. The remaining discrepancies were attributed to fabrication tolerance, textile anisotropy, non-uniform material thickness, compression, conductive-textile variability and connector effects. The overall agreement confirms that the characterization and antenna development framework was sufficiently representative of the practical fabricated structure.

The experimental validation was nevertheless conducted under controlled laboratory conditions. Although planar and controlled bending measurements provided evidence of mechanical robustness, they did not reproduce every condition encountered in real wearable operation. Body proximity, repeated movement, moisture, perspiration, washing, compression, environmental exposure and long-term material ageing may further affect dielectric properties, conductivity, impedance response and polarization stability. This represents a trade-off between controlled laboratory repeatability and complete real-world wearable representation.

Overall, this research demonstrates that high-performance wearable GPS antenna development depends on the coordinated control of three interrelated domains: textile material behaviour, orthogonal-mode excitation and ground-current distribution. The material characterization stage established a reliable textile platform; the corner truncation and mirrored dual L-shaped slots generated the required circular-polarization modes; and the integrated DGS improved frequency-domain circular-polarization stability through ground-current redistribution. The resulting antenna achieved wide axial-ratio beamwidth, enhanced axial-ratio bandwidth, improved polarization discrimination and acceptable performance under bending within a fully textile, single-feed and single-layer configuration.

The broader implication is that future wearable GPS antenna development should not focus only on achieving resonance and circular polarization under planar conditions. Reliable wearable operation requires adequate frequency bandwidth, wide angular circular-polarization coverage, deformation tolerance and representative material modelling. The framework developed in this study can therefore support future investigations of textile antennas for satellite navigation, body-centric communication and other wearable systems requiring polarization stability under variable orientation and mechanical deformation. Future work should extend the validation to on-body and outdoor satellite-reception measurements and examine the influence of body loading, repeated bending, moisture, washing and long-term material degradation. Further optimization may also investigate DGS configurations that preserve the improved axial-ratio bandwidth while minimizing reductions in axial-ratio beamwidth. The use of textile conductors with higher conductivity and improved mechanical durability may enhance efficiency and fabrication repeatability. Such investigations would support the transition of the proposed antenna from controlled laboratory validation towards more reliable real-world wearable deployment.

6.2 Research Contributions

This research contributes an integrated electromagnetic framework for the development of a fully textile circularly polarized antenna for GPS-L1 applications. The originality of the work does not arise from the individual application of corner truncation, L-shaped slots, or a defected ground structure, as these techniques have been reported previously. Rather, the contribution lies in the systematic integration of textile material characterization, circular-polarization mode control, defected-ground engineering, and bending-performance evaluation. Through this integrated approach, the study addresses the simultaneous requirements of reliable material modelling, wide angular circular-polarization coverage, enhanced bandwidth, and robustness under wearable deformation presented briefly in the following key contributions:

6.2.1 Systematic Electromagnetic Characterization of Textile Materials

The first key contribution of this research is the establishment of a systematic electromagnetic characterization framework for conductive textile materials using the Transmission Line Method, with explicit consideration of substrate thickness variation. In contrast to conventional characterization approaches that treat the substrate at manufactured-condition, the proposed method evaluates how different textile substrate thicknesses influence the measured and simulated transmission behaviour. From an electromagnetic perspective, variation in substrate thickness modifies the field distribution surrounding the transmission line and the coupling between the conductive strip and ground plane. These changes influence the propagation constant and the measured scattering parameters, particularly S_{11} and S_{21}.

The simulation analysis was subsequently validated through fabricated transmission-line samples and measurement. The comparison between simulated and measured responses confirmed the importance of incorporating the actual substrate thickness in the characterization model. This reduces uncertainty in the material properties extraction, improves the reliability of conductive-textile modelling, and provides more representative input parameters for the subsequent antenna simulation and design. Accordingly, the contribution is not merely the application of the Transmission Line Method, but the development of a validated, substrate-thickness-

optimized characterization procedure that links textile geometric variation to electromagnetic propagation and antenna-modelling accuracy.

6.2.2 Integrated Single Layer Fully Textile Circularly Polarized Antenna with Wide Angular Coverage

The second contribution is the development of an integrated single-layer, single-feed, fully textile circularly polarized antenna for GPS-L1 applications. The proposed configuration incorporates the radiating patch, circular-polarization perturbation features, textile substrate, and ground plane within a structurally simple single-layer antenna architecture, without requiring stacked radiators, multilayer substrates, additional parasitic elements, or a complex feeding network. This is particularly significant for wearable implementation, as a single-layer structure reduces profile, fabrication complexity, alignment error, material interfaces, and mechanical rigidity, while improving flexibility and conformability.

The antenna combines corner truncation and mirrored dual L-shaped slots to control the excitation of two orthogonal resonant modes. Although corner truncation and L-shaped slots are established techniques, their coordinated integration within a single-layer fully textile configuration enables the required modal amplitude balance and an approximately 90° phase difference for circular polarization. The slot arrangement lengthens and redistributes the surface-current paths, while the corner truncation perturbs the near-degenerate orthogonal modes. The electromagnetic significance of this integration is that circular polarization is achieved without introducing additional layers or supplementary radiating elements that could increase thickness and disturb the flexibility of the textile structure.

The significance of this contribution is therefore not merely the achievement of circular polarization at broadside, but the realization of wide axial-ratio beamwidth using a compact single-layer architecture. This wide angular circular-polarization coverage is important for wearable GPS reception because the relative orientation between the antenna and the satellite is not fixed. The contribution lies in the integrated electromagnetic behaviour of the radiating structure, which produces stable circular polarization over a wide angular region while retaining a low-profile, flexible, lightweight, and fully textile construction. Hence, the novelty is associated with achieving wide angular circular-polarization coverage through a structurally

uncomplicated single-layer textile antenna rather than through multilayer, stacked, or multi-feed configurations.

6.2.3 Out-of-Patch-Footprint DGS for Bandwidth Enhancement, Beamwidth Preservation, and Bending Mitigation

The third and principal antenna design contribution is the strategic placement of DGS outside the projected footprint of the radiating patch. The DGS was deliberately positioned outside the patch footprint to reduce direct perturbation of the principal radiating fields beneath the patch. A DGS placed directly under the radiating region may strongly disturb the patch-current distribution and the amplitude and phase relationship of the two orthogonal modes. Although this may broaden the bandwidth, it can also distort the radiation pattern or reduce the axial-ratio beamwidth. By placing the DGS outside the patch footprint, the proposed design spatially separates the bandwidth-enhancement mechanism from the main radiating region. This enables controlled peripheral ground-current redistribution while largely preserving the orthogonal-mode balance responsible for wide angular circular-polarization coverage.

The contribution therefore addresses the trade-off between frequency-domain CP performance represented by impedance bandwidth and axial-ratio bandwidth, and angular-domain CP performance represented by axial-ratio beamwidth. The integrated configuration improves bandwidth while preserving the wide-beamwidth characteristic at an acceptable level. The same configuration also contributes to the mitigation of bending degradation. Bending changes the antenna curvature, effective electrical length, patch-to-ground spacing, fringing-field distribution, and current-path orientation. These changes may shift the resonant frequency and disturb the orthogonal-mode amplitude and phase relationship. Since the DGS is positioned outside the main radiating region, the dominant patch-current distribution is less directly disturbed during deformation. This helps reduce the severity of bending-induced changes and enables the antenna to retain useful impedance matching, circular-polarization performance, gain, front-to-back ratio, and polarization purity under E-plane and H-plane bending. The contribution does not imply that bending effects are eliminated. In fact, the proposed design mitigates the severity and improves the robustness of the antenna under wearable deformation.

6.3 Recommendations for Future Works

This research successfully developed a fully textile circularly polarized wearable antenna incorporating a dual L-slot perturbation and DGS to achieve enhanced axial-ratio bandwidth, wide axial-ratio beamwidth, and stable performance under bending for GPS-L1 applications. Although the proposed design demonstrates satisfactory performance and experimental validation, several potential research extensions can be explored to further enhance its capability and broaden its application scope. The following recommendations are proposed for future work:

i. Multi-Band or Wideband Circularly Polarized Design for GNSS Applications

The proposed antenna is optimized for GPS-L1 (1.575 GHz). However, modern Global Navigation Satellite Systems (GNSS) operate across multiple bands such as GPS L2 and L5. Future work may extend the dual L-slot and DGS methodology to support dual-band or tri-band circular polarization while maintaining wide axial-ratio beamwidth and bending robustness. This would enhance the antenna's applicability for advanced positioning and multi-system GNSS receivers.

ii. Advanced Mechanical Deformation and On-Body Performance Evaluation

Although bending analysis under controlled E-plane and H-plane curvature was performed, future work may involve comprehensive on-body measurements, including dynamic deformation, twisting, and long-term textile fatigue analysis. Investigating human tissue loading effects, SAR evaluation, and real-time satellite signal acquisition performance would provide deeper validation for practical wearable deployment.

iii. Miniaturization and Integration with Wearable Platforms

Further miniaturization strategies may be investigated using fractal geometries, meandered slots, or high-impedance ground concepts while preserving circular polarization stability. Additionally, integration into garments, flexible substrates, or smart wearable platforms can be explored to evaluate long-term durability and electromagnetic performance under real-world usage conditions.

REFERENCES

Abd Rahman, N. H., Yamada, Y., & Ahmad, M. R. (2019). Parameters and factors affecting reliability and accuracy in measuring electro-textile conductivity using transmission line method. IEEE Access, 7, 179690–179700. https://doi.org/10.1109/ACCESS.2019.2959323

Abd Rahman, N. H., Yamada, Y., & Nordin, M. S. A. (2018). Reliability of strip line method for determination of conductivity for lossy conductive materials. IEEE Access, 6, 64630–64638. https://doi.org/10.1109/ACCESS.2018.2877399

Abd Rahman, N. H., Yamada, Y., Zulkipli, M. S., & Nordin, M. S. A. (2019). Transmission line measurement for characterization of new textile sample. 2019 IEEE Asia-Pacific Conference on Applied Electromagnetics (APACE), 25–27. https://doi.org/10.1109/APACE47377.2019.9020821

Abdalrazik, A., Gomaa, A., & Kishk, A. A. (2022). A wide axial-ratio beamwidth circularly polarized oval patch antenna with sunlight-shaped slots for GNSS and WiMAX applications. Wireless Networks, 28, 3779–3786. https://doi.org/10.1007/s11276-022-03093-8

Adam, I., Kamarudin, M. R., Rambe, A. H., Haris, N., Rahim, H. A., Wan Muhamad, W. Z. A., et al. (2021). Investigation on wearable antenna under different bending conditions for wireless body area network (WBAN) applications. International Journal of Antennas and Propagation, 2021.

Arnaiz-Morales, J. L., López-Espi, C., Allen-Cordero, A. J., Martínez-Rojas, J., & Bendahmane, A. (2019). Bending and moisture effects on the performance of a U-shaped slotted wearable antenna for off-body communications in the industrial, scientific and medical (ISM) 2.4 GHz band. Sensors, 19(8). https://doi.org/10.3390/s19081804

Atanasova, G. L., & Atanasov, N. T. (2020). Impact of electromagnetic properties of textile materials on performance of a low-profile wearable antenna backed by a reflector. International Workshop on Antenna Technology (iWAT), 1–4. https://doi.org/10.1109/iWAT48004.2020.1570609739

Baudh, R. K., Sahu, S., Parihar, M. S., & Kumar, V. D. (2024). A wideband circularly polarized all-textile on-body antenna for defense applications. IEEE Transactions on Circuits and Systems II: Express Briefs, 71(2), 567–571. https://doi.org/10.1109/TCSII.2023.3308213

Blotti, F., & Vegni, C. (2010). Design of high-performing microstrip receiving GPS antennas with multiple feeds. IEEE Antennas and Wireless Propagation Letters, 9, 248–251. https://doi.org/10.1109/LAWP.2010.2046874

Budiastuti, D., Ilyas, A. K., & Rahardjo, E. T. (2020). Design and assembly of textile microstrip antenna for global positioning system application. IEEE Region 10 Annual International Conference (TENCON), 909–913. https://doi.org/10.1109/TENCON50793.2020.9293869

Cui, P.-F., Lu, W.-J., Yu, Y., Xue, B., & Zhu, H.-B. (2018). Off-body spatial diversity reception using circular and linear polarization: Measurement and modeling. IEEE Communications Letters, 22(1), 209–212.

De Cos Gómez, M. E., Berdasco, A. F., Álvarez, H. F., & Las-Heras, F. (2020). On the way to green IoT antennas: Compact ultra-thin CPW-fed monopole on Tencel. 14th European Conference on Antennas and Propagation (EuCAP 2020), 1–5.

Douhi, S., Eddiai, A., Idiri, M., Cherkaoui, O., & Mazroui, M. (2023). Investigation of SAR reduction and gain enhancement using an all-textile antenna with metamaterial structure for wireless body area network applications. Materials Today: Proceedings. https://doi.org/10.1016/j.matpr.2023.12.034

Elsikh, T., Sayed, A., Eid, A. M., & Ailedin, A. (2019). A low-cost circularly polarized antenna array for GPS receivers. Proceedings of the 13th European Conference on Antennas and Propagation (EuCAP).

Gupta, N., Desai, P., & Bhavsar, P. (2016). Design and evaluation of a textile-integrated GPS receiver. Progress in Electromagnetics Research Symposium (PIERS 2016), 82–86.

Hussain, N., Jeong, M. J., Abbas, A., Kim, T. J., & Kim, N. (2020). A metasurface-based low-profile wideband circularly polarized patch antenna for 5G millimeter-wave systems. IEEE Access, 8, 22127–22135. https://doi.org/10.1109/ACCESS.2020.2969964

Ilyas, A. K., Budiastuti, D., & Rahardjo, E. T. (2020). Effect of textile substrate on antenna performance for GPS application. IEEE Region 10 Annual International Conference (TENCON), 914–918. https://doi.org/10.1109/TENCON50793.2020.9293920

Jais, M. I., Malek, M. F., Jamlos, M. F., & Jusoh, M. (2012). Conductive e-textile analysis of 1.575 GHz rectangular antenna with H-slot for GPS application.

Loughborough Antennas and Propagation Conference (LAPC 2012). https://doi.org/10.1109/LAPC.2012.6402958

Joshi, R., et al. (2020). Dual-band, dual-sense textile antenna with AMC backing for localization using GPS and WBAN/WLAN. IEEE Access, 8, 89468–89478. https://doi.org/10.1109/ACCESS.2020.2993371

Kaivanto, E., Salonen, E., & Khaleel, H. (2014). Circularly polarized wearable antennas. 82, 145–161. https://doi.org/10.2495/978-1-84564-986-9/008

Khandelwal, M. K., Kanaujia, B. K., & Kumar, S. (2017). Defected ground structure: Fundamentals, analysis, and applications in modern wireless trends. International Journal of Antennas and Propagation, 2017, Article 2018527. https://doi.org/10.1155/2017/2018527

Kim, Y. D., Le, T. T., & Yun, T. Y. (2025). An enhanced circularly polarized textile antenna using a metasurface and slot-patterned ground for off-body communications. Micromachines, 16(7), 1–15. https://doi.org/10.3390/mi16070799

Kolusu, D., & Nanda, S. (2026). Developing and examining a compact dual band circularly polarized ultra-wideband antenna covering C-band and X-band applications. Scientific Reports, 16, 5283. https://doi.org/10.1038/s41598-026-35607-1

Kumar, C., & Guha, D. (2020). Asymmetric and compact DGS configuration for circular patch with improved radiations. IEEE Antennas and Wireless Propagation Letters, 19(2), 355–359.

Le, T. T., Kim, Y. D., & Yun, T. Y. (2023). All-textile enhanced-bandwidth polarization-conversion antenna using a nonuniform metasurface. IEEE Antennas and Wireless Propagation Letters, 22(10), 2432–2436. https://doi.org/10.1109/LAWP.2023.3290159

Le, T. T., Kim, Y. D., & Yun, T. Y. (2024). Bandwidth-enhanced circularly polarized all-textile wearable antenna using an LP-to-CP metasurface. IEEE Access, 12, 173749–173757. https://doi.org/10.1109/ACCESS.2024.3501282

Li, M., Yu, J., Shen, X., Lemma, L. N., Zeng, D., & Yi, Z. (2025). Compact broadband GNSS antenna with wide AR beamwidth. IEEE Antennas and Wireless Propagation Letters, 24(10).

Li, X., Ma, R., Cai, H., Pan, Y.-M., & Zhang, X. Y. (2023). High-gain dual-band aperture-shared CP patch antenna with wide AR beamwidth for satellite

navigation system. IEEE Antennas and Wireless Propagation Letters, 22(8), 1888–1892.

Loss, C., Gonçalves, R., Pinho, P., & Salvado, R. (2020). A review of methods for the electromagnetic characterization of textile materials for the development of wearable antennas. Wireless Power Transmission for Sustainable Electronics: COST WiPE - IC1301, 27–56. https://doi.org/10.1002/9781119578598.ch2

Madhuri Sahal, & Tiwari, V. N. (2016). Review of circular polarization techniques for design of microstrip patch antenna. In Proceedings of the International Conference on Recent Cognizance in Wireless Communication & Image Processing (pp. 663–669). https://doi.org/10.1007/978-81-322-2638-3_74

Mahfuz, M. M. H., Islam, M. R., Park, C. W., Elsheikh, E. A. A., Suliman, F. M., Habaebi, M. H., Malek, N. A., & Sakib, N. (2022). Wearable textile patch antenna: Challenges and future directions. IEEE Access, 10, 38406–38427. https://doi.org/10.1109/ACCESS.2022.3161564

Mahmood, S. N., Ishak, A. J., Saeidi, T., Soh, A. C., Jalal, A., Imran, M. A., et al. (2021). Full ground ultra-wideband wearable textile antenna for breast cancer and wireless body area network applications. Micromachines, 12(3), 1–16.

Malaysian Communications and Multimedia Commission. (2022). Spectrum plan 2022.

Malaysian Communications and Multimedia Commission. (2023). Spectrum management. http://mcmc.gov.my/en/spectrum/spectrum-management

Memon, A. W., de Paula, L. L., Malengier, B., Vasile, S., Van Torre, P., & Van Langenhove, L. (2021). Breathable textile rectangular ring microstrip patch antenna at 2.45 GHz for wearable applications. Sensors, 21(5), 1–17. https://doi.org/10.3390/s21051635

Meng, L., Li, Y., & Huang, Z. (2022). A simple single-fed left/right-hand circular polarization antenna for GPS applications. Applied Computational Electromagnetics Society Journal, 37(12), 1216–1224.

Moharana, M., & Dwivedy, B. (2024). Circularly polarized planar antennas with enhanced characteristics for contemporary wireless communication use cases: A review. IEEE Access, 12, 134594–134613. https://doi.org/10.1109/ACCESS.2024.3415483

Najim, H. S., Mosleh, M. F., & Abd-Alhameed, R. A. (2023). Design and simulate a new and simple circular polarization antenna for applications in C-band. AIP Conference Proceedings, 2804(1). https://doi.org/10.1063/5.0154505

Narbudowicz, A. (2021). Antenna technology for GNSS. In GPS and GNSS Technology in Geosciences (pp. 99–117). https://doi.org/10.1016/B978-0-12-818617-6.00003-2

Nasimuddin, Anjani, Y. S., & Alphones, A. (2015). A wide-beam circularly polarized asymmetric-microstrip antenna. IEEE Transactions on Antennas and Propagation, 63(8), 3764–3768. https://doi.org/10.1109/TAP.2015.2438397

Nasimuddin, Qing, X., & Chen, Z. N. (2014). A compact circularly polarized slotted patch antenna for GNSS applications. IEEE Transactions on Antennas and Propagation, 62(12), 6506–6509. https://doi.org/10.1109/TAP.2014.2360218

Noor, S. K., Ramli, N., Rahman, N. H. A., & Najib Mohd Yasin, M. (2021). Performance comparison between polyester and denim textile antenna on non-identical human upper arm sizes for 5G mid-band. IconSpace 2021, 40–45.

Paracha, K. N., Abdul Rahim, S. K., Soh, P. J., & Khalily, M. (2019). Wearable antennas: A review of materials, structures, and innovative features for autonomous communication and sensing. IEEE Access, 7, 56694–56712.

Park, M., Lee, W., & Son, T. (2016). Composite GPS patch antenna for the AR bandwidth enhancement. International Journal of Antennas and Propagation, 2016, 1–7. https://doi.org/10.1155/2016/3250920

Pazil, A. F. M., Abd Rahman, N. H., Ramli, N., & Awang, R. A. (2020). Study on the effects of fabric thickness and human phantom to wearable textile antenna performance. IEEE RFM 2020, 1–4.

Pazil, A. F., Huda, N., Rahman, A., Ramli, N., Farhana, N., & Razak, H. A. (2021). Comparative analysis on different feeding techniques of textile antenna for GPS-L1 application. Journal of Engineering & Technological Advances, 6(1). https://doi.org/10.35934/segi.v6i1.20

Potey, P. M., & Tuckley, K. (2018). Design of wearable textile antenna with various substrate and investigation on fabric selection. ICMAP 2018, 1–2.

Prajapati, B. D., Jaiswal, B., & Dalvadi, P. J. (2025). Wideband elliptical patch antenna integrating a circular notch and defected ground structure. Progress in Electromagnetics Research C, 156, 161–168.

Rahman, H. M. A., Shovon, M. N. A., & Khan, M. M. (2025). Conformal design of a 60 GHz textile based self-complementary antenna for wireless body area network. E-Prime - Advances in Electrical Engineering, Electronics and Energy, 11, 100892. https://doi.org/10.1016/j.prime.2024.100892

Rajavel, V., & Ghoshal, D. (2023). A compact triband antenna using artificial magnetic conductor for wireless body area network communications. Wireless Networks, 29(6), 2773–2795.

Resmi, S., Hake, S., Sulaikha, S., & Behera, R. (2020). Slit loaded textile microstrip antennas. IETE Journal of Research. https://doi.org/10.1080/03772063.2019.1709572

Rizwan, M., Syedjahrome, L., & Ur Rehman, M. (2015). Impact of bending on the performance of circularly polarized wearable antennas. Progress in Electromagnetics Research Symposium (PIERS 2015), 732–737.

Saha, P., Mitra, D., & Parui, S. K. (2021). Control of gain and SAR for wearable antenna using AMC structure. *Radioengineering, 30*(1), 81–88. https://doi.org/10.13164/re.2021.0081

Samat, A. A., Zaidel, D. N. A., Mat, D. A. A., Sharip, M. R. M., Muhamad, I. I., & Then, Y. L. (2020). Surface current distribution and performance analysis of different feeding techniques for microstrip patch antenna. In 2020 13th International UNIMAS Engineering Conference (EnCon 2020). https://doi.org/10.1109/EnCon51501.2020.9299340

Scarpello, M. L., Nguyen-Trong, N., & Crozier, S. (2013). Bending investigation of broadband wearable all-textile antennas. Australian Journal of Basic and Applied Sciences, 7(10), 91–94.

Shakhirul, M. S., Jusoh, M., Ismail, A. H., Kamarudin, M. R., & Ijas, M. R. (2015). Analysis of circular polarization textile antenna in bending condition. 2015 2nd International Conference on Computer, Communication, Control and Information Technology (C4IT), 360–363. https://doi.org/10.1109/IC4IT.2015.7219598

Sharma, D., Tiwari, R. N., Singh, D. K., & Matekovits, L. (2025). A pocket-integrated miniature, dual-band, and high gain textile MIMO antenna for 5G and WiFi wearable applications. Scientific Reports, 15(1), 1–27.

Singh, J., Kalra, P., Singh, A., & Sidhu, E. (2016). High gain textile rectangular microstrip patch antenna design employing jeans substrate for satellite space to earth downlink applications. Progress in Electromagnetics Research Symposium (PIERS 2016), 338–343.

Singh, S., & Mishra, R. (2025). Conformal dual-band high-gain antenna for ISM bands with low SAR on textile for wireless BAN. Engineering Research Express, 7(2).

Singh, S., & Verma, S. (2021). Compact wearable dual wideband circularly polarized L-strip fed slotted textile antenna with parasitic elements for ISM band applications. Journal of Electromagnetic Waves and Applications, 35(2), 185–197.

Suraya, A. N., Sabapathy, T., Jusoh, M., Ghazali, N. H., Osman, M. N., Ismail, S., & Awal, M. R. (2019). Wearable antenna gain enhancement using reactive impedance substrate. Indonesian Journal of Electrical Engineering and Computer Science, 13(2), 708–712. https://doi.org/10.11591/ijeecs.v13.i2.pp708-712

Tekneci, G., Cinar, A., Gorgun, A. R., & Cumhur Basaran, S. (2025). Dual-band compact textile antenna design based on nested split-ring resonators. AEU - International Journal of Electronics and Communications, 191, 155654.

Wang, M.-S., Zhu, X.-Q., Guo, Y.-X., & Wu, W. (2018). Compact circularly polarized patch antenna with wide axial ratio beamwidth. IEEE Antennas and Wireless Propagation Letters, 17(4), 714–718. https://doi.org/10.1109/LAWP.2018.2813160

Wichaidit, P., Dentri, S., Janpangern, P., Lertwinyaraporn, T., Krairiksh, M., & Phongcharoenpanich, C. (2024). Broadband CP corner-truncated microstrip antenna with irregularly hexagonal AMC for 2.45 GHz applications. Alexandria Engineering Journal, 97, 88–99.

Yan, H., Awan, W. M., Ali, S., Subahir, M. S. N., & Kamarudin, M. R. (2016). Comparative analysis for multilayer stacked substrates microstrip patch antenna. 2016 IEEE Asia-Pacific Conference on Applied Electromagnetics (APACE), 34–37.

Yang, H., Liu, X., & Fan, Y. (2022). Design of broadband circularly polarized all-textile antenna and its conformal array for wearable devices. IEEE Transactions on Antennas and Propagation, 70(1), 209–220.

Zhai, J., Chen, G., Wang, W., Liu, Y., & Wang, Z. (2022). A novel low-profile circularly polarized GNSS antenna with wide 3 dB axial ratio beamwidth. Progress in Electromagnetics Research M, 111, 199–208.

Zhong, Z.-P., Zhang, X., Liang, J.-J., Han, C.-Z., Fan, M.-L., Huang, G.-L., Xu, W., & Yuan, T. (2019). A compact dual-band circularly polarized antenna with wide axial-ratio beamwidth for vehicle GPS satellite navigation application. IEEE Transactions on Vehicular Technology, 68(9).

APPENDICES

APPENDIX 1

Radio Spectrum Allocation in Malaysia

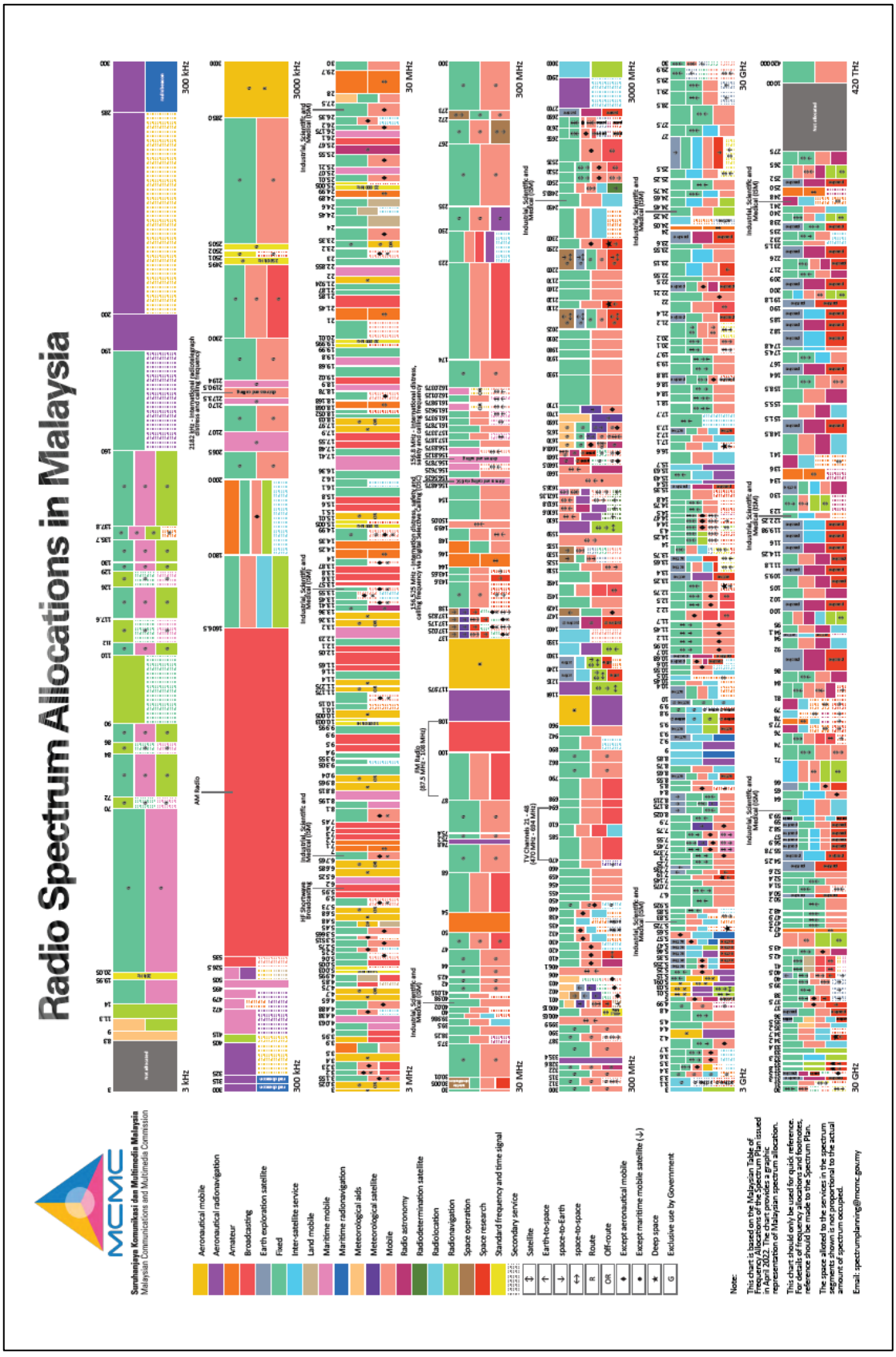

APPENDIX 2

SMA Connector Datasheet

SMA Square Flange Jack Receptacle

multicomp PRO

RoHS Compliant

Specifications

Electrical

Frequency Range	: DC – 18GHz
Nominal Impedance	: 50Ω
Voltage Rating	: 500V Max.
VSWR	: 1.23 Max.

Material

Body	: Brass, 3µ" Gold Plated
Center Contact	: Beryllium Copper, 50µ" Gold Plated
Insulation	: PTFE

Mechanical

Interface in Accordance with	: MIL-STD-348A

Environmental

Temperature Range	: -65°C to +165°C



Diagram

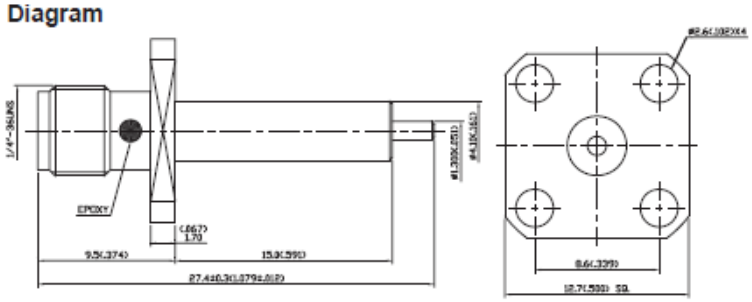

Dimensions : Millimetres (Inches)

Part Number Table

Description	Part Number
SMA Square Flange Jack Receptacle, 50Ω	MP-19-13-11-TGG

Important Notice : This data sheet and its contents (the "Information") belong to the members of the AVNET group of companies (the "Group") or are licensed to it. No licence is granted for the use of it other than for information purposes in connection with the products to which it relates. No licence of any intellectual property rights is granted. The information is subject to change without notice and replaces all data sheets previously supplied. The information supplied is believed to be accurate but the Group assumes no responsibility for its accuracy or completeness, any error in or omission from it or for any use made of it. Users of this data sheet should check for themselves the information and the suitability of the products for their purpose and not make any assumptions based on information included or omitted. Liability for loss or damage resulting from any reliance on the information or use of it (including liability resulting from negligence or where the Group was aware of the possibility of such loss or damage arising) is excluded. This will not operate to limit or restrict the Group's liability for death or personal injury resulting from its negligence. Multicomp Pro is the registered trademark of Premier Farnell Limited 2019.

APPENDIX 3

Felt Datasheet

ENGLISH

Datasheet

Viscose, Wool Felt Sheet, 1000 x 500mm x 12.5mm

RS Stock number 733-6788



Description:

Medium density white felt sheet 0.25sg, ideal for filtration, absorption, cladding and sealing applications. Manufactured from 70% wool and 30% viscose

Specifications:

Density:	0.25gm/CC Tolerance 3mm and below +/- 20% 3.1 to 10.0mm +/- 15% above 10.0mm +/- 10%
Colour:	Natural White
Composition:	Wool 70% (nominal) Viscose 30%
Thickness:	1.0 to 25.0mm (1/16 inch to 1 inch) Tolerance 3mm and below +/- 20% 3.1 to 10.0mm +/- 15% above 10.0mm +/- 10%
Width:	500mm
BS SPEC:	Tolerances to BS.4060

RS, Professionally Approved Products, gives you professional quality parts across all products categories. Our range has been testified by engineers as giving comparable quality to that of the leading brands without paying a premium price.

APPENDIX 4

Shieldit Super Datasheet

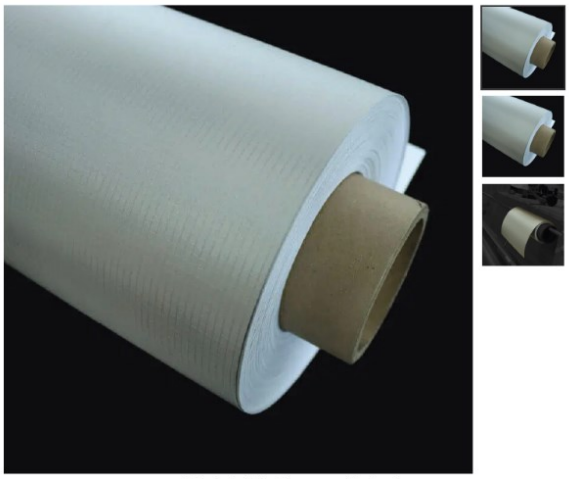

Shieldit Super Fabric

Description | Additional Details

Description

This is the best EMF shielding patch material, combining superior performance with unmatched versatility. Shieldit Super Fabric features a rugged rip-stop polyester substrate coated with Nickel and Copper for excellent shielding efficiency and low corrosion. One side is treated with a non-conductive hot melt adhesive that activates at 130°C (266°F), allowing you to easily iron it onto cotton, wood, glass, or paper.

With shielding performance exceeding 60 dB up to 40 GHz, this fabric is perfect for blocking radiofrequency and microwave radiation. Grounded applications also block ELF and VLF electric fields, offering comprehensive protection in a lightweight, durable material. Whether you're lining clothing, shielding cables, or creating custom patches, this RF shielding patch material provides flexibility and reliability for your projects.

Why Choose Shieldit Super Fabric?

1. **Exceptional Shielding Performance**: Blocks >60 dB from 10 MHz to 3+ GHz, protecting against RF, microwave, ELF, and VLF fields.
2. **Flame Retardant**: Certified to UL 94V-0 standards for added safety.
3. **Versatile Adhesive Application**: Easily bonds to cotton, wood, glass, or paper with heat activation.
4. **Durable and Flexible**: Rugged rip-stop polyester for strength and easy handling. Can also be cut and sewn like ordinary fabric.
5. **Customizable Use**: Perfect for shielding cables, making patches, or lining clothing and drapes.

Specifications

- **Material Composition**: Polyester base, Nickel/Copper plated
- **Weight**: 230 g/m²
- **Thickness**: 0.17 mm
- **Width**: Approximately 13 inches
- **Resistivity**: <0.07 Ohms per square
- **Temperature Range**: Hot melt adhesive activates at 130°C (266°F); max temperature 200°C (392°F)
- **Flame Retardant Certification**: UL 94V-0
- **Color**: Gray

Applications

The best RF shielding patch material, Shieldit Super Fabric is ideal for:

- **Shielding Patches**: Iron onto cotton, glass, wood, or paper for versatile protection.
- **Cable Shielding**: Wrap extension cords, computer cables, and other electronics.
- **Custom RF Shields**: Create sheet shields for beds, walls, or drapes.
- **Clothing Liners**: Line hats, vests, or other garments to protect vital organs from radio waves.
- **DIY Projects**: Heat-seal seams to form custom tubes or shapes for specialized needs.

Care and Handling Instructions

1. Avoid direct skin contact with the Nickel-coated side; line with cotton if necessary.
2. Activate the adhesive with an iron set to 130°C (266°F).
3. Do not expose to temperatures exceeding 200°C (392°F).
4. Clean with a damp cloth; avoid harsh chemicals.

Email: lessemf@lessemf.com

Phone: +1-518-608-6479

Less EMF shielding fabrics, plastics, and paints are lab tested, ensuring you achieve the highest level of shielding: Keystone Compliance

Terms and Conditions

APPENDIX 5

OTA-500 Atenlab Anaechoic Chamber



Atenlab

Atenlab introduction

When precision, speed and reliability are critical to your key investments in research and development, mere savings in cost and time may not be enough. Atenlab's wireless measurement solutions go further, guaranteeing flawless results and absolute peace of mind.

Atenlab's proprietary OTA measurement systems have been approved by the CTIA, guaranteeing their quality and reliability.



antennas

Product: Dual Polarization Horn Antenna
Frequency: 700MHzâ€“7GHz
Connector: N-Type



Passive Components

Product: Rotary Joint
Frequency: DCâ€“6GHz
V.S.W.R.: 1.5@6GHz
Connector: SMA Female



Waveguides

Product: WR UG Series
Frequency: 1.7GHzâ€“40GHz
Type: Straight, Bend, Flexible, Twist



Chambers

Product: Shielding Room, Absorber
Frequency: 30MHzâ€“18GHz
Attenuation: -100 dB

ota measurement system diagram

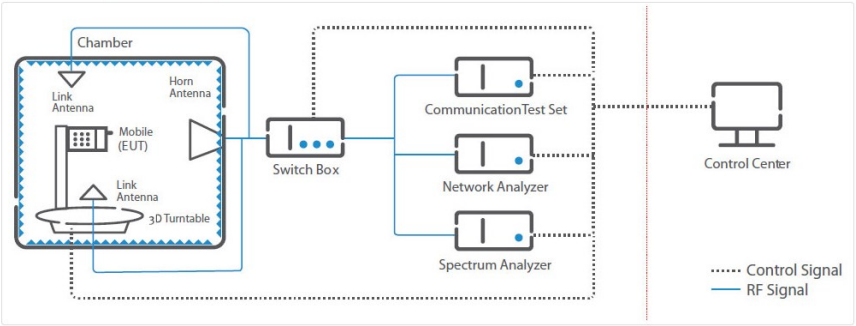

Chamber

The electromagnetic simulation chamber is designed to maximize the effectiveness and efficiency of the measurement space.

3D Turntable

The design and material used reduces electromagnetic reflection, improves the quality of measurements, and allows developers to easily switch the equipment under testing (EUT).

Link Antenna

The circular polarization broadband antenna allows the signal from the equipment under testing (EUT) to be measured from all angles.

Broadband Horn Antenna

A dual-polarization broadband horn antenna avoids antenna motion error and improves measurement accuracy.

Instrumentation

Atenlab systems are designed to function with all client instrumentation

Switch Box

Atenlab-developed path switches greatly improve the measurement speed and quality of automated measurements, with low return loss and high speed switching.

Golden Sample

Standard calibration procedures are essential for system stability and accuracy. Atenlab calibration results aid clients when comparing analyses with their own validation processes.

chamber sizes / cm

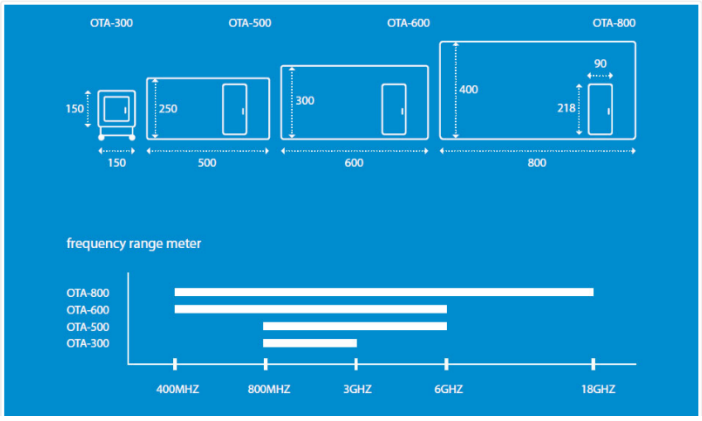

ota-300

- 3(l) x 1.5(w) x 2(h) meter
- EUT type: cellphone
- Frequency: 800MHz - 3GHz
- Measurement length: 2 meters
- Transportable chamber
- Suitable for products under 12 inches long and locations with limited space

ota-500

- 5(l) x 2.5(w) x 2.5(h) meter
- EUT type: cellphone, laptop
- Frequency range: 800MHzâ€“6GHz
- Measurement range: 3.5 meters
- Suitable for office installation
- Suitable for products 30 x 30 cm and under

ota-600

- 6(l) x 3(w) x 3(h) meter
- EUT type: cellphone, laptop
- Frequency range: 400MHzâ€“6GHz
- Measurement length: 4 meters
- Suitable for wide band testing labs

ctia ota-800

- 8(l) x 4(w) x 4(h) meter
- EUT type: cellphone, laptop
- Frequency range: 400MHzâ€“18GHz
- Measurement range: 5.5 meters
- CTIA accredited

Agilent

Communication Test Set

Agilent 8960 (E5515C) Wireless Communication Test Set

- GSM Option
- GPRS/EGPRS Option (Requires GSM Option)
- WCDMA Option
- HSDPA Option (Requires WCDMA Option)
- CDMA-2000 Option
- 1 x EV-DO Option (Requires CDMA Option)
- TD-SCDMA Option



Spectrum Analyzer

- E44xx Series
- 85xx Series
- E74xx Series
- N90xx Series
- N93xx Series



Network Analyzer

- E50xx Series
- N52xx Series
- E83xx Series



Signal Generator

- Agilent E4438C ESG
  Vector Signal Generator



Rohde & Schwarz (R&S)

CMU-200 Wireless Communication Test Set

- GSM Option
- GPRS/EGPRS Option (Requires GSM Option)
- WCDMA Option
- HSDPA Option (Requires WCDMA Option)
- CDMA-2000 Option
- 1 x EV-DO Option (Requires CDMA Option)
- TD-SCDMA Option



Spectrum Analyzer

- FSC Series
- FSL Series
- FSP Series
- FSV Series
- FSG Series
- FSQ Series
- FSU Series



Network Analyzer

- ZVA Series
- ZVB Series
- ZVL Series
- ZVT Series



AUTHOR'S PROFILE



Anis Fariza Md. Pazil obtained the Bachelor of Computer System and Communications Engineering from University Putra Malaysia in 2001 and subsequently MSc. in Information Technology from Universiti Teknologi MARA (UiTM) in 2006. She is a Senior Lecturer in the Electrical & Electronics Engineering department at SEGi University and currently pursuing her PhD. in Electrical Engineering at UiTM, Shah Alam. She was also the recipient of Gold Award, Special Jury Award, IEEE VTS/Comm Award in the Innovation and Invention Challenge College of Engineering, UiTM and also won the International Gold Award in Malaysia Technology Expo (MTE) in 2022. Her research interests include wearable textile antenna, RF & microwaves design and satellite communications.

LIST OF ACHIEVEMENTS

List of Publication:

A. F. Md. Pazil, N. H. . Abd Rahman, N. . Ramli, R. A. . Awang, and N. H. . Abdul Aziz, "Textile Characterization for Wearable Antenna Application Using Transmission Line Method", International Journal of Integrated Engineering (IJIE), vol. 15, no. 3, pp. 153–162, Aug. 2023.

A. F. M. Pazil, N. H. A. Rahman, N. Ramli, and R. A. Awang, "Bending Analysis of a Dual L-shaped Slotted Circularly Polarised Wearable Textile Antenna for GPS Application,"2021 IEEE Asia-Pacific Conference on Applied Electromagnetic (APACE), Penang,2023, pp 1-4.

A. F. M. Pazil, N. H. A. Rahman, N. Ramli, and R. A. Awang, "Study on the Effects of Fabric Thickness and Human Phantom to Wearable Textile Antenna Performance," 2020 IEEE Int. RF Microw. Conf. RFM 2020 - Proceeding, no. 1, pp. 8–11, 2020.

A. F. Pazil, N. Huda, A. Rahman, N. Ramli, and N. F. H. A. Razak, "Comparative Analysis on Different Feeding Techniques of Textile Antenna for GPS-L1 Application," J. Eng. Technol. Adv., vol. 6, no. 1, 2021.

A. F. Pazil, N. Huda, A. Rahman, N. Ramli, and N. F. H. A. Razak , "Textile-Based Antenna using Aperture-Coupled Technique for Global Positioning System (GPS) Application" J. Eng. Technol. Adv., vol. 5, no. 2, pp. 34-42 (2020).

Nurulazlina Ramli, **Anis Fariza Md. Pazil**, Noor Farhana Halil Abdul Razak, Design of Reconfigurable Stacked Patch Microstrip Antenna (RSPMA) at 1.8 GHz and 2.3 GHz, Journal of Engineering & Technological Advances, Vol. 5, Issue 1, pp. 34-46 (2020).

Khalifa, T., Ramli, N., **Pazil, A.F.M**., Abd Rahman, N.H., Alias, A.J. (2022). Simulation on Circularly Polarization Cotton Textile Antenna for Wireless Communication System. In: Ab. Nasir, A.F., Ibrahim, A.N., Ishak, I., Mat Yahya, N., Zakaria, M.A., P. P. Abdul Majeed, A. (eds) Recent Trends in Mechatronics Towards Industry 4.0. Lecture Notes in Electrical Engineering, vol 730. Springer, Singapore.

Awards:

1. **Gold Award** – Malaysia Technology Expo 2022 (MTE2022) SDG International Innovation Awards & Expo (SDGIIA), 17th -21st October 2022, Virtual Platform.
2. **Gold Award** & **Special Jury Award & IEEE VTS/Comm Malaysia Chapter Award** - Innovation and Invention Challenge College of Engineering (IICCE2022), 18th – 19th July 2022, Kolej Mawar, UiTM Shah Alam.
3. **Gold Award** and **Best Presenter** - Engineering, Science & Technology Exhibition 2021 (ESTE 2021), MAHSA University.